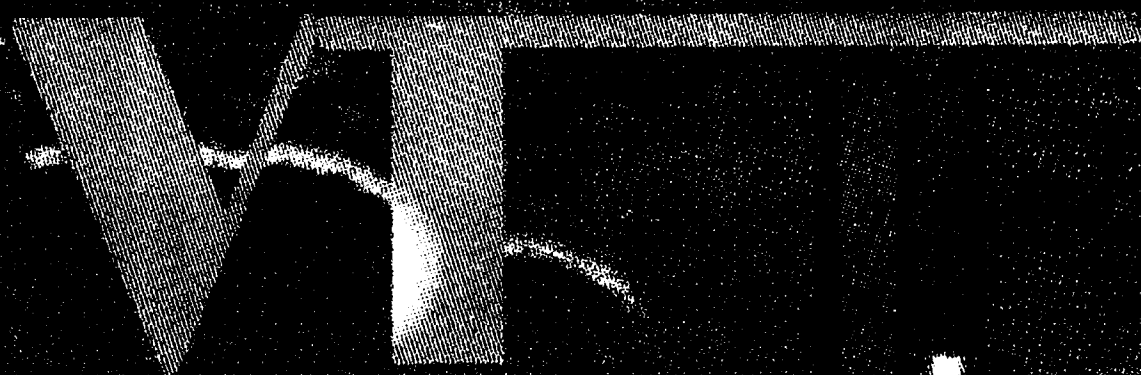1992-93 Space Design

(NASA-CR-195533)   LOLA: LUNAR
OPTICAL LONG-BASELINE ARRAY.
1992-1993 SPACE DESIGN (Virginia
Polytechnic Inst. and State Univ.)
206 p

N94-24582

Unclas

G3/32   0204264

VT

Virginia Polytechnic &
State University

LOLA

Lunar Optical Long-baseline Array

USRA/NASA Advanced Design Program
June 1993

Daniel Bronte
Joanne Chaney
Christine Curran
Keith Ferguson
Eric Flint
Tony Giunta
Duane Knill

Daniel Levesque
Donald Lyon
Sean Murphy
Chris Shively
Angela Wesner
Tom Yablonski

Advisor:
Dr. Antoni K. Jakubowski

Department of Aerospace and Ocean Engineering
Virginia Polytechnic Institute and State University
Blacksburg, VA 24060

LOLA - VT Space Design

LOLA

Lunar Optical Long-baseline Array

Abstract

The Lunar Optical Long-baseline Array consists of 27 telescopes elements arranged in a Y-configuration, nine elements per arm. The 2.9 km array arms point north, southeast, and southwest with 120° between each arm, providing a 5 km maximum baseline and a 220 m minimum baseline. The array is designed primarily to operate in the optical wavelengths, allowing a resolution of 10^{-5} arcseconds at a wavelength of 500 nm, but its full spectral range spans from 200 to 10,000 nm.

The 1.5 m diameter primary mirror and 0.25 m diameter secondary mirror, both parabolic with a focal number of 2.46, are mounted in a Mersenne configuration. The optical cylinder is mounted off axis 1.3 m above the lunar surface.

A two-staged coarse and fine beam delay is utilized to equalize the optical path lengths of all 27 beams. Prior to entering the fine delay lines, the beams are compressed using a Cassegrain system from 25 to 4 cm diameter. The laser metrology system actively measures the optical path lengths and provides nanometer path length corrections to the fine delay system. The pointing and control system positions the telescopes to an accuracy of 10^{-6} arcseconds by targeting a guide star near the object to be studied. An achromatic nulling system allows direct planet detection in the infrared wavelengths.

Four scientific instruments, contained in a rotating carousel, provide object resolution and spectroscopic analysis over a spectral range from 150 to 10,000 nm. A fifth instrument, operating from 1000 nm to 10000nm is provided specifically for the achromatic nulling interferometer. The field of view for all instruments ranges from 15 arcseconds down to 10^{-6} arcseconds, selected using various focusing apertures. The instruments, along with the associated data systems, are actively cooled through a thermal control system. The instrumentation room is shielded from cosmic radiation by a 5 m thick blanket of lunar regolith.

A satellite orbiting the second libration point of the Earth-Moon system mediates the data transfer between the lunar base and the Earth-based Deep Space Network. The communication system operates in the X-band and provides 100 Mbps downlink and 50 Mbps uplink for Earth-Moon communications.

The array will be constructed in two stages, an initial stage of 9 elements and a final stage of 18 elements. The final array will be powered by three 2.5 kW Dynamic Isotope Power Systems.

Emplacement of the array on the lunar surface is designed to require minimal labor, equipment, and costs. The Lunar Optical Long-baseline Array is designed to be fully operational by the year 2010.

Contents

List of Figures

List of Tables

1.0 Introduction

In the fall of 1992, the design and analysis of a lunar-based optical interferometer telescope array was initiated by a group of students in the Department of Aerospace Engineering at Virginia Tech. This project was undertaken at the suggestion of the Space Exploration Initiative Office at the NASA Langley Research Center.

The original array design requirements, listed below, centered on the primary objective of resolving Earth-type planets about stars out to a distance of 10 parsecs.

- spectrum coverage spanning wavelengths from 5 nm to 5 mm, with a primary operating mode in the visible spectrum
- a total collecting area providing a signal-to-noise ratio (SNR) of no less than 10.0 for a median wavelength of 500 nm
- the individual array elements must be identical and have a maximum optical diameter of 2.0 m
- lunar site selection is limited to 10° north and south of the lunar equator on the lunar far side while not closer than 15° to either near-side limb

Following construction by astronaut crews, array operation will be conducted from Earth and astronomical observations will not be conducted during the lunar day. The entire system was to be designed for minimum achievable mass.

The majority of the original design requirements for the telescope array were met.

1.1 Objectives

As stated above, the primary objective of the Lunar Optical Long-baseline Array (LOLA) is to detect and resolve Earth-sized planets around stars at a distance up to 10 parsecs from Earth. With the LOLA design, the observable spectrum spans 150 to 6000 nm with the visible spectrum from 400 to 700 nm as the region of primary interest. At completion, LOLA provides a resolution of 10^{-5} arcseconds and a SNR of 10.0 at a wavelength of 1000 nm for long integration times. This resolution is an improvement of two orders of magnitude over the Hubble Space Telescope.

In addition to the observation of distant planets, LOLA provides a variety of astronomical opportunities unavailable with current Earth-based or space-based telescopes. This includes the ability to study white dwarf stars, stellar and black hole accretion disks, and galactic nuclei. Further, LOLA will offer observations of planets and other bodies within this solar system at a resolution equalling that obtained by the Voyager spacecrafts.

1.2 Scope

In this report, the design and construction of the lunar interferometer is outlined. This report focuses on the design of individual telescopes and the optical requirements necessary for interferometric imaging. Communications, power, thermal, and metrology requirements were also addressed. In addition, launch manifesting, transportation to the Moon, lunar site preparation, and array construction were considered. An estimation of the projected costs for array construction and operation were also investigated. The design of the telescopes, along with the supporting structures and systems, is driven by two factors; maximum optical performance and minimum mass.

1.3 Background

In order to achieve high resolution optical astronomy, large apertures are required. For a single monolithic telescope system, this translates into a large diameter primary mirror on the order of 10 meters or greater. Such a design is prohibitive both from a production and a structural point of view, particularly because of the optical aberrations produced as the mirror deforms under its own weight. Large diameter segmented mirrors have been studied and constructed (Ref. 1.3-1) although there are structural drawbacks to these designs as well.

An alternative to a single mirror telescope is an interferometric array of several small telescopes. By the process of interferometry, the resolution obtained corresponds to a single telescope having an aperture equal to the maximum spacing between the telescopes of the array. A more detailed explanation of the underlying principles of interferometry is provided in a later section of this report. Although the complexities associated with optical interferometry are significant, the success of radio interferometry in astronomy (Ref. 1.3-2) has demonstrated the viability of this concept.

Earth-based interferometry has been the subject of considerable study (Ref. 1.3-3) and currently several systems are in operation (Ref. 1.3-4). To overcome the limitations imposed by the Earth's atmosphere, both space-based and lunar-based (Ref. 1.3-5,6) interferometers have been considered. Optical interferometric astronomy requires extremely high accuracy with optical paths known to nanometer precision. Because of the rapid thermal cycling and the relatively short observation times associated with orbiting telescopes, large-scale space-based interferometry is impractical at this time. In contrast, the lunar surface provides a seismically stable surface and a 14 Earth-day thermal and observation cycle. These features make the Moon an ideal site for optical interferometric astronomy.

Several recent studies have examined the feasibility of the design and operation of a lunar-based optical interferometric array (Ref. 1.3-7). These reports imply that optical interferometry is possible, but they often do not explore the array design beyond that of the major component level. It is the intention of this study to provide a more detailed design down to the subsystem level and to quantify the critical factors which govern all aspects of the array design.

1.4 Design Approach

The LOLA design was based on the primary objective of detecting and resolving Earth-size planets at a distance of up to 10 parsecs. This objective determined the size and number of the individual telescopes. Another factor which strongly affected the array design was u-v plane coverage. These considerations were addressed through the Y-configuration array layout and its orientation on the lunar surface, as well as the manner by which the optical beams are combined and analyzed. Requirements placed on the precise knowledge of optical path lengths throughout the array drove the evolution of the array layout and design. Further, launch and construction requirements were considered in both the array design and the individual telescope design.

For this study, several assumptions were required prior to the detailed design of the array. Actual site selection requires lunar surface maps with accuracies of at least one meter. Currently, such maps are not available. Further, surface and subsurface composition, along with other relevant geological data, are required for each of the

candidate sites. To transport array materials to the Moon, it was assumed that a heavy lift launch capacity and an orbital transfer capacity are available. In addition, continuous, two-way audio, video, and data transmission are necessary between the lunar observatory and Earth. To provide this capability, it is suggested that a communications satellite be placed in orbit above the lunar far side. Both the Earth-Moon transportation and the communications system are discussed in this report. State-of-the-art and near term technologies were assumed in the design of the array. Additional technological developments which would significantly reduce the complexity of the array are noted in the report where applicable.

1.5 Design Summary

At completion, the array will be comprised of 27 individual telescopes, each with a 1.5 meter primary mirror. The array elements are arranged in a north-southwest-southeast Y-configuration with 120 degrees between each of the three branches (Fig. 1.5-1). Each of the 2.9 km branches has a unique telescope spacing to provide the maximum number of unequal baselines between any two telescopes, thus maximizing u-v plane coverage. In this arrangement, the maximum baseline is approximately 5 km.

Each telescope beam is directed to a delay system and then to the central receiving facility where a portion of the optical delay lines, the laser metrology system, and the instrument suite are housed. Data transfer to and from Earth is accomplished through a satellite orbiting the second libration point above lunar far side. Power is supplied from three 2.5 kW Dynamic Isotope Power Systems that are located approximately three kilometers from the central receiving station.

The LOLA design emphasizes flexibility in both the scientific application and construction of the array. Telescope instrumentation and electronics are designed to be easily replaced and upgraded, while emerging technologies can be integrated into the design to increase the performance of the telescope array. In addition, the individual telescopes are designed to be movable so that periodic positioning can tailor the u-v plane coverage for observations of particular cosmic phenomena. Construction is planned for two phases of 9 and 18 telescopes each. This provides a validation phase for a scaled down system before committing to construction of the full 27 element array. The design of this facility will enable LOLA to yield an abundance of astronomical discoveries well into the twenty-first century.

FINAL
STAGE

INITIAL
STAGE

DETAILED CENTRAL VIEW
Scale 3:1

TO SCALE
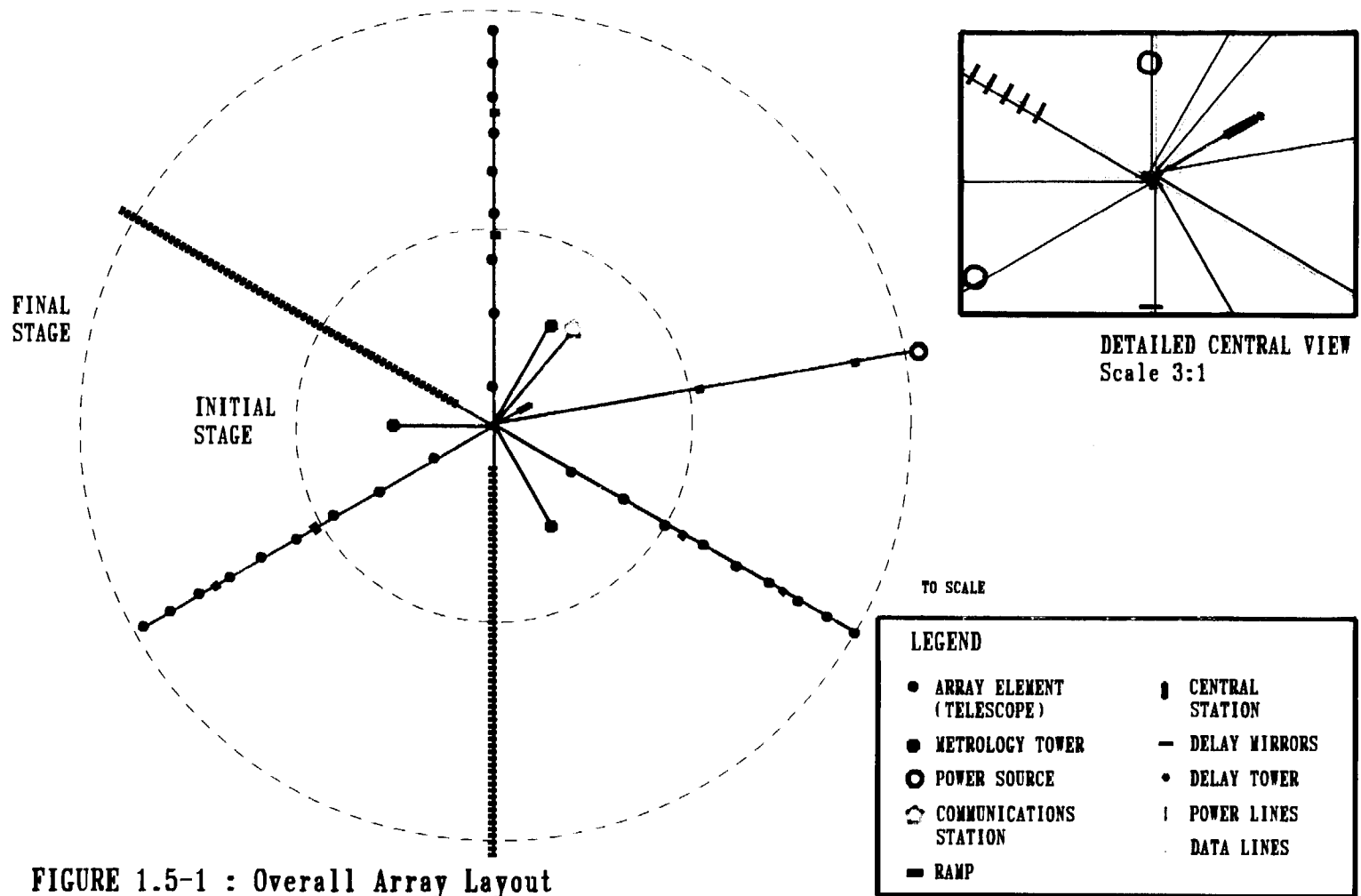
FIGURE 1.5-1 : Overall Array Layout

LEGEND

● ARRAY ELEMENT
  (TELESCOPE)

● METROLOGY TOWER

○ POWER SOURCE

◠ COMMUNICATIONS
  STATION

▬ RAMP

▮ CENTRAL
  STATION

— DELAY MIRRORS

● DELAY TOWER

ı POWER LINES

  DATA LINES

2.0 Background

2.1 Optical Interferometry Background

In conventional monolithic telescopes, the resolving power is directly related to the viewed wavelength and inversely related to the aperture diameter through the following equation:

Angular Resolution = 1.2 $\frac{wavelength}{diameter}$ in radians

The only way to increase the resolution in a conventional telescope is to increase the mirror diameter. Future astronomical observations will necessitate extending this angular resolution into the micro- or milliarcsecond range, requiring mirror diameters in the kilometer range.

Radio astronomers have, for the past several decades, circumvented the problem of the telescope diameter requirement by using interferometry. This process, known as aperture synthesis, was developed by Michelson in the 1920's for measuring the diameters of stars at optical wavelengths (Ref 2.1-1). Figure 2.1-1 shows a simple schematic for an optical interferometer.

1) The pair (or array) of telescopes receive radiation from a distant source.

2) When the source direction is normal to the baseline, D, the two light beams constructively interfere. This produces a signal maximum (Fig. 2.1-2a).

3) As the source drifts through the field of view, the source direction shifts and the path difference increases. This difference in light wave path length causes a reduction in the signal due to partial destructive interference. Once a path length difference of λ/2 is reached, the received signal is zero (Fig. 2.1-2b).

4) The signal then begins to increase until a path difference of λ is achieved and the signal is again at a maximum (Fig. 2.1-2c).

5) As the source continues to move, the waves alternately come in and out of phase, producing a series of minima and maxima. A change of Θ in the source direction produces a optical path difference of $D*\Theta$. The signal alternates from one maxima to the next when:

$$D*\Theta = \lambda$$

Therefore,

$$\Theta = \lambda/D \quad \text{in radians}$$

Therefore, Θ is the width of each lobe of resolution of the interferometer (Fig. 2.1-2d).
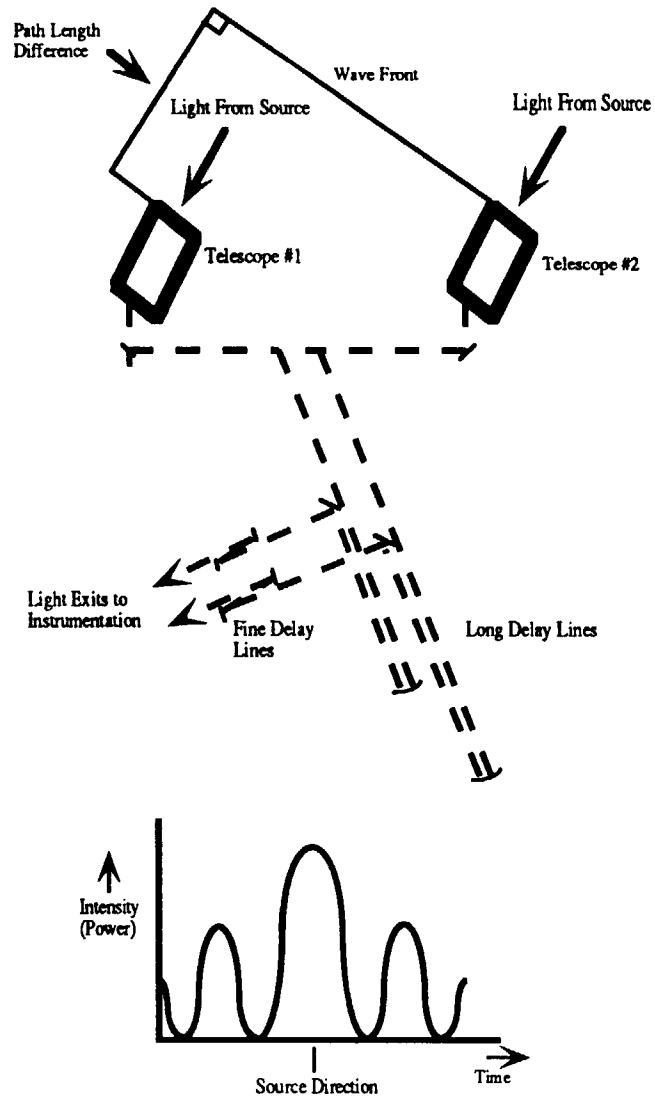
Figure 2.1-1: Basic Lunar Optical
Interferometer - Optical Layout and
Interference Pattern
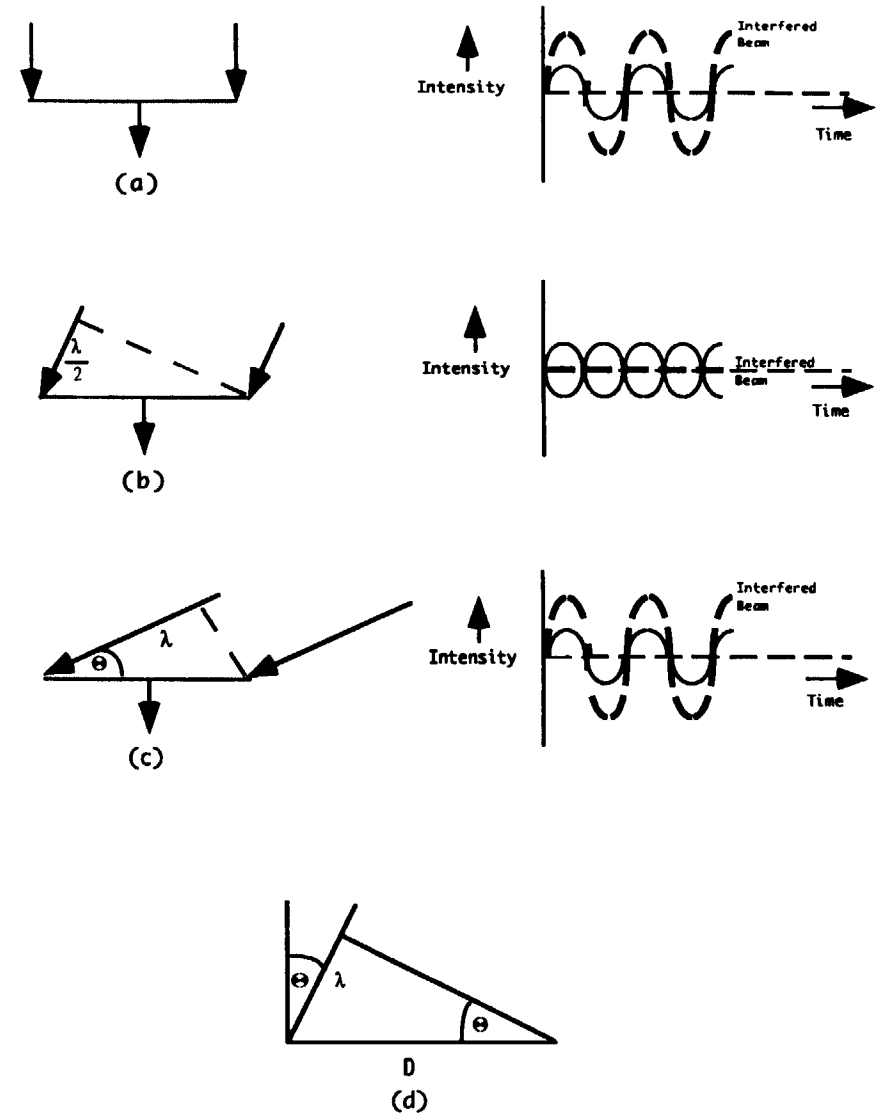
Figure 2.1-2: Schematic for Simple
Interferometry

The fringe spacing of this interference pattern is determined by the projected normal baseline D' and the incoming wavelength. The angular resolution is now a function of the incoming wavelength and the array baseline.

Resolution = 1.2 $\underline{\text{wavelength}}$ in radians
                        baseline

To produce the required interference pattern, a time delay must be inserted to retain the phasing of each array element light beam. Thus, the source spacings in the field of view, not a source motion, produce the constructive and destructive pattern of interference. If the time delay is set to match the beam delay perfectly, all the light beams will be in phase and the central (peak) fringe will have full amplitude. As the phase difference grows; however, the interference conditions will cause the fringe amplitude to diminish over the angle Θ_D. Θ_D is approximated by $1/(B\tau_B)$, where B is the bandwidth and τ_B is the baseline length measured in light travel time. Therefore, the number of fringes observed is of the order of the $\underline{\text{inverse}}$ of the fractional bandwidth.

The interferometer output is the convolution of its sinusoidal fringe pattern with the maximum source brightness B(x,y) where x,y are the angular coordinates on the sky. The interferometer output is equal to the Fourier transform B(u,v) of the brightness distribution, where the conjugate coordinates (u,v) are defined by the baseline coordinates on a plane normal to the source direction and the interferometer baseline, measured in wave number (Fig. 2.1-1).

The u-v plane image is formed by the interference of the incident light waves of each baseline telescope pair onto a photo-counting (photon) detector or other comparable instrumentation. Small separations in the x,y image produce a high spatial frequency and contribute to the outer radius of the u-v plane image, whereas extended image structure produces a low spatial frequency and contributes to the inner radius of the u-v plane image. This u-v image is then returned to an x,y image through the use of an inverse Fourier transform scheme.

To derive detail about the structure of a source, the fringe visibility must be measured at many different spacings. By varying the aperture spacing or providing a large number of properly configured array telescopes, the elemental sine waves of various amplitudes and phases can be found.

Signal-to-noise calculations are only approximate, empirical and depend on the signal level and the amount of noise. Noise sources include background radiation, zodiacal temperature, scatter, stray light, and instrumentation errors such as photon shot noise. However, the quantification of the signal-to-noise ratio (SNR) is directly related to the square root of the total array collecting area. This is determined by multiplying each individual array collecting area by the total number of array elements. Since most stellar objects of interest are not brighter than 12th magnitude, and most are substantially fainter, a net collecting area of at least 30 m^2 is required to achieve any apparent scientific rewards (Fig. 2.1-3).
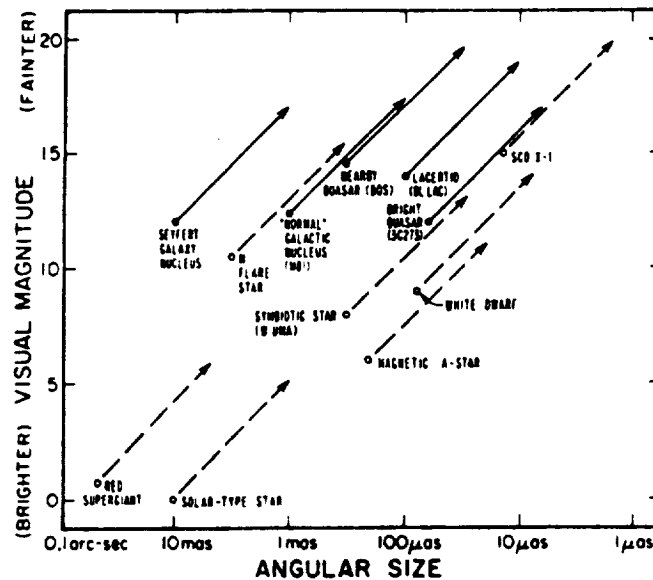
Figure 2.1-3: Magnitude and Maximum Sizes for a Selection of Stellar and Extragalactic Objects. The scales are chosen so that an object of a given class moves in the direction of the arrow, whose length corresponds to a factor of ten in distance. (Ref. 2.1-1)

2.2 Site Selection

A site on the lunar far side will be chosen with sky coverage as the driving factor. Because of the lunar rotation, the best sky coverage can be achieved at a site near the equator. The site should be within +/-10° of the equator. A second concern is to make certain that no interference from the Earth reaches the array. Therefore, the site should not be located too close to the longitudes dividing the far side and the near side. Also, physical and longitudinal libration allow a maximum of 7°54' longitude of the far side to be exposed to earthshine. A site located at a longitude between 115°-180° west longitude or 115°-180° east longitude should be permanently out of earthshine and earth interference (Fig. 2.2-1).

The actual site will be relatively flat and free of craters to minimize construction time. The chosen site also will not be located near any large scarps - cliffs common to the lunar surface - or mountains that will impede sky coverage.

Stratigraphy and soil property tests will be required at candidate sites to determine the exact make-up and properties of the soil with which the construction engineers must contend. The surface regolith itself will be of relatively high density and low compression index. This allows for soil with an acceptable ground bearing capacity and little settlement. Bedrock cannot be encountered during excavation and any site that has bedrock within the first meter of surface will be considered unacceptable.

A maria has the characteristically flat surface that would be favorable for a site. Some of the larger marias on the far side that could be potential candidates are marias IX, XV, and XVIII. However, detailed surveying of the lunar far side, and particularly of the candidate construction sites, is required before a definite location is selected.

Figure 2.2-1: Site Selection Map of Lunar Far Side
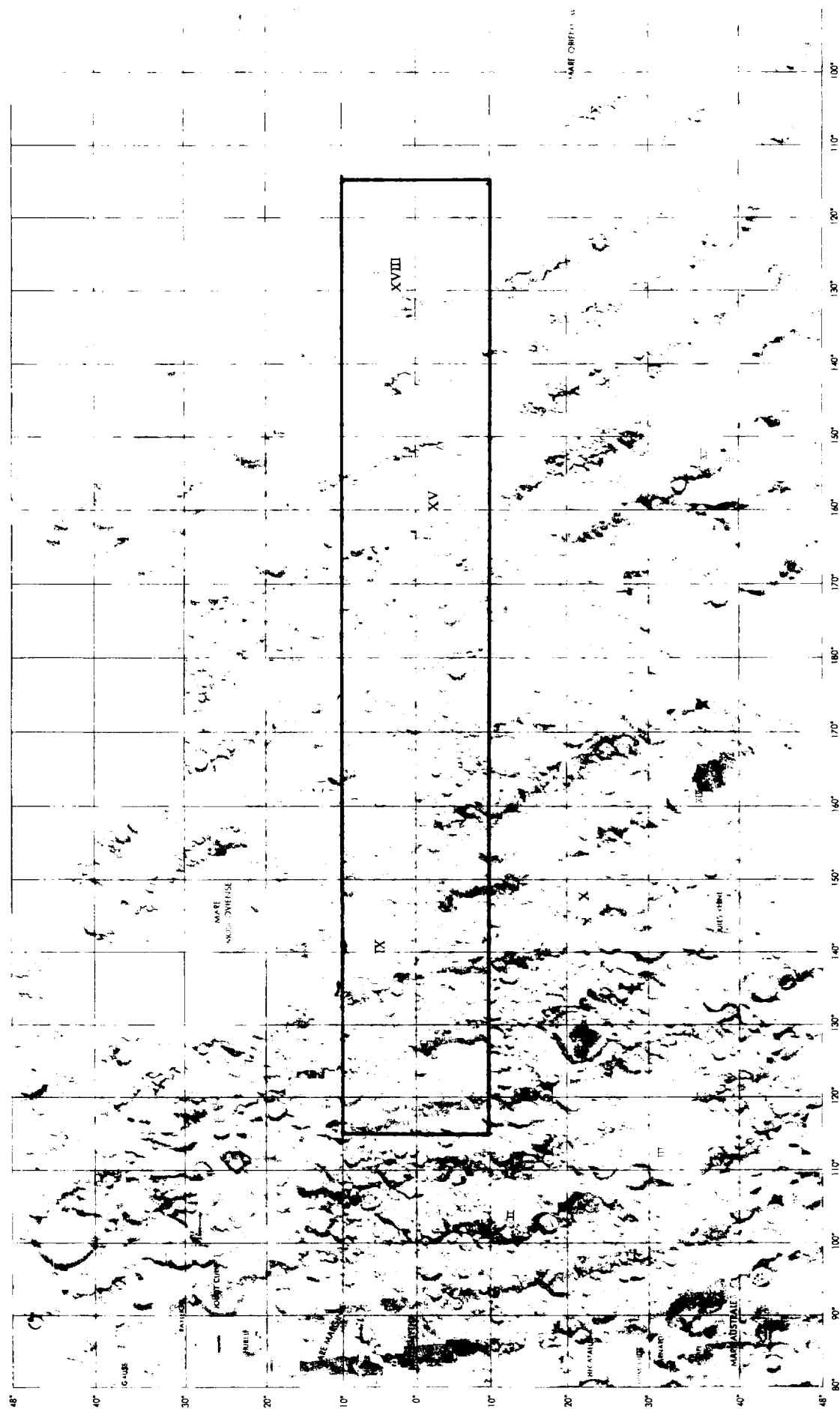
2.3 Lunar Environment

Scientists have long desired observatories on the moon. Examining a decision matrix comparing the earth, LEO and the moon (Table 2.3-1) shows that the lunar far side is the best place, scientifically, to perform astronomical observations.

One advantage of a lunar site is the lack of atmosphere. This allows a complete viewing spectrum and prevents viewing difficulties. The far side has low background radiation levels with no reflected or man-made radiation from earth. A low night time temperature of 100 K reduces infrared spectrum noise and lessens the need for active component cooling. The slow rotation rate allows 14 earth day integration times. A weaker gravity field (1/6th of Earth's) allows lighter structural components. The rate and intensity of natural disturbances (Ref. 2.3-1) are low and man made disturbances are controllable.

Dangers lie in direct micrometeorite impact on optics and secondary lofting of regolith. Lofting and impacts obscure, pit and lower surface finish, resulting in data loss. A detailed study of this potential hazard is contained in Appendix 2.3-1 showing that the risks are minimal. Shielding further reduces these risks. Regolith is also periodically disturbed by the terminator static charge effect. Lasting for about an hour as a region passes from night to day, it levitates particles 3-30 cm above the local horizon (Ref. 2.3-2). The behavior of the regolith requires optical elements to be 1) at least 0.3 meters above ground level, 2) protected from dust during manned activity and 3) cleaned periodically.

Significant levels of radiation bombard the lunar surface, causing instrumentation, structural integrity and human safety problems. Ranging from 1 MeV to 10 GeV, galactic cosmic radiation (GCR) is the most dangerous. Upon striking matter, GCR slows down rapidly, but the kinetic energy is transferred into a cascade of other particles known as the Bremsstrahlung effect. Protection of instrumentation from this phenomena requires approximately 5 m of lunar regolith (Ref. 2.3-3).

The Sun also emits a primary source of radiation - solar flares. Solar flares occur in 11 year cycles during which the sun rapidly erupts and emits up to 10^{10} protons per cm^2 with energies from 10 to 30 MeV (Ref. 2.3-4). This radiation can be deadly to unshielded humans and causes large amounts of noise in data collection.

The moon's changing orientation to the sun causes a diurnal temperature variation from 100 to 385 K. This places severe thermal strains on structural elements and requires either shielding or a "cool down" phase for optics before operation can begin in the infrared spectrum.

Table 2.3-1: Decision Matrix for Lunar Site

	Earth	LEO	Near Side	Far Side
Atmosphere				
* Meteorites	Excel.	Fair	Poor	Poor
* Viewing Window				
UV	Poor	Excel	Excel	Excel
Visible	Fair[1]	Excel	Excel	Excel
IR	Poor	Excel	Excel	Excel
Temperature				
* Range	Excel	Poor	Poor	Poor
deg K	100	350	250	250
* Min	Poor	Good[1]	Excel	Excel
deg K	273	0	100	100
UV Coverage	Good	Poor	Excel.	Excel
time(hr)	12	1.5	336	336
Stability Sources				
* natural	Poor	Excel	Good	Good
* man induced	Fair	Poor[3]	Excel	Excel
Radiation				
* Galactic	Excel	Poor	Poor	Poor
* Solar Flare	Excel	Poor	Poor	Poor
* Solar Wind	Excel	Excel	Poor	Poor
* From Earth	Poor	Fair	Good	Excel
Gravity	Poor	Excel	Good	Good
vs. earth	(1)	(0)	(1/6)	(1/6)
Radiation	Excel	Good	Fair	Fair
Cost				
* Construct	Excel	Fair	Poor	Poor
* Maint.	Excel	N/A	Poor	Poor
Technical Complexity	Excel	Poor	Fair	Good
Knowledge / Risk	Excel	Good	Fair	Poor

Notes:
[1] due to seeing effects
[2] reduced to good due to the short time span at this minimum
[3] jitters due to orbit keeping, solar panel snaps, etc.

3.0   Optics

Energy can be thought of as waves vibrating at a characteristic speed. The level of energy is characterized by the frequency of vibration or wavelength (Fig. 3.0-1). For this report, wavelengths less than 400 nm are ultraviolet, between 400 nm to 750 nm, visible and greater than 750 nm, infrared.

When energy hits a surface it may be reflected, absorbed or transmitted. The wavelength at which the maximum amount of energy is released for a given temperature can be determined using Wien's Displacement Law :

$$\lambda_{max} = 2890 \text{ micrometers K/T}$$

where T = temperature in Kelvin. This law gives the positions of the peak predicted by Plank's Equation (Fig. 3.0-2) which relates spectral emissivity, temperature and radiant energy.

As light enters a material it is bent (refracted) according to Snell's law. Refractive optical elements are highly frequency dependent and lenses can only be successfully made in sizes approaching 30 cm in diameter.

Also, when light strikes a surface, some portion of it is reflected at an equal and opposite angle to the normal of the surface. This property has been used by telescope designers to exceed the 30 cm limit of practical lens size and build solid aperture telescopes of up to 6 m in diameter. Reflectivity is frequency independent, avoiding the difficulty of chromatic dispersion

If light travels too far it will begin to loose its definition, phase and coherency. This maximum length can be determined by:

$$R = \pi * d^2 / (4 * \lambda)$$

where   R =   the maximum length of light travel before degradation
        d =   diameter of light beam
        λ =   wavelength

The driving factor in determining the collecting area of the array is the signal to noise ratio (SNR) (Appendix 3.0-1). The most demanding task is detection of an Earth-like planet 10 parsecs away. The array was originally sized to accomplish this with a SNR of 10 at a wavelength of 500 nm using an assumption of 95% efficiency of the collecting area. Detailed study of surface and reflectance characteristics of the entire system revealed that expected efficiency was 35% at 1000 nanometers for dielectric silver coated mirrors (Appendix 3.0-2).

Figure 3.0-3 shows the SNR for 3 targets, an Earth-like planet at 5 parsecs, at 10 parsecs and a Jovian planet at 10 parsecs. Jovian planets are easier to detect because they are physically larger and reflect light better than Earth type planets. SNRs can be improved by increasing the integration time. Figure 3.0-4 shows this relationship for 1/2 day, 3 day and 9 day viewing of an earth like target 10 parsecs away. Clearly, longer integration times can greatly improve SN ratios.

Several factors that influence the estimates of signal to noise were not considered in the above calculations. First, the temperature of the optical elements can generate noise dependent on Plank's equation. This danger was eliminated by ensuring that all optical
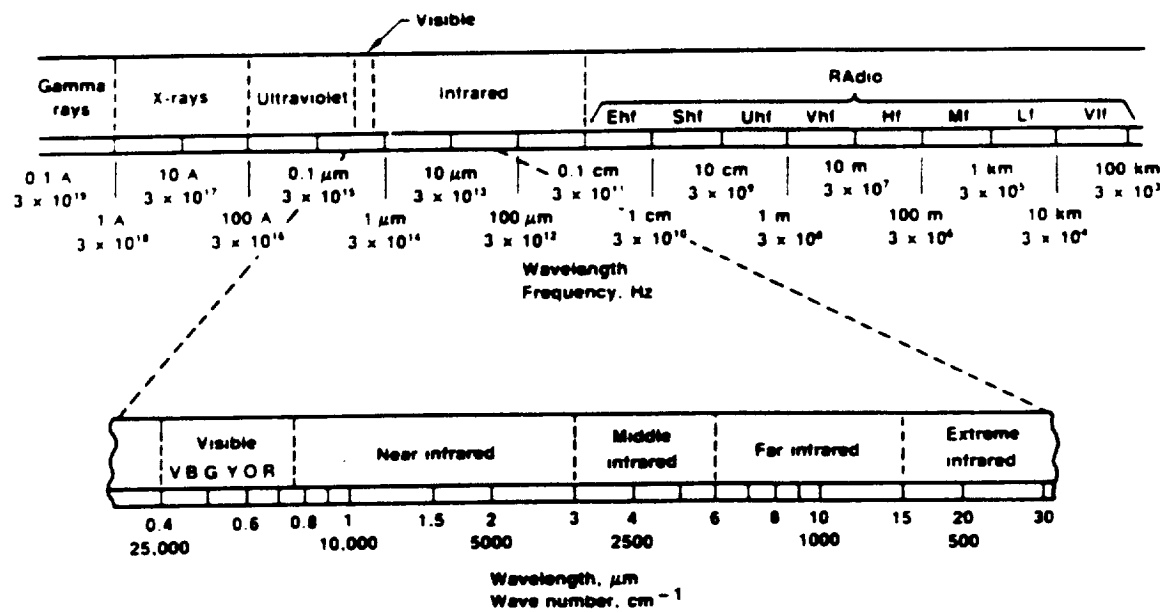
Figure 3.0-1: Electromagnetic Spectrum
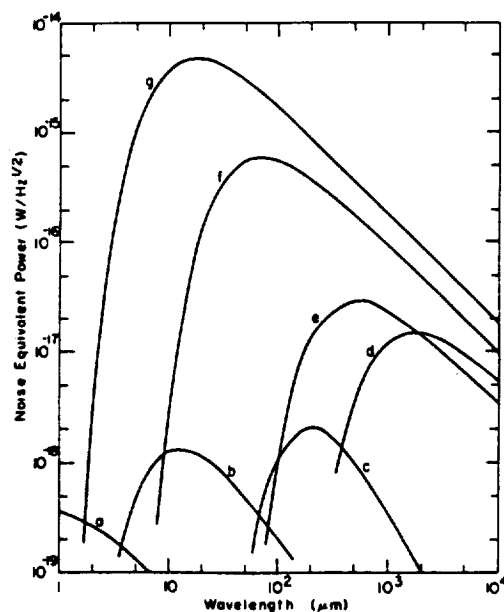
Charge coupled device noise equivalent
power versus wavelength for various
detector temperatures:

(a) zodiacal scattered light at the ecliptic pole
(b) zodiacal dust emissions at the ecliptic pole
(c) interstellar dust emissions at high galactic latitudes
(d) the 3 K cosmic background radiation
(e) a 10 K, 10 percent emissive telescope
(f) a 77 K, 10 percent emissive telescope
(g) a 300K, 10 percent emissive telescope

Figure 3.0-2: Noise Equivalent Power vs. Wavelength

Signal to Noise Ratio
Integration time = 1 day
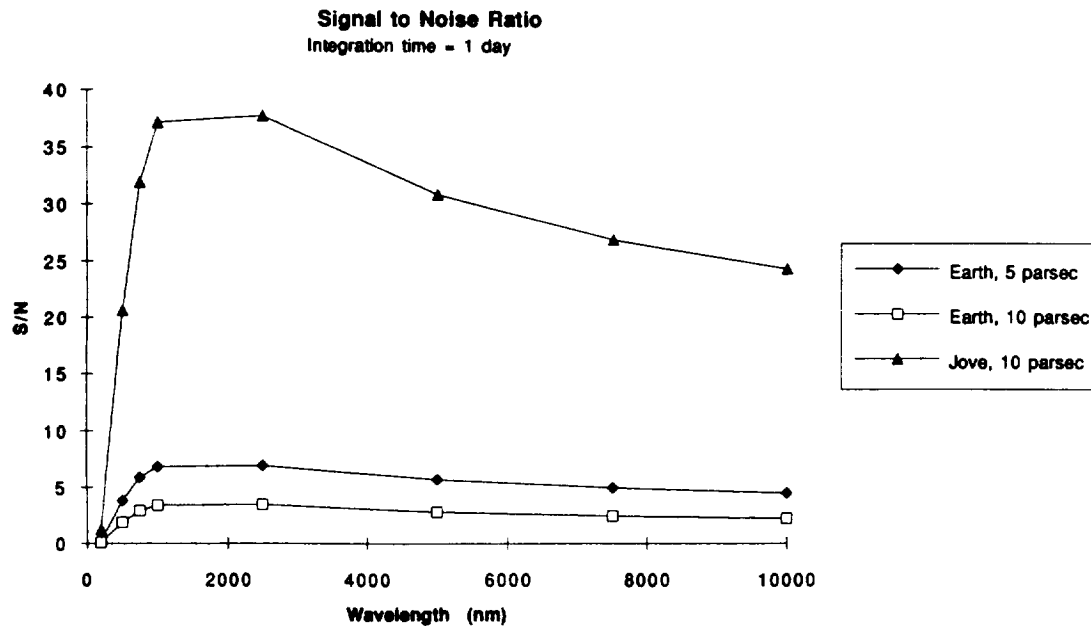
Figure 3.0-3: Signal to Noise Ratio vs. Wavelength

Signal To Noise Ratio
Earth Type Planet
10 Parsec, 35% effc.
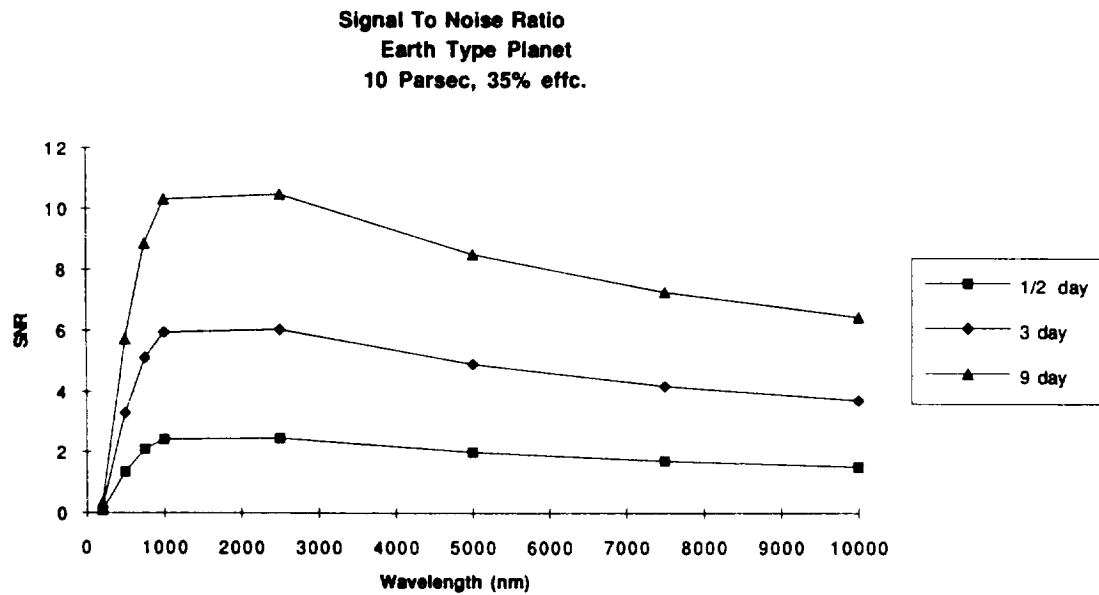
Figure 3.0-4: Signal to Noise Ratio Earth Type Planet
vs. Wavelength

elements would be cooled to at least 70 deg K during operation. Surface finish and scattering also can play major roles in noise generation and were reduced by the surface finish requirement of $\lambda/100$.

3.1 Array Geometry / U-V Plane Coverage

The required image complexity and resolution of the stated application presupposes adequate u-v coverage. The main coverage drivers of u-v plane sampling are the total number of baselines and the array configuration.

The array will be set up in two stages, the initial and final configurations. The initial stage will consist of 9 array elements with a total of 36 baselines. The final stage will consist of 27 array elements with a total of 351 baselines.

> # of baselines = (n)(n-1)/2
> where n is the total number of array elements.

A well-sampled visibility function is critical for producing accurate, reliable brightness distributions. The general requirements for desirable u-v sampling are:

> 1) a roughly circular region of coverage
> 2) a tapered sampling density from the center to the edge
> 3) minimal deviations for observations at accessible declinations (Ref. 3.1-1)

3.1.1 'Y' versus Circular Configuration

The two array configurations studied in depth were the 'Y' and the circular. Though a circular array gives a circular region of coverage and minimal deviations for observation at accessible declinations, there are a number of intrinsic problems associated with the configuration. In most practical circular configurations, the number of baseline lengths peaks sharply at long baselines (Fig. 3.1-1), creating weak u-v coverage at smaller spatial scales. This effect is particularly pronounced at 40 and 60 degrees declination where significant holes exist in the center of the coverage (Fig. 3.1-1). The effect of such central holes on the fringe pattern is to increase the strength of the sidelobes (Ref. 3.1-1). The high intensity sidelobes of the system's solar body already mask any nearby objects; thus, any increase in the solar sidelobe intensity will likely make planetary detection impossible. The appearance of poor taper ratio characteristics is most pronounced in uniformly spaced arrays, though appears to a lesser extent in most circular configurations. This causes the taper ratio of a circular array to be extremely sensitive to the placement of each individual array element.

Other problems with the circular array stem from the required radial optical feed (a non-radial optics feed requires very complex delay line schemes with large numbers of optical reflections, reducing the SNR drastically from optical losses) and include difficult image rotation and signal polarization maintenance (Ref 3.1-2). Economic and practical considerations strongly favor some linear arrangement, simplifying the layout of the power and signal cables and requiring the site-preparation of land only in narrow corridors (Ref 3.1-3). Lastly, to get adequate u-v plane coverage, a circular array must employ maximum non-redundant spacing. With maximum non-redundant spacing (i.e., no redundant or near redundant baselines), it is currently impossible to recover any phase sampling information at optical wavelengths. Therefore, a phaseless reconstruction
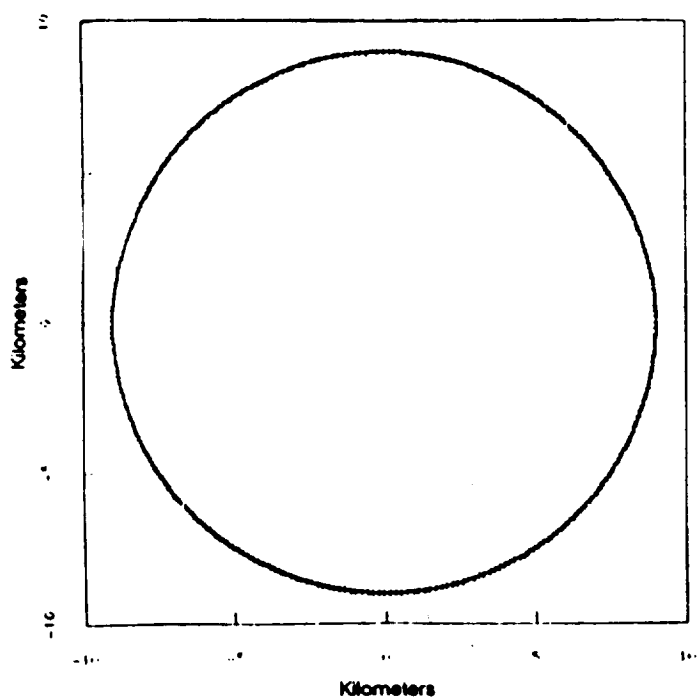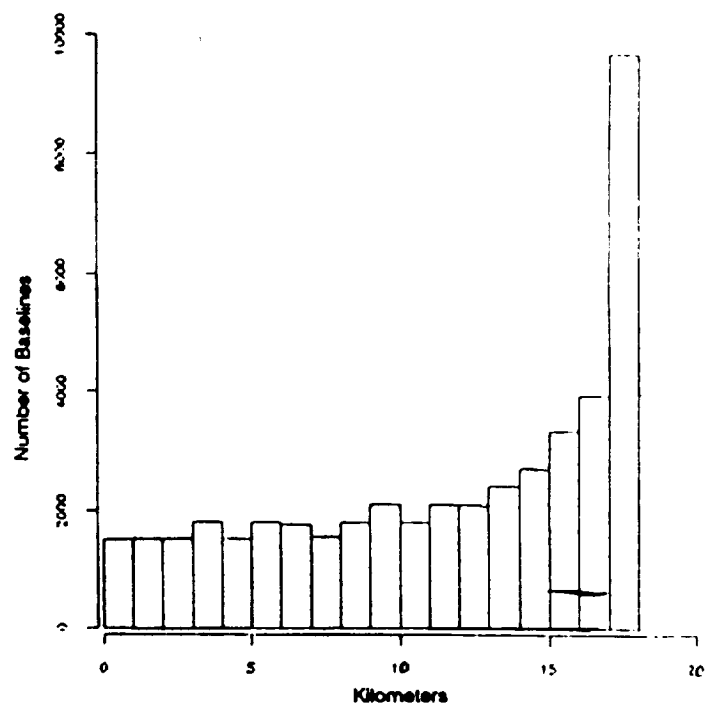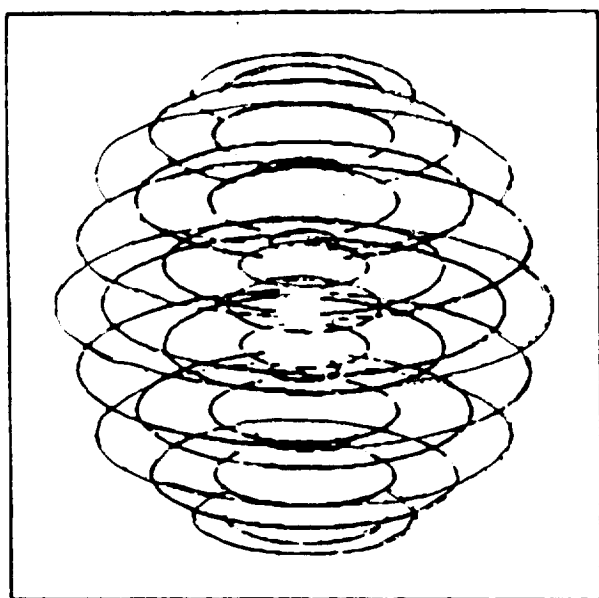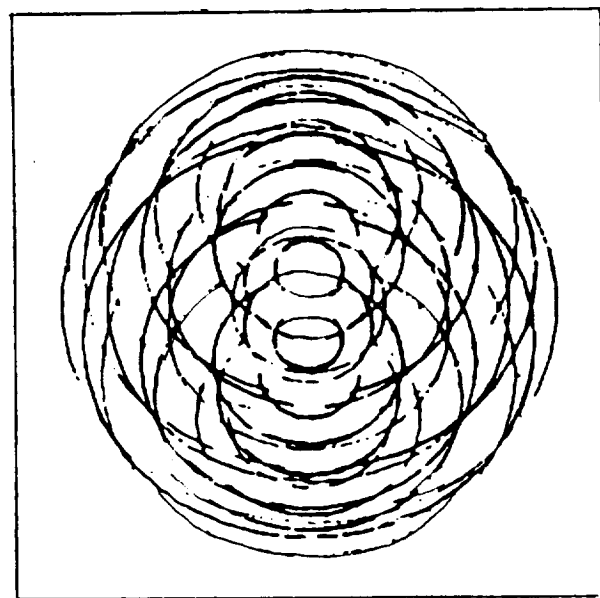
Figure 3.1-1: VLFA Circular Configuration. (a) Physical layout, (b) Baseline histogram, (c) u-v coverage at 20° inclination, (d) u-v coverage at 60° declination

algorithm, which lowers the dynamic range, must be employed (Reference Appendix 3.9-1). Since the primary goal of the lunar based interferometer is to detect and resolve planetary object at a 10 parsecs distance, the circular array is considered a poor choice.

The 'Y' configuration is by far the most practical and popular configuration; employed extensively throughout the astronomical community. The 'Y' array configuration meets all the requirements for acceptable u-v coverage, as well as providing additional advantages over other array configurations, including the circle.

They are as follows:
1) provides a roughly circular region of coverage
2) provides a tapered sampling density from the center to the edge
3) provides minimal deviations for observations at accessible declinations
4) provides superior rotation synthesis (Ref. 3.1-1)
5) easy to maintain image rotation
6) easy to maintain signal polarization
7) simple to expand in the future by adding additional elements along the arms
8) future 1-D mobility along arms a strong possibility
9) most Fourier schemes currently developed apply to
    the 'Y' configuration (Ref. 3.1-2)
10) economic and practical considerations strongly favor
    a linear array arrangement to simplify the power and
    signal cabling, and require site-preparation in
    narrow corridors only (Ref. 3.1-3)

Also, a 'Y' configuration allows the interferometer to be constructed in two stages while providing invaluable scientific data during the initial stage. Finally, because of the 'linear' design, the array can be periodically re-configured by moving one or more of the individual array elements along the arms, producing alternate u-v plane coverage. Table 3.1-1 provides a summary of the comparison between the 'Y' and the circular array.

3.1.2 'Y' Trade Studies

In order to determine the final array element spacings, a u-v plane coverage code was modified from an S-code produced for Lockheed Engineering and Management Services Company.

Appendix 3.1-1 shows the u-v code computations. These computations were made assuming purely polar lunar rotation; however, the moon axis of rotation actually has a 18 degree tilt and a slight wobble. The tilt and wobble will actually increase the u-v synthesis of the interferometer, improving the coverage circularity of the 'Y' type array and degrading the coverage circularity of the circular array. Appendix 3.1-2 shows the modified BASIC code and the original S-code is shown in Appendix 3.1-3. Figure 3.1-2 shows two VLA plots produced by the S-code (Ref. 3.1-1) accompanied two VLA plots made by the BASIC code for code validation. The u-v coverage maps were made assuming an array location of -20° latitude and a synthesis of +/- 6 hours of right ascension coverage, requiring one half of a lunar day. Figure 3.1-3 shows four representative VLA plots (Ref. 3.1-3) accompanied four VLA plots made by the BASIC code for code validation. The u-v coverage maps were made assuming a array location of 34 degrees latitude and a variety of integration times for right ascension coverage.

The basic 'Y' configuration will consist of three array arms, 120° apart. One array arm will point due north, one will point south-east and one will point south-west. This

Table 3.1-1: Summary of 'Y' vs. Circular Array

PARAMETER	'Y'	CIRCLE
Roughly Circular Coverage	YES	YES
Tapered Sampling Density	YES	NO - PROMOTES SIDELOBE GROWTH
Minimal Declination Deviation	YES	YES
Good Rotation Synthesis	YES	YES
Simple Delay Line Scheme	YES - DUE TO ONE DIMENSIONALITY OF ARRAY	YES - FOR RADIAL FEED NO - FOR NON-RADIAL FEED (PROMOTES SNR DEGRADATION)
Image Rotation	EASY TO MAINTAIN DUE TO 1-D ARMS	DIFFICULT TO MAINTAIN WITH RADIAL OPTICAL FEED
Signal Polarization	EASY TO MAINTAIN DUE TO 1-D ARMS	DIFFICULT TO MAINTAIN WITH RADIAL OPTICAL FEED
Image Reconstruction	PRACTICAL	NOT PRACTICAL - PHASELESS RECONSTRUCTION REQUIRED IN MAX. NON-REDUNDANT ARRAY
Staged Construction	PRACTICAL AND INFORMATIVE	NOT PRACTICAL
Future Expansion	SIMPLE TO ADD ELEMENTS ALONG 1-D ARMS WITHOUT DRASTIC DELAY LINE RE-CONFIGURATION	DIFFICULT TO EXPAND DUE TO RADIAL CONSTRUCTION
Re-Configuration	ELEMENTS EASILY MOVED WITHOUT DELAY LINE CHANGES	DUE TO DELAY LINE COMPLEXITY NOT PRACTICAL
Future 1-D Mobility	SIMPLE TO MOVE ELEMENTS ALONG 1-D ARMS WITHOUT DRASTIC DELAY LINE RE-CONFIGURATION	DIFFICULT TO MOVE DUE TO RADIAL CONSTRUCTION
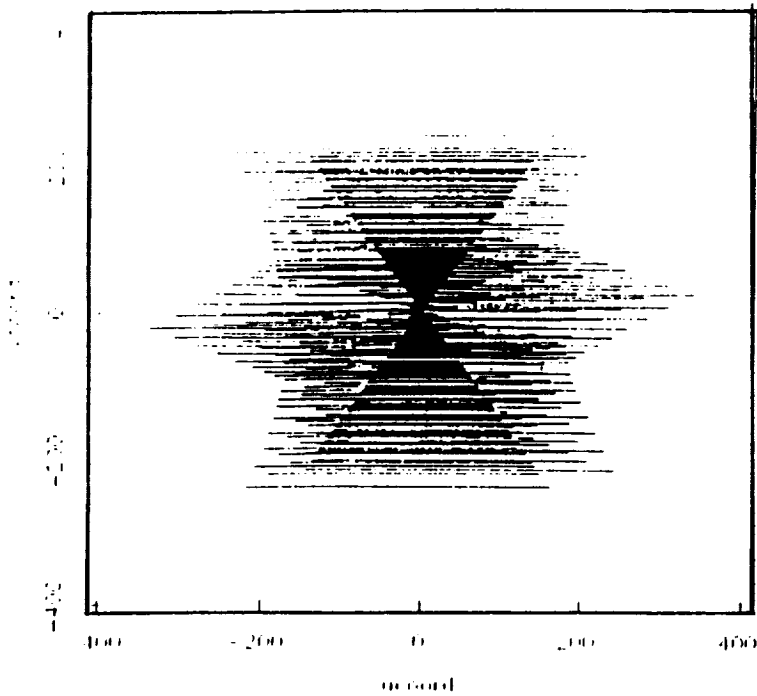
(a)
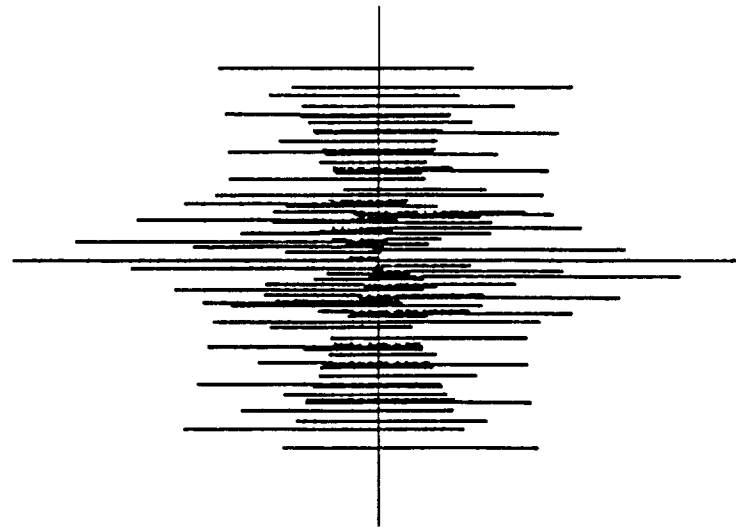
(c)
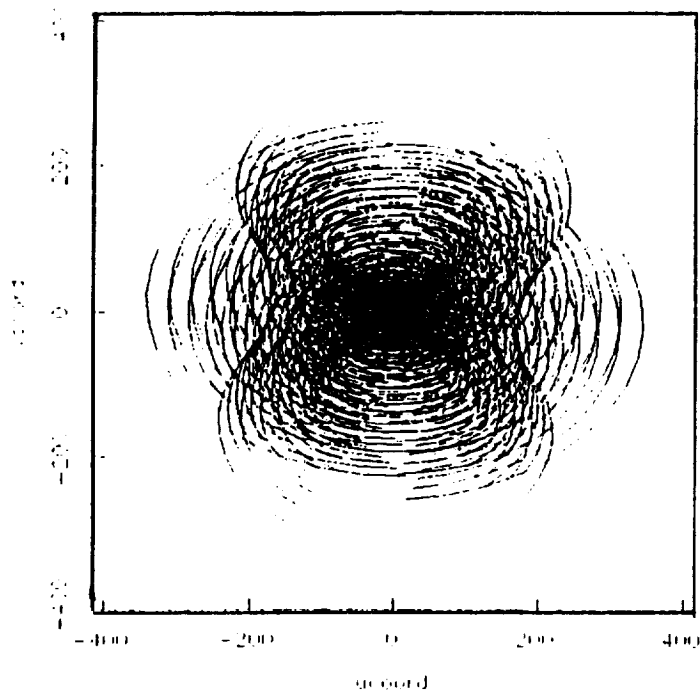
(b)
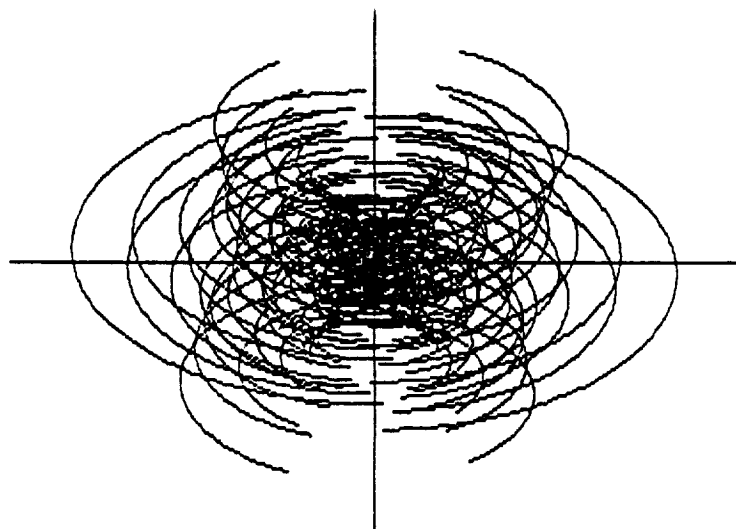
(d)

Figure 3.1-2: Validation of BASIC Code vs. S-code. (a) and (b) are
S-code u-v coverage plots at 0° and 45° declinations, respectively.
(c) and (d) are the corresponding BASIC plots.
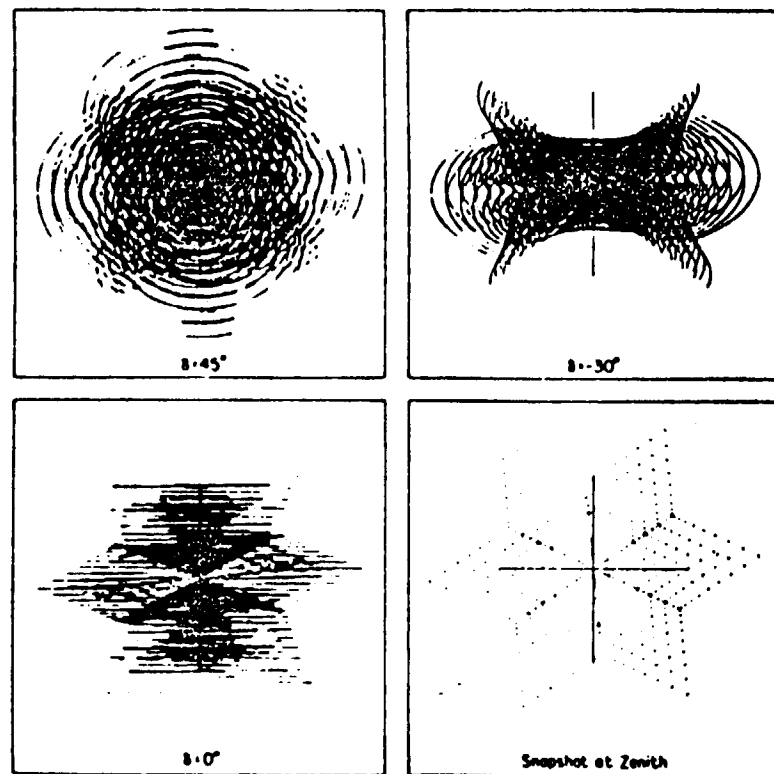
(a)
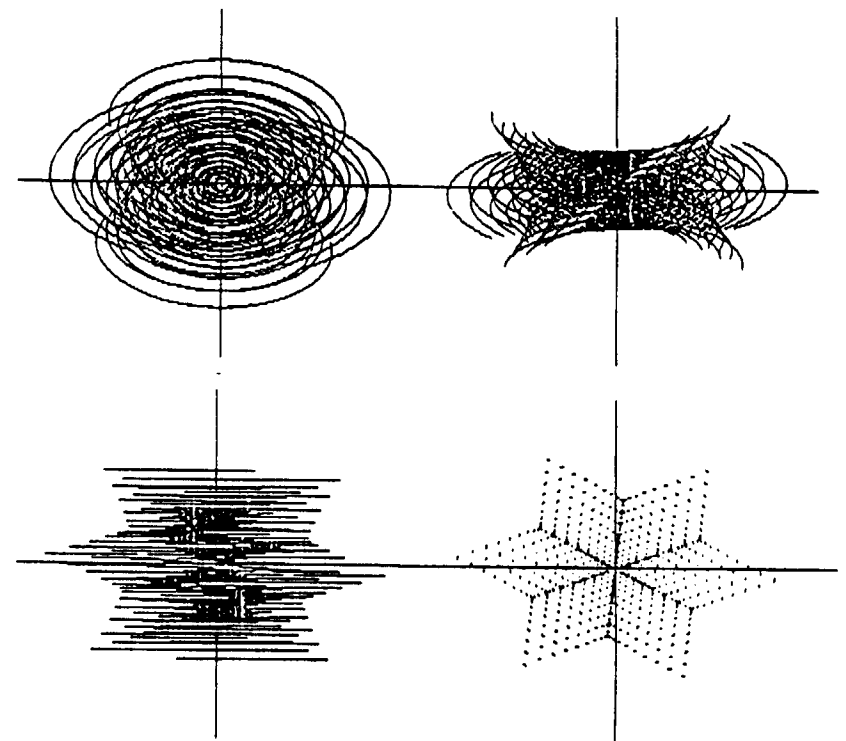
(b)

Figure 3.1-3: Validation of BASIC Code vs. VLA Coverage. (a) Various u-v plots for the VLA. (b) Corresponding BASIC plots. The coverage in hour angle is ±4h for 45° and 0°, ±3h for -30° and ±5 min for the snapshot.

orientation will allow maximum exploitation of the moon's rotation, termed rotation synthesis - required for imaging of complex objects. However, it should be mentioned that because of the moon's slow rotation rate, rotation synthesis is extremely limited for rapidly changing objects (Ref. 3.1-2).

Four spirals of varying tightness were overlaid on the inverted 'Y' configuration and the intersection points became the array element positions. The longest array arm will point to the southeast, allowing for maximum exploitation of the lunar rotation for the longest baseline. The spiral-like spacing was used to produce baseline non-redundancy (while still retaining some near redundant baselines currently required to retrieve optical phase information) and create the required baseline length taper (Ref. 3.1-1). The power law design adopted as the VLA nominal spacings (Ref. 3.1-3) was used for the fifth test configuration as a control.

The equations for the five test configurations are given below, Figures 3.1-4 through 3.1-8 show plots of the representative configurations.

SPIRAL CONFIGURATIONS
$x=r^*cos(\Theta)$
$y=r^*sin(\Theta)$
E=2900*x meters
N=2900*y meters
Note: these equations produce a maximum array arm of
2900 meters.

CONFIG #1 $r=\Theta/\pi/17.83333$
CONFIG #2 $r=\Theta^\wedge(1/1.5)/\pi/4.66056311$
CONFIG #3 $r=\Theta^\wedge(1/1.7)/\pi/3.398681$
CONFIG #4 $r=\Theta^\wedge(1/2)/\pi/2.3825462$

VLA CONFIGURATION
Distance along the arm = n^a
where a = 1.716
and n is the array element number along the arm

3.1.3 Conclusions and Recommendations

All five configurations displayed excellent u-v plane coverage throughout a range of declinations, with no appreciable difference between the coverages. Figures 3.1-9 and 3.1-10 show the u-v coverage maps for all five array configurations at 30° and 45° target source declinations. The u-v coverage maps were constructed assuming an equatorial array location and a lunar rotation synthesis of +5.93 and -5.57 hours of right ascension coverage corresponding to the maximum array viewing angle. The maximum array viewing angle assumes an array cool-down period of 30 Earth days and a minimum viewing angle of approximately 5° above the lunar horizon. Due to BASIC resolution restrictions, only the initial 9 elements (corresponding to the initial stage of array development) of each array configuration were used in the coverage comparisons. This provides maps representative of full configuration coverage while allowing coverage differences to be easily distinguished and studied. It should be noted that the maximum baselines for the initial stage of array construction vary between configurations. Since the shape and distribution, not
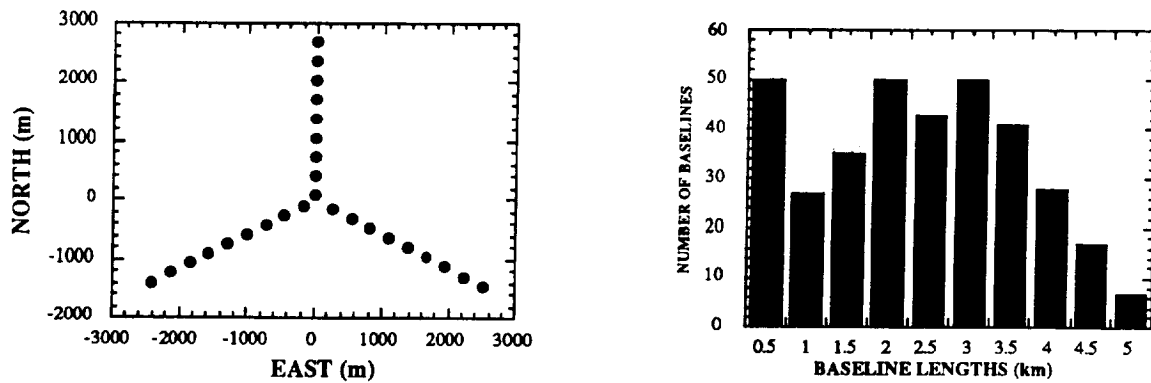
Figure 3.1-4: Configuration #1 (a) Physical layout, (b) Baseline histogram
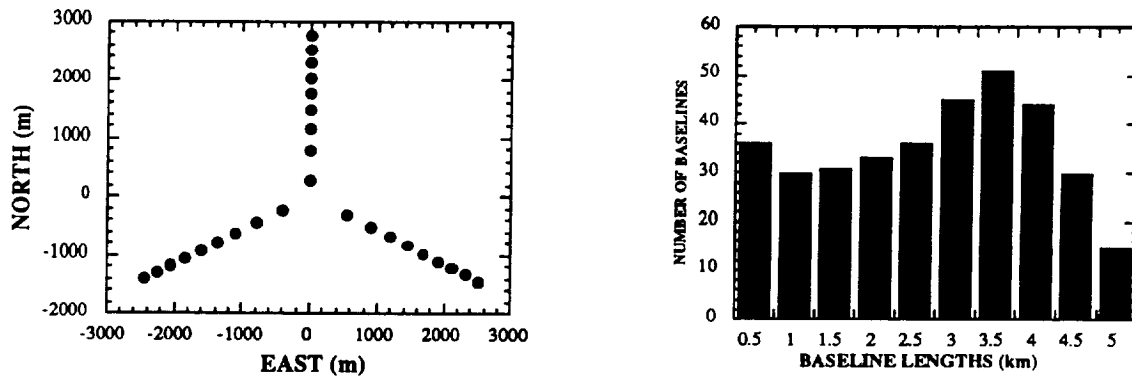
Figure 3.1-5: Configuration #2 (a) Physical layout, (b) Baseline histogram
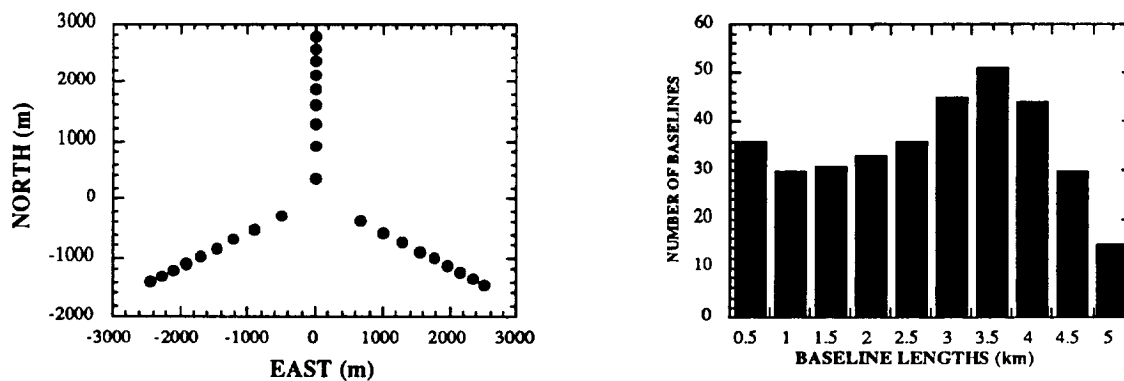
Figure 3.1-6: Configuration #3 (a) Physical layout, (b) Baseline histogram
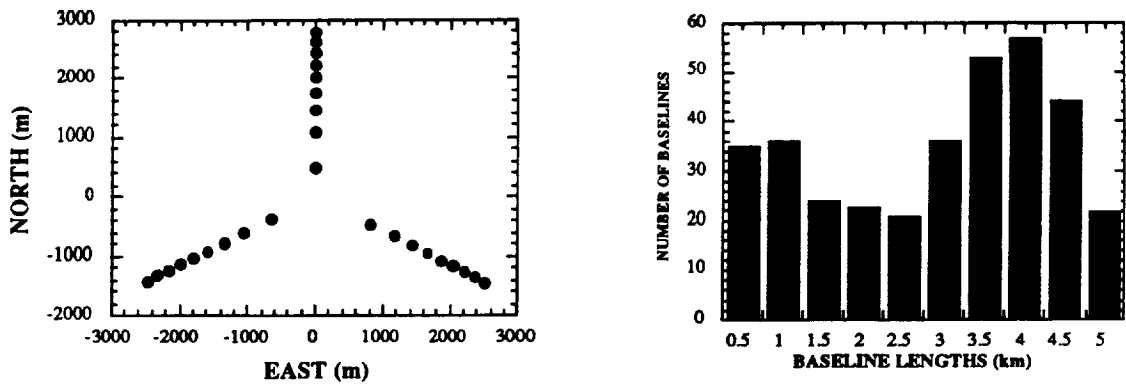
Figure 3.1-7: Configuration #4 (a) Physical layout, (b) Baseline histogram
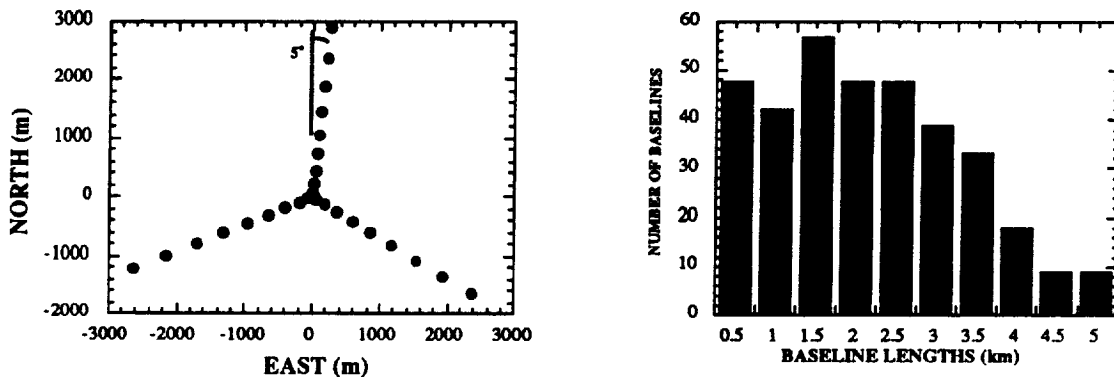
Figure 3.1-8: Configuration #5 (a) Physical layout, (b) Baseline histogram

the size, of the coverage is to be compared, the coverage maps of the first four configurations were not scaled to equate maximum baselines. The VLA control configuration (configuration #5) was scaled by a factor of 32.5 due to the small maximum baseline length.

It is apparent that configurations #2 and #3 provide the most uniform and efficient coverages of the u-v plane. Configurations #1 and #5 show poor coverage about the outer edge of the plane, while configuration #4 demonstrates weak central and mid-range coverage. By studying the histograms of all five configurations (Figs. 3.1-4 through 3.1-8), it is apparent that configuration #2 provides excellent spatial taper (Appendix 3.1-3). Therefore, configuration #2 is the recommended array configuration. The final spacings for the array are provided in Table 3.1-2. U-V coverage maps for a larger range of declinations are provided for the recommended configuration (Fig. 3.1-11).

(a)

(b)

(c)

(d)

(e)
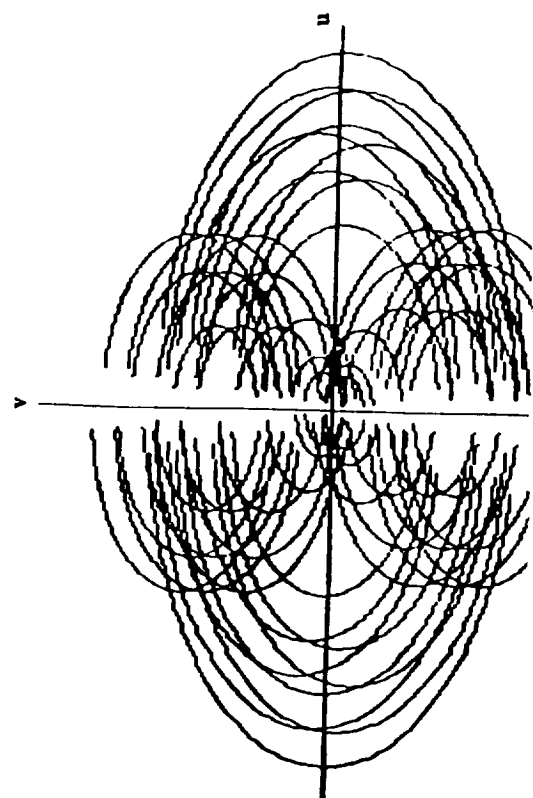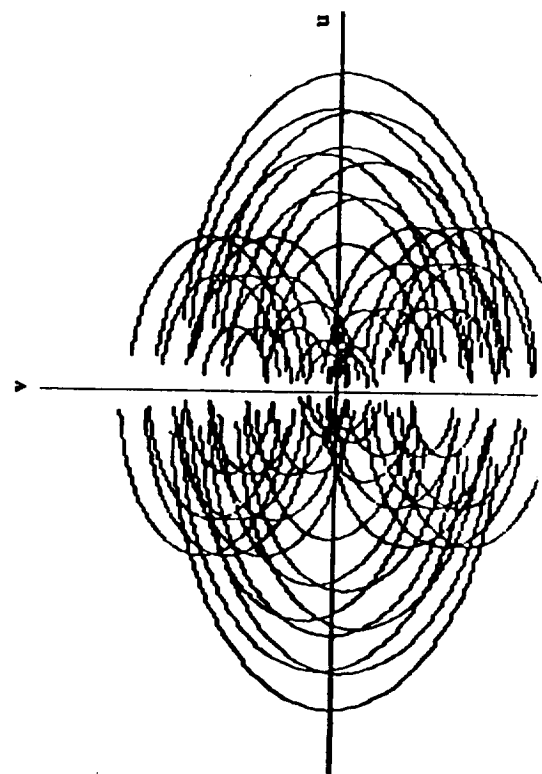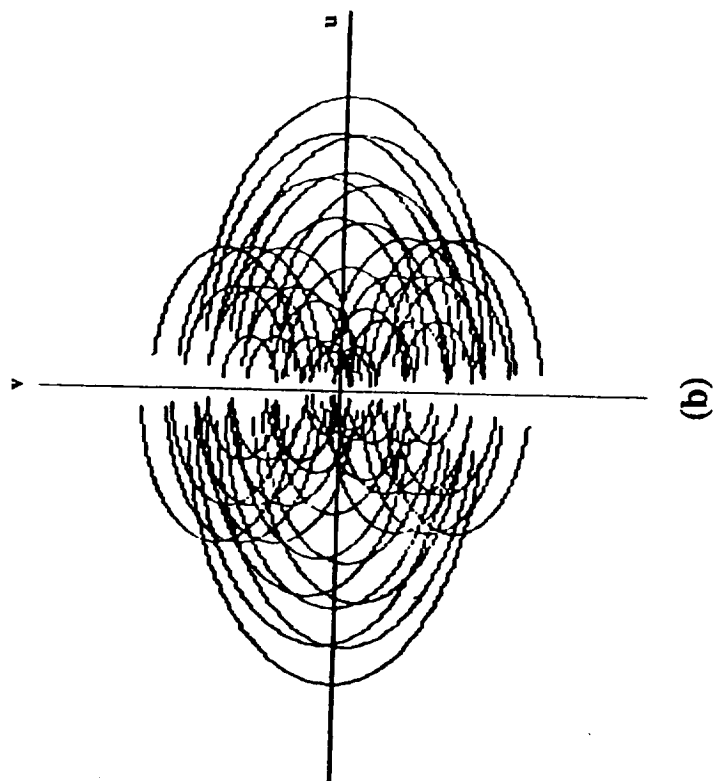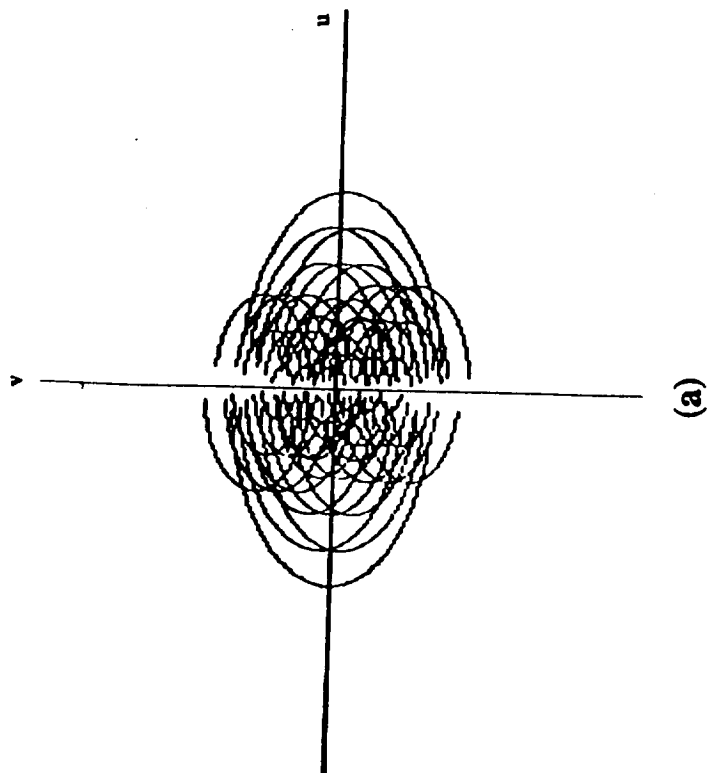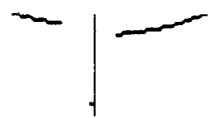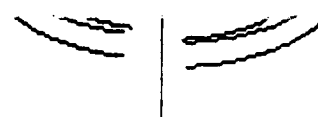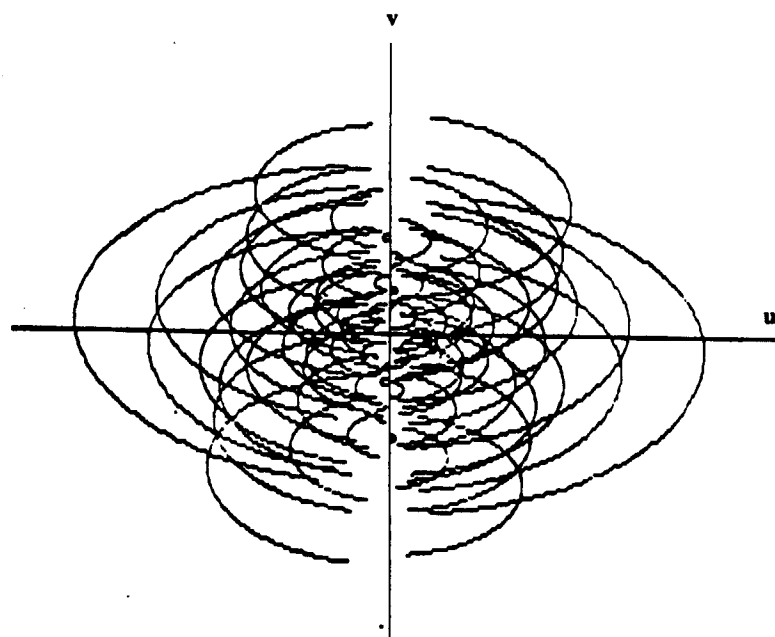
Figure 3.1-10: U-V Coverage at 45° Target Declination with 9 Array Elements. (a) Configuration #1. (b) Configuration #2. (c) Configuration #3. (d) Configuation #4. (e) Configuration #5.

(a)

(b)

(c)

(d)

(e)

(f)
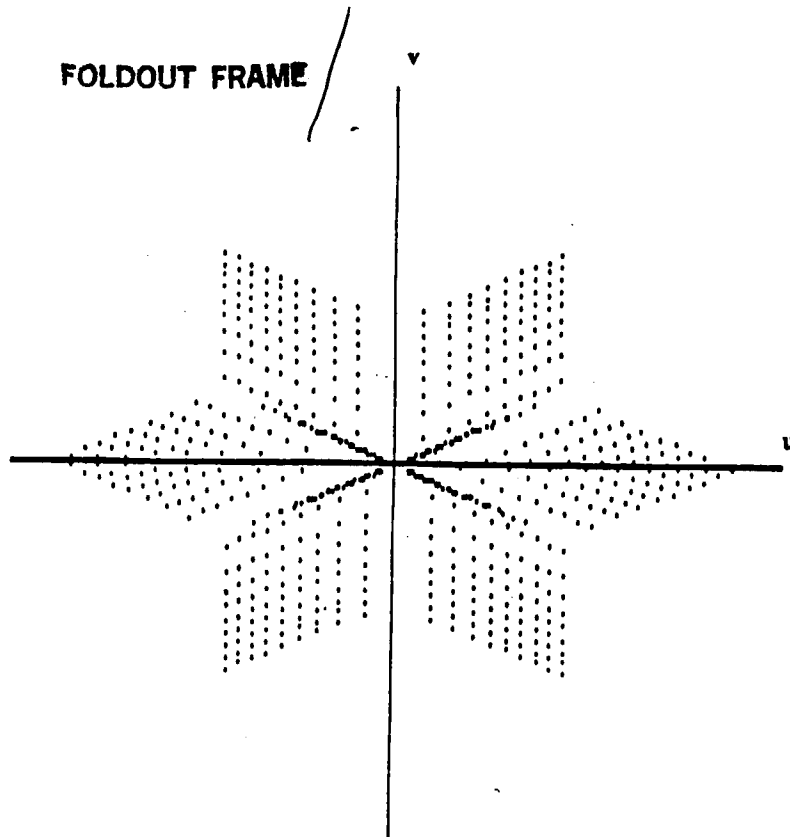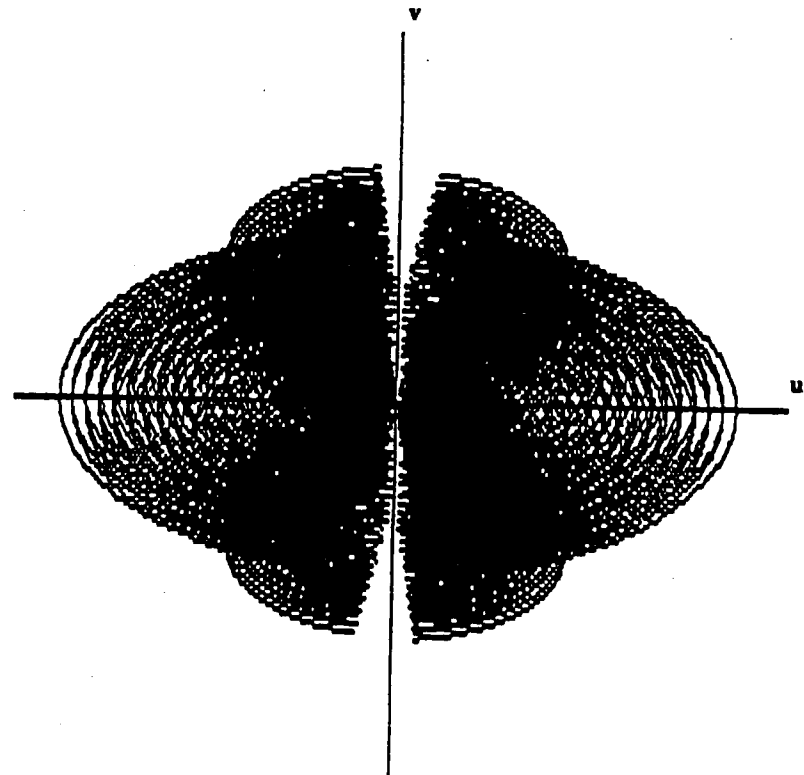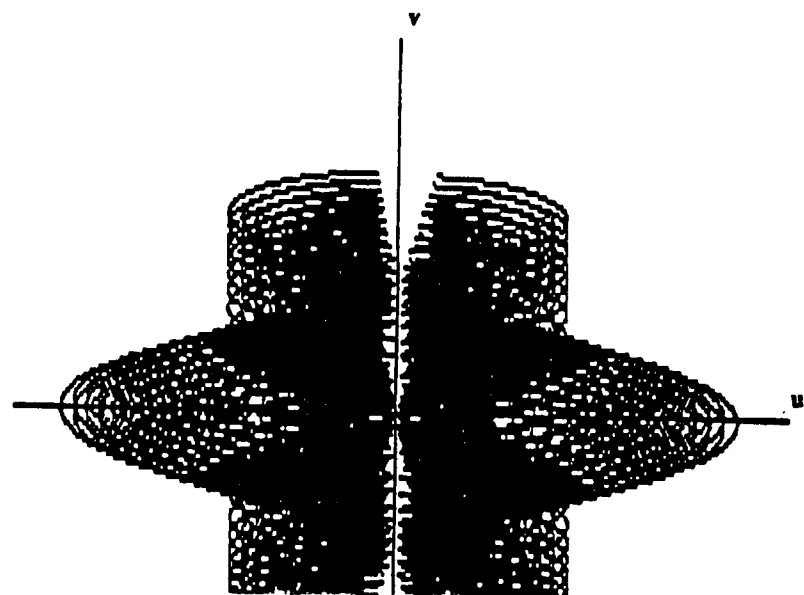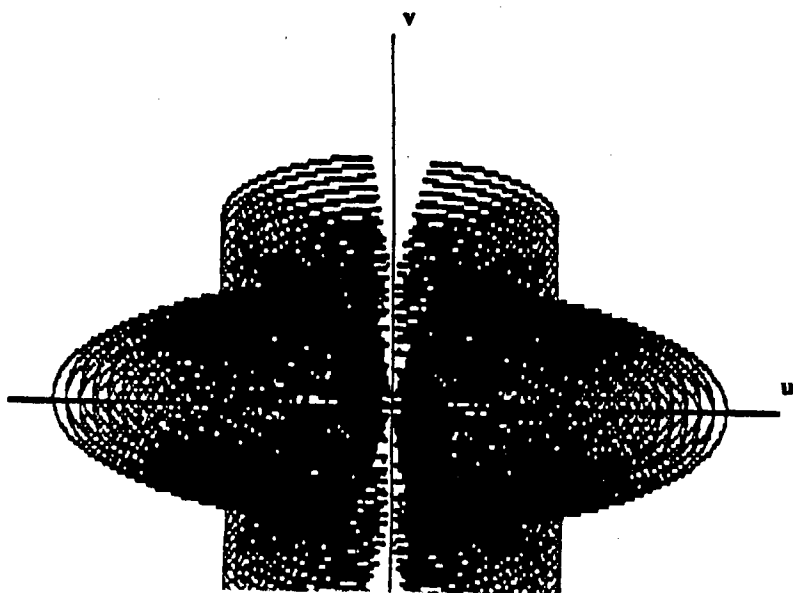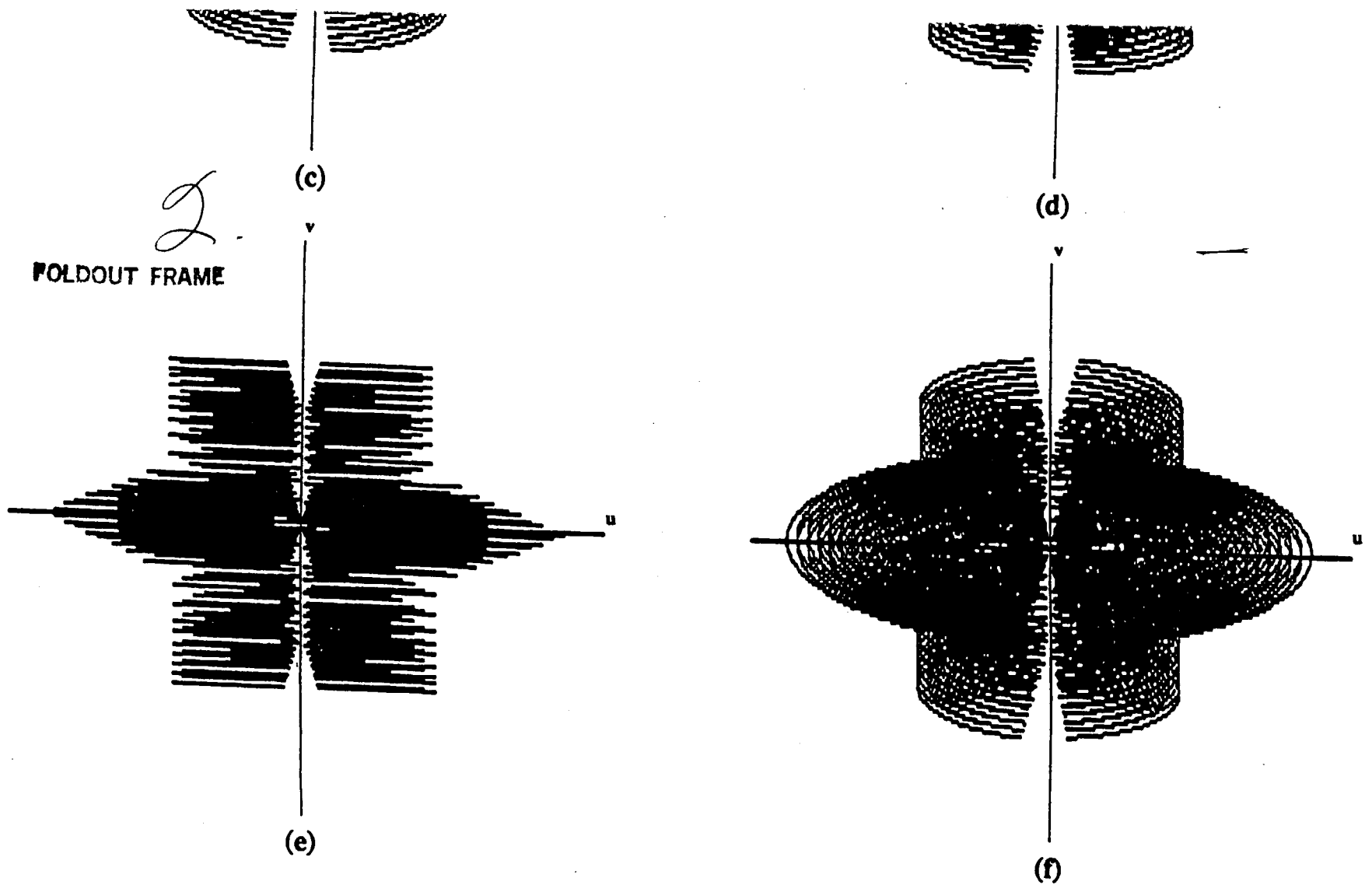
Figure 3.1-11: Additional u-v Coverage Plots for Configuration #2 with 27 Array Elements. (a) Snapshot at zenith. (b) 45°declination. (c) 30°declination. (d) 20°declination. (e) 0°declination. (f) -30°declination.

Table 3.1-2: Configuration #2. Array Element Spacings East and North of Array Center

	NORTH ARM (meters)		SOUTH WEST ARM (meters)		NORTH EAST ARM (meters)	
	E	N	E	N	E	N
1	0.0	267.6	- 407.8	- 235.4	551.4	- 318.2
2	0.0	782.6	- 793.4	- 458.1	901.2	- 520.3
3	0.0	1158.0	-1099.6	- 634.9	1192.3	- 688.4
4	0.0	1479.7	-1367.7	- 789.6	1451.2	- 837.9
5	0.0	1769.5	-1611.6	- 930.4	1688.8	- 975.0
6	0.0	2037.2	-1838.2	-1061.3	1910.6	-1103.1
7	0.0	2288.4	-2051.6	-1184.5	2120.3	-1224.1
8	0.0	2526.3	-2254.4	-1301.6	2320.0	-1339.5
9	0.0	2753.6	-2448.5	-1413.6	2511.5	-1450.0

3.2 Telescope Optics

3.2.1 Light Collection

Examination of the SNR requirements reveals that approximately 48 square meters of collecting area are required after secondary mirror blockage effects are considered. This can be accomplished with sixteen 2.0 m diameter mirrors, sixty 1.0 m mirrors, etc. The factors effecting this choice included u-v plane coverage, the number of elements, reliability/survivability, cost, etc.

The Y-array style (Sect. 3.1) needs many telescopes to insure good u-v plane coverage. Analysis showed that twenty seven, 1.5 meter diameter elements would provide the needed u-v coverage and collecting area at an acceptable cost in delay lines and complexity.

Another constraint was provided by the Rayleigh length and its three variables: wavelength, beam diameter and travel length. The worst case wavelength is 10,000 nm, and the longest travel length is 9100 meters. This requires a beam width of 34 cm. Due to structural constraints, this beam width was restricted to 25 cm which gives the Rayleigh length limit at 5394 nm. The quality of the received signal begins to drop off gradually for longer wavelengths.

Two systems were studied for collecting light: siderostats and telescopes. Siderostats consist of 2 large flat mirrors that collect the incoming light. The light is then usually compressed and collimated with a Cassegrain focusing system. Siderostats also have a variable collecting area dependent on the target declination. Siderostat complexity arises from larger mirror sizes requiring bulkier, heavier motor systems. Mass comes from the primary focusing mirror being rigidly mounted, involving stiff (i.e. higher mass) structures to reduce vibration and jitter. The only benefit to a siderostat is a central layout and easy control of the focusing system for less baseline instability in the Cassegrain compressors. Because this advantage (one of the few), a more accurate baseline, is not a stringent requirement of an interferometer not performing astrometric measurements, the more elegant system, telescopes, were chosen.

Due to the need to keep the light at 25 cm and the desire not to focus the light before it reached the instrumentation plane (see Sect. 3.4), a modified Mersenne afocal system was chosen. Several methods of directing light out of the structure with the aim of using the least number of bounces possible were developed and a 3 bounce system was chosen.

A Mersenne afocal system can be designed so that there is no spherical aberration, coma and stigmatism by making both mirror surfaces Cartesian (App 3.2-1).. Structural requirements made it necessary to have the secondary mirror plane at the same height or lower than the pupil plane entrance. This requirement made it impossible to reduce the remaining field curvature and distortion to zero. Appendix 3.2-1 shows these equations in detail.

With a primary aperture of 1.5 meters, a secondary mirror size of 25 cm due to Rayleigh length considerations and a pupil plane height of 3.3 meters, the primary mirror (#1) has a focal length of 3.692 meters (Fig 3.2-1). This gives it a fast F# of 2.46 and a compression ratio of 6:1. The equation of the parabolic mirror shape is given by:

$$H^2 = 14.678*z \qquad \qquad Eq.\ 3.2\text{-}1$$

where $H^2 = x^2 + y^2$
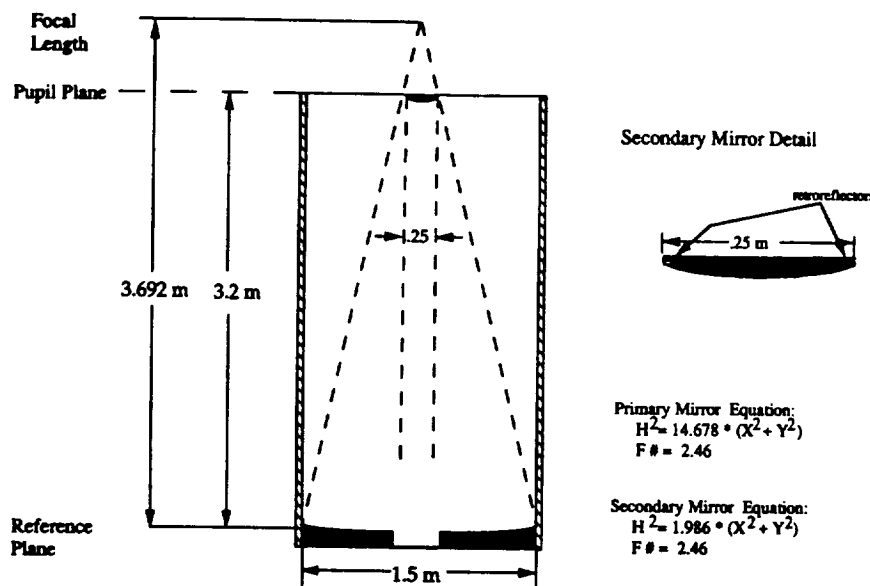
Figure 3.2-1: Primary and Secondary Mirror System

z = distance along primary mirror axis
x = planar direction at right angle to z
y = planar direction at right angle to x and z

The secondary mirror (#2) takes the converging beam from the primary mirror and converts it to a nearly planar wave 0.25 meters in diameter. The mirror is centered 3.3 meters above the primary mirror and has a parabolic shape $H^2 = 1.968*z$ following the same conventions of Eq. 3.2-1. The mirror itself is 25 cm in diameter and supported by 4 struts from the central cylinder.

The third mirror, or fold mirror, directs light out of the telescope cylinder (Fig 3.2-2). It is mounted about the rotation axis of the telescope 20.6 cm above the primary mirror and is held at a 45 deg angle to the light path from the secondary mirror. The mirror is elliptical (25 cm by 35.4 cm) and is 3rd order curved to allow removal of distortion and field curvature side effects of the afocal system.

Mirror #4 turns the light path 90 deg downward through the rotation axis. It is solidly mounted at a 45 degree angle to the incident light and completely planar. The light path, having cleared the bottom of the telescope structure, is turned another nominal 90 degrees by the final telescope exit mirror (#5). This 25 cm by 35.4 cm elliptically, completely planar mirror is two axis controllable (Appendix 3.2-2) to 1.778 arcsec (0.0004939 deg). This mirror is nominally 1 meter above the ground plane.

Each telescope is set up in a splayed pattern from the nominal telescope line axis in order to insure no interference in the light path will exist further downstream (Appendix 3.2-3). This makes for a maximum horizontal angle of 1.01 deg from telescope N1 (Fig. 3.2-3). All other horizontal angles are less than this and are listed in Table 3.2-1.

Vertical angles are kept to a minimum as well. The closest telescope, N1, is directed to the lowest receiving mirror through an angle of 1.001 deg. The farthest telescopes of each arm are directed towards the highest receiving mirror at an maximum angle of 0.163 deg (for N9)
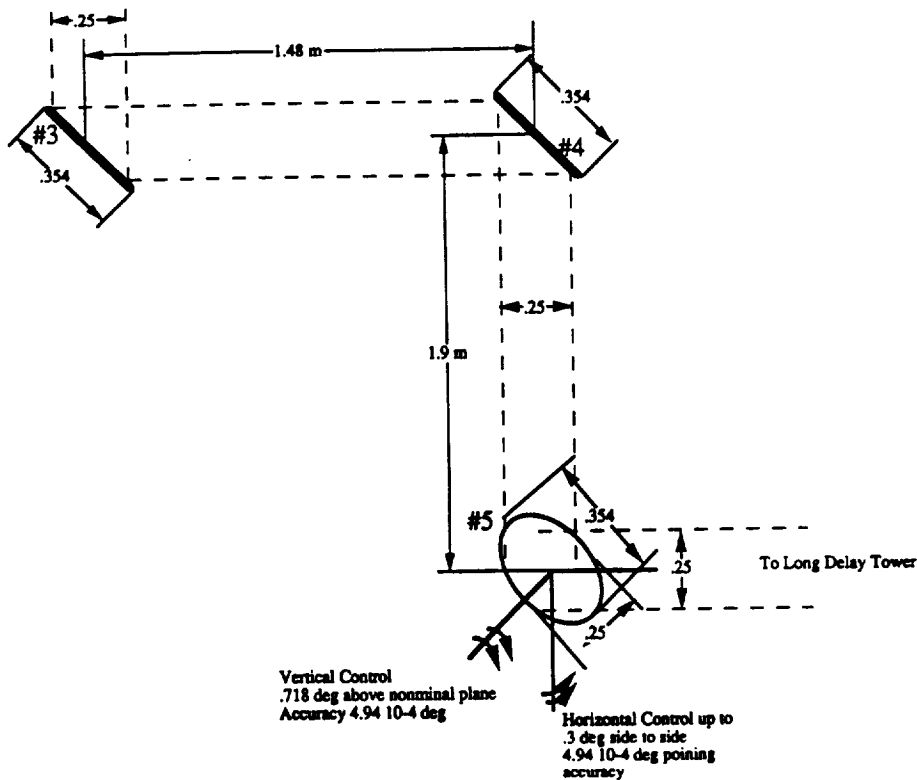
Figure 3.2-2: Telescope Exit Light Path

3.3 Delay Lines

After light has been gathered in each telescope, it must be transmitted to the instrumentation. However, all the light that left the source at the same time must reach the instruments at the same time in order to get phase coherent results. This requires that light from some telescopes (depending on location and target declination) be delayed. In radio wave astronomy this is achieved electronically, but this is impossible with current technology for the visible and infrared spectrums. Therefore, the light must be physically delayed by sending light through longer or shorter path lengths.

The amount of delay comes from two sources. First, as light from the telescopes closest to the center travel the least distance, they must be delayed to the length of the farthest telescope. This requires a maximum travel delay of 2632.1 meters by telescope N1. The second source of required delay comes from the fact that light from the same source does not always reach each telescope at the same time. For low viewing angles light from certain telescopes must be delayed. Light at the furthest telescope from the source must arrive 4960 meters later than the first struck telescope. Thus, light from N1 must be delayed (in the worst case viewing angle) 2711 meters. This yields a maximum required delay of 5343 meters. Taking into account construction variations in telescope and delay mirror placement, and the possible movement of telescopes to achieve redundancy, the maximum total delay line was required to be 5400 meters.

Several different options were considered for delay line design. The optimal choice for this design was one with a minimum number of bounces (to keep losses down), mirrors, expandability and a desire to maintain bounce angles within an acceptable limit. The system decided upon consists of one steering tower, two independent banks of 61 long delay mirrors each and a 27 element fine delay system.

Side View, North Arm (vertical displacement exagerated)

1.001°   .378°   .275°   .231°   .205°   .189°   .177°   .169°   .163°

Top View, North Arm (displacement from center exagerated)

1.019°   .339°   .182°   .079°   0.0°

.572°   .305°   .168°   .072°

1157   2037   2753

500 m   1000 m   1500 m   2000 m   2500 m
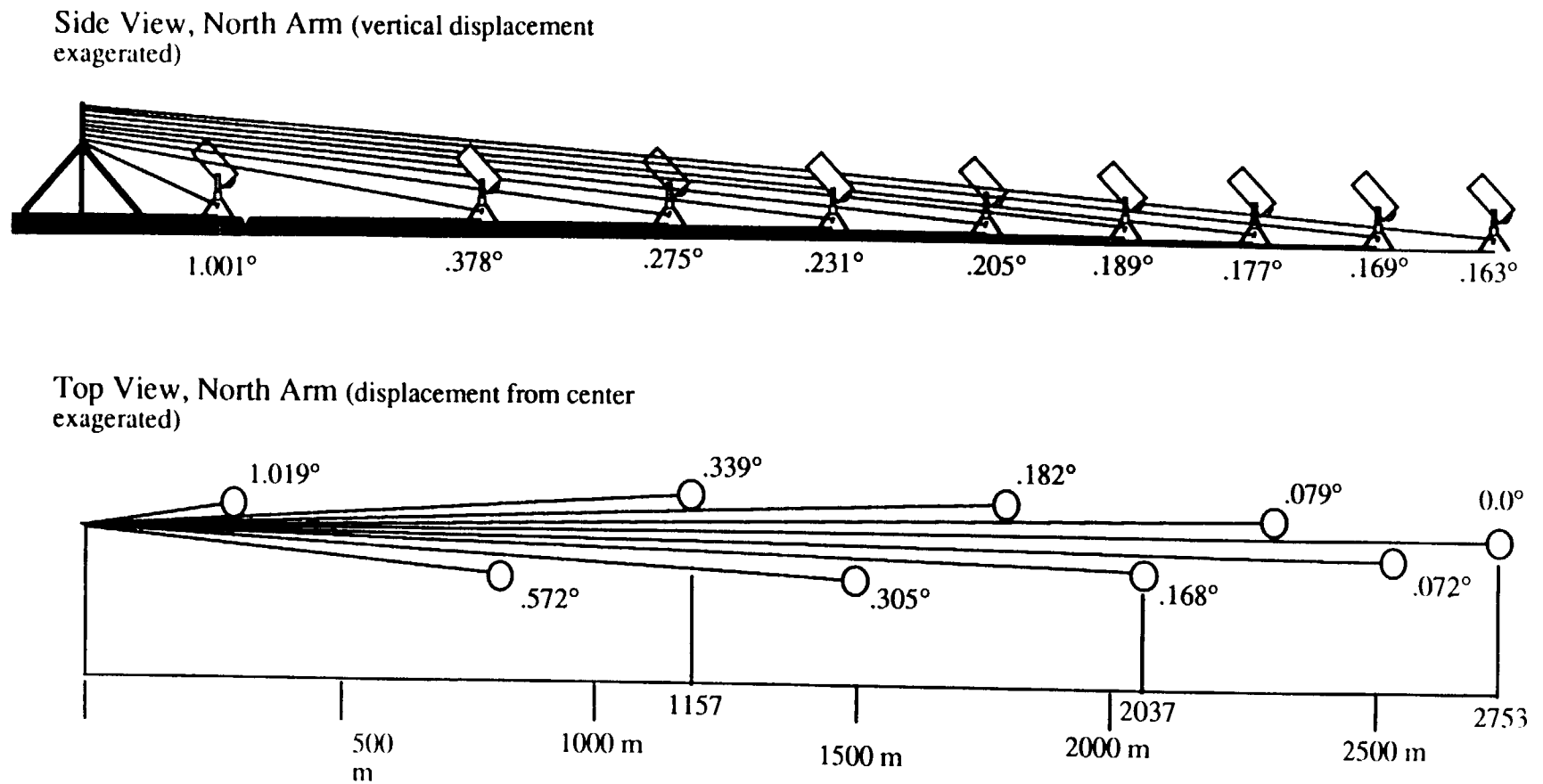
Figure 3.2-3: Telescope Placement Example (North Arm)

Table 3.2-1: Telescope Placement

						3 Structure					
						0.05 Clearance					
						0.125 Beam					
Placement (Nominal)			Horizontal Angles		3.175 Total		Vertical Angles			Max Required Delays East Rising		
								0.3 Mirror				
	North	East	Length		Distance Off	Angle (deg)	Distance Abov Curve		Angle (deg)	Travel	Low Angle	Total
N1	267.62	0.00	267.62	N1	4.7604	1.0191	4.6500	0.0749	1.0115	2632.11	2480.00	5112.11
N2	782.52	0.00	782.52	N2	7.8107	0.5719	4.9500	0.2191	0.3785	2117.21	2480.00	4597.21
N3	1157.92	0.00	1157.92	N3	6.8596	0.3394	5.2500	0.3242	0.2758	1741.81	2480.00	4221.81
N4	1479.60	0.00	1479.60	N4	7.8832	0.3053	5.5500	0.4143	0.2310	1420.13	2480.00	3900.13
N5	1769.35	0.00	1769.35	N5	5.6302	0.1823	5.8500	0.4954	0.2055	1130.37	2480.00	3610.37
N6	2037.02	0.00	2037.02	N6	6.0016	0.1688	6.1500	0.5704	0.1890	862.71	2480.00	3342.71
N7	2288.10	0.00	2288.10	N7	3.1750	0.0795	6.4500	0.6407	0.1776	611.62	2480.00	3091.62
N8	2526.08	0.00	2526.08	N8	3.1750	0.0720	6.7500	0.7073	0.1691	373.65	2480.00	2853.65
N9	2753.33	0.00	2753.33	N9	0.0000	0.0000	7.0500	0.7709	0.1628	146.40	2480.00	2626.40
SW1	-235.40	-407.72	470.80	SW1	5.7867	0.7042	4.6500	0.1318	0.5819	2428.93	2072.28	4501.21
SW2	-458.04	-793.36	916.09	SW2	8.2570	0.5164	4.9500	0.2565	0.3256	1983.64	1686.64	3670.28
SW3	-634.81	-1099.53	1269.63	SW3	7.0432	0.3178	5.2500	0.3555	0.2530	1630.10	1380.47	3010.57
SW4	-789.56	-1367.55	1579.11	SW4	7.9861	0.2898	5.5500	0.4422	0.2174	1320.61	1112.45	2433.06
SW5	-930.35	-1611.41	1860.70	SW5	5.6690	0.1746	5.8500	0.5210	0.1962	1039.03	868.59	1907.61
SW6	-1061.18	-1838.01	2122.35	SW6	6.0197	0.1625	6.1500	0.5943	0.1821	777.37	641.99	1419.36
SW7	-1184.38	-2051.40	2368.75	SW7	3.1750	0.0768	6.4500	0.6633	0.1721	530.98	428.60	959.58
SW8	-1301.47	-2254.20	2602.93	SW8	3.1750	0.0699	6.7500	0.7288	0.1646	296.80	225.80	522.60
SW9	-1413.50	-2448.26	2827.00	SW9	0.0000	0.0000	7.0500	0.7916	0.1589	72.73	31.74	104.47
SE1	-318.18	551.10	636.35	SE1	6.5042	0.5856	4.6500	0.1782	0.4347	2263.38	3031.10	5294.47
SE2	-520.26	901.12	1040.53	SE2	8.6187	0.4746	4.9500	0.2913	0.2886	1859.20	3381.12	5240.32
SE3	-688.31	1192.19	1376.62	SE3	7.2020	0.2997	5.2500	0.3855	0.2346	1523.11	3672.19	5195.30
SE4	-837.79	1451.10	1675.59	SE4	8.0766	0.2762	5.5500	0.4692	0.2058	1224.14	3931.10	5155.24
SE5	-974.93	1688.63	1949.86	SE5	5.7039	0.1676	5.8500	0.5460	0.1879	949.87	4168.63	5118.50
SE6	-1103.00	1910.46	2206.01	SE6	6.0361	0.1568	6.1500	0.6177	0.1758	693.72	4390.46	5084.18
SE6	-1224.02	2120.07	2448.05	SE6	3.1750	0.0743	6.4500	0.6855	0.1670	451.68	4600.07	5051.75
SE8	-1339.33	2319.79	2678.66	SE8	3.1750	0.0679	6.7500	0.7500	0.1604	221.07	4799.79	5020.86
SE9	-1449.86	2511.24	2899.73	SE9	0.0000	0.0000	7.0500	0.8119	0.1553	0.00	4960.00	4960.00

3.3.1 Long Delay System

After the light has left each telescope, it is directed to the center of the array into the long delay system. It hits the receiving mirror and is redirected through a nominal 60 deg turn towards the appropriate long delay bounce mirror after which it comes back to the transmitting mirror of the delay tower. Figure 3.3-1 shows the general arrangement of the central long delay tower and bounce mirrors. Such a system provides incremented steps of 90 meter delay. The remaining delay is corrected in the fine delay systems (Sect. 3.3.2). Computer algorithms taking target declinations, azimuth, baseline and optical path length data, calculate the needed delay for each telescope and direct the controllable mirrors of the fine and long delay systems to achieve this.

The long delay system (Figure 3.3-1) starts once the light from each telescope reaches its receiving mirror. Each telescope has its own dedicated receiving mirror in the receiving stack leading to a total of 27 receiving mirrors arranged in a triangular pattern about the central post. Each mirror is centered to nominally face directly the telescope arm, is 30 cm in diameter and controllable to 0.845 arcsec (0.000235 deg) about two axes (Appendix 3.2-1). Once the light hits the receiving mirror, it is turned 60 deg towards the appropriate bounce mirrors with the proper horizontal and vertical angle so that it will hit the proper transmitting mirror afterwards.

Each long delay bounce mirror is placed 45 meters from the previous one along the nominal baseline. 61 mirrors are required for each arm. Arranged in a splayed pattern similar to the telescopes (Table 3.3-1), the closest is located 300 meters away from the center. This requires it to be 2.64 meters off the nominal delay line and causes an angle toward the center of 0.505 deg which is well within acceptable limits. Each delay tower (Fig. 3.3-2) is constructed of a boron/epoxy truss system 3.6 m high, with a 1.0 m square base. The flat 1.05 m x 0.30 m mirror on each tower has a thickness of 0.5 cm, weight of 3.47 kg, and is made of Corning U.L.E. with a dielectric silver coating.

Twenty-eight transmitting mirrors are on two of the support tower legs (14 mirror per leg). Each is 30 cm tall, 46.12 cm wide, 0.5 cm thick and made of Corning ULE glass coated with a dielectric silver reflector. The centers of the mirrors start at 0.45 m above the ground and go to 4.05 meters and they are spaced along the leg so that the center of each beam is 30 cm from the next in the horizontal plane. As the center of the entrance to the fine delay system is 0.43 meters above the ground plane and 210 meters away, the maximum vertical plane angle change is 1 deg. The transmitting mirrors are required to be 2 axis controllable to 4.911 arcsec (0.00136 deg).

The tower consists of a 2.7 m hollow circular rod supported by a tripod of 6.155 m legs. All four components are constructed of 2.5 cm. thick, 10 cm diameter hollow boron/epoxy tubes.

Long Delay Receiving and Transmitting Top View

1040 m

1376 m

South East Arm
(Etc., out to 2900 m,
9 telescopes total)

636 m

To Fine Delay

300 m

345 m   390 m

Long Delay Line #1
(Etc., Out to 5400 meters,
61 mirrors total)

435 m
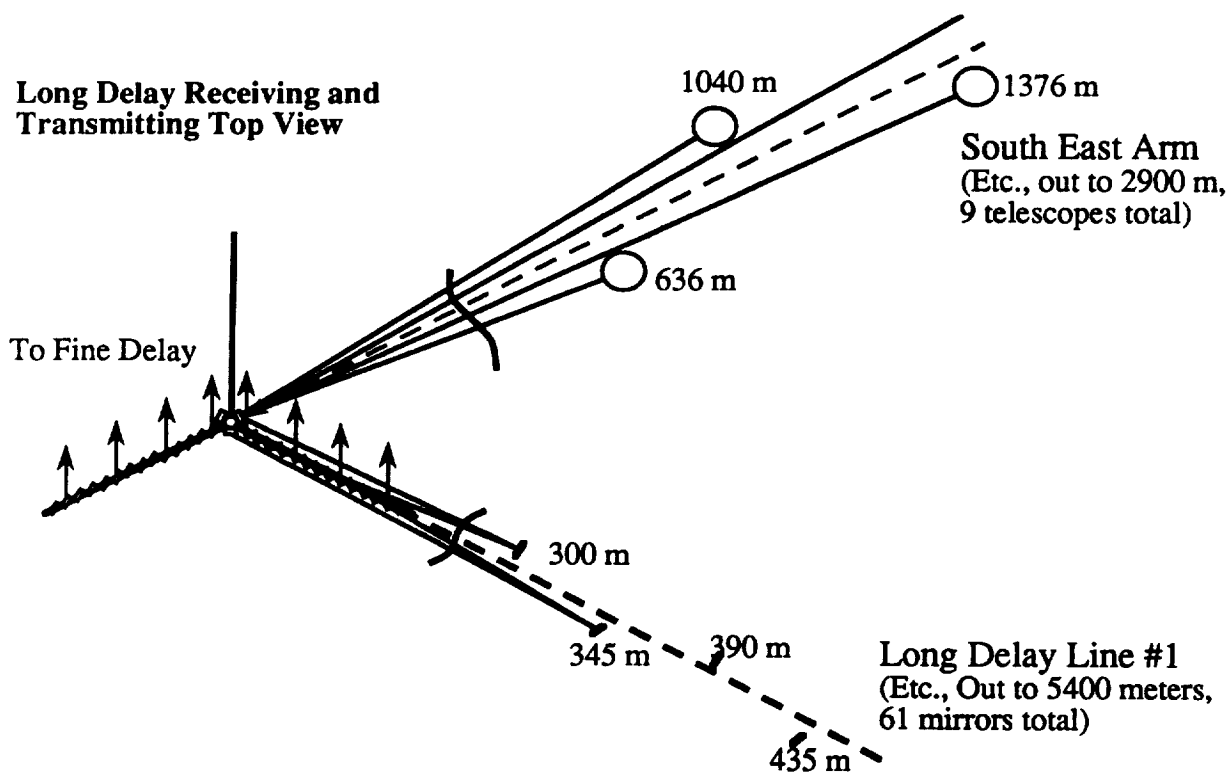
**Long Delay -Bounce Mirror
Interface Side View**

Central
Tower

Receiving

300- 3000 m

Bounce
Mirror
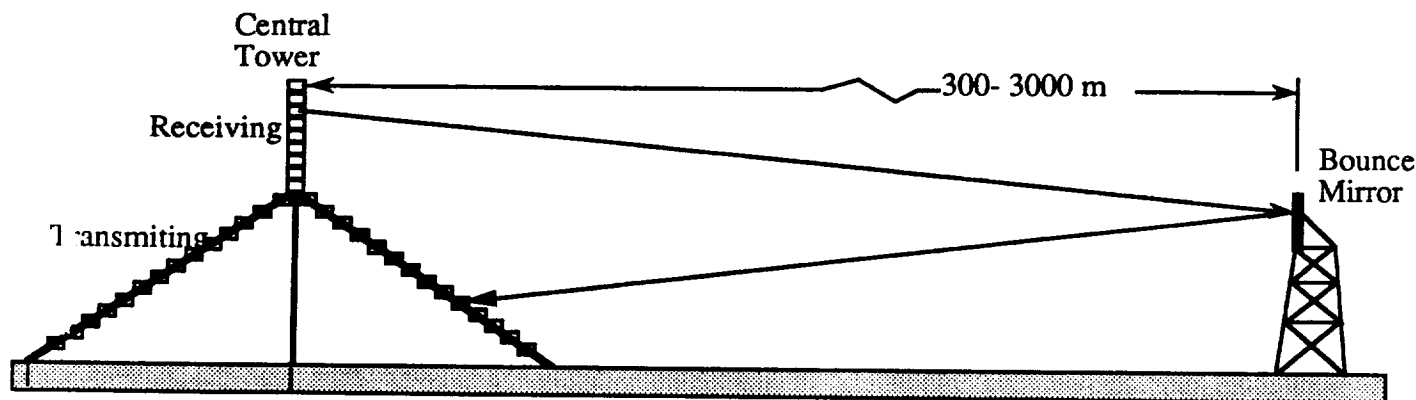
Transmiting

**Long Delay Transmitting to
Fine Delay Interface Side View**

Receiving

200 m

Transmiting

Fine Delay Bldg
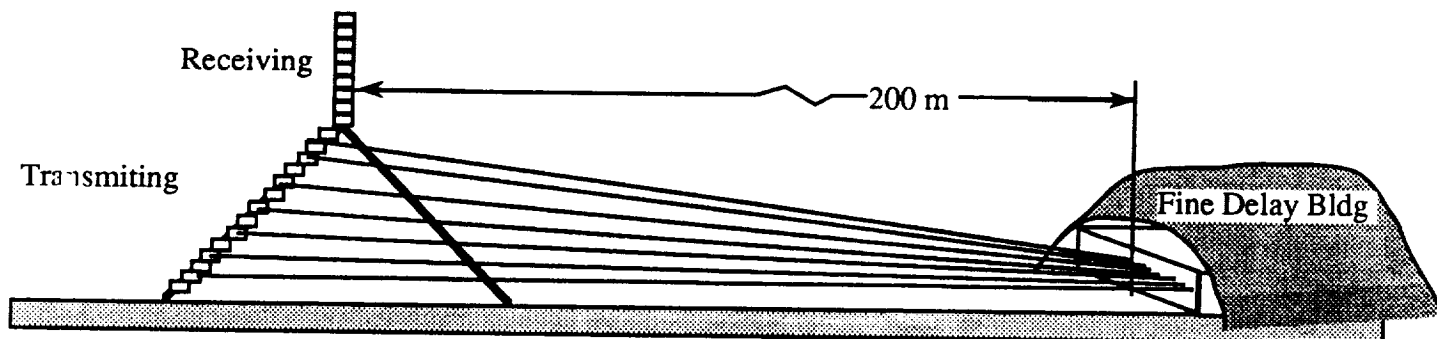
Figure 3.3-1: Long Delay System

Table 3.3-1: Long Delay Mirror Placement

Spacing	45	0.15	Structure
Start	300	0.05	Clearance
Max Delay	5400	0.125	Beam Width
		0.325	Total

#	Length	Off	Angle
1	300	2.6487	0.5058
2	345	2.9972	0.4978
3	390	3.0208	0.4438
4	435	3.3319	0.4388
5	480	3.3179	0.3960
6	525	3.5985	0.3927
7	570	3.5541	0.3572
8	615	3.8090	0.3549
9	660	3.7389	0.3246
10	705	3.9717	0.3228
11	750	3.8795	0.2964
12	795	4.0927	0.2950
13	840	3.9810	0.2715
14	885	4.1769	0.2704
15	930	4.0477	0.2494
16	975	4.2278	0.2484
17	1020	4.0830	0.2293
18	1065	4.2488	0.2286
19	1110	4.0896	0.2111
20	1155	4.2422	0.2104
21	1200	4.0698	0.1943
22	1245	4.2102	0.1938
23	1290	4.0257	0.1788
24	1335	4.1548	0.1783
25	1380	3.9588	0.1644
26	1425	4.0773	0.1639
27	1470	3.8708	0.1509
28	1515	3.9794	0.1505
29	1560	3.7629	0.1382
30	1605	3.8621	0.1379
31	1650	3.6363	0.1263
32	1695	3.7266	0.1260
33	1740	3.4919	0.1150
34	1785	3.5738	0.1147
35	1830	3.3307	0.1043
36	1875	3.4046	0.1040
37	1920	3.1535	0.0941
38	1965	3.2198	0.0939
39	2010	2.9611	0.0844
40	2055	3.0201	0.0842
41	2100	2.7541	0.0751
42	2145	2.8062	0.0750
43	2190	2.5332	0.0663
44	2235	2.5786	0.0661
45	2280	2.2990	0.0578
46	2325	2.3379	0.0576
47	2370	2.0519	0.0496
48	2415	2.0847	0.0495
49	2460	1.7925	0.0417
50	2505	1.8193	0.0416
51	2550	1.5212	0.0342
52	2595	1.5423	0.0341
53	2640	1.2384	0.0269
54	2685	1.2540	0.0268
55	2730	0.9445	0.0198
56	2775	0.9547	0.0197
57	2820	0.6399	0.0130
58	2865	0.6450	0.0129
59	2910	0.3250	0.0064
60	2955	0.3250	0.0063
61	3000	0	0

Send Receive Tower

2.7 m

4.2 m

.3 m

4.5 m

North

120 deg.

Top View

30 cm x 30 cm Mirrors

Long Delay Bounce Mirror

Side

Front

.3 m

1.05 m

3.6 m
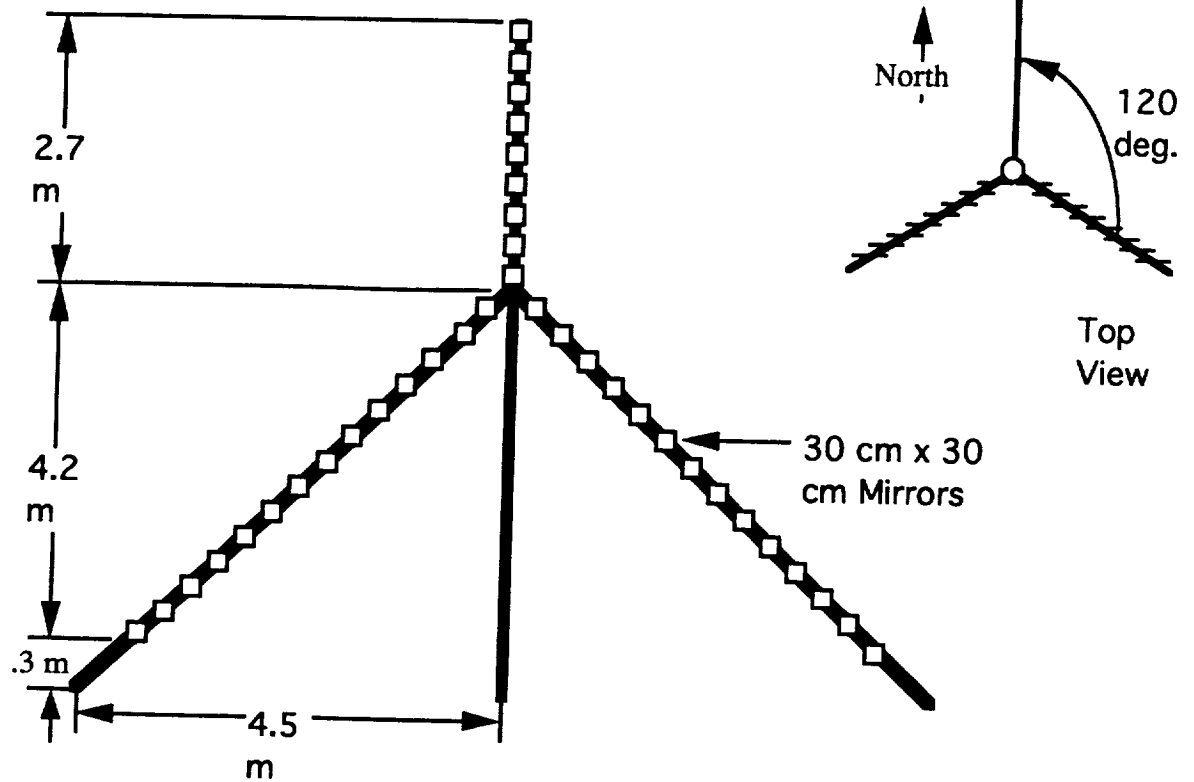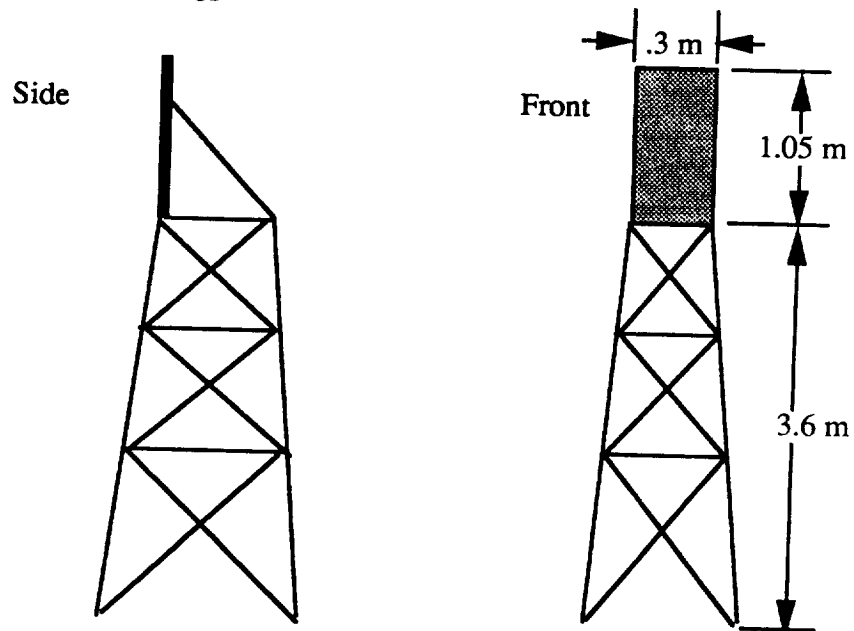
Figure 3.3-2: Long Delay System Details

3.3.2 Fine Delay Lines

The function of the fine delay lines is to make fine corrections in the optical path length and compensate continuously for lunar rotation. Because of the long lunar day, the required speed of the fine delay lines is quite small, on the order of 10 mm/s of optical path delay, corresponding to 5.0 mm/s of physical mirror motion. Therefore, with a total optical path range in the fine delay of 90 meters, approximately 2.5 hours of continuous motion is available for the longest baseline. After approximately 2.5 hours of continuous viewing, the long delay line would move to the next stationary mirror, the fine delay would quickly move to its other extreme, and the observation would continue as before. The fine delay lines will be controlled by the metrology system.

All 27 delay lines will be laid out horizontally across the lunar surface and placed flush against each other. The set-up of the fine delay lines in the central receiving station is shown in Figure 3.3-3. Each fine delay line will be a total of 55.5 meters long. The 25 cm diameter light beam will enter into one end of the fine delay, be compressed in a Cassegrain beam compressor down to a 4 cm diameter, travel a maximum distance of 54 meters to the adjustable mirror, reflect back to the stationary mirror at a maximum distance of 45 meters, and then travel out of the fine delay in a direction opposite to the incident light (Fig. 3.3-4). The movable fine delay mirror will have a minimum approach distance to the stationary mirror of 9 meters and the mobile and stationary mirror centers will be offset by 8 cm (Fig. 3.3-4). This configuration will produce a maximum reflection angle of approximately 0.25 degrees, eliminating any polarization problems caused by the light beams reflecting through unequal angles.

Both the mobile and the fixed mirror will be flat, have a $\lambda/100$ surface finish and be constructed of Corning's U.L.E. glass (Refer to 6.2.2 - Mirror Material). The mobile mirror will be 8.0 cm in diameter and 0.25 cm thick (Fig. 3.3-5 and 3.3-6) and the fixed mirror (Fig. 3.3-7) will be 6.0 cm in diameter and 0.25 cm thick (to accommodate both the incident beam
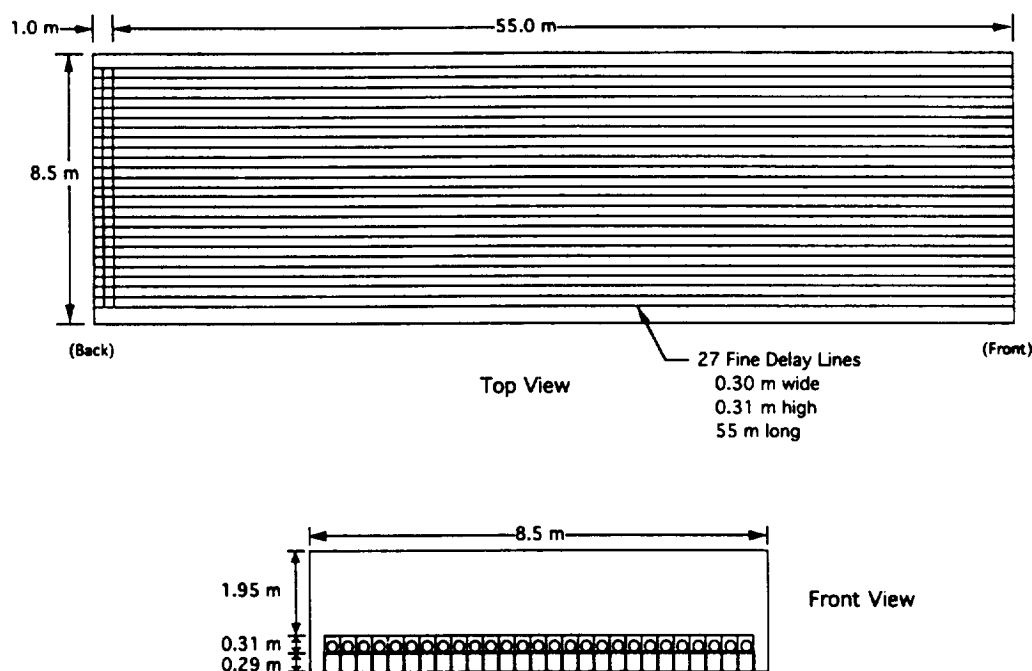
Figure 3.3-3: Layout of Fine Delay Lines

BEAM COMPRESSOR

25 cm. dia. BEAM

MOBILE MIRROR

4 cm. dia. BEAM

INSTRUMENTATION BOX

FIXED MIRROR

FINE DELAY LINE STANDS
ONE EVERY 3.67 METERS

LUNAR SURFACE

To Scale
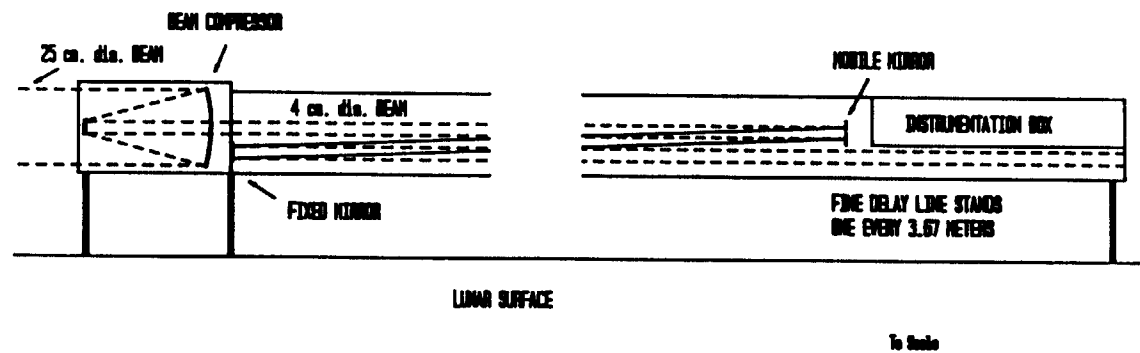
Figure 3.3-4: Full Fine Delay Line Configuration

90.00

10.00

INSTRUMENTATION BOX

12.00

16.00

MOBILE MIRROR ASSEMBLY

Dimensions in cm.
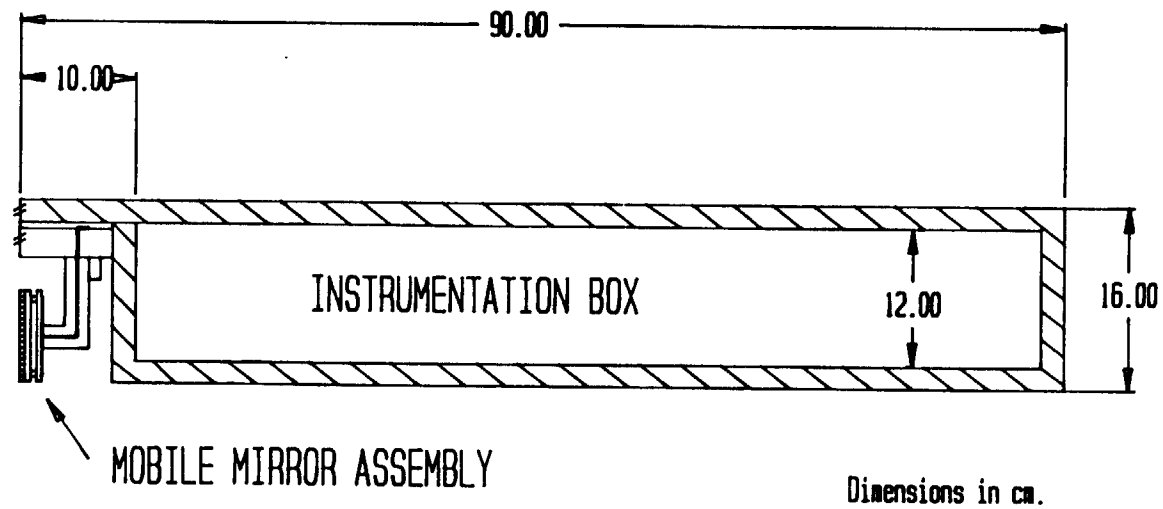
Figure 3.3-5: Instrumentation Box and Mobile Mirror
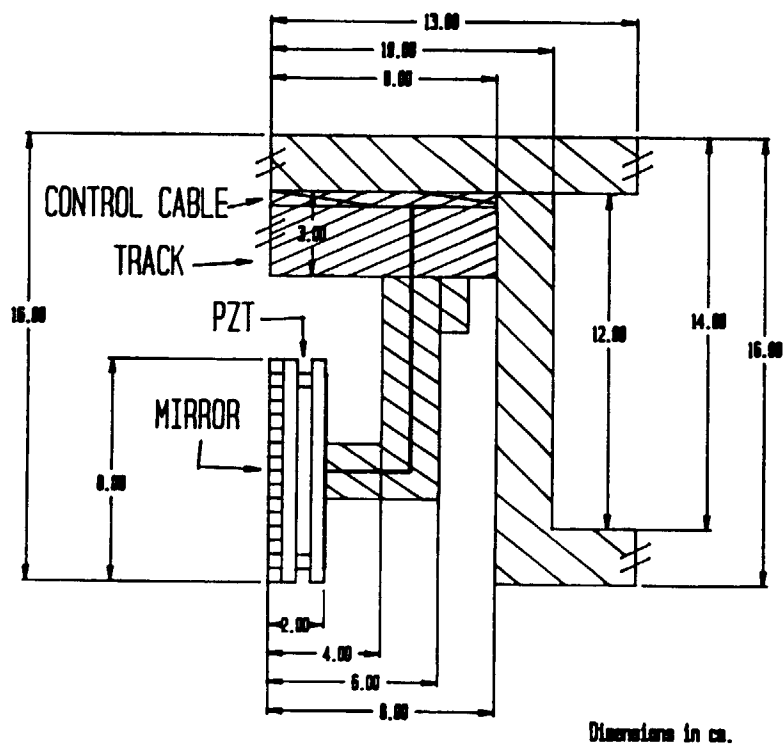
Figure 3.3-6: Mobile Mirror Assembly
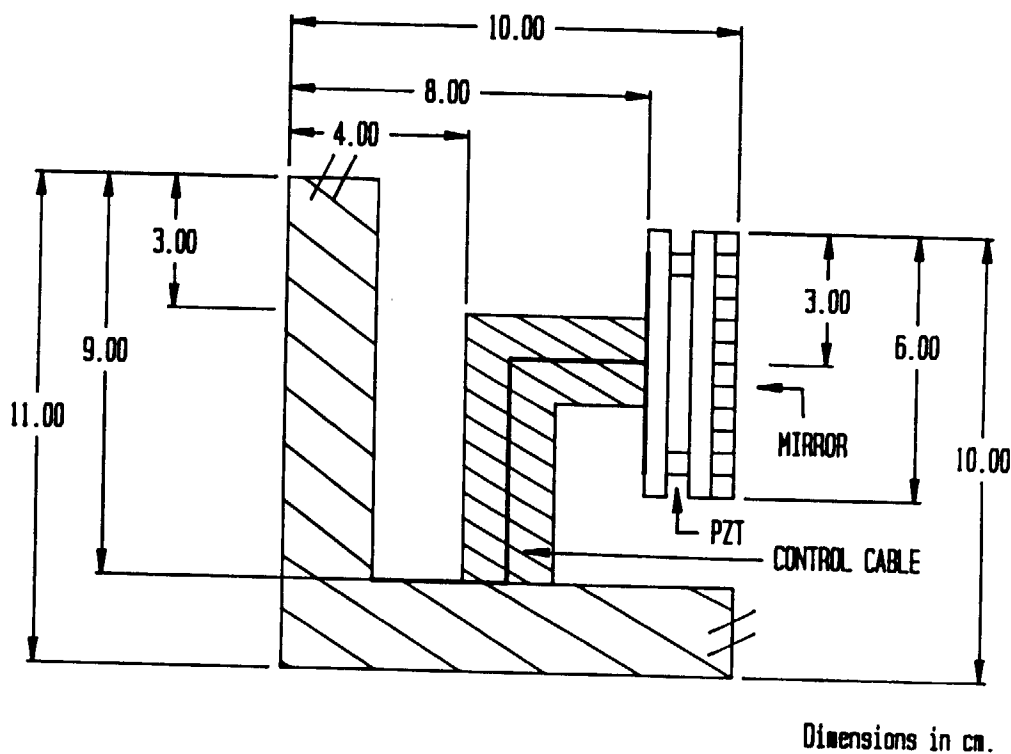
Figure 3.3-7: Fixed Mirror Assembly

and a metrology system to produce the required positioning accuracy). All 27 fine delay lines will be housed in a sealed structure and will be contained in segmented box-like housings of 11 segments, each segment 5 meters long, 30 cm wide and 27 cm high (55 meters long, 30 cm wide and 27 cm high, for the total reconnected structure). The 27 fine delay line housings will be contained in a central receiving station (a minimum of 56 meters long, 8.5 wide, and 1 meter high), allowing for radiation, thermal, and dust protection. The delay lines will be raised from the surface by stationary 2-leg supports (Fig. 3.3-4) so the bottom of the incident light ray will be a minimum of 30 cm off the lunar surface. This will help suppress dust entry into the delay line system.

A Cassegrain beam compression system will be mounted at the fine delay lines entrance. This compression system will consist of two paraboloidal mirrors, constructed of Corning's U.L.E.. glass with a $\lambda/100$ surface finish. The first mirror will be 26 cm in diameter with a 4.25 cm central hole. The second mirror will be 5 cm in diameter. The 25 cm diameter incident light beam will strike the first mirror, reflect onto the secondary mirror while being compressed to a 4 cm diameter. The light beam then reflects off the secondary mirror and exits the compression system in a direction opposite to the 25 cm diameter incident light beam. The each beam compression system is contained in a 50 cm x 30 cm x 31 cm box that is connected to the entrance of each fine delay line and rests on two stationary stands (Fig. 3.3-4).

Boron/epoxy will be utilized in the construction of the fine delay line walls. Refer to the structures section for the thermal and material properties of this composite, as well as the justification for lunar use. The fine delay line wall will be a total of 2 cm thick, and consist of two 0.25 cm thin walled panels separated by stringers. The use of stringers will reduce the weight of the fine delay line walls, while resisting any bending deformations in the structure. The entire fine delay line system will be covered in aluminum foil for thermal considerations. Expansion joints will be employed in the fine delay line structure to account for material expansions expected during the lunar day.

Inside each fine delay line, the mobile mirror will move along the length of the line transported on a small cart. The cart design is shown in Figure (3.3-8). It consists of the mobile mirror, controlled by four PZT actuators to adjust for small vibrations in any of the optical structures (both the fixed and mobile mirrors currently have PZT actuators to control their horizontal and angular positioning), a fixed support which is connected to a small step motor, and a support guide which moves along the track at the top of the fine delay line. The guide rests on bearings inside the track support. The movement of the cart is controlled by the motor, which rotates small rubber wheels that "ride" along the track. An information cable is attached to the motor, and is suspended from the top of the inside of the track support.

The only openings into this fine delay line and instrumentation housing structure during the operation of the interferometer will be 27 holes, with a circular diameter of 26 cm, to allow the entrance of the light beams into the structure. Each opening will consist of a small tube, 26 cm in diameter and approximately 0.5 meters long. The tubes will have flaps on the end that seal when the interferometer is out of operation, as well as when any large lunar surface disturbance is detected. During operation, the tubes will trap any dust attempting to enter the structure. The tubes will receive thorough cleaning during the periodic scheduled maintenance to remove any particle accumulation.

Guide

Information Cable

Wheels

Motor

Mirror Support

PZT

8 cm diam. Mirror

Side View

Back View
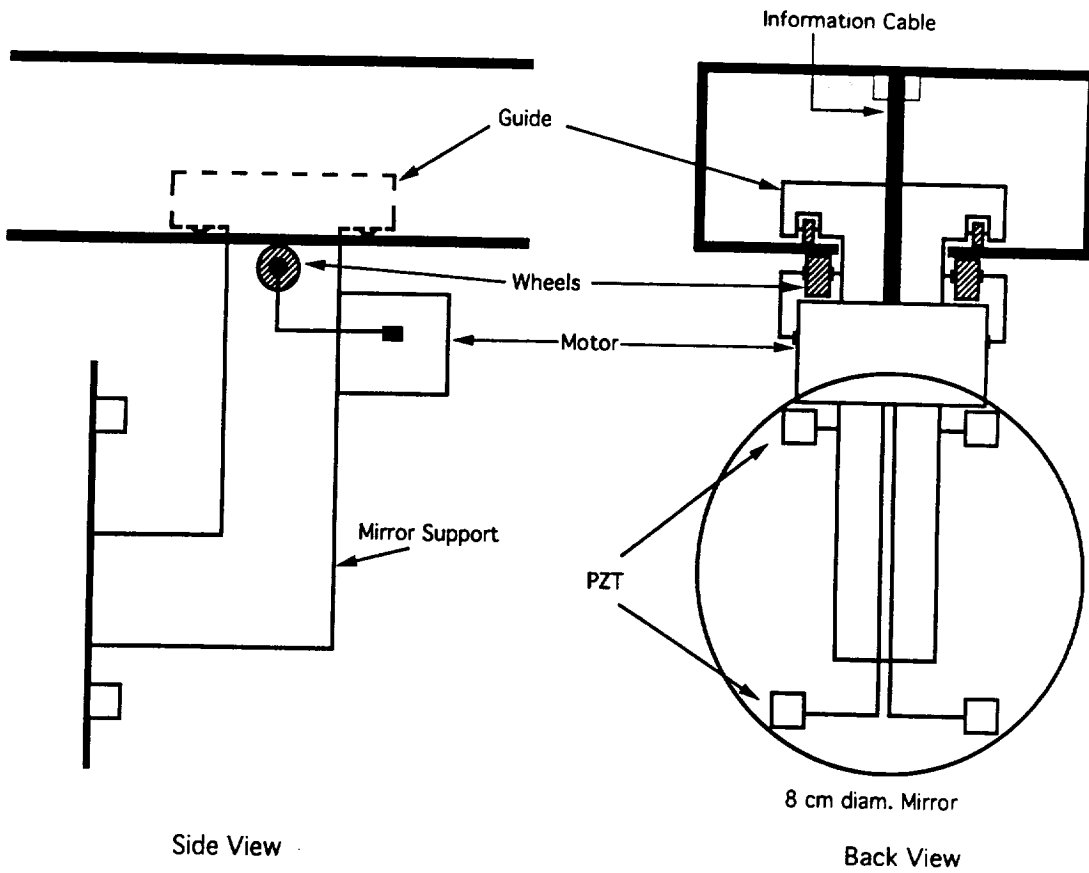
Figure 3.3-8: Fine Delay Line Cart Design

3.4 Beam Manipulation

3.4.0 Beam Splitting

To avoid losses from extra mirror bounces, the beams from the fine delay lines are kept 30 cm apart and 4 cm in diameter. The overall layout of the central station is presented in Figure 3.4-1. After exiting the fine delay modules, all 27 beams are split. Ninety percent of the incoming beam is split to the instruments while the remaining ten percent is distributed evenly between metrology and guidance by secondary beam splitters. A third split divides the beam for coarse and fine guidance purposes.

All beam splitting is accomplished by cube beam splitters which are 4.5 cm on each edge. These splitters are produced by cementing two angle prisms along their hypotenuse. The hypotenuse of one prism is coated prior to cementing. This dielectric coating controls the reflectance/transmittance (R/T) ratio.

The cube splitter was chosen over other types of splitters since they cause no beam shift or unwanted reflections. Their compact size and convenient orthogonal geometry are also significant advantages. Table 3.4-1 presents the characteristics for various types of beam splitters listed in the Oriel optical catalog (Ref. 3.4-1).

Other types of splitters were investigated but their characteristics made them less suited for the purpose of astronomical observation. Although inexpensive, uncoated windows and wedges produce multiple reflections and beam shift. Dielectric coated windows operate only in the visible wavelengths and introduce ghost reflections and beam shift. Polka dot windows are not suited for this application because of the spatial separation of the reflecting dots. This would mask an entire portion of the field of view. Pellicles are fragile and may not withstand launch conditions or the harsh lunar environment. Bifurcating optic cables introduce unacceptable losses in the split, and necessitate the use of additional focusing and collimating optics. This would introduce unnecessary complexity and extra losses.

Some care must be taken in the use of cube beam splitters since they are sensitive to the wavelength of the incoming radiation. The outer rings of telescopes are primarily used of infrared (IR) reception, while the inner telescopes will be used for ultraviolet (UV) reception. The splitters corresponding to outer telescopes are manufactured for optimum operation in the 700 nm to 3000 nm IR region, while the inner ones are optimized for the 200 to 400 nm UV region. Intermediate settings in the visible range are used for the mid-range baselength telescopes.

3.4.1 Beam Combination

The primary beam split is designed to serve another purpose besides dividing the beam. It also spaces the beams in a non-redundant fashion before they are combined and analyzed by the instruments. Non-redundant spacing is necessary to ensure that the Fourier components in the image reconstruction correspond to unique baselines. Determination of the non-redundant spacings was performed using an analysis similar to that used by P. D. Atherton et al for the Oasis Correlator (Ref. 3.4-2). A computer program was written in FORTRAN to calculate the spacings necessary for 27 telescopes (App. 3.4-1). The program takes the distance between the first and second telescopes to the one unit, a. All subsequent spacings are based on that unit space (Fig. 3.4-2). The computed telescope spacing data is presented in Appendix 3.4-2.

After passing through the planet detection optics, the non-redundantly spaced
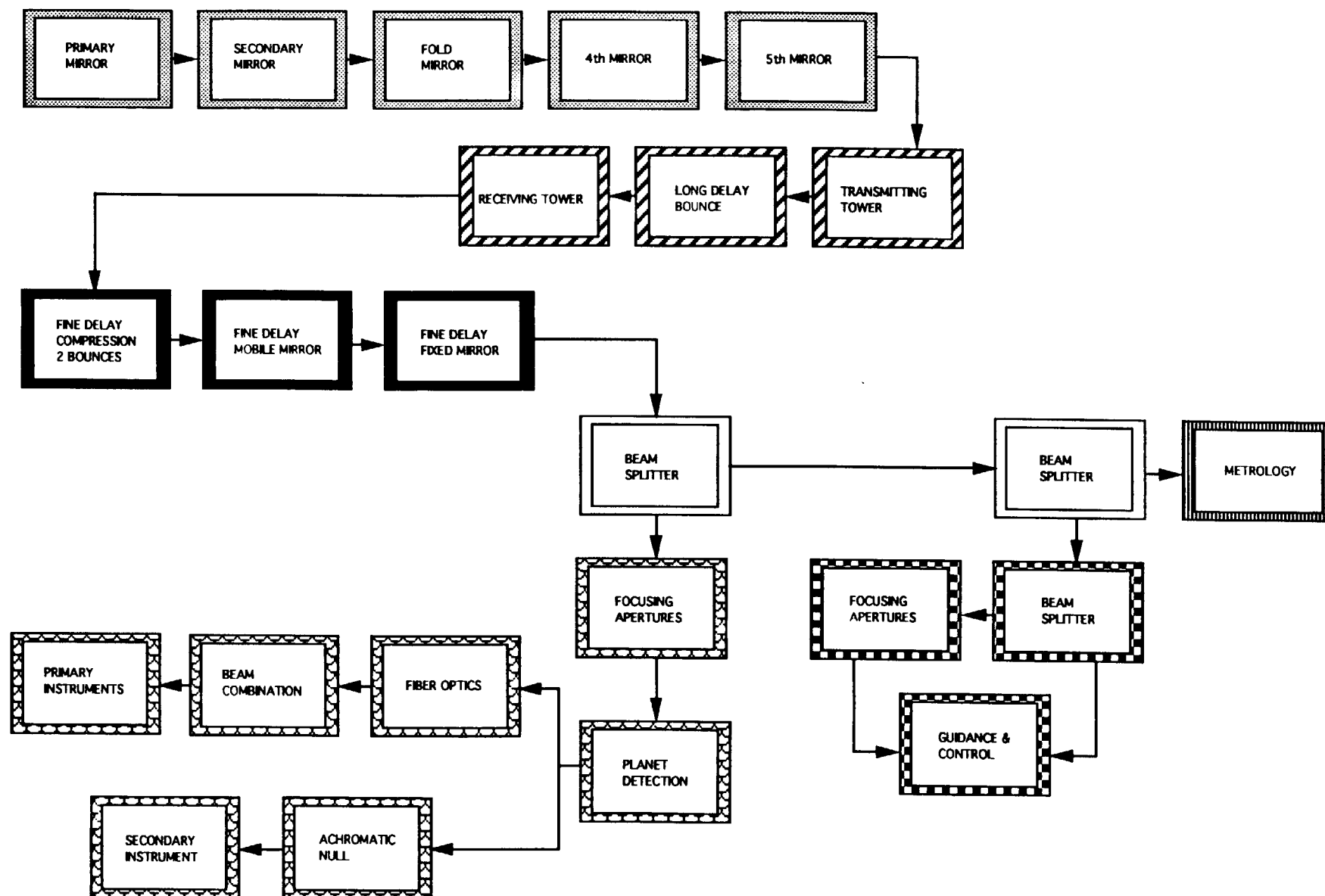
Figure 3.4-1: LOLA Telescope Optical Path Diagram

telescope

long delay
tower

long delay
mirror

central station

EXTERNAL OPTICAL PATH

F

D

c

G

E

A

B

H

I

J   K

L
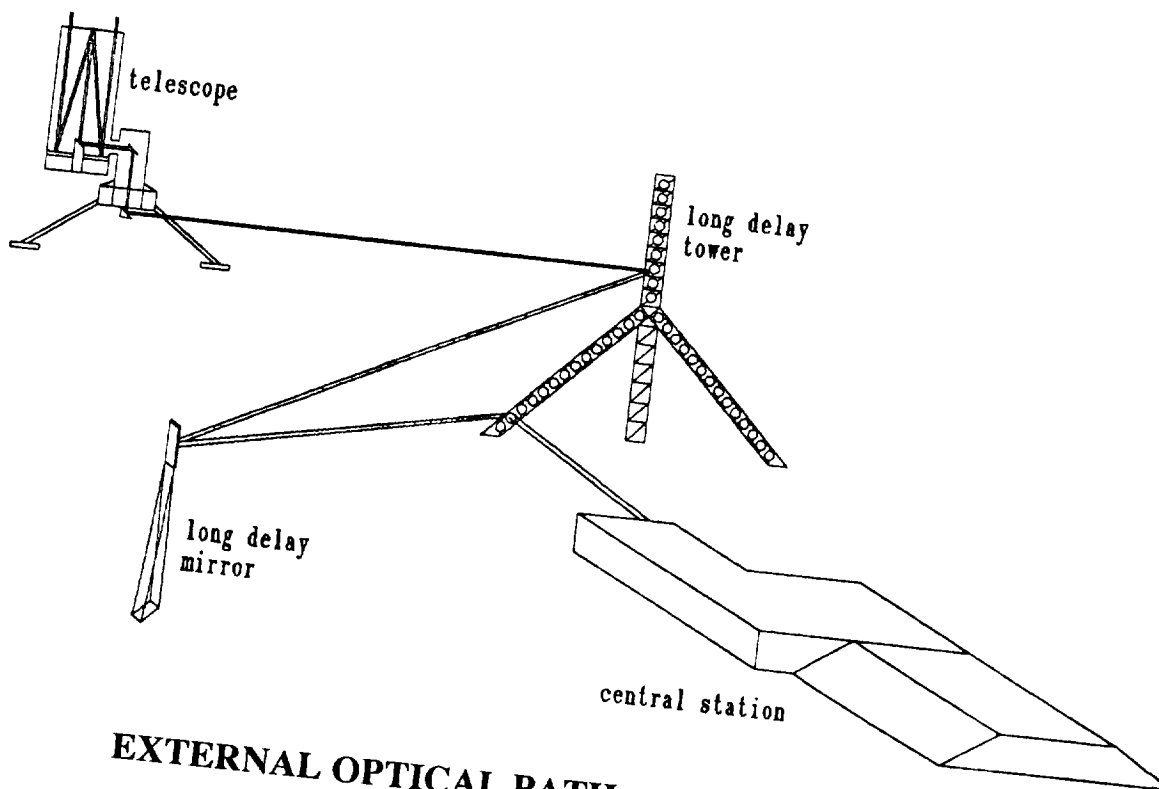
Central
Processing
Station
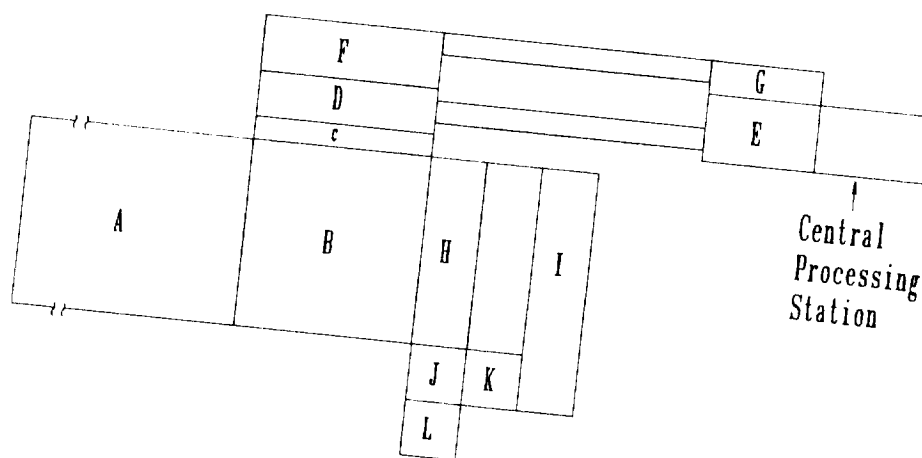
CENTRAL RECEIVING STATION

Figure 3.4-2: Schematic of Full Optic

LEGEND

A	Fine Delay Modules	F	Directing Carts
B	Primary Beam Split	G	Achromatic Null
C	Planet Detection	H	Secondary Beam Split
	(Phase Two)	I	Metrology
D	Beam Focusing	J	Guidance Split
E	Primary	K	Fine Guidance
	Instrumentation	L	CoarseGuidance
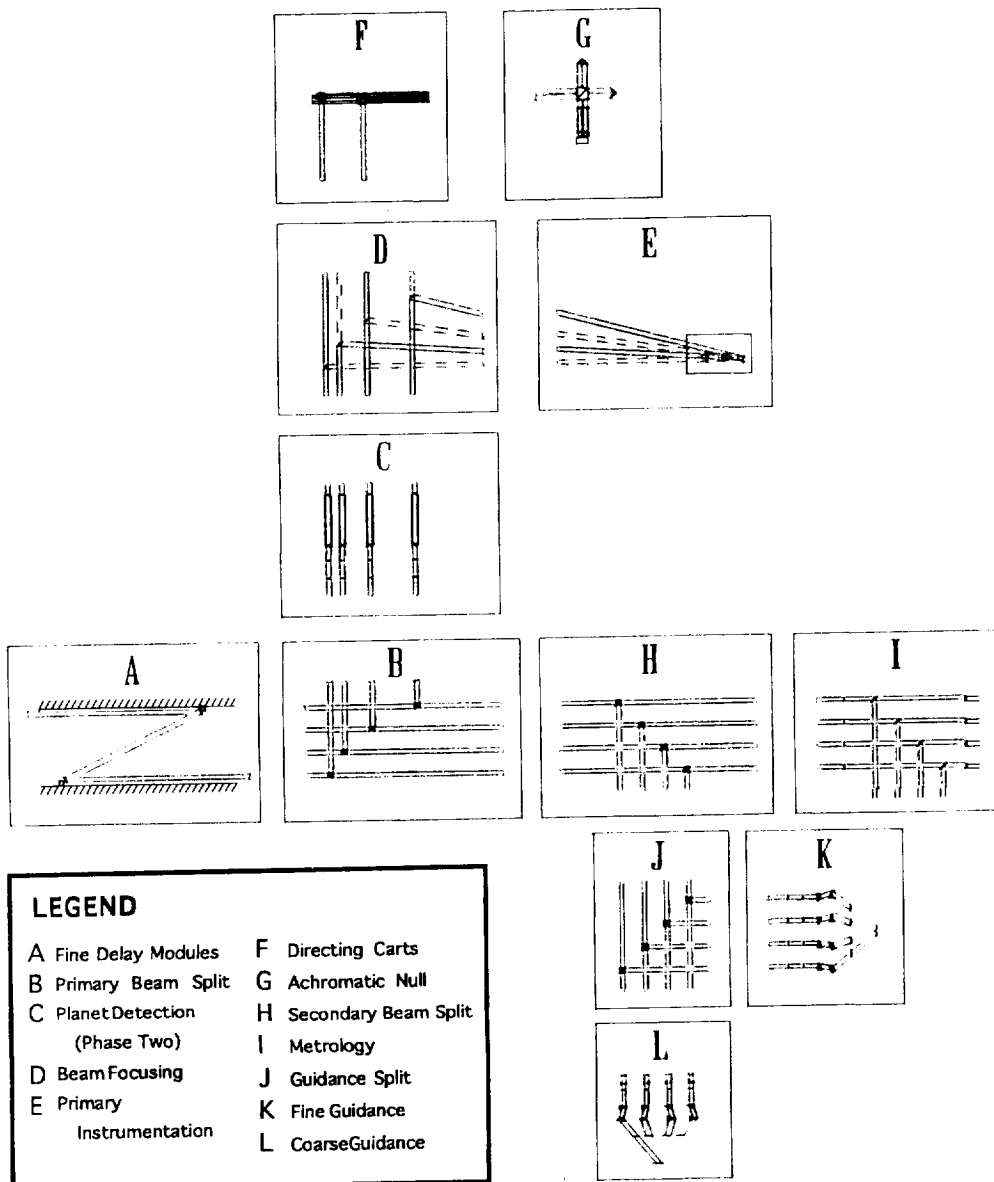
INTERNAL OPTICAL PATH

:al Path

Table 3.4-1: Beam Splitter Characteristics

Type	Operation Technique	Advantages	Disadvantages
Uncoated Windows or Wedges	Fresnel Reflection Typically 10/90 R/T	Broadband Inexpensive Large Aperature Capability High Power Capability	Introduces Astigmatism in Non-Parallel Beams Multiple Reflections Beam Shift
Dielectric Coated Windows or Wedges	Thin Film Reflection Various R/T Ratios Possible	Efficient Can be Achromatic	Narrowband Angle and Polarization Sensitive Minor Reflections
Polka Dot Windows	Patterned Coating on Substrate Spatial : Reflecting Dots	Efficient and Broadband Thin Substrate	Spacial Separation Not Suitable for All Applications
Cube Beam Splitters	Thin Film Reflection	No Beam Shift Orthogonal Beam Geometry Compact Easy to Hold	Polarization, Wavelength, and Angle Sensitive Small Aperature Focal Shift and Aberration in Uncollimated Light
Pellicles	Fresnel Reflection Thin Film Reflection	Eliminates Multiple Reflections Adds no Aberration to Optical Train	Film Fragility Spectral Channelling
Bifurcated Fiber Optic Bundles	Fiber Bundles Split into Two Branches	Broadband Simplifies Light Collection and Delivery Can Improve Beam Uniformity	Requires Focusing and Collimating Optics

beams are focused into the instrument room. This is accomplished with the use of flat elliptical mirrors which redirect the beams to combine onto the face of the detecting CCD. These mirrors are arranged to simulate the effects of a single Herschel mounted mirror (Ref. 3.4-3). All of the flat elliptical mirrors are suspended on linear actuators to allow removal for implementation of the planet detection module. There is a difficulty encountered in this method of combination. The beams cannot converge into a perfect 4 cm circle on the CCD. The beams coming in at angles will have some light overspray and spreading (Fig. 3.4-3). This effect can be sufficiently reduced, however, by minimizing the included angle between the incoming beams. This has been done by minimizing the perpendicular distance from the first beam to the point where the last beam is redirected to the instruments. In addition, the distance from the mirrors to the instrument room was increased to reduce the maximum angle to less than five degrees. This increased distance was already needed to shield the instrument room with regolith and did not pose extra problems.
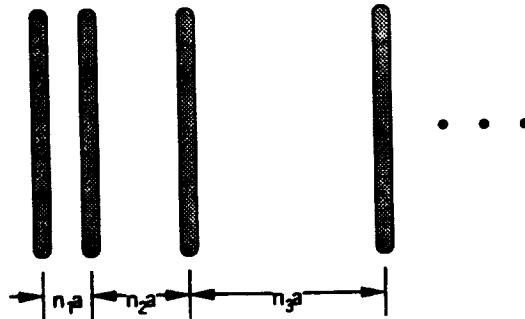
Figure 3.4-3: Non-redundant Spacing

3.5 Planet Detection

3.5.1 Planet Detection Theory

Planet detection involves locating an extrasolar system planet by directly studying the light and thermal emissions of the planet or by studying the radial velocity fluctuations associated with the existence of orbital bodies. These two techniques are categorized as direct detection and indirect detection methods, respectively.

Indirect Methods of detection use stellar disturbances to locate planets. These detection methods include astrometry, measurement of precision radial velocities, photometry, and Doppler Spectroscopy (Ref. 3.5-1). However, the detection of Earth-size planets at 10 parsecs requires direct observations of radiation from the planet itself (Ref. 3.5-2).

Direct detection observes the radiation emissions of the planet in both the visible and infrared spectrum. The main difficulty in direct detection is that the contribution of light from the planet is faint in comparison to the stellar intensity. The total flux at optical wavelengths for an Earth-size planet is one photon per second per square meter at a distance of 5 parsecs. This photon count increases to four for Jupiter-sized planets and triples if infrared wavelengths are observed. The intensity of planet light is approximately 10^{-5} to 10^{-9} the magnitude of the stellar intensity. Detection without spatial discrimination is impossible (Ref. 3.5 - 1,2).

Three capabilities are fundamental to the detection and characterization of Earth-sized planets. First, the inherent angular resolution must be adequate to spatially distinguish the objects of interest. Second, radiation from the planet must be sufficiently intense to produce a high signal-to-noise ratio. Third, planet light must be discernible from the diffracted and scattered light from the bright central star. The first two concerns were addressed earlier and will not be discussed here. The third fundamental is the most important since the Airy diffraction pattern governs the stellar intensity (Ref. 3.5-2).

Radiation intensity of a stellar image in the focal plane follows the Airy pattern shown in Figure 3.5-1. The curve is governed by the intensity function:

$$I = \frac{[\, 2\, J_1\, w\,]^2}{w^2}$$

The value w represents the radial distance from the center and the symbol J_1 refers to the first-order Bessel function. The majority of the incoming light falls within the first two or three rings of the Airy disk. In order to use direct detection to find an Earth-size planet the light energy of the outer Airy radii must be studied while the central rings are filtered (Ref. 3.5-3).

Apodization is a technique that in principle can enhance the contrast for planetary detection by suppressing the wings of the stellar diffraction pattern. The benefit gained by apodization is countered by any light scattering due to roughness or dust on the telescope optics (Ref. 3.5-1).

The key to very high dynamic range imaging is to optically prevent the starlight from scattering into the planetary position. By taking the light from the star at two spatially separated locations and interfering it destructively it is possible to eliminate the star's shot-noise component. Because the planet light enters the interferometer off-axis, it does not suffer destructive interference. Since the sidelobes also enter the interferometer off-axis, they will not be completely cancelled. For a two-element interferometer, the leakage
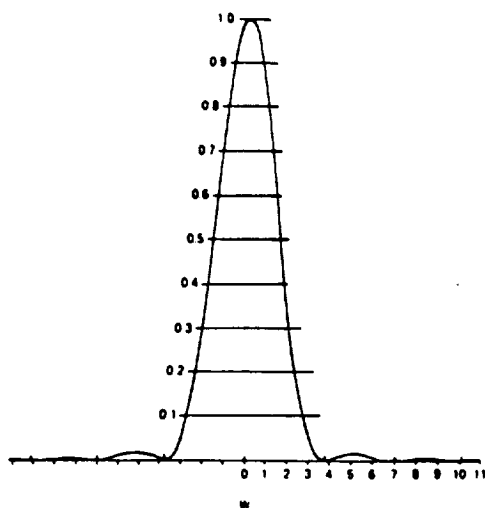
Figure 3.5-1: Airy Diffraction Pattern (Ref. 3.5-2)

of the light from a star of diameter, theta, is given by the following equation:

$$\text{Leakage} = (1/8)(\pi \text{*}\theta\text{*}B/\lambda)^2$$

where B is the array baseline.

Figure 3.5-2 shows the nulling concept developed by Shao and Colavita. The light from two array telescopes is split at a beamsplitter (one in plane and one out of plane), reflected from two dihedrals, and then recombined at the beamsplitter. The null is achromatic since it is achieved by a polarization flip rather than a phase delay. Also, the beamsplitter does not need to be precisely 50/50 since it is used once in transmission and once in reflection along each arm. Each arm has two S-type reflections and two P-type reflections. Therefore, with identical mirrors in each arm, all polarization effects are eliminated and with slightly mismatched mirrors the fold angles can be adjusted to tune out polarization differences. Finally, the single mode fibers serve as spatial filters (Ref. 3.5-4).

The interferometric approach to planet detection will consist mainly of finding a statistically significant increase in brightness at a reasonable distance from a star. Confirmation at this stage will depend on repeated detections in a series of positions that could reasonably represent the planetary orbit (Ref. 3.5-2).

Figure 3.5-2 : Schematic of Achromatic Nulling Interferometer

3.5.2 Planet Detection

The method of planet detection and resolution designed for the LOLA array is a two phase system. The first and primary phase of the system consists of an achromatic nulling interferometer. The function of this system is to directly detect and study a planet-sized object at an infrared wavelength of 10 microns. This information is then provided to the second phase of the planet detection system which will attempt to resolve the detected planet in the visible and UV spectrums. Since the achromatic null requires only two of the 27 light beams, it is possible to operate both phases of the system concurrently by temporarily removing all planet detection optics upstream of the achromatic nulling interferometer. Both phases of the LOLA planet detection system are capable of suppressing parent star light by a factor of 10^6 or more.

Figure 3.5-3 shows the achromatic nulling device designed for LOLA. First, two light beams are allowed to propagate past the primary beam focusing optics (positioned on linear actuators for easy removal from the beam path). The beams are then directed through two nominally 45 degree turns producing 1.0 cm vertical and horizontal beam separations and aligning them for entry into the nulling optics. This is accomplished by two directing carts (Fig. 3.5-4) on tracks similar to those in the fine delay system. From the directing carts, the beams then travel through the nulling optics, isolated on a vibrational damping platform (Fig. 3.4-3). The beams are finally directed through single-mode birefringent fiber optic cables with a 1.5 dB/km attenuation into the planet detection instrumentation module.

Phase two of the planet detection system is designed primarily to enhance, not replace, the first phase of planet detection. This phase consists of a hybrid occulting disk with an aperture wheel, single-mode fiber optic cables and an electronic masking system (Fig. 3.5-5). The variable aperture wheel and the hybrid occulting disk are positioned, by the use of various focusing lenses and linear actuators, in the first and second image planes of each light beam. The variable aperture wheel allows different areas of the field of view to be studied. Each lens in the wheel acts as a magnifier, expanding a small portion of the field of view. The changing of the apertures is accomplished by a step motor designed to rotate the new lens into place. The hybrid occulting disk, used in conjunction with the aperture wheel, is a graded transmission mask which acts as a high pass filter. The disk reduces stellar light by a factor of ten while allowing light close to the star to pass. The disk will have a radius of 3 micrometers, which will block the first three radii of the stars Airy disk.

The third starlight suppression technique used in phase two is provided by single-mode fiber optic cables identical to those used in the nulling interferometer. The light from each array element is focused on to the fiber optic cable 1.2 micrometers, or one Airy disk, from the entrance of the cable, producing a shearing effect that reduces the sidelobe starlight and decreases the overall stellar light by a factor of ten. The light traveling through the cable is preserved in a state of polarization and light scattering is partially removed from the system (Ref 3.5-5).

The final technique for starlight suppression is phase two is accomplished by electronic masking. Using the positional information provided by the first phase of planet detection, the CLEAN and Maximum Entropy Method algorithms are used in the data reduction to resolve the planet about the parent star. CLEAN iteratively removes the high intensity light from the brightness of the star, reducing both core and sidelobes (Ref 3.5-6).

Maximum Entropy Method deconvolves the remaining image. The combination of these two techniques can approximate the true image of the planet by comparing differences in light intensity detected by the array. These methods are covered in section 3.9.2 of this report.

Side
View

Back
View

PZT

Nominal 4.1 cm
diam. Elliptical
Mirror

Mirror
Support

Motor

Wheels

Guide

Information
Cable
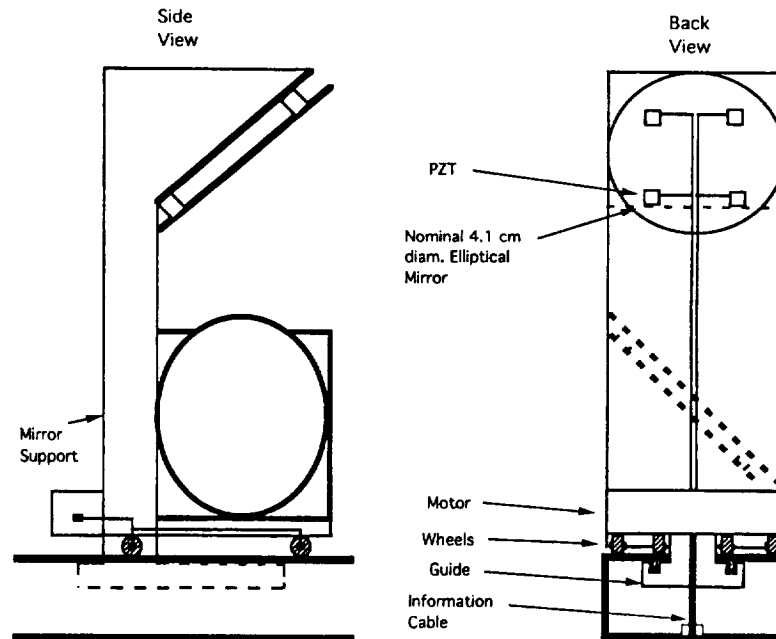
Figure 3.5-3 : Achromatic Null Directing Carts

OUT OF PLANE DIHEDRAL
WITH PZT ACTUATORS

IN PLANE DIHEDRAL
WITH PZT ACTUATORS

FOLD MIRROR
WITH PZT ACTUATORS

FOLD MIRROR
WITH PZT ACTUATORS

POLARIZING BEAM SPLITTER

BEAM INPUTS

BEAM OUTPUTS
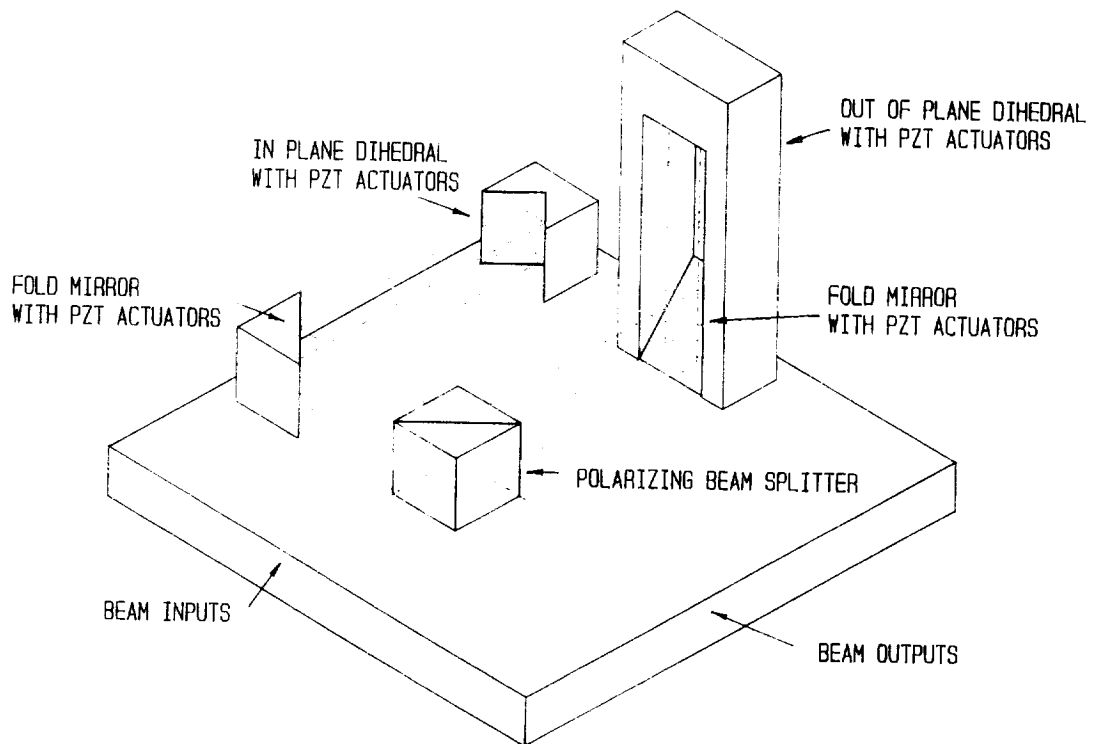
Figure 3.5-4 : Achromatic Null Optics
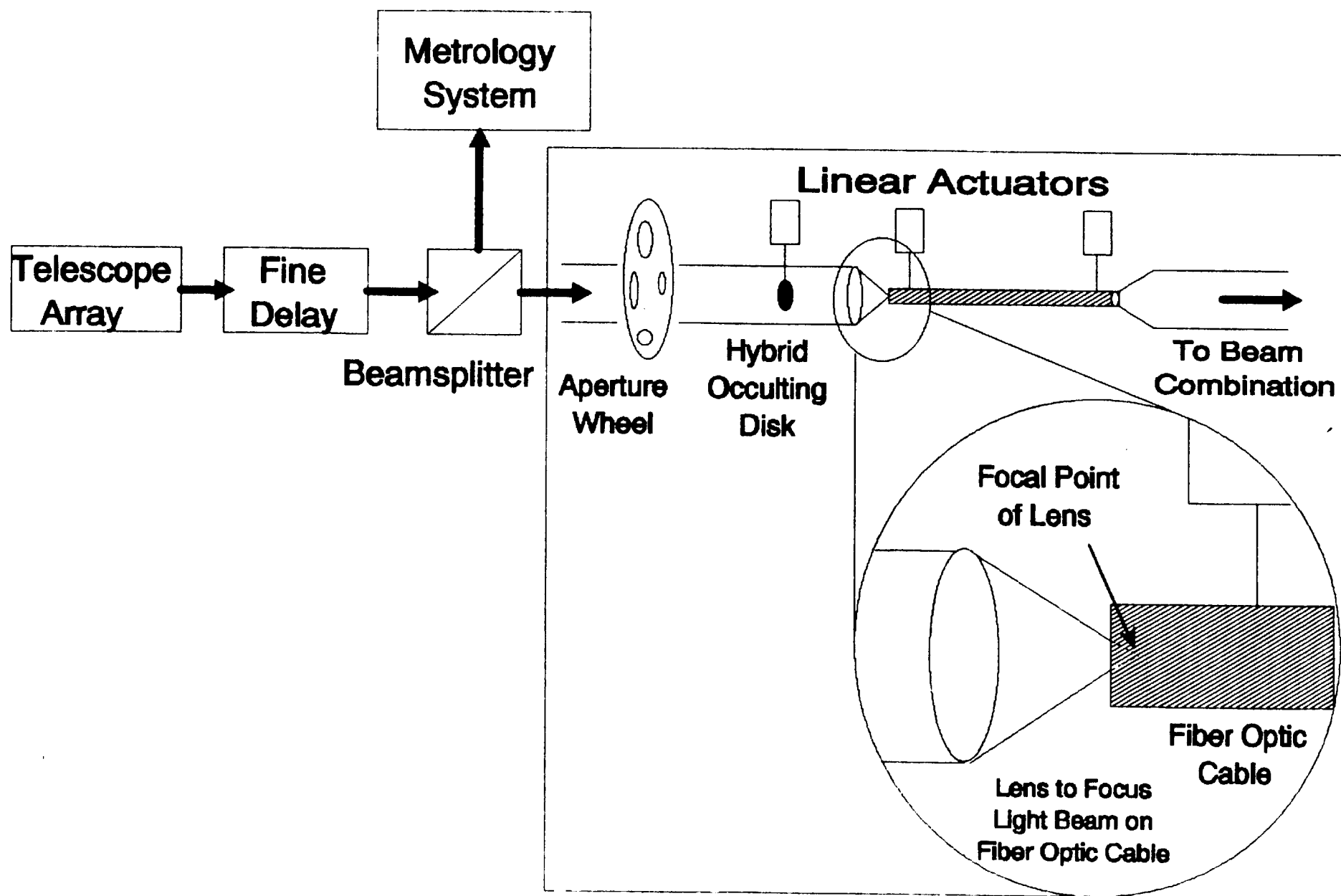
Figure 3.5-5: Planet Detection Scheme (Phase Two)

3.6 Metrology

In order to properly control the 27 telescope array elements and synchronize the beam combination, a metrology system is required. This metrology system will be divided into two subsystems. One subsystem will provide optical path length measurements while the other will provide baseline measurements. Both subsystems will employ lasers to obtain the high degree of accuracy required by the LOLA array.

3.6.1 Optical Path Measurement

Accurate measurements of the optical path length of all 27 incoming light beams is crucial for proper control of the mirrors of the fine and long delay lines. To provide the required measurements, a portion of each light beam is directed to the metrology housing from beam splitters. Those 27 beam splitters are located immediately following the fine delay lines. In the metrology housing, 54 lasers are positioned to shoot two beams down the edges of each of the 27 light beams. These laser beams travel back through the beam splitters, the fine delay lines, the long delay lines and into each of the telescope elements. At the telescopes, the beams hit retroreflectors located on either side of the secondary mirror and are reflected back along the optical path to the metrology housing. The distance the laser beams traveled along the optical paths are then computed and relayed to the delay lines for optical path length adjustments. These measurements are made continuously to allow for constant slewing of the fine delay mirrors. (Fig. 3.6-1)
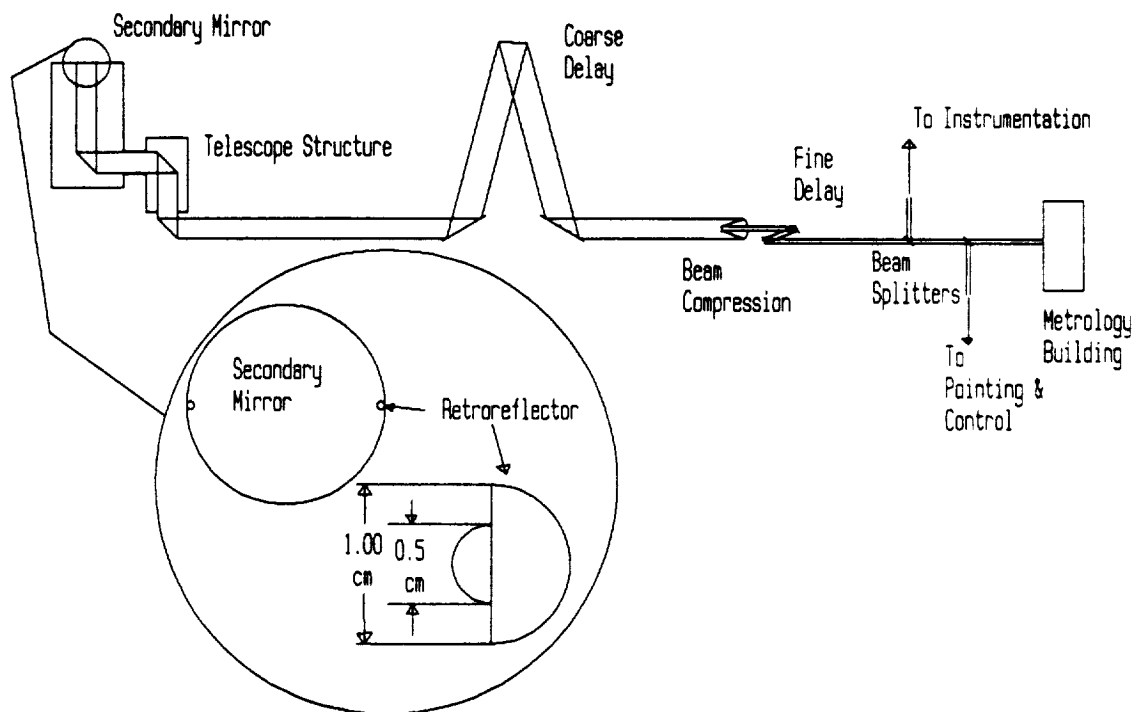
Figure 3.6-1: Optical Path Metrology

3.6.2 Baseline Measurement

The second metrology subsystem provides accurate measurements of each telescope's position and orientation. This will be accomplished by combining measurements from a Mark III laser system located at each array element location with nominal baseline measurements made from 3 metrology towers.

Each of the towers is responsible for nominal baseline length measurements along a single array arm. The towers are positioned 700 meters from the center of the array and 30° to the right of each arm. Using east as 0°, there are towers at 60°, 180°, and 300°, each 700 meters from the center (Fig 1.5-1). The bottom 10 cm section of each tower is vacant, but each of the remaining eleven 10 cm levels holds one laser each and the entire structure itself is supported 30 cm above ground level. This provides room for one laser each for the nine telescopes and two for measuring tower separations.

The second part of the baseline measurements are performed by Mark III systems located at the base of each telescope. Each system consists of four lasers located on a "laser plate" and aimed at a zerodur hemisphere located on the bottom of the telescope (Fig. 3.6-2). Also located on the 1 m by 1 m "laser plate" is a small retroreflector which reflects the beams from the metrology towers. The plate is mounted 50 cm off the ground on four pylons. In order to accommodate full telescope motion, four systems will be placed at each telescope, one in between each set of legs. Only one system will be operating at any given time, depending to which quarter the telescope has rotated. (Fig 3.6-3)

The Mark III measurements are used for two purposes. First, they will be combined with the measurements made from the metrology towers to determine the baseline length.

Zerodur "Bowling Ball"

Neodymium-Yag Laser

Retroreflector
for tower laser
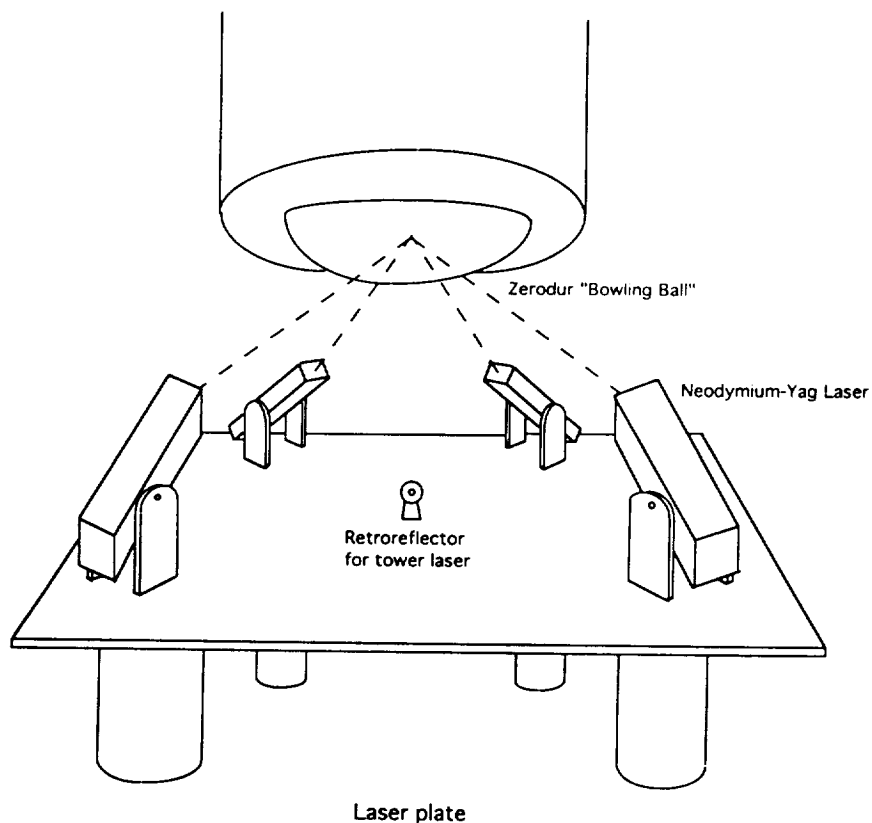
Laser plate

Figure 3.6-2: Mark III Metrology System
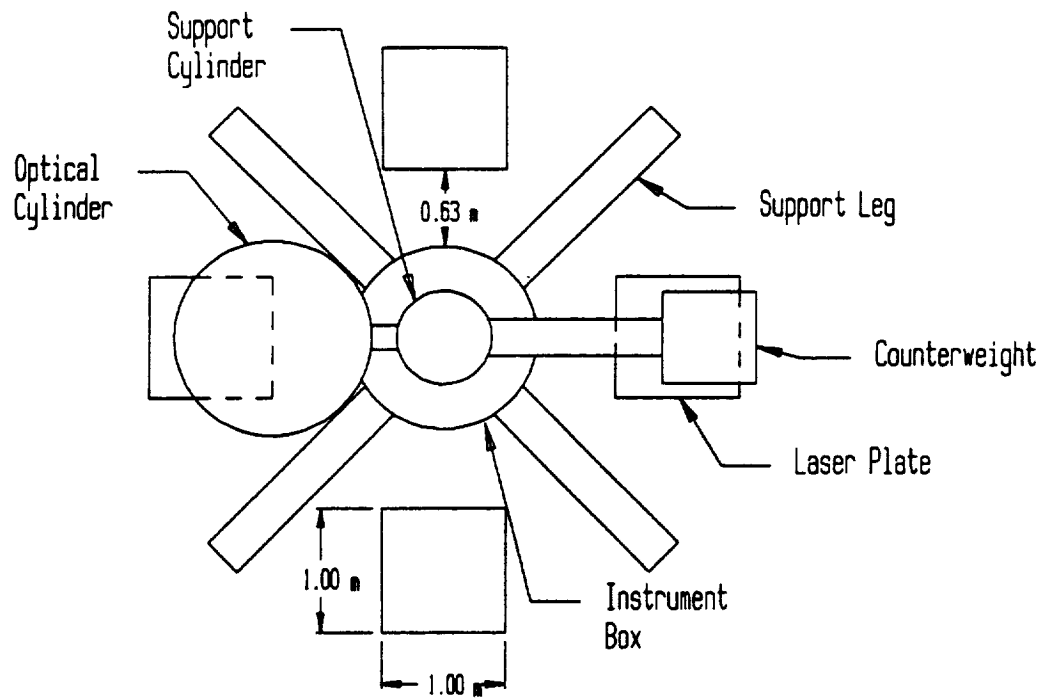
Figure 3.6-3: Laser Plate Placement
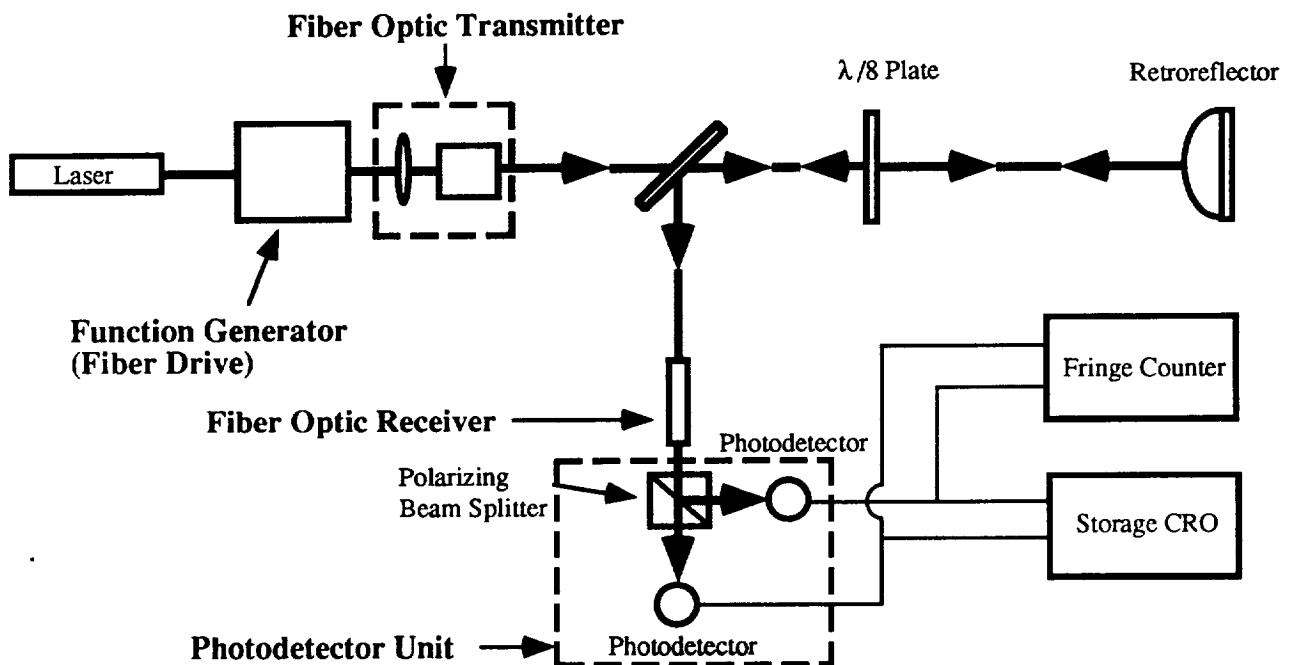
Figure 3.6-4: Schematic for Optical Path Length Measurements

Second, the measurements will be transferred to the pointing and control system for precise telescope positioning.

3.6.3 Optical Path Length Instrumentation

By combining conventional heterodyning and fringe counting metrology techniques, it is possible to measure optical path lengths to nanometer precision. Figure 3.6-4 shows the schematic of the optical path length metrology system. Interference takes place between a reference beam reflected from the front surface of a $\lambda/8$ thick plate mirror and the signal beam reflected from the telescopes secondary mirror producing circularly polarized beams. The two beams are divided at a polarizing beam splitter resulting in fringe patterns whose intensities vary in quadrature. By varying the laser frequency with a function generator at the rate of df/dt, a beat signal with a frequency, $f = (L/c)(df/dt)$, will be produced; where L is the optical path length and c is the speed of light. The frequency of the beat signal is found with a fringe counter and the optical path length is determined (Ref 3.6-2).

NOTE: The specific system employs components from a laser Doppler velocimeter system marketed by Aerometrics for high precision wind tunnel measurements (Ref. 3.6-3).

3.6.4 Retroreflectors

The retroreflector used on the secondary mirror is a cat's-eye retroreflector. It is made of two glass hemispheres cemented together with the rear surface aluminized for high reflectivity. The relationship between the two hemispheres is given by $R_2 = R_1/(n - 1)$, where n is the index of refraction of about 1.5 (Ref 3.6-4). The retroreflector has an outer diameter of 1 cm and an inner diameter of 0.5 cm.

The zerodur "bowling ball" retroreflector on the bottom of the telescope is used because the Mark III measures relative position and it has the advantage of a high acceptance angle. The hemisphere has a radius which coincides with the point about which the telescope rotates. On the LOLA telescopes, the hemisphere extends 0.1 m below the telescope structure, and is 0.81 m wide (Fig. 3.6-5), adding 65.86 kg of weight to the telescope. This coincides with a sphere of radius 0.862 m.

3.6.5 Lasers

The lasers to be used in all components of the metrology system are Neodymium Yag lasers with stability ranging from 10^{-9} to 10^{-12}. These were chosen for their accuracy and efficiency. Each laser uses on the order of 100 mW of power, and is approximately 10% efficient (Ref 3.6-5). These lasers will give measurements of the optical path length down to the nanometer.

3.6.6 Metrology Housing and Towers

The 54 lasers and all accompanying instrumentation and optics are housed in a building, shown in Figure 3.6-5, that is 11.00 m long, 2.5 m high, and 2.5 m deep. The building is constructed similar to a tent, with boron/epoxy poles comprising the frame-work, and a reflective thermal blanket covering the top, ends, and back. Because one of the purposes of this housing is dust protection, the blanket will have to be securely fastened along all edges. There is a door in the rear of the building to allow access for maintenance.

The front of the building is constructed of truss panels. A 15 cm high opening 26 cm above the lunar surface extends the length of the building to allow the laser beams to exit. This opening is covered by a sliding shield during the lunar day. This shield is a thin aluminum panel with rollers on each end, which is controlled by a step motor.

Inside the building, the lasers, transmitting and receiving optics, function generators and photodetector units (all connected by fiber optic cableing) are placed on tables 31 cm high, 10 cm thick, and 70 cm deep (Fig. 3.6-5). Each table has 8 legs constructed of boron/epoxy with an outer diameter of 5 cm and thickness of 1 cm. Each set of 4 legs is located 2 cm inward from the front or back edge of the tables. (Fig 3.6-5). A detailed view of the transmitting and receiving optics is found in Figure 3.6-6.

The 3 metrology towers, shown in Figure 3.6-7, are each 1.2 m high with a 0.5 m square base. They are divided into twelve 10-cm sections, the top eleven of which contain lasers. Two sides of each tower are solid panels. The other two sides have sliding panels that cover the lasers during the lunar day. These towers are constructed of aluminum, with step motors controlling the movable panels.
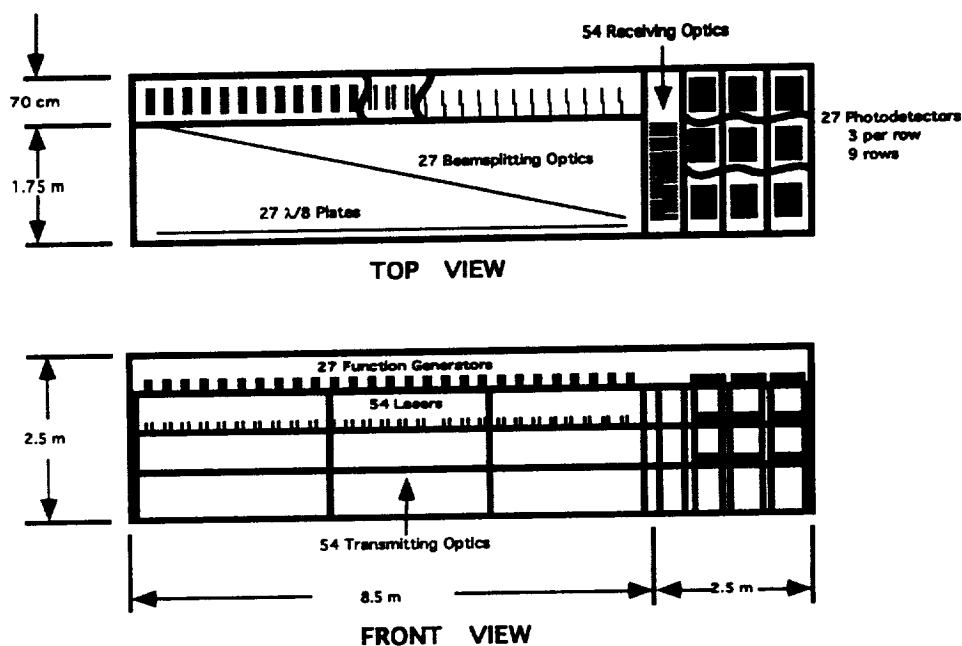
Figure 3.6-5: Laser Housing
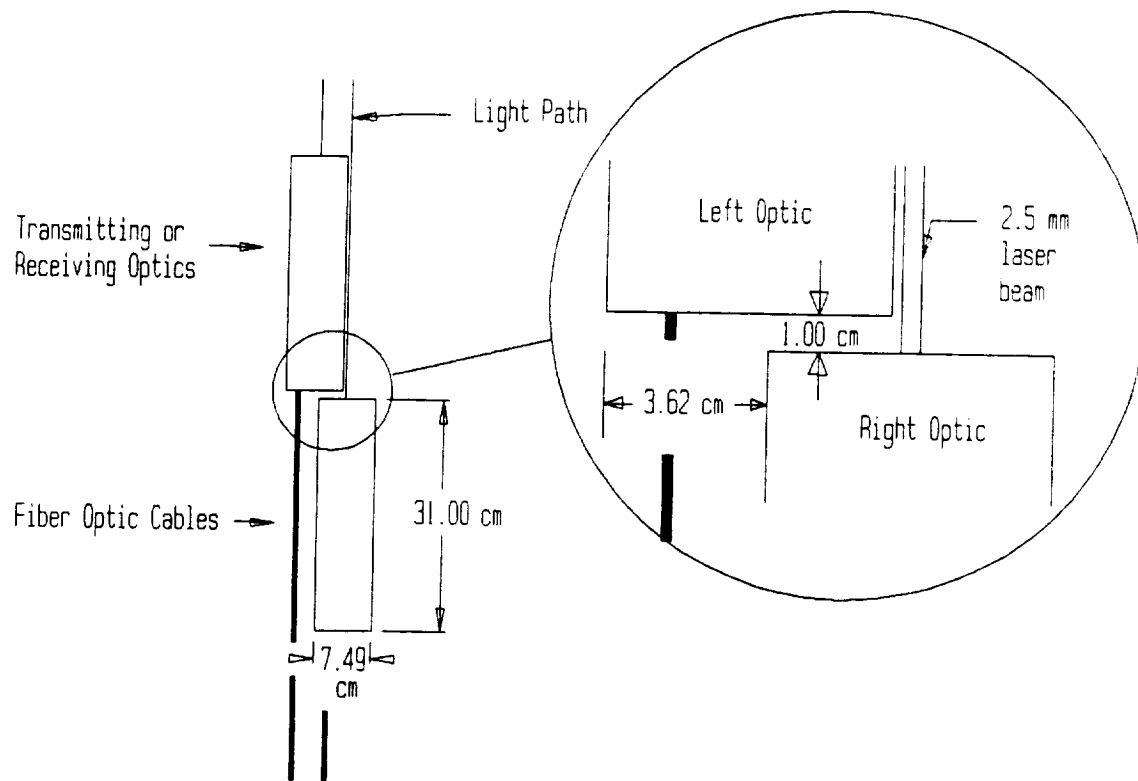
Figure 3.6-6: Transmitting and Receiving Optics Arrangement
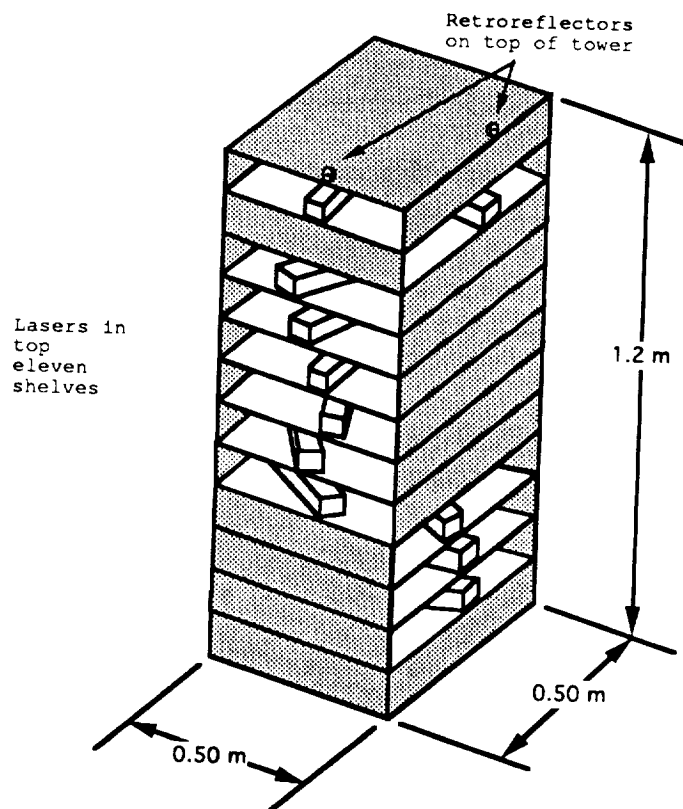
Figure 3.6-7: Metrology Tower

3.7 Guidance and Control

The high resolution requirement for interferometric detection of earth-like planets places a critical restriction on the accuracy of telescope pointing. The resolution requirement of 10^{-5} for the LOLA array places a criteria of 10^{-6} arcseconds accuracy for the guidance system. (Ref 3.7-1).

Since both the orbital motion of the moon and the stellar positions relative to Earth can be calculated very accurately, the control system will use these calculations to initially position the telescopes. A central computer will be used to transform the computed coordinates to required altitude and azimuth angles for the telescopes. Three separate systems will be used to close the control loop. These systems consist of a laser metrology system to compute the actual telescope position, a coarse guidance camera to track the star, and a fine guidance camera to maintain the accuracy requirements and measure the errors in the optical system.

Several pieces of information will be uploaded from the ground control station at the start of the target image acquisition phase. The right ascension and declination of the target image will be processed to the current epoch by the ground control station and the appropriate astronomical corrections will be applied. These include correcting for the proper motion of the target image, precession of the planet, and parallax. The central microprocessor will have the capability of correcting for the orbital motion of the target image. The information necessary to compute the orbital motion of the target image over long integration periods will also be uploaded from the ground station into the control program.

The target coordinates will then be transformed into the required altitude and azimuth angles for the telescopes. The target velocity will be determined from the present stellar position minus the position in the previous cycle. Signals from the laser metrology system will be read to determine the actual telescope positions allowing the telescope velocities to be determined. If the position error for a given telescope is skewed 0.25 of a pixel from the centroiding algorithm for the CCD, the command velocity for that telescope will be the target velocity plus a velocity which is proportional to the square root of the position error. This will cause the telescope to move in a parabolic motion such that the position and velocity errors go to zero at the same time (Fig. 3.7-1). As the telescope approaches the target location, the position error will be small, and it will take a long time for the command velocity to reach the target velocity. Hence, if the position error is below a predefined limit, the command velocity is set proportional to the sum of the position and velocity errors.

The tracking of each individual array element is accomplished by using a coarse and fine guidance camera. The schematic for each camera is shown in Figure 3.7-2. The elements in each camera are the same with the exception of the CCD and the aperture wheel. The coarse guidance CCD has a 1024 x 1024 pixel display which will allow 0.1 AU field of view (FOV). The fine guidance uses a 2048 x 2048 pixel display which has a FOV of 0.02 AU.

Light from the array elements are split between the fine guidance and the coarse guidance by a 50/50 beamsplitter. A variable density filter, as developed by Newport, is placed in the path of each beam (Ref 3.7-2). The filter is self adjusting and changes according to the intensity of the incoming light. The purpose of the filter is to protect the CCD from the extremely high intensities associated with stellar light.

The adjustment of the light path to the CCD is accomplished by two achromatic wedge

prisms. The purpose of the prisms is to bring an off center tracking star into the center of the field of view. A wedge prism is a plate whose opposite faces deviate slightly from parallelism. Because of the extreme accuracy required in the pointing and control system, the chromatic aberration caused by a single prism can not be tolerated (Ref 3.7-3). It would cause a shift in the interference pattern across the CCD. These aberrations can be eliminated by combining positive and negative elements, or by using two elements of different refractive indices (Ref 3.7-4). The use of two achromatic wedge prisms changes the path of the light without aberrations.

The second achromatic wedge prism directs light to the CCD. A masking disk controlled separately for each of the 27 beams allows each beam to be studied by the CCD individually. The positioning of each masking disk is accomplished by a ultra precision linear actuator as developed by Newport (Ref 3.7-2). During fine tracking any error detected by the CCD is registered by the computer. The computer then masks each element to determine which telescope is in error. The light paths to the CCD remain open during continuous tracking.

A centroiding algorithm expands the incoming light on to the CCD. The light beams are expanded to cover four pixels on the CCD display. This allows any disturbances or movements of array elements to be detected without moving a full pixel. During continuous tracking each array beam is focused to the center of the CCD screen. The movement of one element will show on the display as a separation from the cluster (Fig. 3.7-1). An error signal will be sent to the metrology and drive systems to correctly position the array element in error.
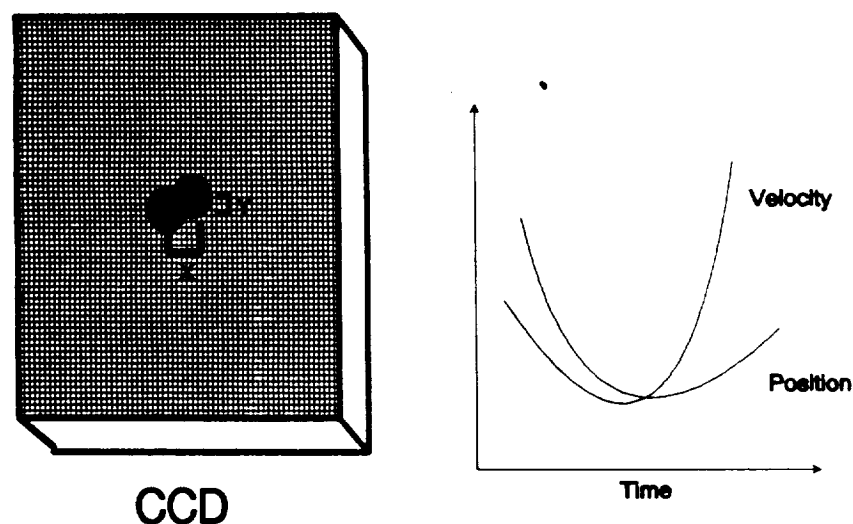
Figure 3.7-1: Pointing and Control Positioning Scheme
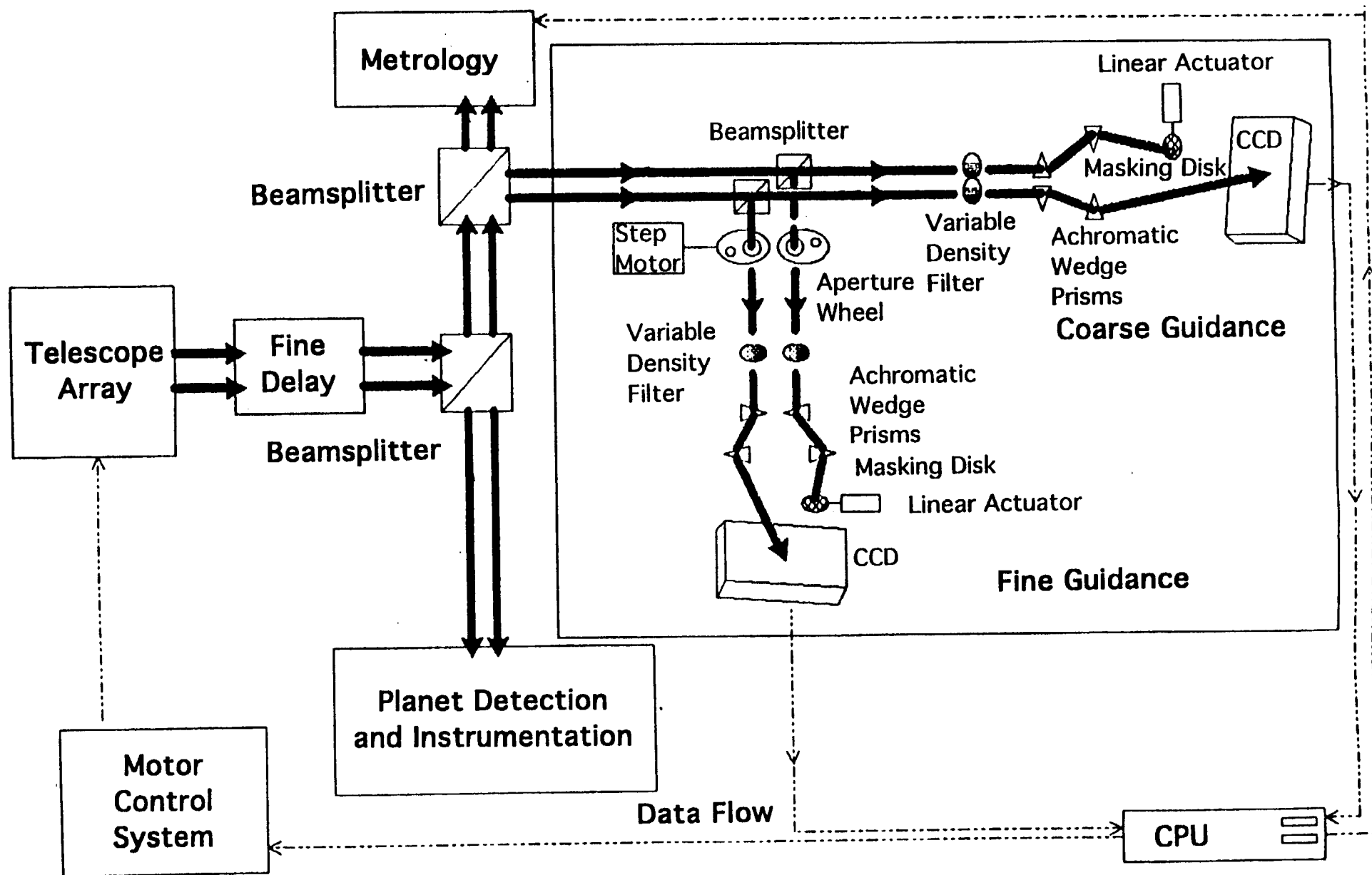
Figure 3.7-2: Pointing and Control Schematic

3.8 Instrumentation

3.8.1 Instrumentation Facility

The side view of the instrumentation facility is shown in Figure 3.8-1. This structure shields the instrumentation from lunar dust, micrometeoroid impacts, radiation, and the thermal extremes of the lunar day. To provide adequate radiation shielding, the instrument housing is covered by 5.0 m of compacted lunar regolith. It is estimated that the compacted regolith will provide shielding equivalent to the level of atmospheric shielding found in low Earth orbit (Ref. 3.8-1).

The 25 to 27 telescope beams are directed from the beam combining optics through the regolith wall to the instrument carousel (Fig. 3.8-2). The cylindrical carousel is 2 m long with a 1 m diameter. A small torque motor rotates the carousel to position either of the four instruments in the converging beam path. Power transmission lines, fiber optic cables for data transfer, and piping for the liquid helium thermal control system are combined for the four instruments and are directed to the exterior of the instrument housing.

During standard operations, the carousel will be held fixed on one of the instruments. When concurrent use of two instruments is desired, the carousel is rotated between the selected instruments approximately every 10 seconds. The simultaneous use of two instruments is accomplished through multiplexing to the computer system and the synchronization of the data sampling with the rotating carousel.

Each instrument is contained within a separate module of the carousel. This design simplifies access to each instrument and allows maintenance on a malfunctioning instrument without disturbing those elements which are functioning properly.
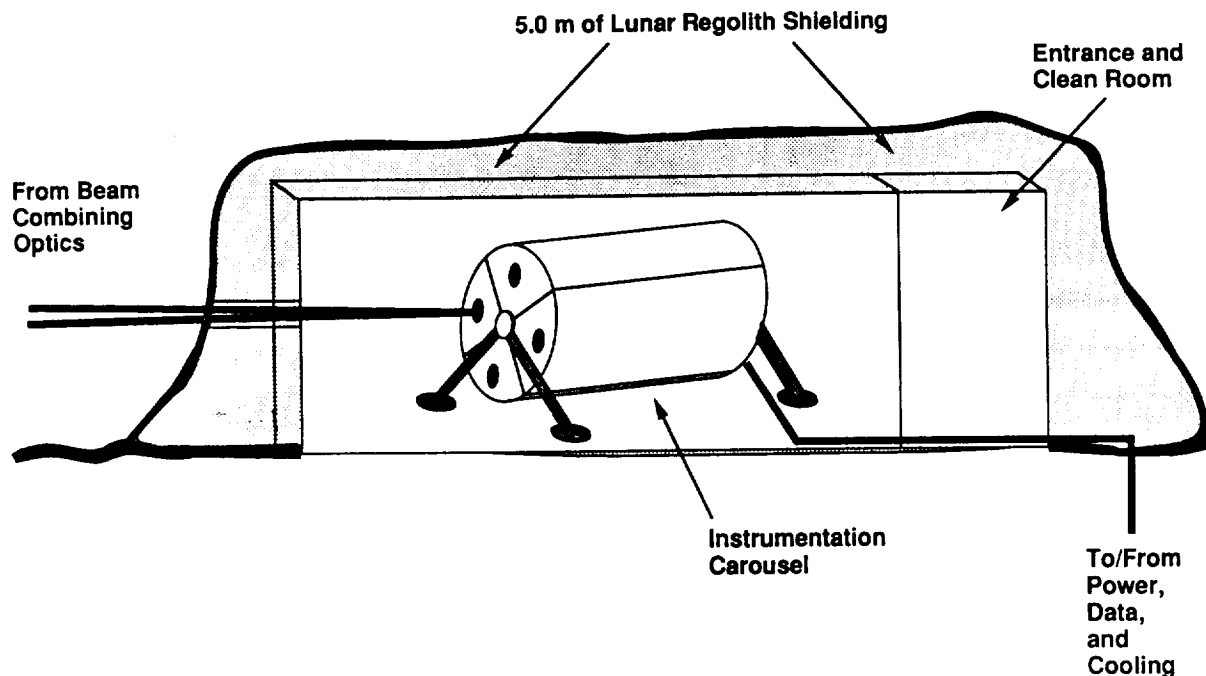
Figure 3.8-1: Primary Instrumentation Housing Shielded by Lunar Regolith. The computer systems and the thermal control systems are in a separate facility.
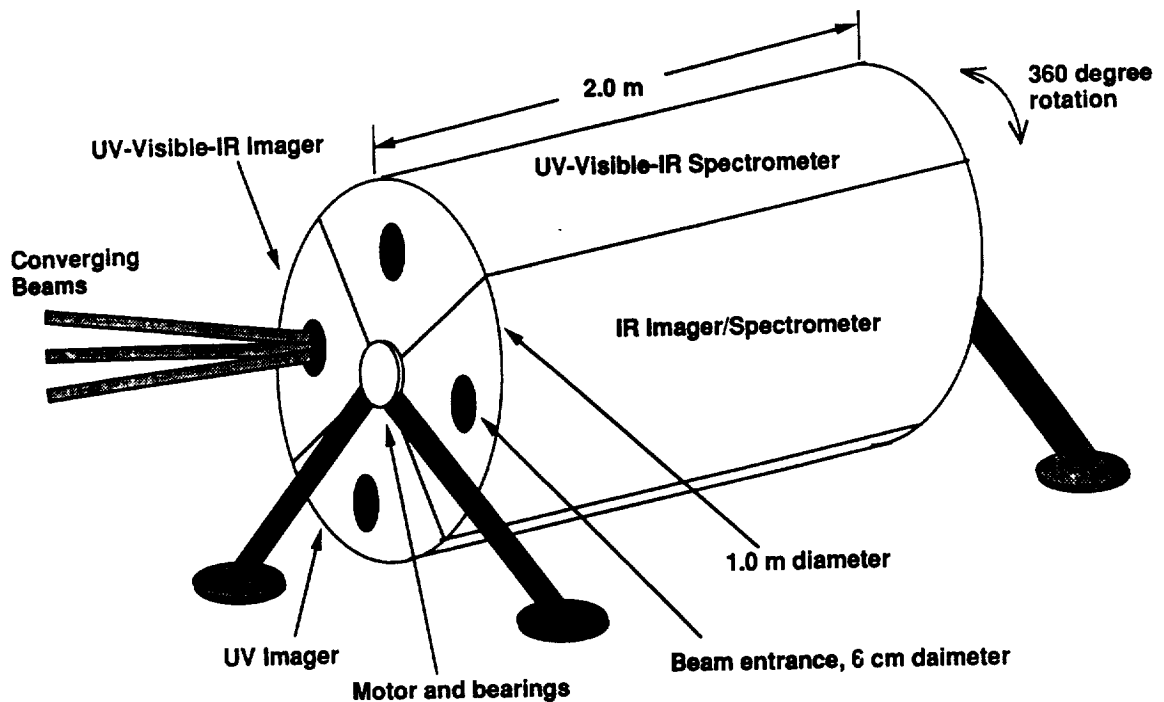
Figure 3.8-2: Instrumentation Carousel. Power, coolant, and data transmission lines are not shown.
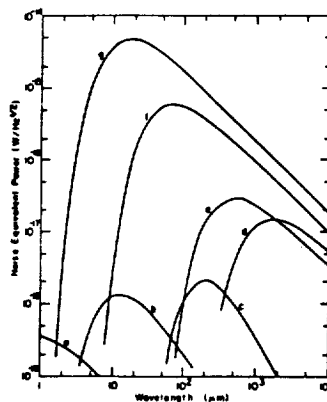
Charge coupled device noise equivalent power versus wavelength for various detector temperatures:

(a) zodiacal scattered light at the ecliptic pole
(b) zodiacal dust emissions at the ecliptic pole
(c) interstellar dust emission at high galactic latitude
(d) the 5 K cosmic background radiation
(e) a 10 K, 10 percent emissive telescope
(f) a 77 K, 10 percent emissive telescope
(g) a 300 K, 10 percent emissive telescope

Figure 3.8-3: Charge Coupled Device Noise Equivalent Power vs. Wavelength

The secondary planet detection module is contained in a separate section within the instrument room. The rectangular module is 0.5 m wide, 0.5 m high and 2.0 m long.

All instrumentation requires an active cooling system to remove the heat dissipated by the instrumentation electronics and the heat radiated from the walls of the regolith covered room. The temperature of the instrumentation must be maintained below 77 K to permit the detection of infrared radiation at wavelengths up to 10 micrometers (Figure 3.8-3, Ref. 3.8-2). To accomplish this, an active closed loop thermal control system utilizing liquid helium is employed. This system is discussed in greater detail in section 7.0 of this report.

3.8.2 Instrumentation

The four instruments in the primary cluster provide coverage from the ultraviolet (UV) portion of the spectrum to the infrared (IR) region. The secondary instrumentation provides coverage in the IR region from 1000 to 10000 nm. The spectrum is extended down to 150 nm and up to 10,000 nm for viewing objects requiring less resolution. The lower wavelength limit of 150 nm is imposed by several factors including the attainable quality of optical components and type of reflective coating used for the mirrors. The upper wavelength limit of 10,000 nm is produced by thermal noise emissions and diffraction effects. The instruments and their associated spectral regions are listed below.

UV Imager:	150 to 400 nm
UV-Visible-IR Imager:	200 to 1000 nm
UV-Visible-IR Spectrometer:	200 to 1000 nm
IR Imager/Spectrometer:	1000 to 10,000 nm
Planet Detection Module	1000 to 10,000 nm

The field of view for all of the instruments is controlled through 27 focusing aperture wheels located downstream of the beam splitter. With the focusing apertures the field of view of the beams may be varied from 15 arcseconds down to 10^{-3} arcseconds, which corresponds to the maximum resolution of the pointing and control system.

The layout of the UV Imager is shown in Figure 3.8-4. The filter wheel is used to position a variety of narrow bandpass filters in the beam path. The charge-coupled-device (CCD) detector is a Tektronix 1024 x 1024 pixel array with each pixel having dimensions of 21 x 21 (Ref. 3.8-3) microns. The quantum efficiency is approximately 5%. Thus, observations in this spectrum are attainable only for objects which produce an extremely high SNR. This detector is particularly suited to study stellar phenomena and to detect helium ion emissions.

The UV-Visible-IR Imager is similar to the UV-Imager in terms of layout (Fig. 3.8-4), however, in nominal operation mode, the filter is positioned so that it does not affect the incoming beams. Filtering is used only when it is required to observe narrow spectral bands of particular interest. The detector for this instrument will use a large format of CCDs with 10^8 pixels. This type of detector provides coverage from 300 nm to 1000 nm with a quantum efficiency of greater than 20 percent (Ref. 3.8-5). However, with the addition of anti-reflection coatings (Ref. 3.8-6) the lower range is extended down to 200 nm at a quantum efficiency of approximately 10 percent. As the primary instrument, this CCD will be used in planet detection and in the long integration time observations to directly image

the target planets in the optical spectrum.

The UV-Visible-IR spectrometer (Fig. 3.8-5) is designed to complement the UV-Visible-IR Imager in that it employs an identical CCD detector to study the wavelength region from 200 to 1000 nm. However, as shown in Figure 3.7-5, a filter/grating wheel is utilized for spectroscopic analysis of the incoming beams. After passing through a filter on the filter/grating wheel, the beams are reflected towards a grating on the outer edge of the wheel which separates the beams into their component spectra. The filtered and dispersed beams are then focused on the CCD detector.
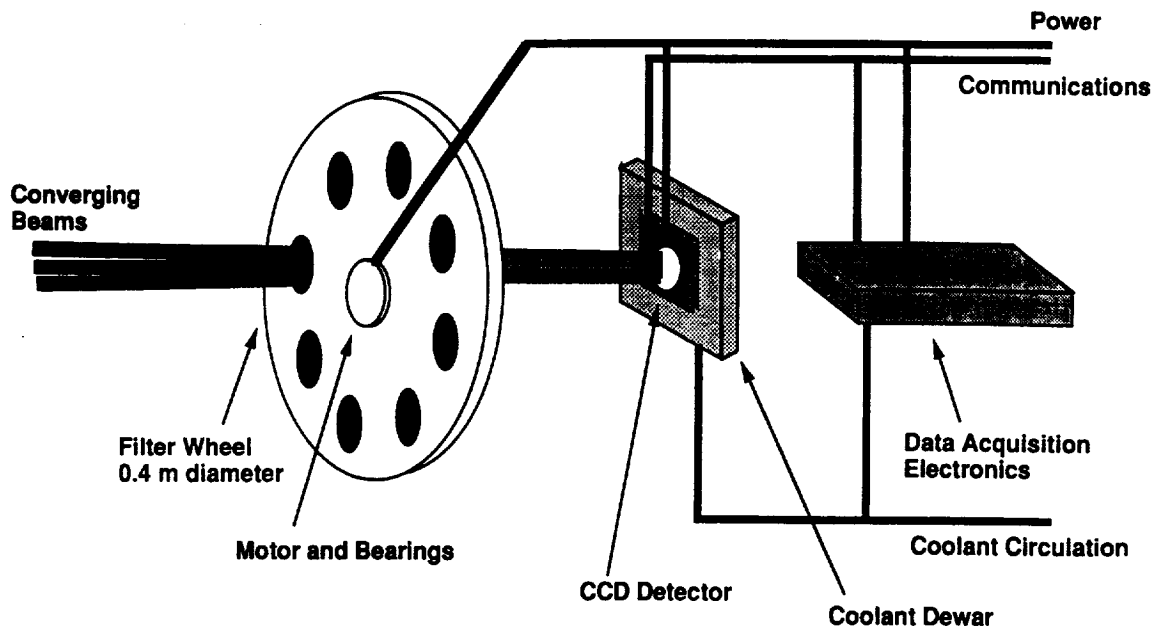
Figure 3.8-4: Interior View of UV Imager and UV-Visible-IR Imager
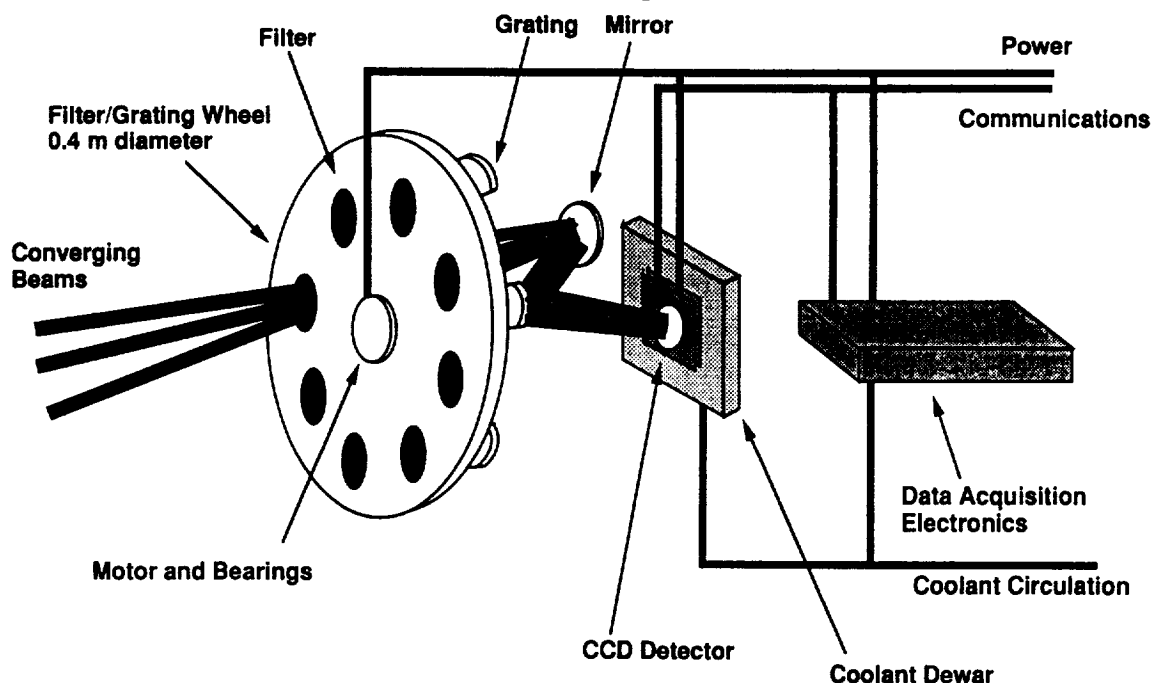
Figure 3.8-5: Interior View of IR Imager/Spectrometer and UV-Visible-IR Spectrometer
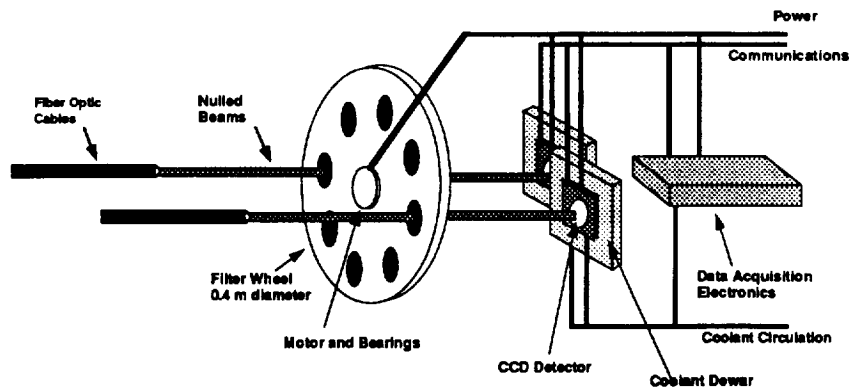
Figure 3.8-6: Interior View of Planet Detection Module

The IR Imager/Spectrometer (Figure 3.8-5) is designed to study the wavelength region from 1000 to 10000 nm and uses a detector constructed of silicon/indium which allows IR wavelength detection.

The Planet Detection Module (Fig 3.8-6) is designed for planet detection in the wavelength region from 1000 to 10,000 nm. A filter wheel is used to position a variety of narrow band pass filters in the beam path. Two Tektronix 2048 x 2048 silicon/indium pixel detectors with pixel sizes of 24 x 24 microns are employed in the imager.

3.8.3 CCD Detector Technology

Photon energy strikes the CCD and enters a channel for a single pixel (Fig. 3.8-6). It then is converted by a voltage difference into a packet of electrons. Available gain is on the order of 10^5 to 10^6 electrons through this stage depending on the frequency of the incident photon energy (Fig. 3.8-7). There are three clock phases per well which return timing information about the event. In the next step, the charge is directed from a group of wells, each well having a maximum of 20,000 electrons, to a single stage source follower amplifier where an additional yield of 2 to 3 microvolts per electron provides enough gain for the analog to digital (A/D) converter to read. Read noise from the instrument, which includes nonuniformity, nonlinearity, shot noise, bulk state limits, and charge traps, is on the order of 5 electrons for a 4 microsecond sample per pixel time.

A type of CCD known as a Skipper CCD can be employed to reduce the sample time and noise by quickly oversampling nonredundant pixels. Using Skipper CCD technology, it is estimated that the read time for a 2048 x 2048 detector would be reduced from 80 seconds to 8 seconds. As of late 1992, Skipper CCD detectors have been used on 1028 x 1028 pixel CCD detectors with success, but the complexity involved in transferring this

technology to a larger format CCD necessitates further research in this area.

A Skipper 2048 x 2048 CCD, oversampling 256 times, would lower the read noise to near 0.5 electrons per pixel, promising detection of a single photo-electron, and providing a SNR of over 10 dB for the range of 200 to 6000 nm with extremely wide dynamic range. Dark current is negligible at room temperature, and is further reduced at lower temperatures.

The Skipper CCD electronics and digital signal processing electronics require approximately 24 and 120 volts respectively. Further, the Skipper CCD requires 110 watts of power of which approximately 50 watts are dissipated as heat. The total mass of the Skipper CCD detector and its associated electronics is 100 kg.

CCD data are directed by fiber optic link to the computer system located at the lunar surface (Fig. 3.8-8). The signal processing architecture for each of the four instruments is based on a Motorola DSP5600 digital signal processing chip operating at a speed of approximately 10 millions of instruction per second. This computer architecture corresponds to the current technology in a Sun SPARCstation or a NeXT computer workstation. In the operations mode, with four instruments operating concurrently and two on standby power, the total data output is approximately 5 megabits/sec. Output data from the CCD detectors may be transmitted directly to the orbiting satellite, or the data can be stored for transmission during the lunar day.
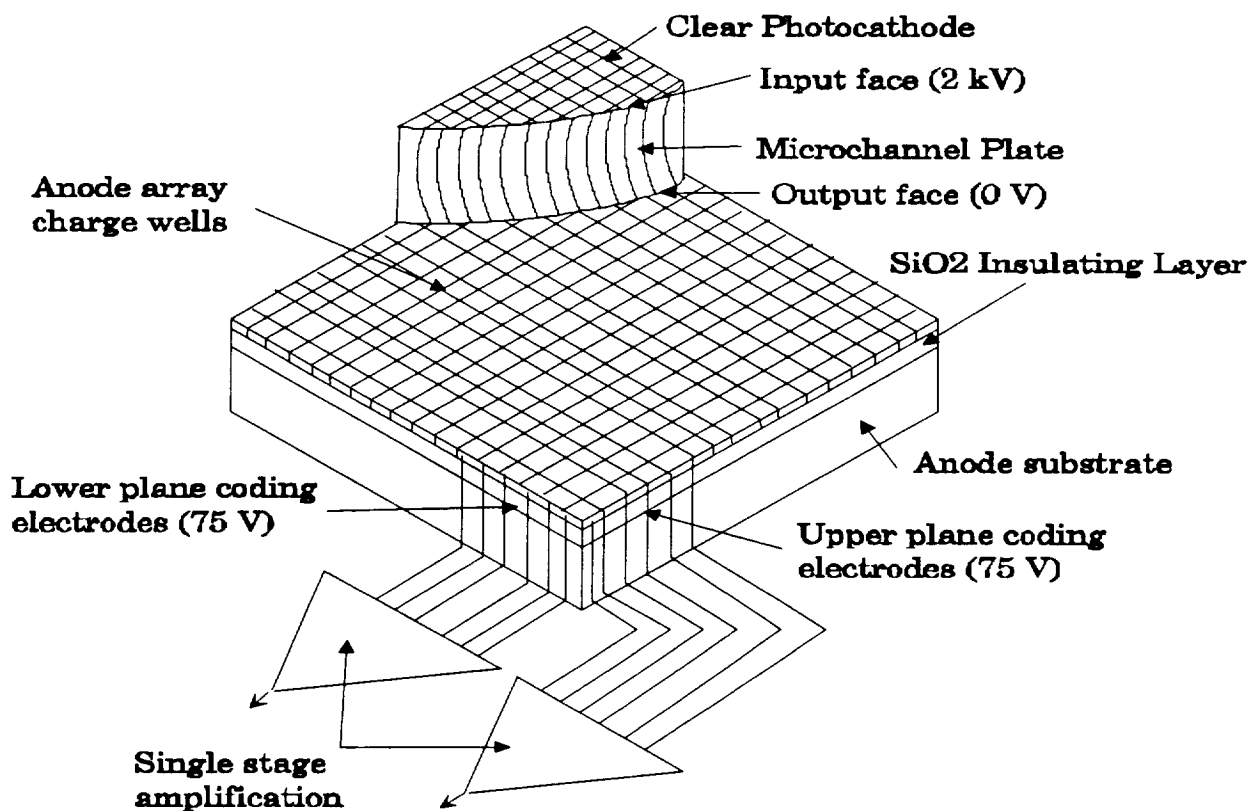
Figure 3.8-7: Photon Counting Detector System

Labels in figure:
- Clear Photocathode
- Input face (2 kV)
- Microchannel Plate
- Output face (0 V)
- SiO2 Insulating Layer
- Anode array charge wells
- Anode substrate
- Lower plane coding electrodes (75 V)
- Upper plane coding electrodes (75 V)
- Single stage amplification
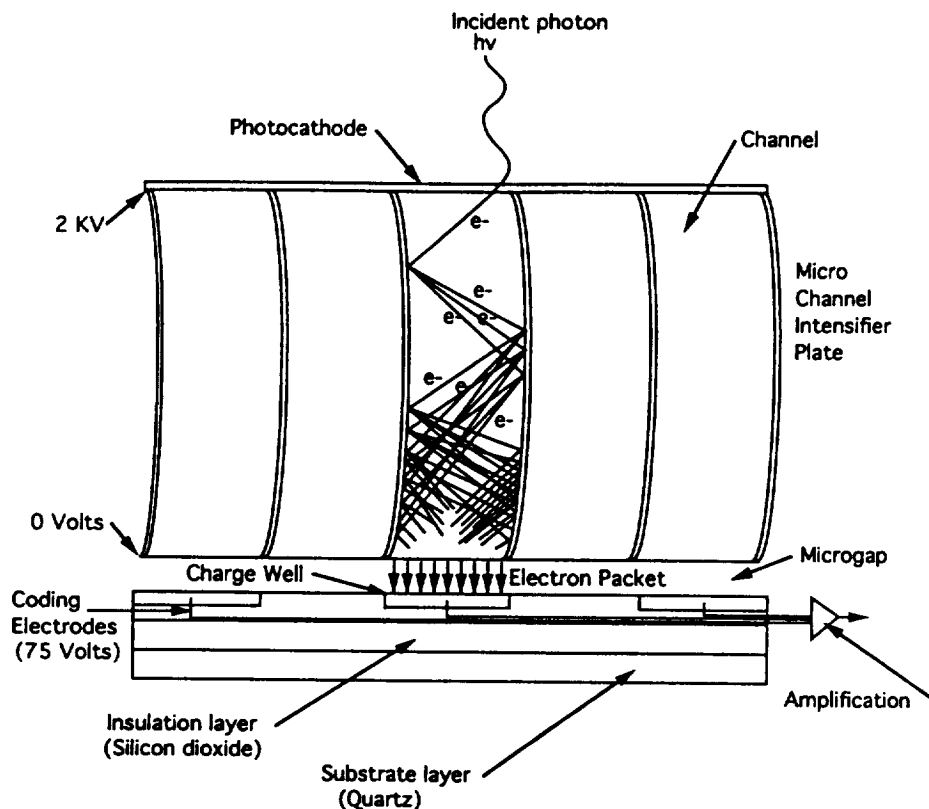
Figure 3.8-8: Photon Counting Detector Electronics

Labels in figure:
- Incident photon hv
- Photocathode
- Channel
- 2 KV
- e-
- Micro Channel Intensifier Plate
- 0 Volts
- Charge Well
- Electron Packet
- Microgap
- Coding Electrodes (75 Volts)
- Amplification
- Insulation layer (Silicon dioxide)
- Substrate layer (Quartz)
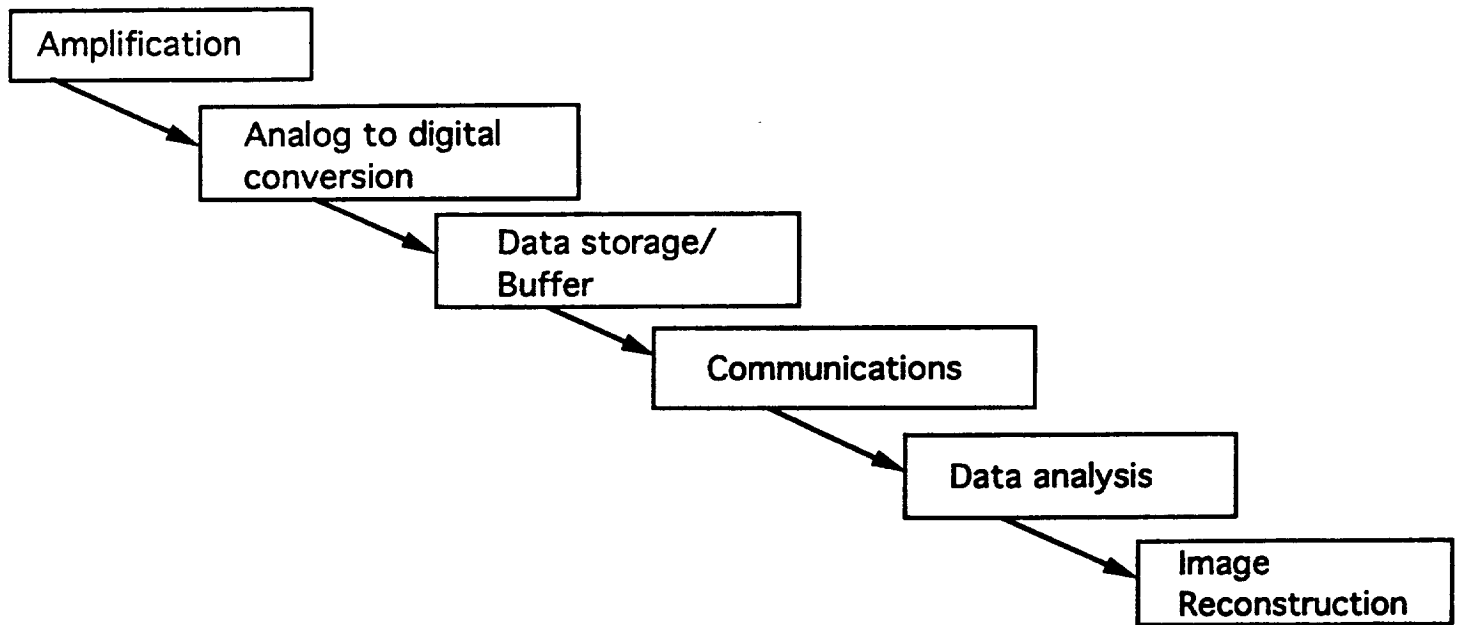
Figure 3.8-9: Data Path from Instruments to Earth

3.9 Image Reconstruction

The u-v plane is the Fourier transform of the X,Y coordinate plane and a measure of the spatial frequency of the array baselines in wavelengths. The u-v plane image is formed by the interference of the incident light waves of each baseline telescope pair onto a photon detector or other comparable instrumentation. Small separations in the X,Y image produce a high spatial frequency and contribute to the outer radius of the u-v plane image. Extended image structure produces a low spatial frequency and contributes to the inner radius of the u-v plane image. This u-v image is then returned to a X,Y image through the use of an inverse Fourier transform.

3.9.1 Detector Scheme

The first possible scheme investigated for this transform was the $^nC_2$ scheme. In this scheme, each of the n main beams is divided into (n-1) identical sub-beams and the resulting n(n-1) sub-beams are combined, pairwise, on n(n-1)/2 identical detectors. This scheme, therefore, requires a single detector for each baseline and complex beam splitting. However, with the $^nC_2$ scheme each detector is identified with a single spatial frequency and the Poisson variance or shot noise is independent of both source structure and pixel index. The second scheme investigated was a ^nC_n scheme which requires only a single detector for all baselines. For large arrays the ^nC_n has comparable signal-to-noise ratio (SNR) as $^nC_2$ array (Fig. 3.9-1) and no beam splitting is required. Beam splitting
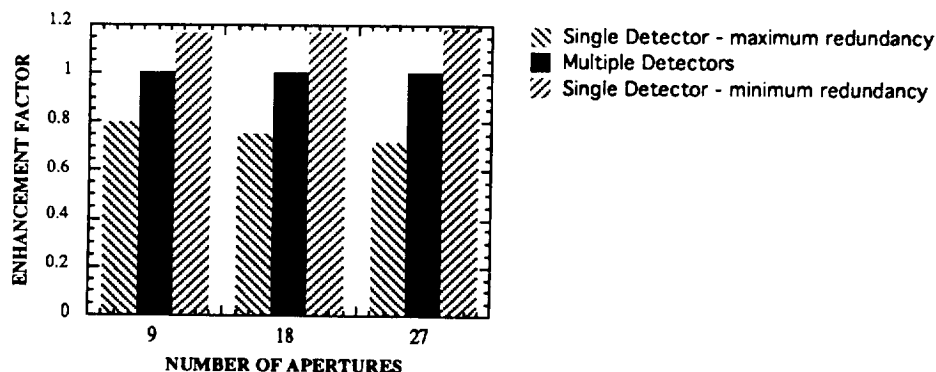
Figure 3.9-1: The Enhancement Factor F of SNR vs. the Number of Apertures, n. The three cases shown are the single detector case with maximum baseline redundancy, the multi-detector case, and the single detector case with minimum baseline redundancy.

automatically reduces the SNR due to optical scattering. However, the integration time is sometimes longer than the $^nC_2$ scheme due to baseline redundancy.

The ^nC_n scheme has been selected as the Fourier transform procedure for this baseline configuration for the following reasons:

1) The large number of array elements in the final configuration provides the same SNR for both imaging schemes.

2) The high cost, weight, and bulk of the required photon detector necessitates the selection of a scheme with the fewest required detectors. The $^nC_2$ scheme requires 351 detectors, where the ^nC_n scheme requires only a single detector.

3) The low photon rate of incoming signal requiring the fewest beam splitting operations possible. The $^nC_2$ scheme requires each of the 27 array beams to be split into 27 separate beams, automatically reducing the intensity by a factor of 27 and requiring 272 beam splitting operations. The ^nC_n scheme does not require beam splitting; allowing all 27 beams to remain at full intensity.

4) The required modularity and simplicity of packaging and construction makes a single detector with out beam splitting optics most attractive. (Ref. 3.9-1).

3.9.2 Image Recovery Algorithms

Figure 3.9-2 is a flowchart for the general image recovery algorithm (Ref 3.9-2). After the interference data is received from the photon detector, data constraints are applied by the simple combination of the measured visibility amplitudes with the model visibility phases. Next, if necessary, a phase closure analysis is performed to correct for phase shifts in the array data. The phase closure analysis combines the measured and model phases so that the hybrid visibilities maintain the same phase-closure sums as the data (App. 3.9-1). A Fourier transform is performed on the data to produce an image. However, due to the incomplete sampling of the u-v plane a "dirty image" - the true sky brightness convolved with a shift invariant point spread function, P - is formed. The beam is deconvolved by a combination of the CLEAN and Maximum Entropy (MEM) algorithms to produce a "clean" image to which the positivity visibility constraint is applied. The image is then transformed to the u-v plane for comparison with the old model data. If the new model visibilities are within the pre-determined tolerance, the image is retrieved. Otherwise, the data becomes the new model data for the next iteration (Ref. 3.9-2).

Both the CLEAN and MEM algorithms have been widely employed in the deconvolution of interferometric data. The CLEAN algorithm iteratively removes the effects of the point spread function. This removal is accomplished by repeated subtraction of a fraction of the peak flux of the remaining image multiplied by the point spread function shifted to the position of the peak visibility (Fig. 3.9-3) (Ref. 3.9-3). The Maximum Entropy Method consists mainly of choosing the single feasible image which has the greatest configuration entropy (Fig. 3.9-4) (Ref. 3.9-2). See Appendix 3.9-2 (Ref. 3.9-4) for detailed descriptions of these algorithms.

MEM is a poor scheme for removing the sidelobes of bright, unresolved components surrounded by a weak extended structure. This situation will be encountered due to the weak planetary visibility as compared to that of the solar body. However, MEM's
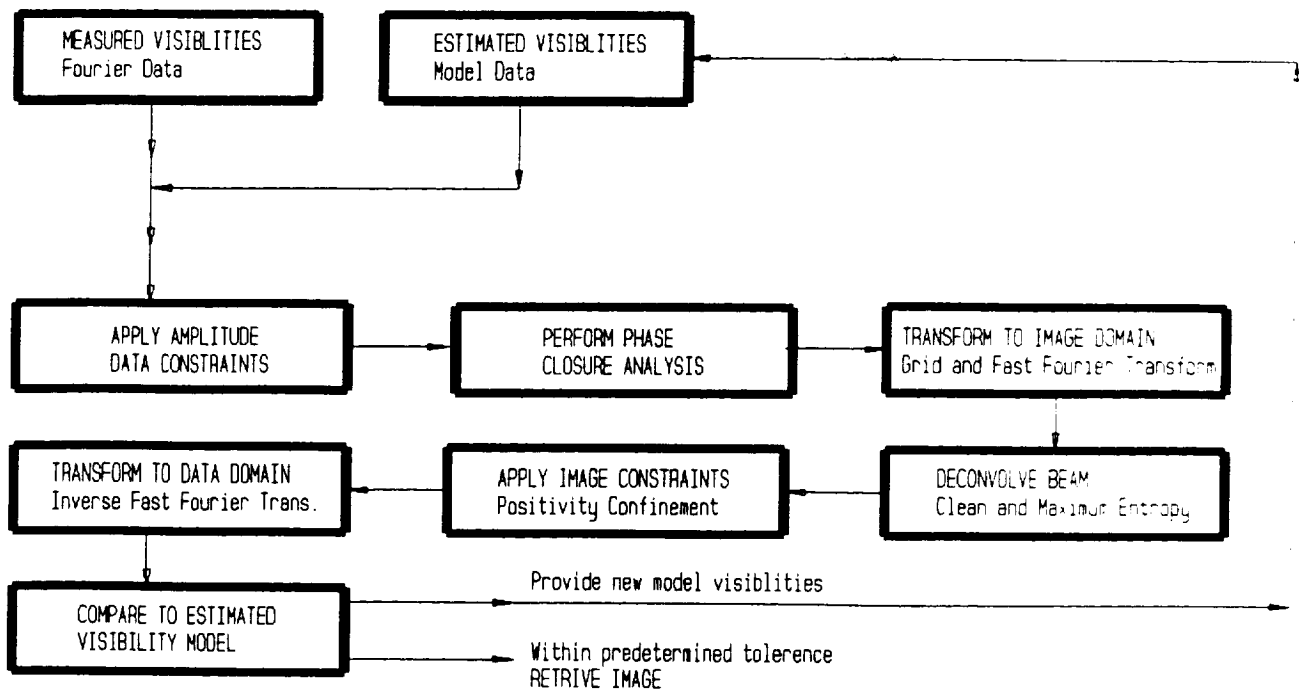
Figure 3.9-2: General Image Recovery (Ref. 3.9-4)

superresolution is perfectly suited for the imaging of dim, extended features. So, it is desirable to iteratively CLEAN the intense core structure in I and P (App. 3.9-3) down to the level of the other image features, then invert and subtract the CLEAN components from the visibility data. The residual visibilities are then imaged by MEM. The CLEAN and MEM images are convolved to produce a single final image (Fig. 3.9-5). The combination of MEM and CLEAN was developed specifically for the VLBI (Very Long Baseline Interferometer) to image data with poor aperture plane coverage, low SNR leading to image infidelity, and sources with very knotty structure where high polarization occurs due to sharp flux gradients in I and P. The algorithm was developed from the Cornwell and Evans algorithm. While many VLBI images deconvolved solely with CLEAN have shown only marginally resolved features, higher resolution VLBI images deconvolved with the combined MEM, CLEAN algorithm are now revealing jets in quasars which appear to extend out to arcsecond scales. The surface brightnesses of these newly resolved features are order of magnitudes lower than the surrounding surface brightnesses (Ref. 3.9-2 and 3.9-3). In fact, a report given in the *Proceedings of IEEE* stated that 'the two techniques most commonly used for reducing sidelobes in [interferometric] images are 'cleaning' and source subtraction', the precise devices employed in the CLEAN algorithm (Ref. 3.9-6)

It should be noted that for any one point on the celestial sphere, the spatial frequencies sampled result from the projection of a 3-D distribution of sample points onto a perpendicular plane. Hence, for non-coplanar baselines, the spatial frequencies sampled may vary significantly as a function of position inside the field. As a result, the relationship between the sky brightness and the coherence function is no longer a simple

NOTE: Smoothed data = G(1)
Reduced data after kth star
is found = G(k+1)
CLEAN ALSO PERFORMED
ON I (INTENSITY)

P^T - Transform of the
Distortion Matrix for
the U,V Plane Point
Spread Function

G(1)

G(1) = P^T D

kth star = S(k) = $\begin{bmatrix} 0 \\ 0 \\ a_k \\ \vdots \\ 0 \end{bmatrix}$

G(k+1)

G(k+1)=G(k)-P PS(k)

DELAY

G(k)

FIND PEAK

S(k)

P^T

P
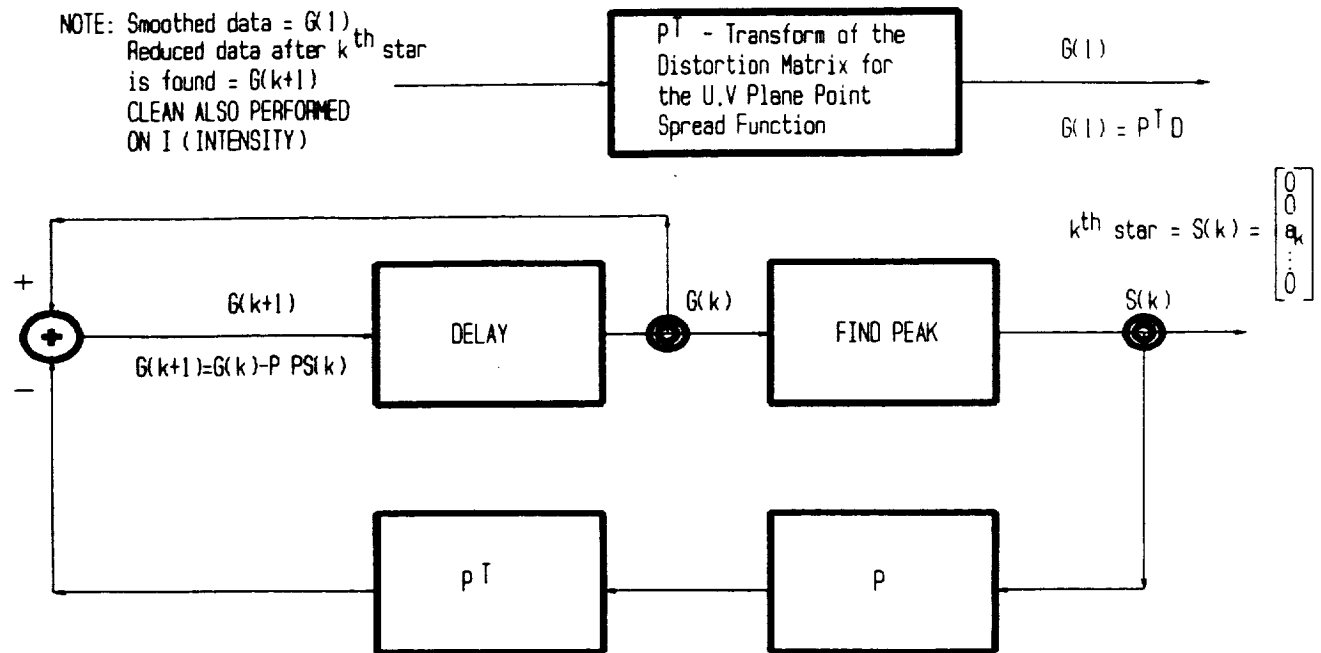
Figure 3.9-3: CLEAN Algorithm (Ref. 3.9-4)

D

P^T

$(PP^T + zI)^{-1}$

$\hat{O}$

$\hat{O}(k+1)$

DELAY

$\hat{O}(k)$

S

G

R^{-1}

IN

NOTE: O is the Object Location Vector
$\hat{O}$ is the Estimate of O
z is the Noise Control
Parameter
$\hat{O}(k+1)$ = $\hat{O}(k)$ + SG
S is the Step Size
G is the Entropy Filtered Data
P is the Point Spread Distortion Matrix
RESTORATION ALSO PERFORMED ON I (INTENSITY)
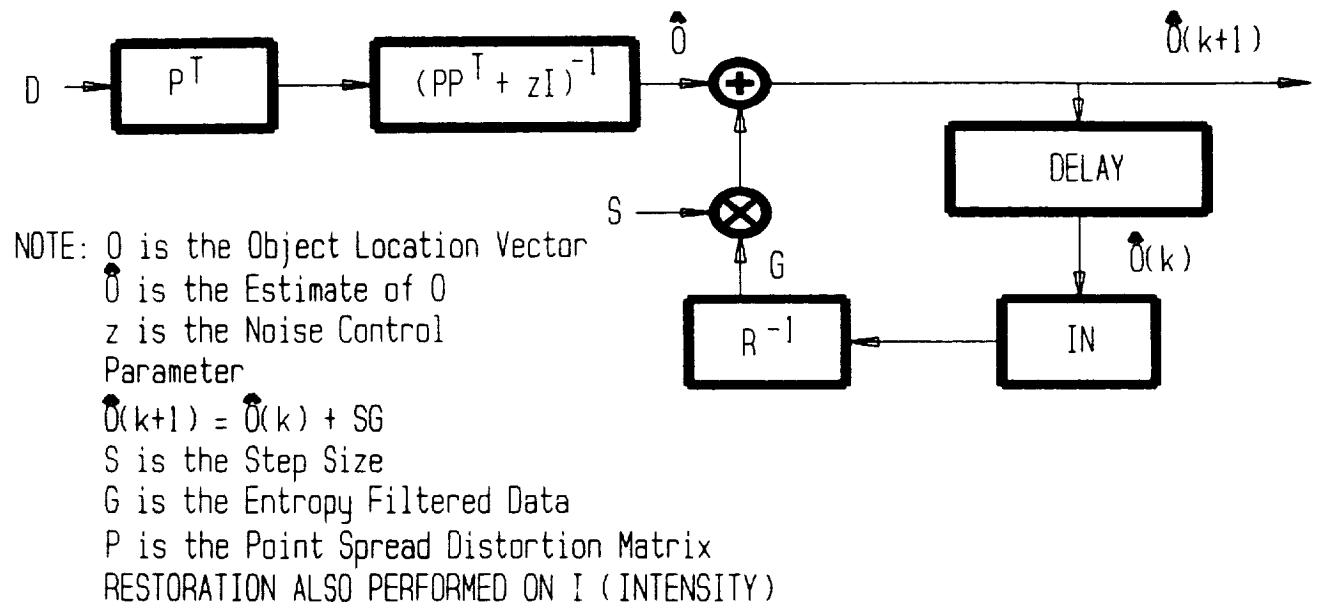
Figure 3.9-4: Maximum Entropy Method (Ref. 3.9-4)

```
┌─────────────────────────────┐
│ CLEAN I and P Core          │          NOTE:
│ to Reduce Light Intensity to│          P is the Real Point Spread Function
│ Surrounding Intensity Levels│          I is the Total Intensity Function
└─────────────────────────────┘
              │
              ▼
┌─────────────────────────────┐
│ Invert and Subtract         │
│ CLEAN Components from        │
│ Intensity Data              │          Residual Visibilities
└─────────────────────────────┘          Below Noise Level
              │
              ▼
┌─────────────────────────────┐        ┌─────────────────────────────┐
│ Image Residual Visibilities │        │ Convolve Image with Gaussian│
│ by the Maximum Entropy      │────────│ to Raise Structure          │
│ Method                      │        │ Above the Noise             │
└─────────────────────────────┘        └─────────────────────────────┘
              │       ◄────────────────────────────┘
              ▼
┌─────────────────────────────┐
│ Add in CLEANED              │
│ Core Components             │
└─────────────────────────────┘
              │
              ▼
┌─────────────────────────────┐
│ Convolve Resulting Images   │
└─────────────────────────────┘
```

Figure 3.9-5: Deconvolution Algorithm (Ref. 3.9-4)

2-D Fourier transform. The simplest approach to correct this effect is to do all the processing in 3-D space, using a 3-D Gaussian distribution in the CLEAN and MEM algorithms. The extension of these algorithms to three dimensions is a simple (Ref. 3.9-5).

3.9.3 Electronic Calibration

In addition to the physical alignment and lunar surface calibration of the optical array elements and optics, electronic synthesis calibration will be performed on the array design. Recently a concept has been developed by the Air Force that utilizes the far-field intensity pattern of a synthetic aperture phased array to measure the effective system performance (Ref. 3.9-7). The procedure provides a quantitative measure of the level of energy delivery to the receiver (telescope array), while incorporating important aspects of system operation into a far-field propagation simulation. Thus, it produces a quantification of system performance under various conditions, including the peak far-field intensity for the configuration and the sensitivity of the system to mis-alignment of the sub-apertures.

A specialized multi-aperture propagation code is utilized in this procedure, allowing the user to define the number and arrangement of the sub-apertures, the relative piston and x- and y- tilt errors on each sub-aperture and any beam obstruction inherent to the design.

Figure 3.9-6 shows a flow diagram for the propagation portion of the simulation. A 2-D Fast Fourier Transform is used to compute the Point Spread Function (PSF). The PSF, along with near- and far-field scaling based on the given piston and tilt errors of each sub-
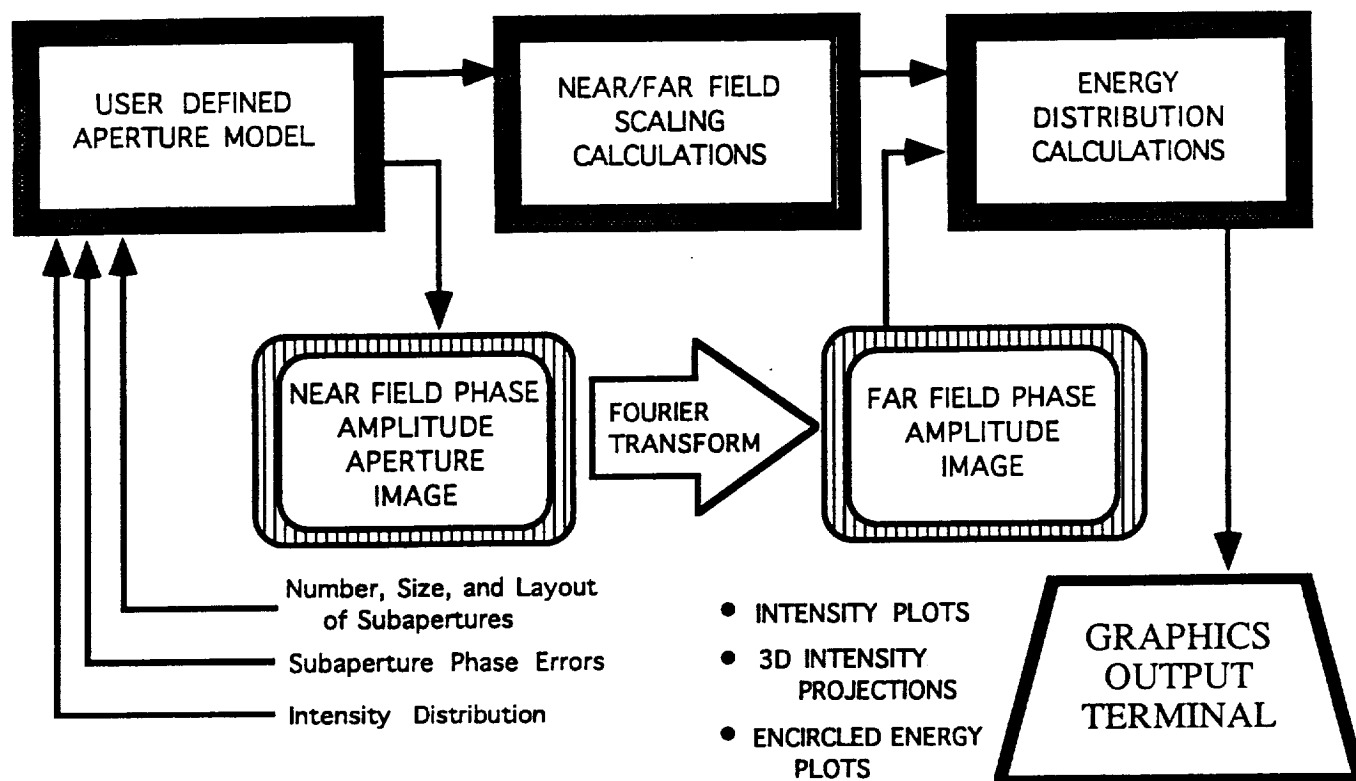
Figure 3.9-6: Simulation Program Flow Diagram
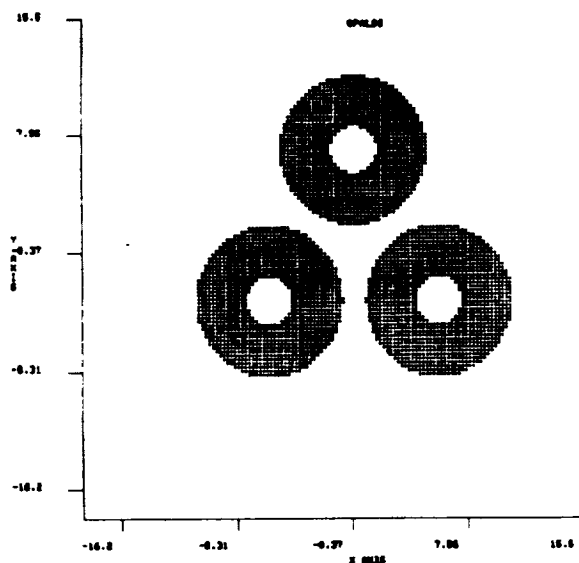
Figure 3.9-7: Near-field Aperture Representation (Ref. 3.9-7)

aperture, allows the computational simulation of the far-field intensity distribution falling on the photon counting detector. A photon counter, connected to a video digitizer and the minicomputer, provides an active controlled comparison for the simulated far-field data.

The simulation process begins with the construction of a near-field phase-amplitude matrix (Fig. 3.9-7). Next the user defines the energy distribution function at the exit of each sub-aperture (Fig. 3.9-8, 3.9-9). A far-field intensity pattern is then generated and displayed (Fig. 3.9-10 through 3.9-12). The plots are then compared to the far-field pattern recorded on the photon-counter (Fig. 3.9-13).

Using this program, an evaluation of the performance of the array under varying conditions would be possible. This data could be used to diagnose and correct sub-aperture alignment errors at the data level. It would also serve as baseline data for the phase-closure, CLEAN, and MEM algorithms in the absence of lower resolution data from alternate sources, such as the Hubble telescope. Further development continues on the program code to allow the modeling of jitter and higher-order aberrations of the sub-aperture optics (Ref 3.9-7).
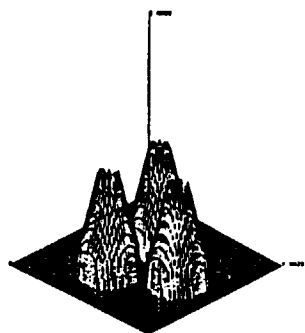
Figure 3.9-8: Centered
Gaussian Intensity
Profiles (Ref. 3.9-7)
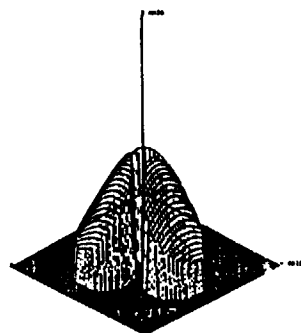
Figure 3.9-9:
Off-centered Gaussian
Profiles (Ref. 3.9-7)
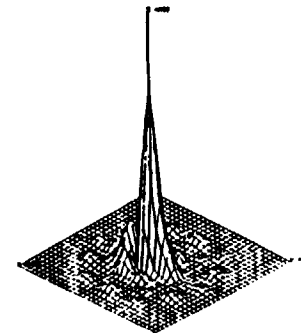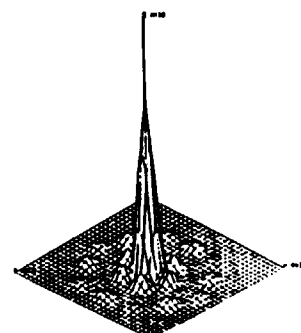
Figures 3.9-11 (a) and (b): 3-D Projections
of Far-Field Pattern (Ref. 3.9-7)
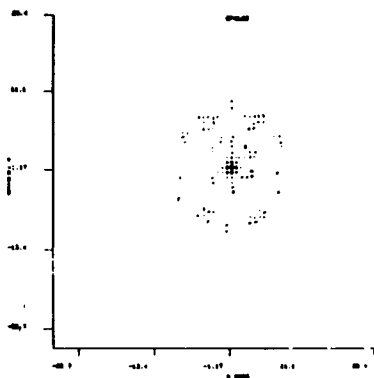
Figure 3.9-10a:
Far-field Intensity
Pattern (Ref. 3.9-7)
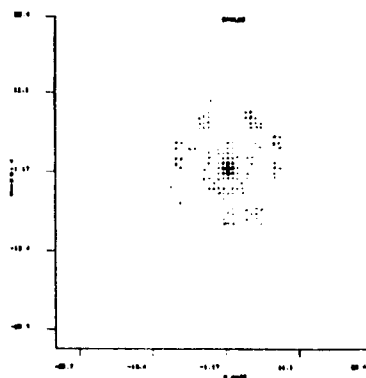
Figure 3.9-10b:
Far-field Intensity
Pattern (Ref. 3.9-7)
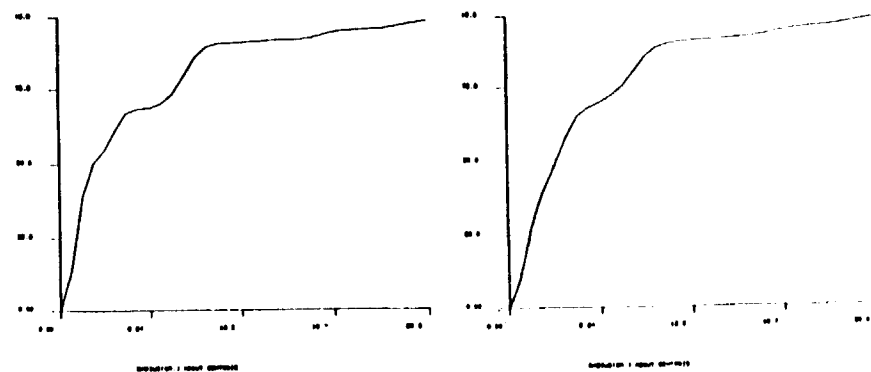
Figures 3.9-12 (a) and (b):
Encircled Energy Plots (Ref. 3.9-7)
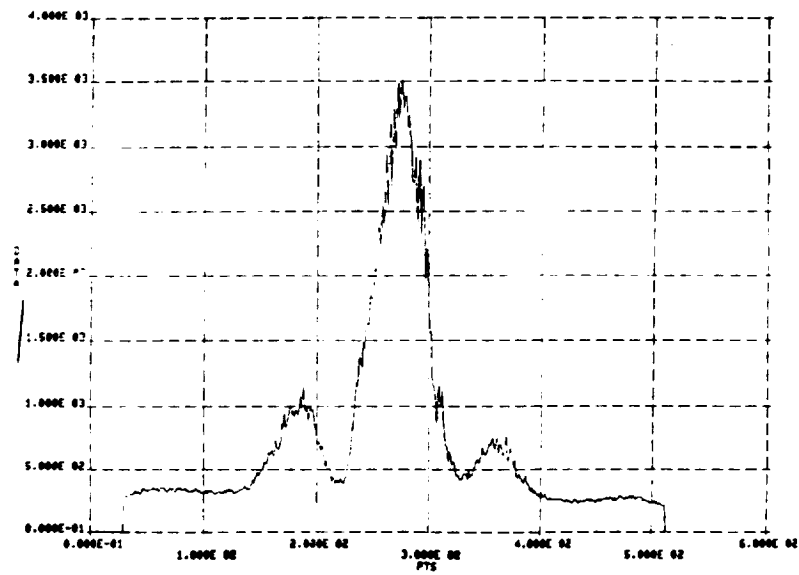
Figure 3.9-13: X-Slice Plot of Experimental Far-Field Data (Ref. 3.9-7)

4.0 Communications

LOLA's communications system was designed for continuous, real time communications. This report is broken down into two sections, relay satellite orbit selections and satellite link analysis.

4.1 Network Selection

Three network types were studied, a lunar surface link from the lunar far-side to a near-side direct transmitter, three satellites in polar orbits spaced at 120 degrees intervals, and one satellite placed in a halo orbit.

The lunar based network consists of either a microwave link similar to Earth based microwave links or fiber optic link between the LOLA array and a near-side transmitter. This link, when regarding the near-side transmit station as part of another lunar base, would be the least expensive.

The problem with the lunar based link is initial implementation and subsequent limited usefulness. It would be in the best interest of the construction teams to have communications upon landing. This is not possible with the lunar based link since thousands of kilometers of fiber optic cables or tens of microwave towers must be constructed prior to communications establishment. The second weakness of this network is its limited capabilities. The link would be dedicated solely to LOLA. Since the rest of the far side will be explored, a communications network for lunar rovers and other vehicles must eventually be established. Once this system is established any previous single purpose lunar link would be obsolete.

The next two options, three satellites in polar orbit or one satellite in a halo orbit, would both give sufficient coverage of the lunar far-side and link the lunar observatory to an earth relay satellite in real time. These two options were further compared on the basis of cost and reliability. The polar orbit was found to be lacking in three areas. First, the polar orbit requires three satellites at higher initial delta-V than the halo orbit. Second, each satellite would have to be tracked and a different satellite would have to be acquired every 12 hours. Tracking is not required in the halo orbit since the satellite will always be in the beamwidth of the lunar station. Third, the polar orbit satellites would have to incorporate complex tracking and pointing mechanisms to maintain link with Earth and the lunar base.

Using a halo orbit has none of these difficulties and the halo orbit satellite's antennas would always include the lunar base and the Earth in its beamwidth. (Fig. 4.1-1) Thus, the halo orbit was chosen. The halo orbit is centered at the L2 libration point of the Earth-moon system. (Fig. 4.1-2) The L2 point is one of five Lagrange points in the Earth moon system. These points are found by solving the "three body problem", the three body problem being the relative strength of the gravitational field around a system of three bodies due to those three bodies. The L2 point is at a mean distance of 64,500 km above the lunar surface. According to the Lagrange equations it is possible to place a satellite in an orbit about this point. Given a 3500 km radius, this orbit would provide continuous coverage of the Earth and the lunar far side. This orbit is unstable and requires a stationkeeping delta-V of 28.5 meters per second (Mps) a year. An additional 103.6 Mps a year is required for period control. Period control is necessary to ensure the satellite is not occulted by the moon during its orbit. An additional 7.62 Mps annually is needed for attitude control. These values were obtained through the evaluation of the equations of motion of a three body system by Robert W. Farquhar of NASA 1971. (Ref. 4.1) The total

value of delta-V is about 25% higher than that of an Earth geosynchronous satellite. The halo orbit requires both period control and station keeping delta-V. The amounts of delta-V required for these purposes decreases significantly as the initial injection becomes more accurate. The delta-V required for a first order approximation is six times that for a second order approximation and twelve that of a third order approximation. Thus initial nominal path is an important factor in the satellites lifespan. (Ref 4.2)

4.2 Link Analysis

The halo orbit is a realistic, cost-effective orbit for far-side real-time continuous communications and was chosen for LOLA. Now that there is a relay satellite in place the link analysis can be calculated for the power and antenna requirements. The link was analyzed to meet power and antenna constraints for C-band, S-band, X-band and Ku-band. The four bands were compared based on their power required as a function of antenna diameter. Figure 4.2-1 a, b and c illustrate this function for each step of the communication link. The X-band was found to meet all of the power and antenna constraints. A link analysis was performed for each step of the communication system and is shown in Tables 4.2-1 through 4.2-4. The link analysis was based on the need for a 100 Mbps (full-motion video = 50 Mbps) downlink and a 50 Mbps uplink. This link was also constrained to a worst case carrier to noise ratio of fourteen decibels. A fourteen decibel carrier to noise ratio corresponds to a bit error rate of 10^{-6} without any type of error detection or error correction. The addition of one parity bit would reduce the error rate to below that of the picture reconstruction instruments.

Through these calculations the lunar base was found to require a 1 meter antenna for both uplink and downlink with power requirements of under 50 watts. This antenna would cover a beam width of 5 degrees, thus including the entire halo orbit. The lunar relay satellite to Earth link was based on the 34 meter diameter antennas of the Deep Space Network. It was found to require a two meter antenna with power requirements of under 50 watts. Since the power requirement of this satellite is small, multiple channels could be incorporated into the design for future needs with minimal reduction of the satellites' lifespan. In fact, since the power requirements are so small a Time Division Multiple Access system could be set up to incorporate up coverage to 6 lunar stations, possibly for construction, with minimal effort.

The communications network consists of the lunar base, the lunar relay satellite and the Deep Space Network (DSN) (Fig. 4.0-4). In choosing the X-band, the communications system uses highly tested and proven microwave technology; technology that is low cost and reliable because of its high volume of use. There is no need to move up to higher frequencies unless the data rate should increase to at least 350 Mbps after compression. If this were the case a Ku-band would be necessary and possibly a dedicated network of LEO satellites similar to the ATDRS.

A real time, reliable communications link from the far side of the moon to an Earth station is possible with today's technology, if and only if, that technology is implemented in a suitable fashion. The satellite link designed in this paper takes into consideration the pros and cons of today's technology in order to avoid the need for projections of futuristic technology.
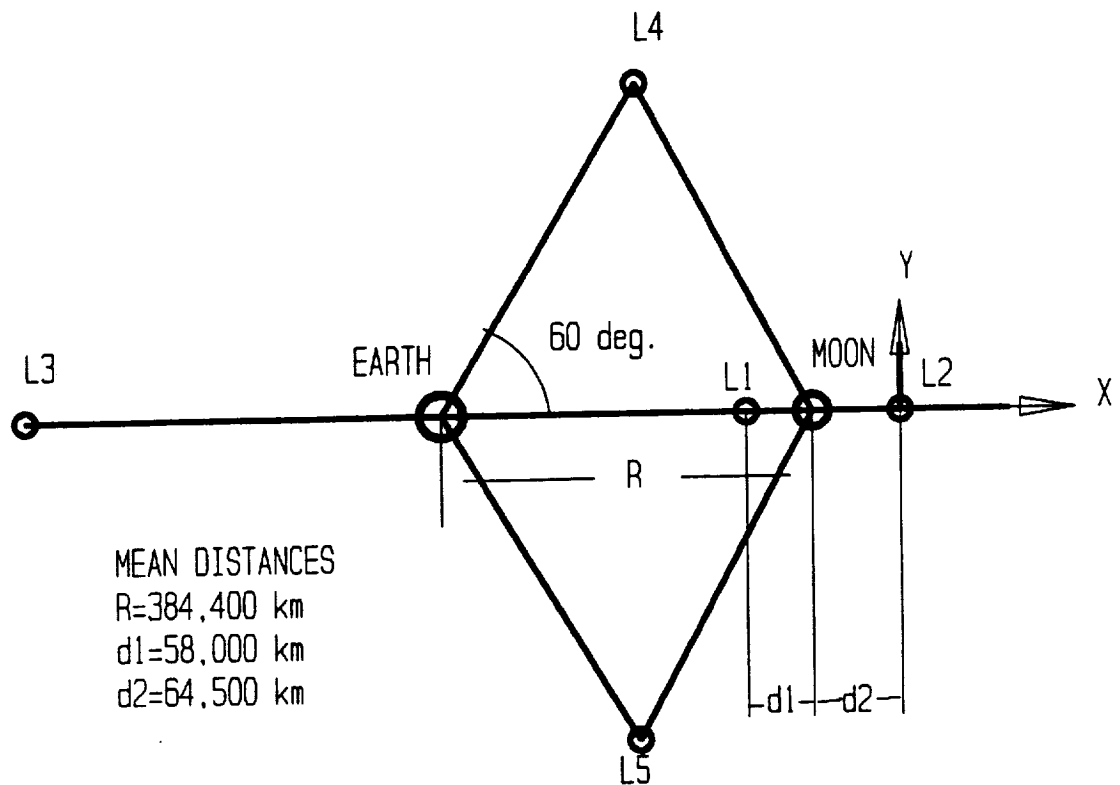
Figure 4.1-1: Libration Points of the Earth-Moon System

MEAN DISTANCES
R=384,400 km
d1=58,000 km
d2=64,500 km
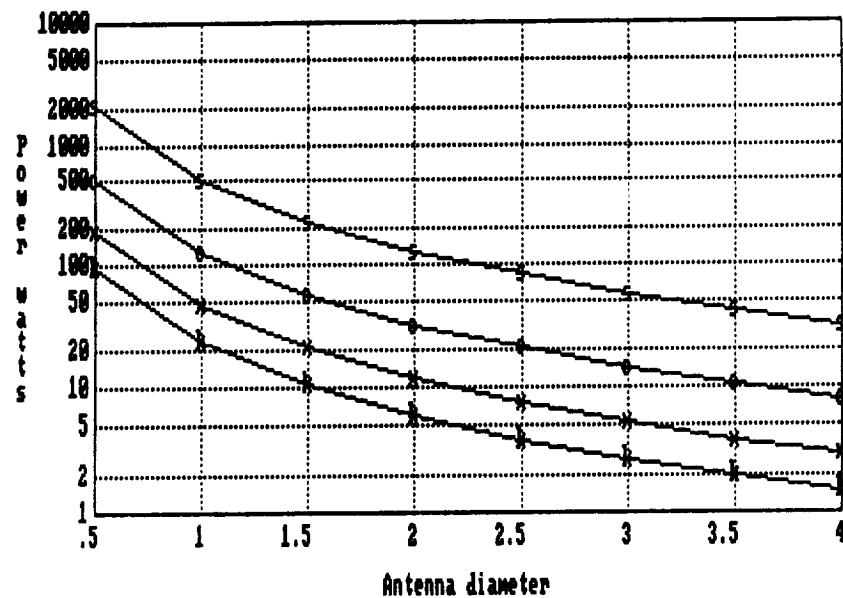
Figure 4.1-2: Antenna Reflector Diameter vs. Power Required
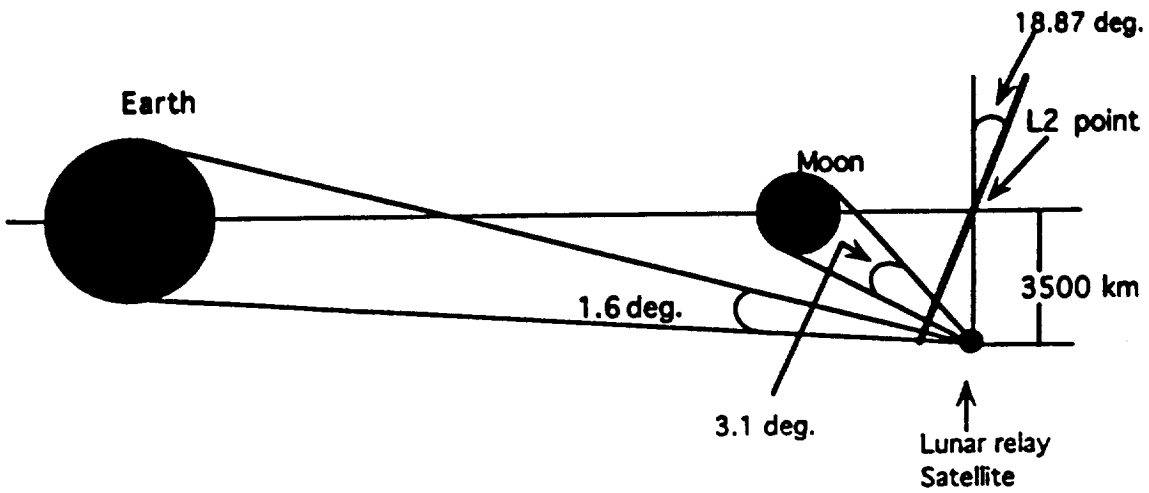
Figure 4.1-3: Halo Satellite Geometry (not to scale)

Uplink   10 GHz
Downlink   9 GHz
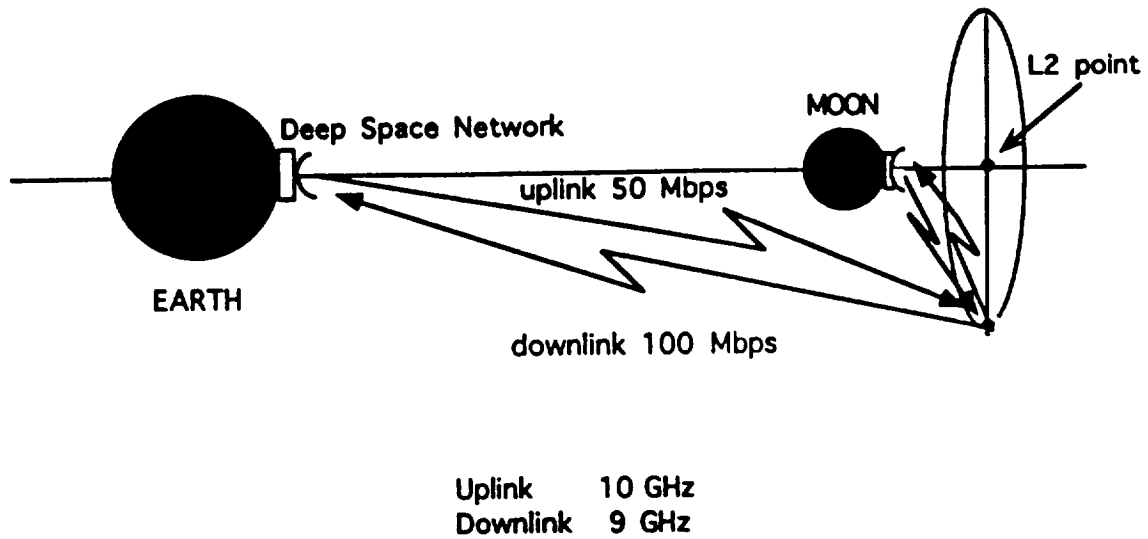
Figure 4.1-4: Uplink and Downlink Paths

Table 4.1-1 Link Analysis from Deep Space Network to Satellite

Frequency X-BAND	9 x 10E9	Hz		Effective area	1.73	meters sq.
Data rate	50.00	mbps		Gain receiver	36.90	dB
Bit duration-bandwidth product	0.60			Theoretical received power	-116.77	dB W
Bandwidth	30 x 10E6	MHz				
Antenna diameter	2.00	meters		**LOSSES**		
Efficiency	55.00	%		Station at edge of coverage	-3.00	dB
EIRP	48.10	dB W		Atmospheric attenuation	0.00	dB
Gain transmitter	54.10	dB		Tracking loss	0.00	dB
Required transmitter power	11.20	dB W		Losses in reciever before LNA	-1.00	dB
	13.10	W		Actual received power (FAe)	-121.00	dB W
Path length	65 x 10E6	meters				
Path loss	208.70	dB		**NOISE POWER BUDGET**		
Flux density	-119.15	dB W/m*m		Boltzman's constant	-228.60	dB W/Hz/K
				Bandwidth	74.77	dB Hz
RECEIVING STATION				Temperture of receiver	20.00	dB K
Antenna diameter	2.00	m		Noise power	-136.00	dB W
Efficiency	55.00	%				
				Carrier to noise ratio	14.00	dB

Table 4.1-2: Link Analysis from Satellite to Lunar Surface

Frequency X-BAND	1 x 10E10	Hz		Effective area	500.00	meters sq.
Data rate	100.00	mbps		Gain receiver	61.50	dB
Bit duration-bandwidth product	0.60			Theoretical received power	-110.80	dB W
Bandwidth	60 x 10E6	MHz				
Antenna diameter	2.00	meters		**LOSSES**		
Efficiency	55.00	%		Station at edge of coverage	-3.00	dB
EIRP	48.55	dB W		Atmospheric attenuation	-1.50	dB
Gain transmitter	36.90	dB		Tracking loss	0.00	dB
Required transmitter power	11.70	dB W		Losses in reciever before LNA	-1.00	dB
	14.60	W		Actual received power (FAe)	-116.30	dB W
Path length	58.5 x 10E7	meters				
Path loss	227.80	dB		**NOISE POWER BUDGET**		
Flux density	-137.80	dB W/m*m		Boltzman's constant	-228.60	dB W/Hz/K
				Bandwidth	74.77	dB Hz
RECEIVING STATION				Temperture of receiver	20.00	dB K
Antenna diameter	34.00	m		Noise power	-136.00	dB W
Efficiency	55.00	%				
				Carrier to noise ratio	14.00	dB

Table 4.1-3 : Link Analysis from Lunar Surface to Satellite

Frequency X-BAND	1 x 10E10	Hz
Data rate	50.00	mbps
Bit duration-bandwidth product	0.60	
Bandwidth	30 x 10E6	MHz
Antenna diameter	34.00	meters
Efficiency	55.00	%
EIRP	77.20	dB W
Gain transmitter	61.50	dB
Required transmitter power	15.60	dB W
	36.60	W
Path length	58.5 x10E7	meters
Path loss	227.80	dB
Flux density	-109.20	dB W/m*m

RECEIVING STATION

Antenna diameter	2.00	m
Efficiency	55.00	%

Effective area	1.73	meters sq.
Gain receiver	36.90	dB
Theoretical received power	-106.70	dB W

LOSSES

Station at edge of coverage	-3.00	dB
Atmospheric attenuation	-1.50	dB
Tracking loss	0.00	dB
Losses in reciever before LNA	-1.00	dB
Actual received power (FAe)	-112.30	dB W

NOISE POWER BUDGET

Boltzman's constant	-228.60	dB W/Hz/K
Bandwidth	74.77	dB Hz
Temperature of receiver	27.00	dB K
Noise power	-126.80	dB W
Carrier to noise ratio	14.00	dB

Table 4.1-4 : Link Analysis from Satellite to Deep Space Network

Frequency X-BAND	9 x 10E9	Hz
Data rate	100.00	mbps
Bit duration-bandwidth product	0.60	
Bandwidth	60 x 10E6	MHz
Antenna diameter	2.00	meters
Efficiency	55.00	%
EIRP	48.10	dB W
Gain transmitter	54.10	dB
Required transmitter power	17.20	dB W
	52.30	W
Path length	65 x 10E6	meters
Path loss	208.70	dB
Flux density	-119.15	dB W/m*m

RECEIVING STATION

Antenna diameter	2.00	m
Efficiency	55.00	%

Effective area	1.73	meters sq.
Gain receiver	36.90	dB
Theoretical received power	-116.77	dB W

LOSSES

Station at edge of coverage	-3.00	dB
Atmospheric attenuation	0.00	dB
Tracking loss	0.00	dB
Losses in reciever before LNA	-1.00	dB
Actual received power (FAe)	-121.00	dB W

NOISE POWER BUDGET

Boltzman's constant	-228.60	dB W/Hz/K
Bandwidth	74.77	dB Hz
Temperture of receiver	17.00	dB K
Noise power	-136.00	dB W
Carrier to noise ratio	14.00	dB

5.0 Powering the Lunar Interferometer

The power system analysis was performed considering that the power system would be autonomous, with no power from a lunar base. In order to make comparisons between power systems, the interferometer power requirements needed to be determined. These electrical requirements were:

Table 5.0-1   Power Requirements

Communication	500W, 24V
Instrumentation, computers	2000W
Instrument cooling system	1500W
Telescope motors	1350W (50W/telescope)
Telescope shields	400W
Laser metrology	1500W
Delay lines	500W
Subtotal	7750W
Contingency 25%	1938W
Total	9688W

Three types of power systems were investigated to fulfill these power needs; solar array/regenerative fuel cells (RFC), Dynamic Isotope Power System (DIPS), and the Topaz nuclear reactor. The system design restraints considered were the mass of the power system, life cycle, reliability, and the required construction intensity, or the amount of construction needed to place the power system.

5.1 Topaz Nuclear Reactor

Topaz II is a thermionic nuclear power plant purchased from the former Soviet Union by the United States government to provide a working baseline system for the developing United States space nuclear power system program. A thermionic reactor was selected over a conventional thermoelectric reactor for the following reasons: 1) higher efficiency, 2) smaller radiators, 3) lower system mass, 4) appropriate conversion technology from 10s to 100s of kWe (Ref. 5.1-1). Also, below 100 kWe, thermionic reactors provide: 1) survivability, 2) safety, 3) reliability (Ref. 5.1-2). Another advantage of using the TOPAZ system is that the TOPAZ I and TOPAZ II technologies have been demonstrated, and TOPAZ I has been space qualified.

Thermionic energy conversion is accomplished by the generation of heat, Qe, from a nuclear fuel source. This heat then produces electron emissions from a substance known as an emitter. These electrons strike a collector, producing a power output of Qe-Qc to the load and waste heat, Qc (Fig. 5.1-1) (Ref. 5.1-2). The nuclear fuel source is an array of removable uranium oxide fuel elements with a zirconium hydride moderator. The nuclear
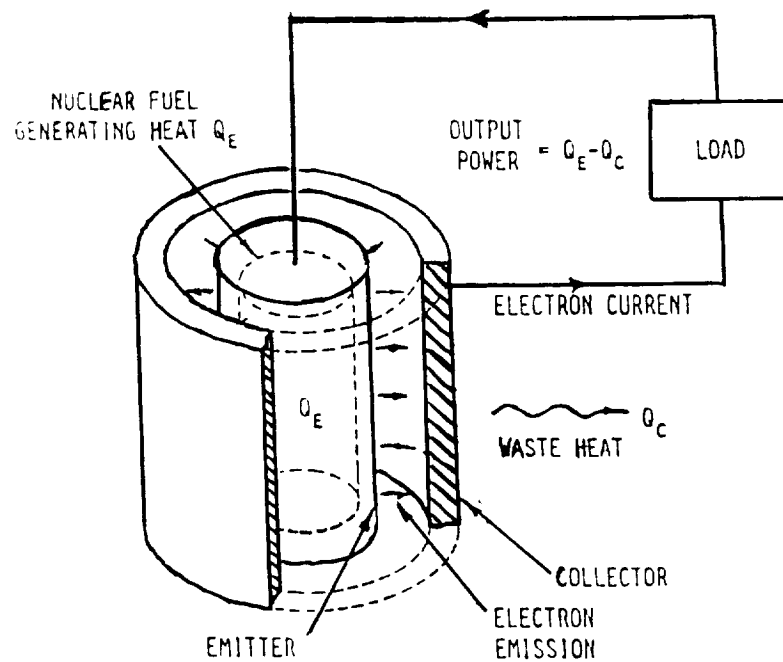
Figure 5.1-1: Thermionic Energy Conversion in TOPAZ
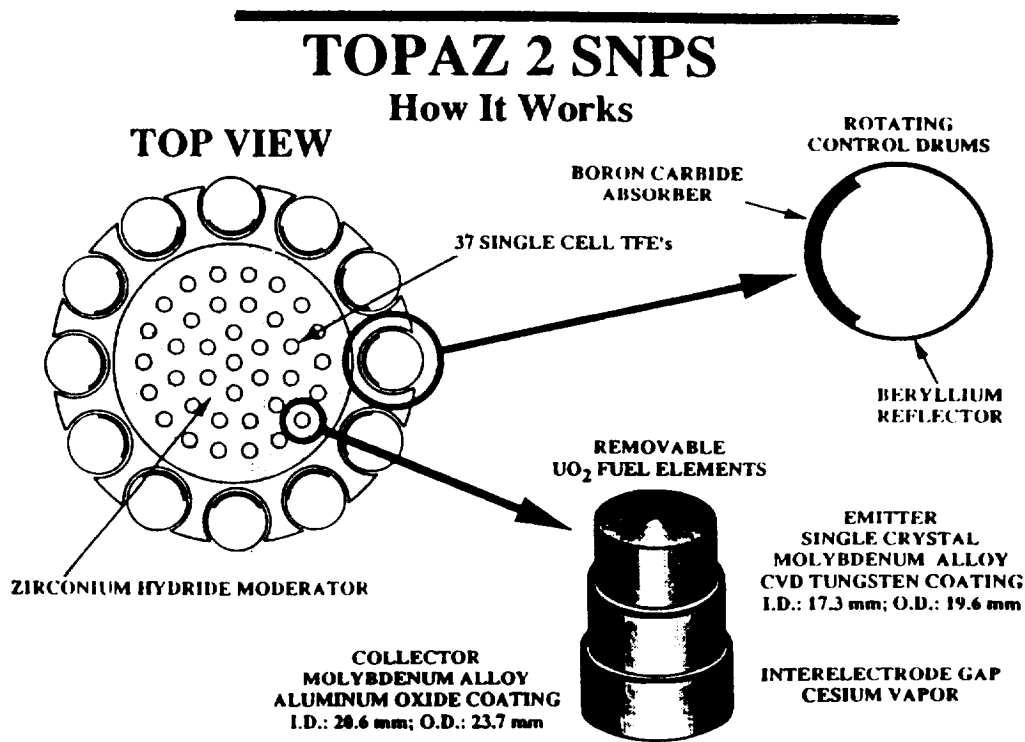
Figure 5.1-2: Power Source Diagram for the TOPAZ 2

reaction is controlled with boron carbide absorbers mounted on beryllium reflector rotating control drums. The emitter is a single crystal molybdenum alloy with CVD tungsten coating and the collector is constructed of molybdenum alloy with aluminum oxide coating (Fig. 5.1-2) (Ref. 5.1-3).

Some of the most important TOPAZ II system parameters include: operational lifetime, 3 years; electrical power at the reactor, 6 kWe; thermal power, BOL (beginning of life) 115kWth, EOL (end of life) 135kWth; system mass, 1061 kg; radiator area, 7.2 m²; and radiator emissivity, 0.86 (Ref. 5.1-4). The TOPAZ II is attractive because of its compact size and low mass. However, there is concern about reactor radiation emissions. This radiation could interfere with the array and is dangerous to the astronauts.

5.2 Dynamic Isotope Power System (DIPS)

DIPS is based upon two previous NASA ventures, the radioisotope thermoelectric generators (RTGs) used to power satellites such as Galileo and Ulysses, and Brayton cycle technology developed in the past few years. For our purposes a 2.5 kWe DIPS was considered. Therefore 6 units will be required to meet the 10+ kWe electrical power requirement resulting in a total mass of 2142 kg. A single unit of higher capacity could be used with a slight decrease in weight. However the modular approach offers some reliability improvement and lends itself to modification in case of power requirement changes (Ref. 5.2-1).

In order to generate power, DIPS uses the radioisotope (Pu 238) as its heat source in a closed Brayton cycle. The isotope heats an inert gas working fluid of Xe-He(NW 60), which is expanded through a turbine (Fig. 5.2-1). A simplified CBC cycle diagram and entropy cycle are shown in Fig. 5.2-2. It contains no contacting moving parts and only one moving part. The turboalternator rotor is suspended on non-contacting working fluid gas foil bearings and there are no contacting seals or brushes, which makes it attractive.

Another advantage of the DIPS is in its method of fueling. Since the fuel is contained in a modular removable Heat Source Unit (HSU) the DIPS can theoretically be used for up to 50 years. The life of the DIPS, however, also depends on the life of the mechanical system which is estimated at 3 years. Each HSU is designed to produce enough heat to the power converter to generate 1 kWe. For the 2.5 kWe design three HSUs are placed in parallel producing a low pressure drop heat source assembly.

As for testing and space flight qualification, the DIPS system is very similar to the flight proven technology of the RTG which reduces the need for costly testing with no loss in safety or increase in risk. DIPS is also attractive because of its low downtime, less than 7 hr/yr (Ref. 5.2-2). However, DIPS would require special handling during activation and shielding would be required to protect the astronauts and instrumentation from radiation. The layout of the 2.5 kWe DIPS is given in Figure 5.2-3.

5.3 Solar

Solar power has been used for many space applications. Photovoltaic cells make up the solar panels which produce electrical energy. They have proven their reliability in space. There are several different types of solar cells, of these the Gallium Arsenide (GaAs) and the Indium Phosphide (InP) cells are more immune to high levels of radiation which the cells would face on the moon. Solar cells can be deployed in either flat plate PV arrays or with concentrators. Concentrators can raise the power output, but at the same time they

State Point	Location	Optimum Temperature (K)	Alternate Temperature (K)
1	Turbine Inlet	1300	1300
2	L.P. Recuperator Inlet	1090	1090
3	Radiator Inlet	493	526
4	Radiator Outlet	340	365
5	Compressor Inlet	350	374
6	H.P. Recuperator Inlet	462	494
7	Heat Source Inlet	1067	1067
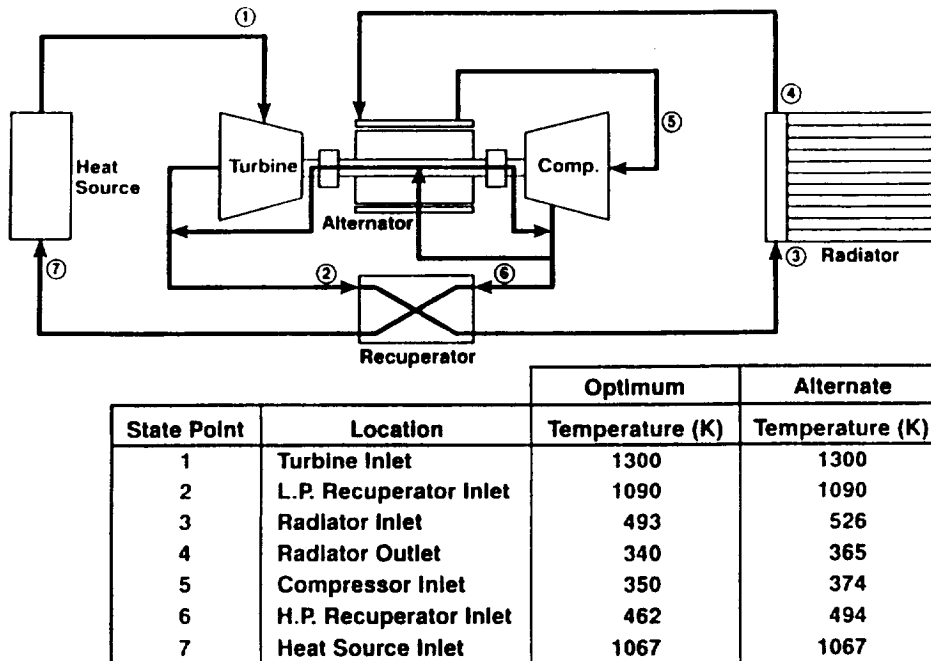
Figure 5.2-1: DIPS Cycle Diagram

TIT   Turbine Inlet Temperature
CIT   Compressor Inlet Temperature
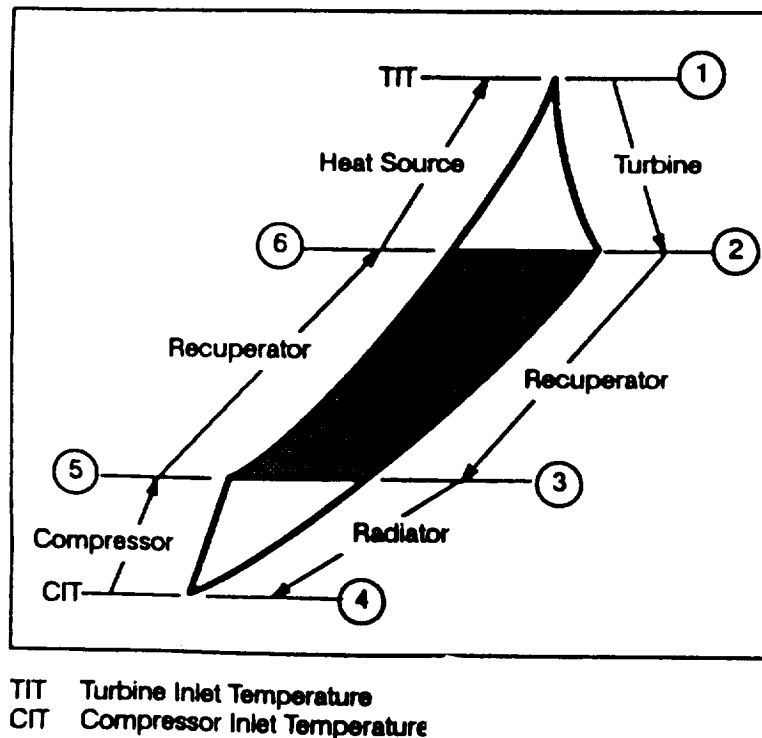
Figure 5.2-2: DIPS CBC and Entropy Cycle Diagram

Heat Source Unit

0.406 m

4.470 m

Fuel
Canister

1.829 m

Cycle
Radiator

0.457 m

Parasitic Load
Radiator

Electronics
Radiator

1.930 m

Recuperator

Power Conditioning
and Control Unit

2.286
Stowed

0.533 m
Stowed

Turbine Alternator Compressor
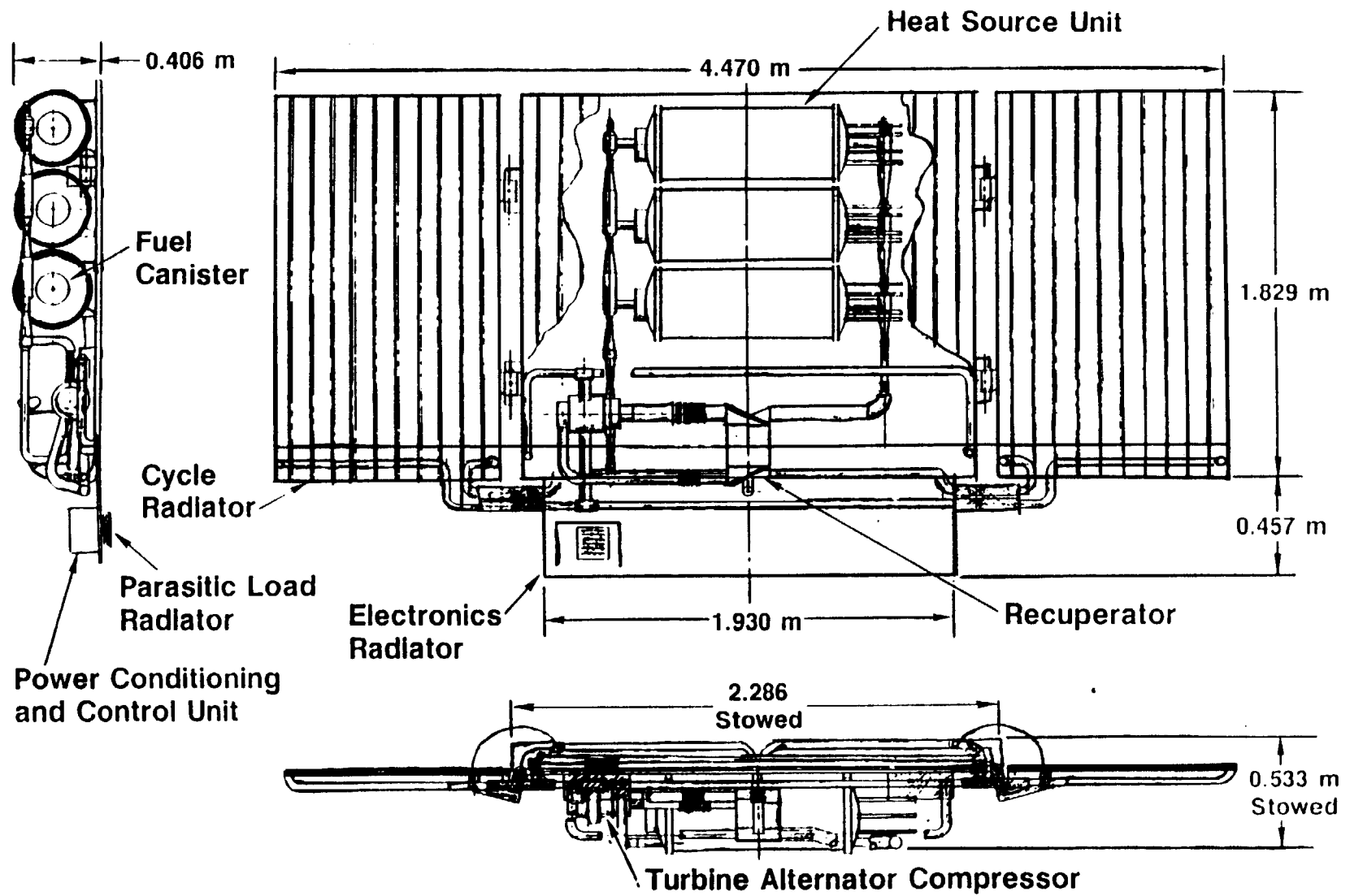
Figure 5.2-3: 2.5 KWe DIPS Power Module - Optimum Design Point

will add weight to the system and complicate installation and controlling of the array. In order to be most effective the solar array would have to have two degree freedom of motion. This would require motors to move the array, adding to the complication of the system and its assembly. Also, since the interferometer will be operating during the fourteen day lunar night, regenerative fuel cells or batteries would be needed to store the power, which would add to the mass of the system. The storage subsystem for a lunar solar power system accounts for more than 95% of the total system mass (Ref. 5.3-1). It is estimated that for a 10 kW array the total mass would be about 4200 kg (Ref. 5.3-2). This along with the fact that the lunar dust, micrometeoroids, and space radiation contribute to the reduced efficiency and output of the array makes solar power unattractive.

5.4 Trade Studies

A comparison of the three power systems is presented in the following table. Based on the available data the power system for the interferometer will be the DIPS. It has the highest energy output per unit mass (7.0 W/kg) and is compact. It involves less construction than the solar array, and less shielding than the TOPAZ II reactor. It also has relatively high reliability and a decent lifetime.

Table 5.4-1 Power System Comparison

System	Power Output (kWe)	Mass (kg)	Life Cycle (years)	Construction Intensity	Misc.
DIPS	15 7 W/kg	2142	3	moderate, may need special handling, compact	needs radiation shield
Solar	10 2.4 W/kg	4200	10	requires significant construction	dust, micro-meteoroids, radiation degrade cells
TOPAZ	12 5.7 W/kg	2122	3	compact, not much setup needed	radiation from the reactor dangerous

Table 5.4-2 Power System Quantifications

Quantification	TOPAZ	DIPS	SOLAR
Mass	2122 kg	2142 kg	4200 kg
Efficiency (BOL/EOL)	5.2/4.4	25/20	19/15
Size	3.9 m high 1.4 m dia	4.47 m x 2.3 m x 0.4 m	10 m x 10 m

5.5 Radiation and Thermal Shielding

Two primary concerns in the use of a power source employing radioactive decay as the primary heat source are radiation and thermal shielding. Since the interferometer will be operating in some areas of the infrared spectrum, the injection of thermal radiation in the vicinity of the array would corrupt the signal. The instruments are extremely sensitive and any electromagnetic radiation could damage the instrumentation. Also, because the interferometer requires periodic human servicing, radiation protection is essential. Several radiation shielding options were investigated, including digging holes, walls of lunar regolith and other structures. These are discussed in detail in the construction section.

5.6 Lunar Dust

Buildup of lunar dust on the power system radiator surface causes degradation in radiator performance. A Kapton Dome dust cover, 25 meters in diameter, will cover the critical heat transfer surfaces. The dust cover is designed for deployment with minimum astronaut involvement, and is simply inflated and back-filled with structural foam (Ref. 5.6-1).

5.7 Power Transmission

Microwave transmission was investigated as a means of transmitting power. However, the low transmitting/reception efficiency of 30% (Ref. 5.7-1) and the construction of towers at each telescope site to receive the beamed power made microwave transmission more complicated. The design of electric transmission lines for use on the lunar surface must take into account not only the cost of transportation and assembly, but also many important environmental parameters. It is very important to consider the effects the lunar environment will have on the transmission line(s) (materials, geometry, location, etc.).

The transmission lines could be suspended above, laying on, or buried beneath the lunar surface. Each option has its advantages and disadvantages.

The major lunar environment characteristics that will influence transmission line design are low gravity, vacuum, temperature, radiation, and characteristics of the soil. The fact that lunar surface gravity is one sixth that of Earth's gravity means fewer support structures are required for suspended lines. Since there is little to no atmosphere on the moon, the atmospheric pressure ranges from 10^{-6} Pa during the day to 10^{-10} Pa at night which means that vacuum insulation techniques of the lines can be used if low pressure is maintained. The temperature changes dramatically from up to 350 K during the day to as low as 100 K during the night. This extreme temperature gradient can damage the insulation as well as cause the line to expand and contract. On the lunar surface charged particles, solar cosmic rays, and galactic cosmic rays reach the surface unimpeded. This radiation could damage the insulation in the transmission lines. Finally, the soil has low thermal conductivity ranging from 10^{-5} to 10^{-4} W/cm-K which makes the cooling of buried transmission line difficult.

The insulations considered for the transmission lines are solid-dielectric or vacuum. The solid dielectric could be TFE, a fluorocarbon commonly used as an insulator because of its relatively good mechanical and physical properties. Compared to solid dielectric materials, vacuum insulation, such as in particle accelerators and electronic tubes, has a very high breakdown strength, is less affected by the thermal effects and radiation on the surface, and has a lower mass which tend to make it the better insulator. However, little work has been done to simulate the lunar environment and determine the total effect of all the environmental stresses on dielectric materials. Therefore an optimum choice cannot be made until experiments have been conducted concerning the lifetime and reliability of the insulation under lunar environment conditions.

Where the cables are placed also determines the effects the lunar environment may have on the transmission lines. If the lines are located above the surface they can be easily accessed for repair and maintenance, but are also directly exposed to the lunar environment. Dielectric materials are especially susceptible to damage at low temperatures. Therefore it may be necessary to warm above ground dielectric insulated transmission lines through load control to keep the lines at relatively constant temperature during the lunar night. To reduce the damaging effects of the environment vacuum insulation could be used for reasons stated above. The transmission lines could also be placed directly on the lunar surface. This may not be the best option because the characteristics of the soil may result in electrostatic charging of the lunar dust which might contribute to electrical breakdown. Burying the transmission lines will protect them from the lunar environment and keep them out of the way. On the other hand, the fact that the lunar soil has low thermal conductivity results in high operating temperatures for high power loss per unit length lines. Therefore buried transmission lines are only possible for small power loss per unit length lines (less than a few W/m). The requirement of equipment to bury the lines, and difficulty in accessing the lines are also significant drawbacks to burying the lines.

The materials that are considered for the conductor material are copper and aluminum. Copper provides a lower volume, lower resistivity, and good ductility. On the down side it is about twice as heavy as aluminum. The density of aluminum is about 2700 kg/m^3 while that of copper is 8900 kg/m^3. This is a major drawback of copper for space uses. Aluminum tends to be soft and difficult to connect, but its cost and mass are substantially lower than that of copper. Using aluminum transmission lines appears to be the best way

to proceed. If these lines were suspended above the lunar surface they would be exposed to thermal expansion. This means that the lines will "sag" a bit during the lunar day and contract during the lunar night. Slack must be designed into the suspension system to account for this "sagging." Using the relationship $d_T = a(dT)L$ (Ref. 5.7-2) where d_T is how much the wire elongates, a is the coefficient of thermal expansion, dT is the temperature change, and L is the length of the line the amount the line expands can be calculated. For aluminum alloy 2014-T6 (has the highest ultimate and yield strengths of the aluminum alloys) the coefficient of thermal expansion is 2.3×10^{-6} /degree C. For a temperature change of 310 degrees C and a line length of 100 meters, the line elongates only 0.0713 meters. So about 10 centimeters of slack when suspending lines during the lunar day should be sufficient to prevent tension between the supports during the night. The height of the supports depends on how high the lines need to be to be out of the way to keep from interfering with the operation of the array.

In conclusion, unless aluminum lines present too much difficulty in connection, they will be used for their reduced mass compared to copper and therefore reduced cost. The transmission lines will be laid on the surface unless there is a great need to suspend them to keep them out of the way. Laying the lines on the surface requires the least work. Plates can be laid over the cables enabling lunar vehicles to pass over them without disturbing them. Vacuum insulation should be used to obtain the best performance under the lunar environment conditions. The lines will be carrying approximately 1000 volts, requiring a line diameter of about 1 mm of aluminum wire. To connect all of the array elements and the power supply approximately 14 km of line will be needed. Power converters will also be needed to divide and regulate the power. At least one at the power source and another near the central hub of the array to divide and transmit the power to the arms of the array.

5.8 Conclusions

The lunar interferometer will require about 10 kWe power for operation. The DIPS along with conventional transmission lines is the most practical and cost effective means of achieving this power output. Since the interferometer will be deployed in three stages, the power system can be deployed in stages, which is possible due to the modular design of the DIPS. With the six DIPS systems in place if one of them goes down, the other five would provide enough power for the interferometer. The chance of two or more going down at the same time is minimal.

6.0 Structures

6.1 Telescope Structure

The LOLA telescope structure has several primary functions. These include structural stability for the optics, physical shielding from micrometeorites, dust protection, and radiation protection from the sun and the lunar surface. Several options were studied to determine the best design for these purposes. A final design was selected after a series of trade studies in mass, cost, size, and overall performance.

6.1.1 Design Options

The four designs studied are shown in Figure 6.1-1. Configurations 1 and 2 are both symmetrically supported, while configurations 3 and 4 are the same asymmetrical design, with and without a counterweight. The supporting base is the same for all four designs, and the motors and bearings are similar for each. The designs were compared on the basis of mass, size, cost, optical performance, simplicity, reliability, and stability. These considerations were weighted to show relative importance, with optical performance, stability, and mass being the most important, as compared to size, cost, and power required. For each characteristic being studied, each design was ranked from 1 to 4 (1 being worst, 4 being best). These rankings were multiplied by the appropriate weight factor and totaled to determine an overall rating for each design. The results of these comparisons are shown in Table 6.1-1, and show clearly that configuration 3, the off-axis design without the counterweight, is the optimum design based on these characteristics. However, a static analysis performed on this design revealed that the center of mass (cm) is not at the center of the support cylinder. To move the cm to the proper location, and hence create a stable structure, a counterweight must be used. Thus, configuration 4 is the LOLA design.

Table 6.1-1: Telescope Options Decision Matrix

Characteristic	Weight Factor	#1 Square Support	#2 Y Support	#3 Cantilever Support	#4 Cantilever with Counterweight
No. of Mirrors	10	1	2	4	4
Geometrical Stability	8	4	3	1	2
Mass	7	2	1	4	3
Reliability	6	3	3	4	4
No. of Components	6	1	2	4	3
Size	3	2	1	4	3
Cost	2	2	1	4	3
Power Required	1	4	3	1	2
TOTAL		94	89	145	136

Ranking: 1 <--> 4 (1 is worst, 4 is best)
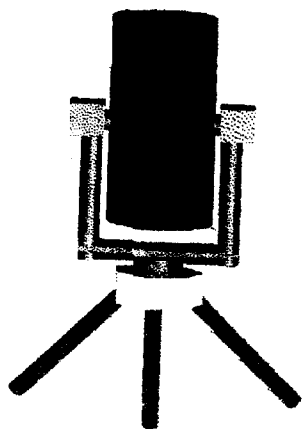
Design #1
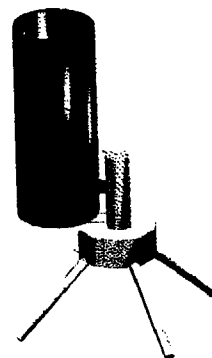
Design #2
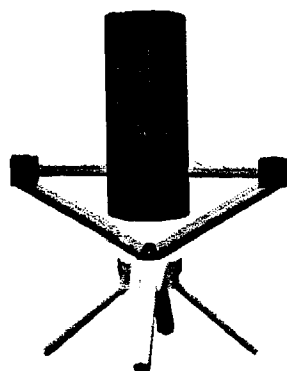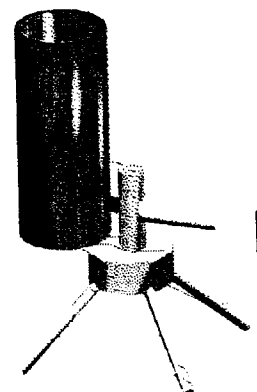
Design #3

Design #4

Figure 6.1-1: Design Options

6.1.2 Main Structure Design

The telescope structure is shown in Figure 6.1-2. The main components are the optical cylinder, cantilevered cylindrical side arm, support cylinder, counterweight, motor chamber, and base. Figure 6.1-3 shows a 2-dimensional cross-section of the side arm and support cylinder, exposing the internal mirrors, motors, gears, and bearings. Figure 6.1-4 gives a 3-dimensional color view of this cross-section.

The optical cylinder contains the primary, secondary, and fold mirrors and their supports. The side arm is surrounded by a sleeve containing the arm bearings, just as the base of the support cylinder is surrounded by a sleeve and the base bearings. The support cylinder contains the fourth mirror and support, and the arm motor to control the rotation of the side arm perpendicular to the lunar surface. Reinforced webs connected to this cylinder help support the side arm. The motor chamber contains the main motor and gears, and amplifiers for the arm and base motors. Extending out from the bottom of the motor chamber is the support for the fifth mirror. It is a rectangular piece with an open front to allow the light beam to pass out of the telescope. PZT or ceramic actuators are located behind the fifth mirror for fine positioning. The four base legs were designed to allow clearance under the telescope to account for the 30 cm of dust rising during the shift from lunar day to night, as well as extra clearance for dust rising due to micrometeorite impact.

Overall, each telescope is 5.85 m high and 4.705 m wide, with a 4.5 m base diameter. The total mass, including mirrors, motors, and bearings, is 1882 kg. Each telescope has a full range of motion about two axes (altitude and azimuth).

6.1.3 Telescope Footing

The footings of the telescope will be shaped like spudcans found on offshore jack-up drilling rigs (Fig. 6.1-5). In laboratory tests in simulated lunar soil at the University of New Mexico, the spudcan footing exhibited greater penetration than rectangular footings with the same eventual stability and stiffness (Ref. 6.1-1). Spudcan footings are usable in a variety of soils and are self-installing. This translates into minimal construction effort, a very important factor in an environment where EVA activities must necessarily be limited. Greater penetration also allows for greater lateral stability than the rectangular footing. This will be of primary importance for resisting man-made influences such as surface movements and lander take-offs, rather than for general stability since the lunar
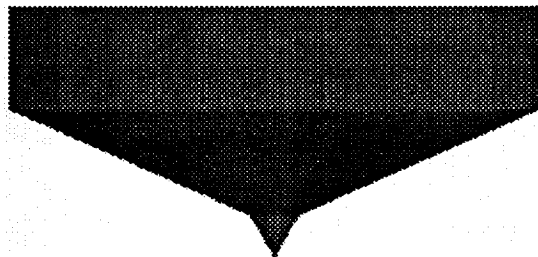
Figure 6.1-5: Spudcan Telescope Footing

TOP VIEW

Ø = 0.25

Ø = 0.04 solid
L = 0.67

90°

0.76

SIDE VIEW

ø = 1.6 , t = 0.005

ø = 0.36 , t = 0.01

ø = 0.77, t = 0.0075

ø = 0.3, t = 0.02

3.75

0.2

0.76

1.562

0.762

1.375

1.062

0.76

0.1

0.81

0.2

t = 0.015

ø = 1.5, t = 0.025

0.5

1.3

0.4

0.4

t = 0.005

Ø = 0.33,
t = 0.075

0.21

0.13

1.75

All dimensions in meters
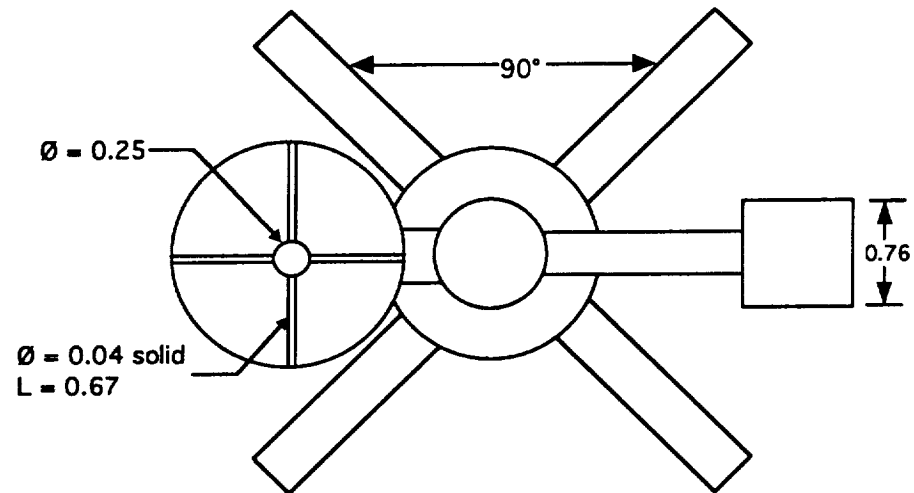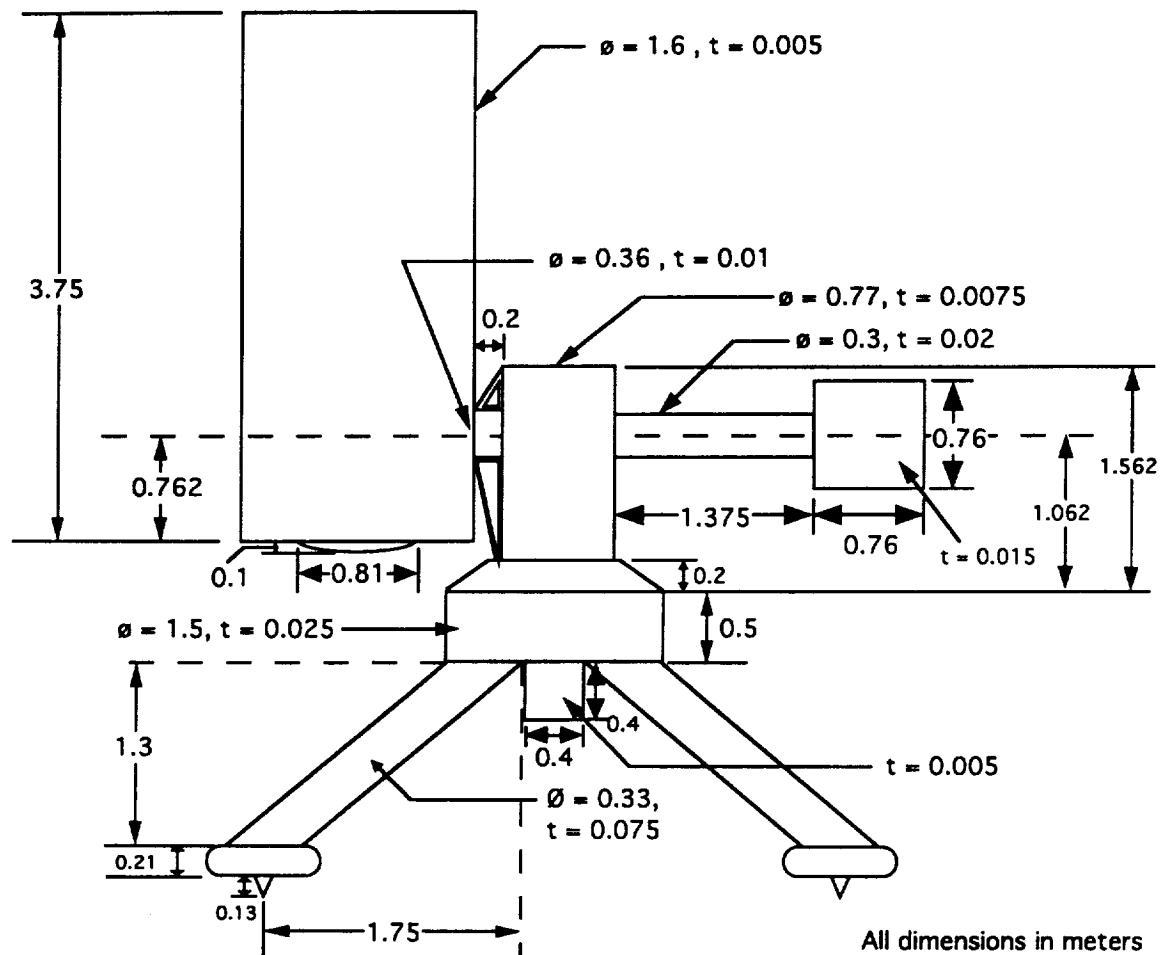
Figure 6.1-2: LOLA Telescope 2-Dimensional Views
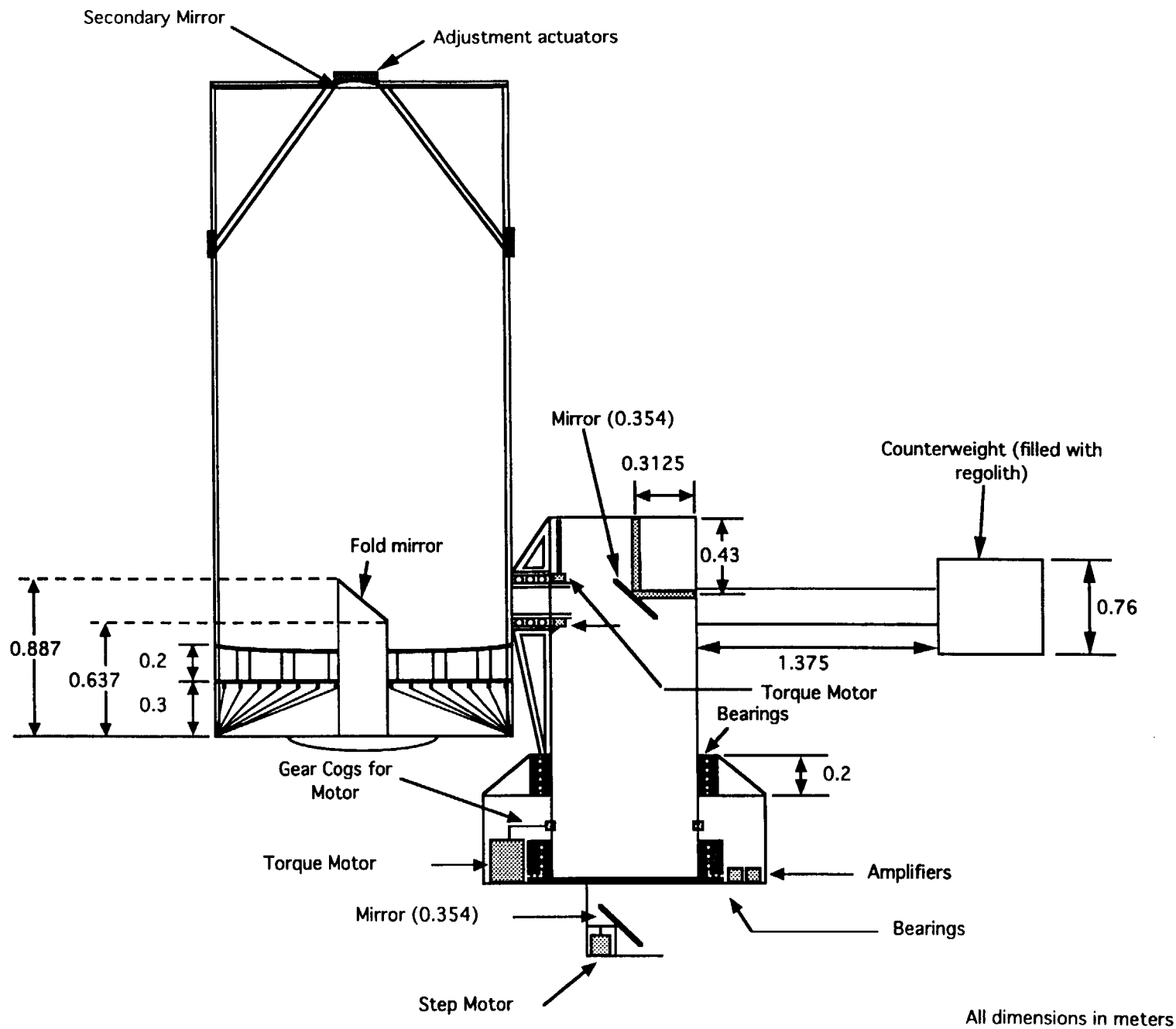
Figure 6.1-3: 2-Dimensional Cross-section

All dimensions in meters

Tertiary mirror

Primary m...

Bearings with outer sleeve

Frameless torque motor controls elevation adjustments

Mirror

Structural stiffener

Motor mount

Primary mirror supports

Zerodur metrology mirror

Bearings with outer sleeve

Torque motor controls azimuth adjustments

Amplifiers for motors

Gear cogs for motor

Bearings (bottom and sides)

Mirror

Mirror 2-axis control motor

Figure 6.1-4: 3-D Cross-section of Internal Telescope

surface itself is naturally stable. These footings are filled with lunar regolith to increase their stability, and then driven into the soil by vibratory pre-loading. The specialized installation equipment required does mean greater mass to transport to the lunar surface. However, some transport mass will be saved because the footings will be filled with regolith. Over the course of 27 telescope installations, the amount of time saved by the equipment will justify any mass trade-off.

Using the 40 kPa bearing capacity estimate of the lunar surface and a safety factor of 1.5, each telescope footing needs to be 0.216 m in diameter, assuming a flat plate footing (Ref. 6.1-2). Since the spudcan is pointed downward the exposed surface area of the true footing is greater than that of a flat plate, and therefore a smaller footing will suffice. The exact shape of the footing will be optimized for the particular lunar location and the exact size will be determined from this.

6.1.4 Motors and Bearings

Torque motors will be used for both the arm and the base rotation, because they allow for "infinite precision" positioning of the telescope. Both motors are determined by the minimum size allowable, rather than by torque requirements, since the required torque is extremely small (Table 6.1-2). This required torque was determined using the mass moments of inertia of the telescope in various positions, and the required acceleration of the motor, to yield $\tau = I\alpha$. Sample calculations are shown in Appendix 6.1-1. A frameless torque motor will be used for the arm (Ref. 6.1-3). It is shaped like a disk, to allow the shaft containing the light beam to pass through its center. This motor should weigh between 3 and 5 kg. The base motor does not need this specific shape, so it will be a general torque motor of similar size. This motor turns gears which rotate the support cylinder.

The bearings in both the arm and the base are required to be extremely rigid for stability. The arm bearings are a frequently-used commercial type. They will have to be specially sealed for use on the lunar surface. These bearings should weigh approximately

Table 6.1-2: Torque Requirements for Telescope Motors

Acceleration Requirement: 180° in 10 min., with 5 min.
  acceleration, 5 min. deceleration; alpha = 1.745E-5 rad/sec^2

Arm Motor:

Moment of Inertia of applicable members: I = 888.737 kg-m^2
Torque required: T = 0.0155 N-m

Base Motor:

Moment of Inertia of applicable members: I = 3912.838 kg-m^2
Torque required: T = 0.0683 N-m

70 kg, and must extend along the length of the 19.5 cm sleeve. Similarly, the base bearings need to extend along the length of a 20 cm sleeve, and have a 77 cm inner diameter. These bearings will have to be specially designed because of the extremely large inner diameter required.

6.1.5 Structural Analysis

Once the final design was chosen, an in-depth structural analysis was performed on the structure. Equations for critical buckling stress and bending stress, shown in Appendix 6.1-2, were taken from Gerard and Becker (Ref. 6.1-4). Equations for applied stresses are also shown in Appendix 6.1-2 (Ref. 6.1-5). For the buckling stress, a "knock-down" factor of 0.4 was used, because experiments have shown that actual structures fail before the critical stress is reached (Ref. 6.1-6). For members under both buckling and bending, a bending/buckling interaction curve was used to verify that the member would not fail (Ref. 6.1-7).

After this analysis was completed, a deformation analysis was begun on the telescope components. The cantilevered side arm and the main support cylinder, due to their geometry and unique loading, require finite element analysis and physical testing in a laboratory. This analysis was not performed due to facility limitations, but would need to be completed before deployment of the telescope. The analysis of the support rods for the secondary mirror and the legs of the structure was completed using beam theory. Equations for this are in Appendix 6.1-2 (Ref. 6.1-8). The desired tolerance was on the order of a few nanometers, but size and weight restrictions on these components caused this tolerance to be relaxed. Results of these analyses yielded deformations of 91.4 μm in the legs, and 5.964 μm in the support rods. Both deformations are acceptable, however, because the array calibration will be performed after deformation has occurred.

6.1.6 Materials Analysis

All structural elements, except for the mirrors, are constructed of a boron/epoxy laminate, $| O_2 / \pm 45 |$. For each main layer of this laminate, the top two sublayers run in the x direction, the third is at a 45° angle, and the fourth is at a -45° angle. As found in Agrowel (Ref 6.1-9), the density of this laminate is 1.49 x 10^3 kg/m^3, and the coefficient of thermal expansion is -0.36 x 10^{-6} /K (Ref. 6.1-9). This implies minimal shrinkage, rather than expansion, of the material during periods of extreme temperature exposure.

Boron/epoxy was chosen because of its high strength and low density in comparison to other common space-usage materials. Table 6.1-3 shows a rating of various materials, taken from Nicolai (Ref. 6.1-10). For the purposes of the LOLA telescopes, boron/epoxy and graphite/epoxy ranked the highest (where H represented the highest rating). Boron/epoxy, though more expensive than graphite/epoxy, was selected because of the outgassing difficulties associated with graphite/epoxy on the lunar surface (Ref. 6.1-11). In reference to the higher costs of the composites as compared to other materials, the decreased weight, and therefore launch costs, counter the increased price. Figure 6.1-6, taken from Reference 6.1-12, supports the choice of boron/epoxy based on strength, thermal expansion, and weight.

Metal matrix materials have the potential of providing extremely lightweight components exhibiting very high strength, stiffness and wear resistance with improved elevated thermal properties. Achieving this potential is currently restricted due to the limited understanding of the design and manufacturing techniques required for metal matrix

Table 6.1-3: Telescope Materials Ranking

Material	Weight	Specific Strength	Specific Stiffness	Temp. Limit	Corrosion Resistance	Fatigue Resistance	Repair-ability	Fabric-ability	Material Cost
Al alloys	M	M	M	L	L	M	H	H	H
Steel alloys	L	M	M	H	M	H	M	M	H
Ti alloys	M	M	M	H	M	M	L	L	M
E-Glass/Ep	H	M	L	L	H	H	H	H	H
S-Glass/Ep	H	H	L	L	H	H	H	H	M
Boron/Ep	H	H	H	L	H	H	H	H	L
Graphite/Ep	H	H	H	L	H	H	H	H	L
Boron/Al	M	M	H	M	L	M	M	L	L
Boron/PI	H	H	H	M	H	H	M	M	L
ABS	H	L	L	L	M	M	M	H	H

The rankings are all relative to the other material systems, and are as follows: H - high, M - medium, L - low.

material fabrication; however, this area is a prime candidate for future technological development and should be reviewed before array construction (Ref 6.1-13).

6.2 Primary Mirror Structural Analysis

6.2.1 General Specifications

The primary mirror has a 1.5 m aperture with a 25 cm central hole diameter to allow for a shaft to support the fold mirror. The focal length will be 3.692 m, and the mirror is parabolically shaped. The shape is described by the equation $h^2 = 2rz$, where $r = 7.384$. "H" is the distance from the optical axis and "z" is the height above the axis. Surface finish requirements have been set to $\lambda/100$. The mirror is a honeycomb support type made of Schott Glasswork's Zerodur glass material. The mirror mass is 197.21 kg. Boron/epoxy supports are required underneath the mirror to reduce possible deflections. The supports weigh approximately 20 kg. Structural calculations have been made using a circular-annular method and maximum deflection of the mirror due to self-weight on the moon has been calculated at or below 3 nm dependent upon radial location. Mass calculations and deformation calculations are given in Appendix 6.2.

6.2.2 Mirror Material

Several materials were considered for construction of the primary mirror. The three materials used most often in the optics industry are borosilicate glasses, Corning's U.L.E. glass, and Schott Glasswork's Zerodur glass. The material properties for these glasses are given in Table 6.2-1 (Ref. 6.2-1). The most important property in an optical mirror material for this moon-based application is a small coefficient of thermal expansion (CTE). This parameter predicts linear expansion due to temperature gradients. Because the telescopes will operate on the moon, where there is a considerable temperature gradient between lunar night and day, a very low CTE is required. Another important parameter
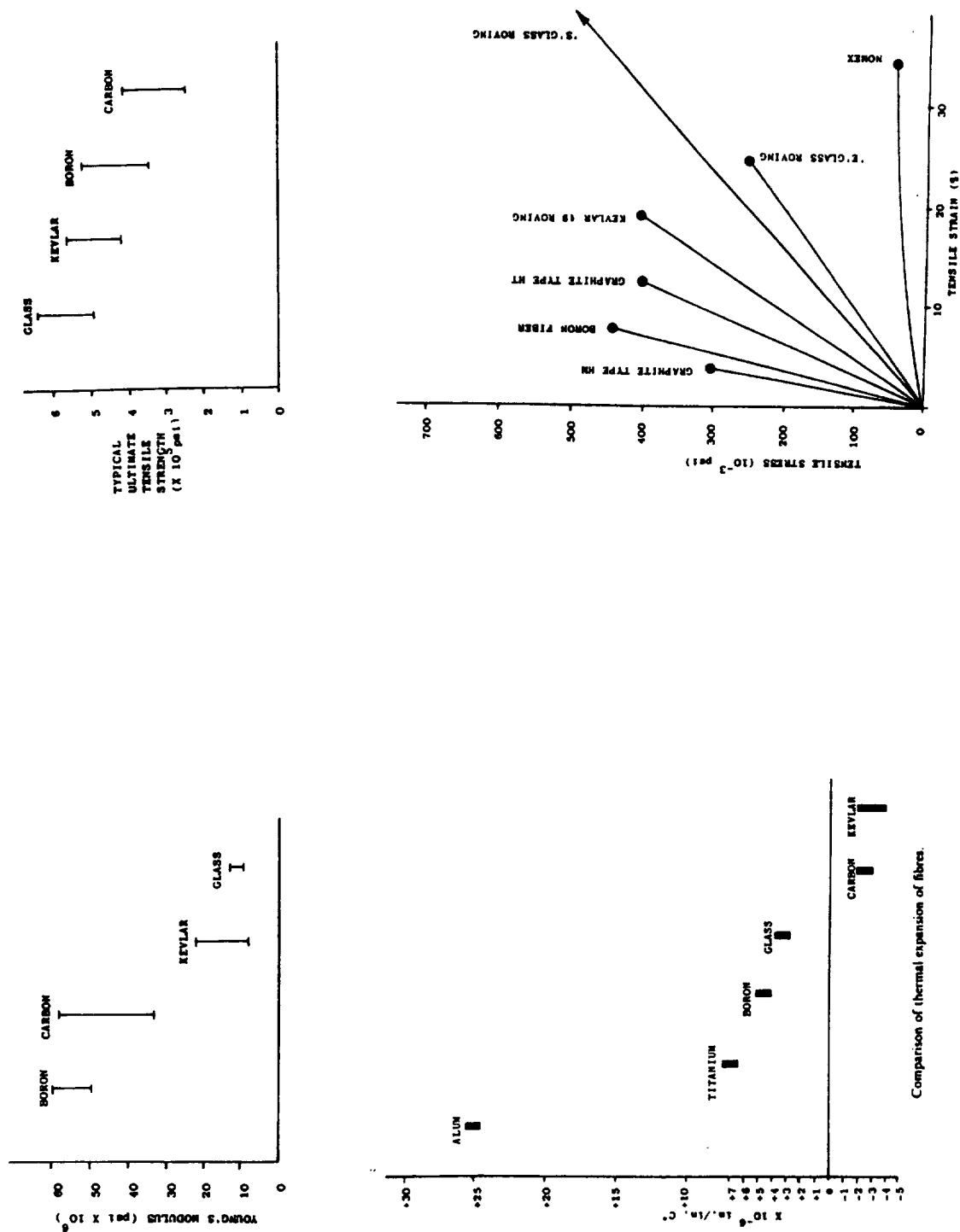
Figure 6.1-6: Graphical Comparison of Telescope Materials

in the selection of mirror material is Young's Modulus, which is directly related to the stiffness of the material. Because the acceptable permanent deformation of the mirror under its own weight is only in the nanometer range, a high modulus of elasticity is required. Schott Glasswork's Zerodur was chosen over borosilicates and U.L.E. primarily because of the low CTE and high modulus of elasticity. One of the main advantages of Zerodur is the near-zero CTE that is attainable by controlled thermal treatment. Zerodur is a two phase glass ceramic with negative CTE for the crystal phase and positive CTE for the residual glass phase. Controlled thermal treatment can adjust the phase mixture of the material and therefore adjust the CTE (Ref. 6.2-2). The only real disadvantage of Zerodur is the higher density. This high density can be countered by the low-mass honeycomb construction technique discussed in the following section.

6.2.3 Mirror Types and Fabrication Techniques

Three main methods of primary mirror fabrication exist today. The areal weight density (W/A) is the most important parameter to consider when choosing a mirror construction type. Estimations of the areal weight density for each of the fabrication techniques are given assuming Zerodur as the chosen material and a 1.5 m aperture length.

Segmented mirrors are small and easier to build and support than a one-piece mirror, but they also introduce complexity to the fabrication. They must be ground to a very specific shape and must be aligned precisely with the other segments. This requires motorized controllers that add much weight to the overall system. A 1.5 m diameter mirror would typically be divided into 25-30 cm hexagonal point-to-point segments with thickness of approximately 5 cm for this application. The areal weight density for this technique is estimated to be 126.5 kg/m². The motorized actuators would add substantial weight to the mirror system.

Another type of mirror is the thin-meniscus mirror. This mirror is one piece of

Table 6.2-1: Mirror Material Properties

MATERIAL	CTE x 10^6 (K^-1)	DENSITY (kg/m³)	YOUNG'S MODULUS x 10³ (N/mm²)	POISSON'S RATIO	THERMAL CONDUCTIVITY (W/mK)	SPECIFIC HEAT (Ws/kgK)
BOROSILICATE GLASS	3.0	2350	68	0.20	1.13	1047
CORNING U.L.E.	0.03±0.06	2200	66	0.17	1.31	770
SCHOTT ZERODUR	-0.03±0.05	2530	91	0.24	1.60	821

constant thickness. The mirror is so thin that it cannot support its own weight, therefore mechanical actuators are required to bend the structure to its correct shape. While this option provides the most active control over mirror shape in case any corrections are needed, it is also the heaviest and most complex option due to the large number of actuators required for axial and lateral support. Refer to section 3.9, Image Reconstruction, for mirror piston and tilt error information. For our application, a thin meniscus thickness estimate is 2-3 cm. The areal weight density in this case is estimated to be 63.3 kg/m^2. Again, substantial actuator weight must be added into this estimate.

The third type of mirror fabrication and the one that has been chosen for this design is the honeycomb structure. The honeycomb mirror is the lightest available because the whole structure is about 75% air due to the hollow hexagonal honeycomb support structure. This type of structure utilizes a technique called "spin casting" which involves pouring molten glass into a circular mold inside a large spinning oven. The structure is comprised of two thin layers of mirror substrate with glass honeycomb supports sandwiched between. The honeycomb structure within the mirror blank is formed by hexagonal blocks that are attached to the bottom of the mirror mold. The blocks are pre-shaped to the desired mirror curvature. The mold is filled with liquid molten glass to a level above the blocks to form the top surface. Because the hexagonal blocks are pre-shaped to the desired mirror curvature, much less grinding is required for the final outcome. For example, scientists from the University of Arizona Steward Observatory spin-casted a honeycomb mirror of 1.8 m diameter. The amount of glass removed through grinding and polishing in this case was about 120 kg. If the mirror had been fabricated out of a conventional flat solid mirror blank, 15 to 28 metric tons of glass would require removal (Ref. 6.2-3). Once the mold is filled it is placed in a glass furnace mounted on a rotating platform so the free surface can be spun to the required curvature. The surface of the mirror is paraboloidal with focal length dependent upon the angular velocity of the rotating platform. Spin-casting furnaces are in existence today for mirrors with apertures up to 8 m, so a 1.5 m diameter mirror can be easily accommodated within current technology. Actuator support is not likely to be needed for this structure because the increased thickness of the honeycomb results in smaller deflections (Refer to section 3.9). A honeycomb mirror for the LOLA application will have top and bottom substrates of 1-3 cm with a honeycomb thickness of 15-20 cm. The areal weight density for a Zerodur 1.5 m honeycomb mirror is 27.6 kg/m^2. Because this mirror type does not require additional actuator support, the areal weight density is clearly the best for this fabrication technique.

6.2.4 Mirror Coating

Because the function of the primary mirror is to reflect light, a reflective mirror coating is required. The Zerodur by itself would act as a high quality lens, as the material has a high transmissivity. For this reason, a thin metallic reflector film must be applied to the highly polished Zerodur substrate. A graph of reflectance versus light wavelength is given in Figure 6.2-1 for several reflector coatings (Ref. 6.2-4). The gold and silver dielectric overcoat films give the best reflectance in IR range. The exorbitant cost of gold films removed them from comparison, and resulted in analysis of only silver and aluminum coatings. The performance of silver and aluminum for this application at the required resolution were plotted against each other and were presented in section 2.1. On the basis of percent loss in the system (assuming the same coating is used for every mirror in the

Figure 6.2-1: Coating Reflectance vs. Wavelength

system), a silver dielectric coating was chosen as the reflector film. Silver has an average of 98-99% reflectivity beyond 500 nm (Ref. 6.2-4).

6.2.5 Mirror Dimensions

A schematic with dimensions for the mirror is given in Figure 6.2-2. The mirror diameter is 1.5 m and the center hole is of 25 cm diameter. The basic honeycomb structure is depicted in both top and side views. The overall thickness of the mirror at the outermost diameter is 20 cm. This thickness was chosen based on decreased deflection discussed in section 6.2.7. The maximum sagitta at the center of the mirror is approximately 3.8 cm as determined by the paraboloidal mirror equation given in section 6.2.1. The thickness of both the top and bottom substrates is 2.0 cm each.

The honeycomb supports comprise the rest of the thickness, which means the outermost supports are 16.0 cm long and decrease in length (by approximately 3.8 cm) from the outer edge to the center of the mirror. The hexagonal support dimensions were designed with the central hole in mind. The side dimension is 15.25 cm which means the top to bottom dimension is 26.42 cm, and the side to side and diagonal dimensions are 30.5 cm.

The boron/epoxy mirror support structure is shown in Figure 6.2-3. Supports were deemed necessary due to the maximum deflection calculations performed and discussed in the next section. The supports will rest at the bottom of the optical housing cylinder. The supports are all circular and are a total of 30 cm high. Concentric circular rings 1.0 cm thick are placed at the following radii stemming from the inner central hole: 0.1250 m, 0.2292 m, 0.3333 m, 0.4375 m, 0.5417 m, 0.6458 m, and 0.7500 m. Cone-like boron/epoxy supports extend from these rings to the outer structural ring as depicted in Figure 6.2-3. These supports are braced at the outer rim for increased structural support. The thickness of these supports is 2.0 mm. The circular nature of these supports allows for storage space at the bottom of the optical housing cylinder for future applications.

CENTER HOLE
DIAMETER = 0.25m

TOP VIEW

HEXAGON SIDE
LENGTH = 0.1525m

HEXAGON SIDE
THICKNESS = 0.02m

OUTER RIM SUPPORT
THICKNESS = 0.03m

1.5 m

SIDE VIEW

TOP SUBSTRATE
THICKNESS = 0.02m

OUTER RIM SUPPORT
THICKNESS = 0.03m

HONEYCOMB
HEIGHT = 0.16m

HONEYCOMB SUPPORT
THICKNESS = 0.02m

BOTTOM SUBSTRATE
THICKNESS = 0.02m

HEXAGONAL SUPPORT DIMENSIONS:

0.1525m

$X = 0.1525 \; SIN(30°) = 0.07625m$

$Y = 0.1525 \; COS(30°) = 0.1321m$

$DIAGONAL = SQRT\{[(0.1321)(2)]^2 + [0.1525]^2\} = 0.305m$

$TOP-BOTTOM = 2Y = 0.2642m$

$SIDE-SIDE = 2X + 0.1525 = 0.305m$

Figure 6.2-2: Mirror Dimensions

BOTTOM VIEW

$r_1 = 0.1250m$
$r_2 = 0.2292m$
$r_3 = 0.3333m$
$r_4 = 0.4375m$
$r_5 = 0.5417m$
$r_6 = 0.6458m$
$r_7 = 0.7500m$

1.5 m

SIDE VIEW

(CUTAWAY AT d=1.5m)

SUBSTRATE
THICKNESS = 0.02m

SUPPORT RING
THICKNESS = 0.01m

SUPPORT THICKNESS =
0.002m

0.2m

0.3m

Figure 6.2-3: Boron/Epoxy Mirror Support Structure

6.2.6 Mirror Weight Calculations

Structural weight calculations have been made and are included in the sample calculations of Appendix 6.2. The mirror mass was calculated in two parts: the upper 3.8 cm of curvature, and the remaining 16.2 cm of circular cylinder. For the curved portion, a volume of revolution was used to determine the upper volume. For the cylindrical portion, the two substrate thicknesses were added to the support height to account for the overall height. The weight estimation technique used is to find the weight of a solid mirror with these dimensions and then subtract 75% of this weight due to the fact that honeycomb mirrors are roughly three-fourths air (Ref. 6.2-5). The weight for the mirror using this estimation technique is 197.21 kg. The weight of the boron/epoxy support structure, as shown in the sample calculations, is 19.62 kg. Total weight of the mirror and support structure is then 237.89 kg.

6.2.7 Maximum Deflection

Maximum deflection calculations for the primary mirror due to self-weight were performed using the circular-annular equations for a flat circular plate simply supported on the outer rim and simply guided on the inner ring (Ref. 6.2-6). The equations used for this analysis are given in Appendix 6.2. Simple guidance was the boundary condition chosen due to the 25 cm diameter fold mirror support placed in the center hole. These equations take into account the thickness of the substrate and honeycomb added together. The thickness of the honeycomb support layer had to increase substantially in order to achieve acceptable inelastic deformation. Results of these calculations are given in Tables 6.2-2, -3, and -4 for three different gravity load scenarios. Symbols used in the table are explained with the illustration and equations given in Appendix 6.2. Table 6.2-2 gives calculations of deflections due to the moon's gravity field. Maximum deflection in this case is approximately 3.0 nm. Table 6.2-3 gives calculations of deflections with a pull of 3 g's. This number was chosen to simulate the launch load of a manned vehicle such as the space shuttle. Table 6.2-4 gives calculations of deflections due to a pull of 6 g's. This number simulates the launch load of an expendable launch vehicle. These load estimations were confirmed by Kennedy Space Center's public information department. As can be seen in the tables, the deflections under these loads are substantially more than those under lunar gravity, the maximum being 0.01 micrometers for the outermost section of mirror. Design engineers at Schott Glassworks have not been able to identify the exact elastic range of Zerodur, but mirrors and other parts made of Zerodur have been launched for many other applications, and no permanent deformation has occurred upon launch conditions. Specific examples include NASA's spaceborne x-ray telescope AXAF, Germany's spaceborne x-ray telescope ROSAT, and laser gyroscopes which guide the navigation of the expendable launch vehicle ARIANNE (Ref. 6.2-7).

6.2.8 Testing of the Primary Mirror

For the primary mirror to achieve the required $\lambda/100$ surface finish, many hours of polishing and grinding are involved. This finishing process will be guided by a null-corrector test. A schematic of the null-correction technique can be found in Figure 6.2-4 (Ref. 6.2-8). The object of this test is to compare the differences between the actual shape

Table 6.2-2: Primary Mirror Deflections due to the Moon's Gravity

a (m)	b (m)	r0 (m)	Volume (m³)	mass (kg)	q (kg/m²)	D (Nm)	C2	L17	C3	L11	y (m)
0.75	0.125	0.6458	0.087667	55.44958	198.4153	64374646	0.218170	0.008872	0.630556	0.0000146	-3E-09
0.6458	0.125	0.5417	0.071647	45.31674	190.7841	64374646	0.209872	0.011777	0.634237	0.0000262	-2E-09
0.5417	0.125	0.4375	0.057152	36.14886	184.3841	64374646	0.197647	0.016440	0.640234	0.0000524	-1.2E-09
0.4375	0.125	0.3333	0.043727	27.65726	179.2122	64374646	0.178459	0.024460	0.651020	0.0001200	-6.7E-10
0.3333	0.125	0.2292	0.031179	19.72066	175.2734	64374646	0.145865	0.040008	0.673448	0.0003420	-2.8E-10
0.2292	0.125	0.125	0.019348	12.23779	172.5658	64374646	0.085477	0.076442	0.733025	0.0014100	-5.6E-11

Table 6.2-3: Primary Mirror Deflections due to Shuttle Launch

a (m)	b (m)	r0 (m)	Volume (m³)	mass (kg)	q (kg/m²)	D (Nm)	C2	L17	C3	L11	y (m)
0.75	0.125	0.6458	0.087667	55.44958	3571.476	64374646	0.218170	0.008872	0.630556	0.0000146	-5.4E-08
0.6458	0.125	0.5417	0.071647	45.31674	3434.114	64374646	0.209872	0.011777	0.634237	0.0000262	-3.6E-08
0.5417	0.125	0.4375	0.057152	36.14886	3318.913	64374646	0.197647	0.016440	0.640234	0.0000524	-2.2E-08
0.4375	0.125	0.3333	0.043727	27.65726	3225.819	64374646	0.178459	0.024460	0.651020	0.0001200	-1.2E-08
0.3333	0.125	0.2292	0.031179	19.72066	3154.921	64374646	0.145865	0.040008	0.673448	0.0003420	-5E-09
0.2292	0.125	0.125	0.019348	12.23779	3106.184	64374646	0.085477	0.076442	0.733025	0.0014100	-1E-09

Table 6.2-4: Primary Mirror Deflections due to an Expendable Launch Vehicle

a (m)	b (m)	r0 (m)	Volume (m³)	mass (kg)	q (kg/m²)	D (Nm)	C2	L17	C3	L11	y (m)
0.75	0.125	0.6458	0.087667	55.44958	7142.952	64374646	0.218170	0.008872	0.630556	0.0000146	-1.1E-07
0.6458	0.125	0.5417	0.071647	45.31674	6868.228	64374646	0.209872	0.011777	0.634237	0.0000262	-7.2E-08
0.5417	0.125	0.4375	0.057152	36.14886	6637.827	64374646	0.197647	0.016440	0.640234	0.0000524	-4.5E-08
0.4375	0.125	0.3333	0.043727	27.65726	6451.639	64374646	0.178459	0.024460	0.651020	0.0001200	-2.4E-08
0.3333	0.125	0.2292	0.031179	19.72066	6309.842	64374646	0.145865	0.040008	0.673448	0.0003420	-1E-08
0.2292	0.125	0.125	0.019348	12.23779	6212.369	64374646	0.085477	0.076442	0.733025	0.0014100	-2E-09

of the mirror during testing and the desired shape. The null corrector is made up of a lens and two curved mirrors and must be specifically designed for the LOLA primary mirror. As is shown in Figure 6.2-4, light beams reflected from a flat reference mirror are brought together with light reflected from the LOLA primary mirror. The light waves in the beams then form an optical interference pattern. This interference pattern is photographed and analyzed to determine differences in desired and actual shape. It is important that the null corrector be set up properly as slight errors in the corrector will lead to sizeable errors in the final curvature of the primary mirror.
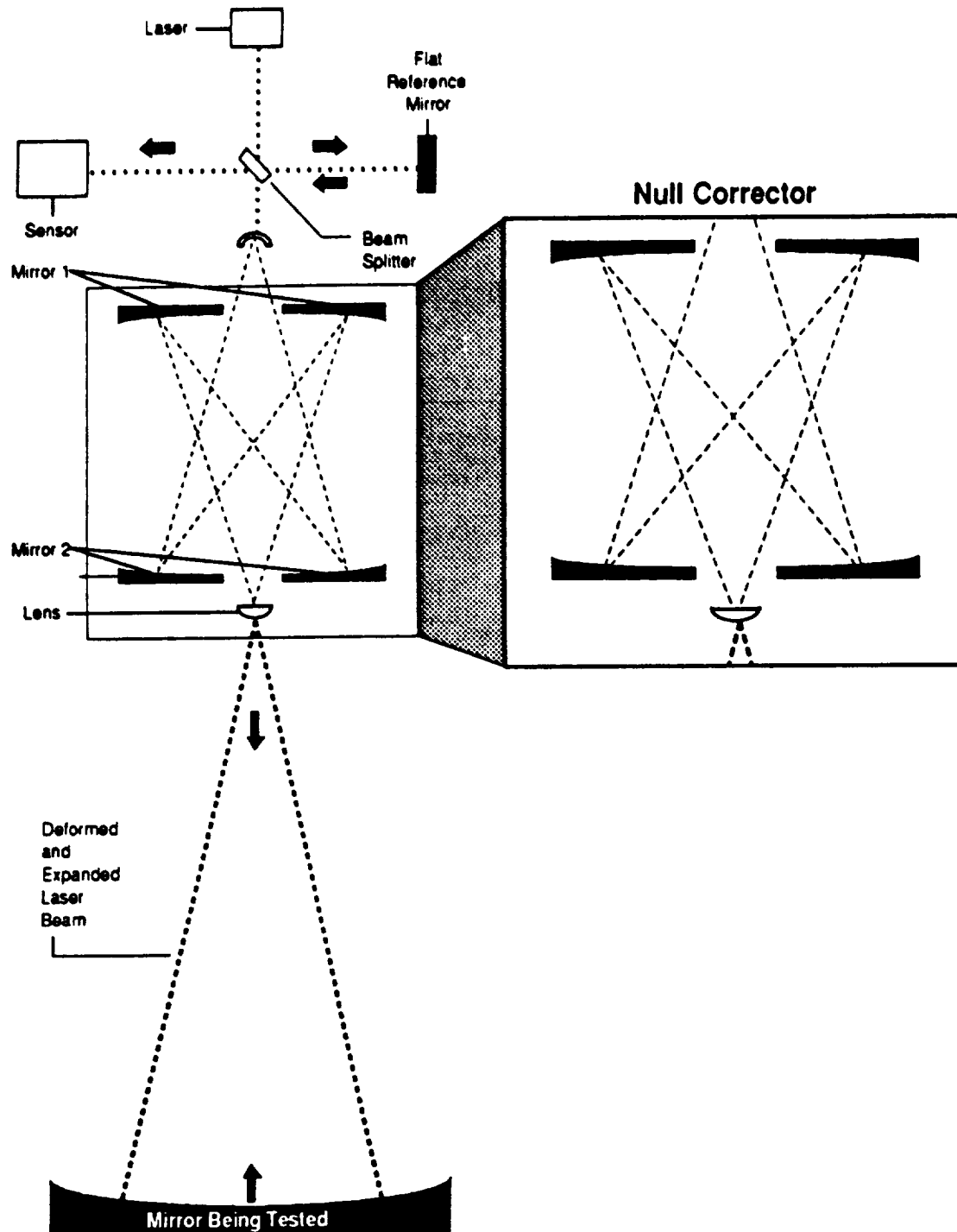
Figure 6.2-4: Null Correction Techniques

7.0 Thermal Analysis and Control

Temperatures in the equatorial region of the lunar surface range from 400 to 90 K during the lunar day-night cycle. If the structures on the surface are unprotected, their temperature versus time histories roughly correspond to that of the lunar surface. However, if the structures are covered by some form of thermal shield, the temperature variations experienced by the structure can be minimized.

At the time of lunar sunset, the surface temperature is approximately 150 K and exponentially decays to 90 K during the lunar night (Ref. 7.0-1). As shown previously in Figure 3.7-3, in order to detect IR signals at wavelengths up to 10 micrometers, all elements in the optical path must be maintained at a temperature of 77 K or below. Without either passive or active thermal control, this temperature cannot be reached during the lunar night.

7.1 Thermal Analysis

The thermal analysis model of the telescope structure has three main components: conductive heat transfer from the regolith to the telescope support legs, radiative heat transfer from the regolith to the telescope, and radiative heat transfer from the telescope to free space. The free space radiation levels correspond to a temperature of 3 to 4 K.

In the Large Lunar Telescope study (Ref. 7.0-1), it was estimated that 98 percent of the radiative heat transfer from the regolith to the structure occurred within a 100 m radius of the telescope. This relationship is utilized in the heat transfer analysis for the LOLA telescope and is detailed in Appendix 7.1-1.

To provide passive cooling during the lunar night each telescope is wrapped in 0.13 mm thick aluminized Teflon multilayer insulation (MLI). This material has an emissivity of 0.64 and an absorptivity of 0.125 (Ref. 7.1-1). Additional passive cooling is provided through the use of a 30 layer, 5mm thick MLI surface radiation shield which surrounds the base of the telescope with an outer radius of 7 m and an inner radius of 1 m.

A thermal analysis of the telescope structure was conducted for the lunar night. This analysis includes calculations for heat transfer to the telescope both with and without a surface shield. Details of this analysis are listed in Appendix 7.1-2. In addition to the telescope thermal analysis, heat transfer calculations were carried out for the long delay line mirrors. The same basic model was used in this analysis, with the substitution of the emissivity and absorptivity coefficients for the mirror material used in place of MLI coefficients.

7.2 Telescope Shielding

To provide thermal protection for each of the telescopes, a collapsible, hemispherical dome will be deployed around each during the lunar day. The dome has a radius of 7 m, which corresponds to a surface area of approximately 300 m². Figure 7.2-1 shows a conceptual design for the enclosure and its deployment. It is collapsible to a height of less than 30 cm, as the shielding material and frame folds upon itself. The shielding material is aluminized Teflon MLI which provides a high emissivity and low absorptivity covering for the dome. With such an enclosure, it has been calculated that the temperature of the protected telescope can be maintained at approximately 120 K during the lunar day (Ref. 7.0-1). In addition to providing thermal shielding, the dome also protects the telescope

from dust contamination and provides limited protection from micrometeoroid impacts.

Figure 7.2-2 shows the temperature versus time history of the telescope during the first five Earth-days of the lunar night. The telescope with the surface shield reaches the 77 K temperature cutoff at approximately 24 hours while the telescope without the surface shield reaches the cutoff at approximately 30 hours. The same general trend is shown in Figure 7.2-3 for the delay mirror temperatures. However, because the mirrors will not be covered during the lunar day, their temperature is approximately 150 K at lunar sunset. With an MLI surface radiation shield, the mirrors require approximately 30 hours to reach 77 K, whereas mirrors without a surface shield require approximately 36 hours to reach the same temperature.

Although the time differences in both cases are small, the usefulness of the lunar telescope array is largely based on the long integration times needed for faint object detection in optical and IR wavelengths. Because of the relative low cost and low mass of the aluminized Teflon MLI (Ref. 7.1-1), the surface shielding should be used around both the telescopes and the long delay mirror structures.

Thermal analysis calculations for the telescope and the mirror structures were extrapolated to include all buildings on the lunar surface which house elements of the optical path. Thus, the exteriors of all surface buildings are covered with aluminized Teflon MLI, and adequate thermal shielding from regolith radiation is provided under and around each optical path structure.

7.3 Instrumentation Thermal Requirements

The temperatures of all elements in the optical path must be below 77 K so that the IR Imager/Spectrometer and the nulling IR imager can detect infrared radiation in the 1000 to 10,000 nm spectrum. However, the CCD detectors in the remaining three instruments require cooling only to 300 K. For this reason, two types of thermal control systems are utilized. An active system is employed to cool the IR Imager/Spectrometer and nulling IR imager, while passive systems are used on the other instruments.

The active system is modeled after the cryogenic cooling techniques applied on the Space Infrared Telescope Facility (SIRTF). In this system the CCD is mounted on a liquid helium dewar which absorbs heat through the wall interface between the CCD and the fluid (Fig. 7.3-1). Once it is heated, the warmed liquid helium is vented to space. For SIRTF, the thermal control system has a lifetime of 2.8 years and uses 550 kg of liquid helium (Ref. 7.3-1). However, for applications to the LOLA instrumentation, the lifetime of this liquid helium system would depend on length of time the IR Imager/Spectrometer and nulling IR imager are operated under full power.

An alternative to the SIRTF thermal control system is a closed loop mechanical system studied for use with the Large Lunar Telescope (Ref. 7.3-2). This system does not require periodic helium replenishment, but is more massive than the SIRTF system.

The other three instruments are designed for imaging wavelengths up to 1000 nm and therefore do not require active cooling. However, the temperatures must be maintained at or below 300 K. The CCD electronics and the data acquisition electronics produce approximately 135 to 190 W of waste heat. To provide cooling for these instruments, a passive heat pipe thermal control system is employed (Ref. 7.3-3). Because the floor of the instrumentation room is held at a constant temperature of 250 K by the lunar regolith, the heat pipes can utilize the regolith as a heat sink.

Aluminum foil shielding

Rails:
Tubular shell ribs slide
inside the rails

Motor:
Motor pulls ribs up
on the rails

Tubular ribs
0.05 m diameter
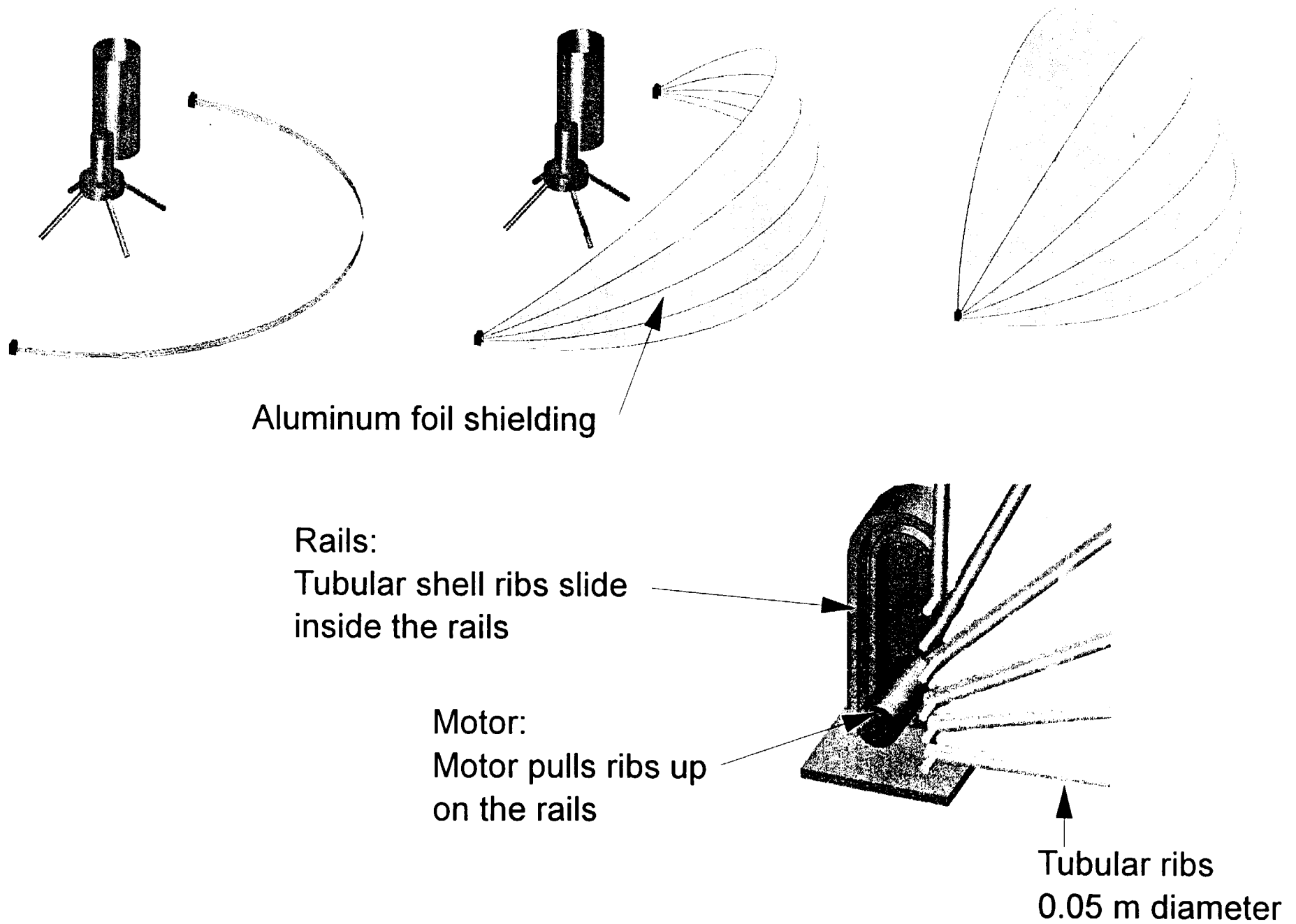
Figure 7.2-1: Telescope Protective Enclosure
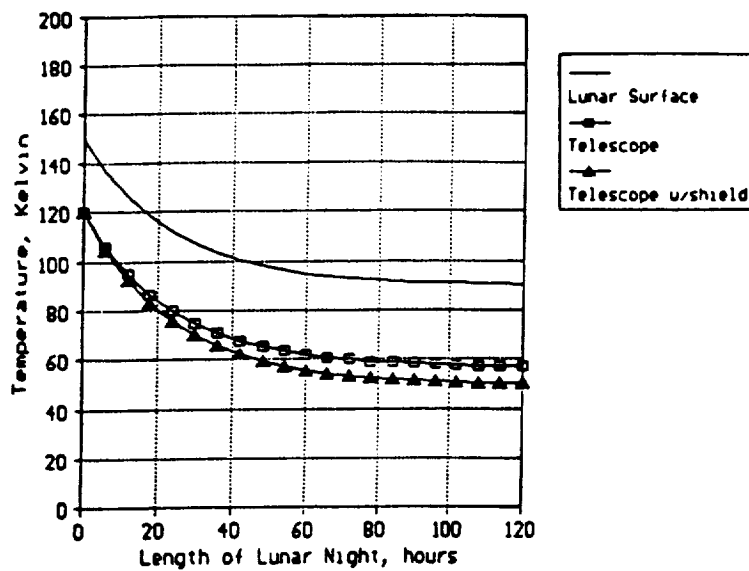
Telescope surface temperature during the first
five Earth days of lunar night. The telescope is
covered with aluminized Teflon MLI. The MLI
surface shield has an inner radius of 1 m and
an outer radius of 7 m.

Figure 7.2-2: Telescope Surface Temperature
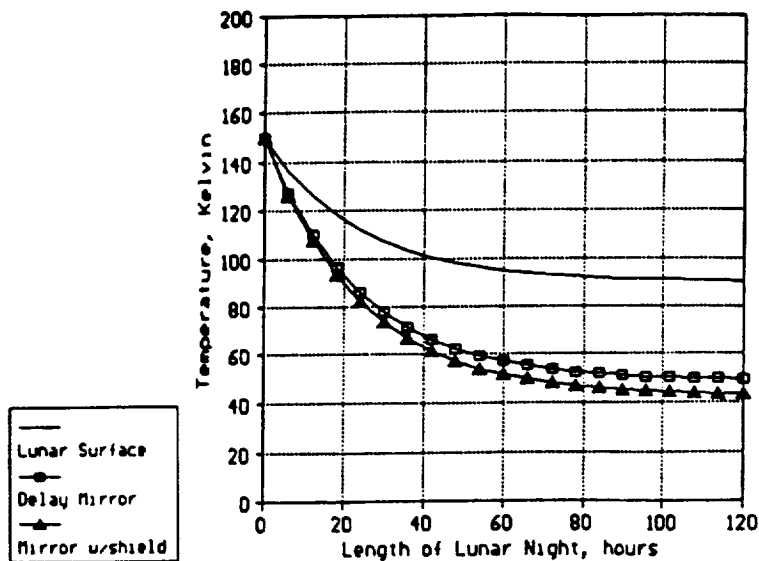
Long delay mirror temperature during the first
five Earth days of lunar night. The aluminized
Teflon MLI surface shield has a radius of 7 m.

Figure 7.2-3: Long Delay Mirror Temperature

8.0 Launch

The total weight to orbit required for the LOLA project is 253.0 mt (Fig. 8.0-1). The weights of the Lunar Transfer Vehicle (LTV), Lunar Excursion Vehicle (LEV), and fuel tanks are included in this estimate and are established following much the same guidelines as the Large Lunar Telescope (Ref. 8.0-1). It takes 12 kilograms of transfer components such as the fuel and the LTV in LEO to establish one kilogram of payload such as the cargo and the LEV on the lunar surface.

There are many options for cargo transfer to the lunar surface. All of these include the initial launching of the cargo modules from Earth; however, they differ as to the means of LEO to lunar surface transfer. Some of the options include:

- Launch of the entire LEV/LTV/cargo system directly to the lunar surface.
- Launch of only the cargo modules that are then coupled with an LTV/LEV in LEO and transferred to the lunar surface.
- Launch of only the cargo modules that are then coupled with an LTV in LEO and transferred to an LEV in Low Lunar Orbit (LLO) for landing of the lunar surface.

There are also combinations of certain portions of the above options; launch of the LEV/cargo to connect with an LTV in LEO, etc. Option 1 is the most cost effective because it involves direct placement of cargo and reduces energy requirements (Ref. 8.0-1). But the LOLA project's cargo modules are bulky and do not exceed the mass constraints of most launch vehicles but their volume constraints (Fig. 7.0-2). The proposed HLLV (Ref. 8.0-1, 8.0-2) will have more than enough lift capacity to launch the entire LOLA package, but its proposed 13.7 m shroud x 38.1 m length cargo space is not wide enough to accommodate the fully-assembled single LTV/LEV proposed (Fig. 8.0-3) for the cargo transfer from LEO to the lunar surface. Multiple transfers would increase the cost. Therefore, a single vehicle transfer is proposed with on-orbit assembly of the cargo modules to the LTV/LEV (Fig. 8.0-4). This proposal assumes some kind of assembly station in LEO although not necessarily a very intricate one; since only minimal assembly will be required of the transfer/landing system. It also assumes that NASA does not have an operational LTV/LEV transfer system at the time of launch. This system would then be the preferred transfer/landing system, and the LOLA project will have to be designed around it.

8.1 Launch Manifest

The LOLA project is launched into LEO by 2 Shuttle C Blk II's and 2 Shuttle C's (Fig. 8.0-1). These two variants of the present shuttle are chosen for their ability to match the specific volume and mass needs of this mission as well as for their realistic nature. They are derivatives of a present launch vehicle and, therefore, have a more realistic chance of coming to be. The Shuttle C Blk II has a 7.6 m shroud x 27.4 m payload envelope and a 61,000 kg payload capacity. The Shuttle C has a 4.6 m shroud x 25 m payload envelope and a 71,000 kg payload capacity. The Shuttle C Blk II is chosen so that assembly on-orbit of the LTV/LEV and on the lunar surface of the LOLA array will be minimized.

There are four cargo modules (Fig. 8.0-2). Two cargo modules contain 4 complete telescopes each, one cargo module contains all of the other LOLA parts, and one module contains the construction vehicles. One Shuttle C Blk II carries the LTV/LEV and vehicles module to orbit. The other Shuttle C Blk II carries the other cargo modules. The two

Shuttle-C Blk II	Shuttle-C Blk II	Shuttle-C	Shuttle-C

LEV	28.6 mt	Tlscpes1	9.6 mt	Tank1	34.4 mt	Tank3	34.4 mt
LTV	14.5 mt	Tlscpes2	9.6 mt	Tank2	34.4 mt	Tank4	34.4 mt
Vehicles	16.1 mt	Misc.	37.0 mt				
Total	59.2 mt	Total	56.2 mt	Total	68.8 mt	Total	68.8 mt
Capacity	61.0 mt	Capacity	61.0 mt	Capacity	71.0 mt	Capacity	71.0 mt
Margin	1.8 mt	Margin	4.8 mt	Margin	2.2 mt	Margin	2.2 mt

Total Weight to Orbit: 253.0 mt

Figure 8.0-1: Launch Manifest

Miscellaneous Module

Power	3950 kg
Instr.	1750 kg
Thermal Ctrl	8425 kg
Metrology	438 kg
Guidance	235 kg
Commun.	125 kg
FDL's	1698 kg
Beam Split.	405 kg
Structures	17500 kg
Container	2500 kg
Total	37000 kg

Telescopes Module

Telescope1	1900 kg
Telescope2	1900 kg
Telescope3	1900 kg
Telescope4	1900 kg
Container	2000 kg
Total	9600 kg

Vehicle Module

Vehicles	13200 kg
Container	3500 kg
Total	16700 kg

Figure 8.0-2: Cargo Modules

TELESCOPE MODULES

VEHICLE MODULE

FUEL TANKS

LEV BASE

MISCELLANEOUS MODULE

LTV BASE
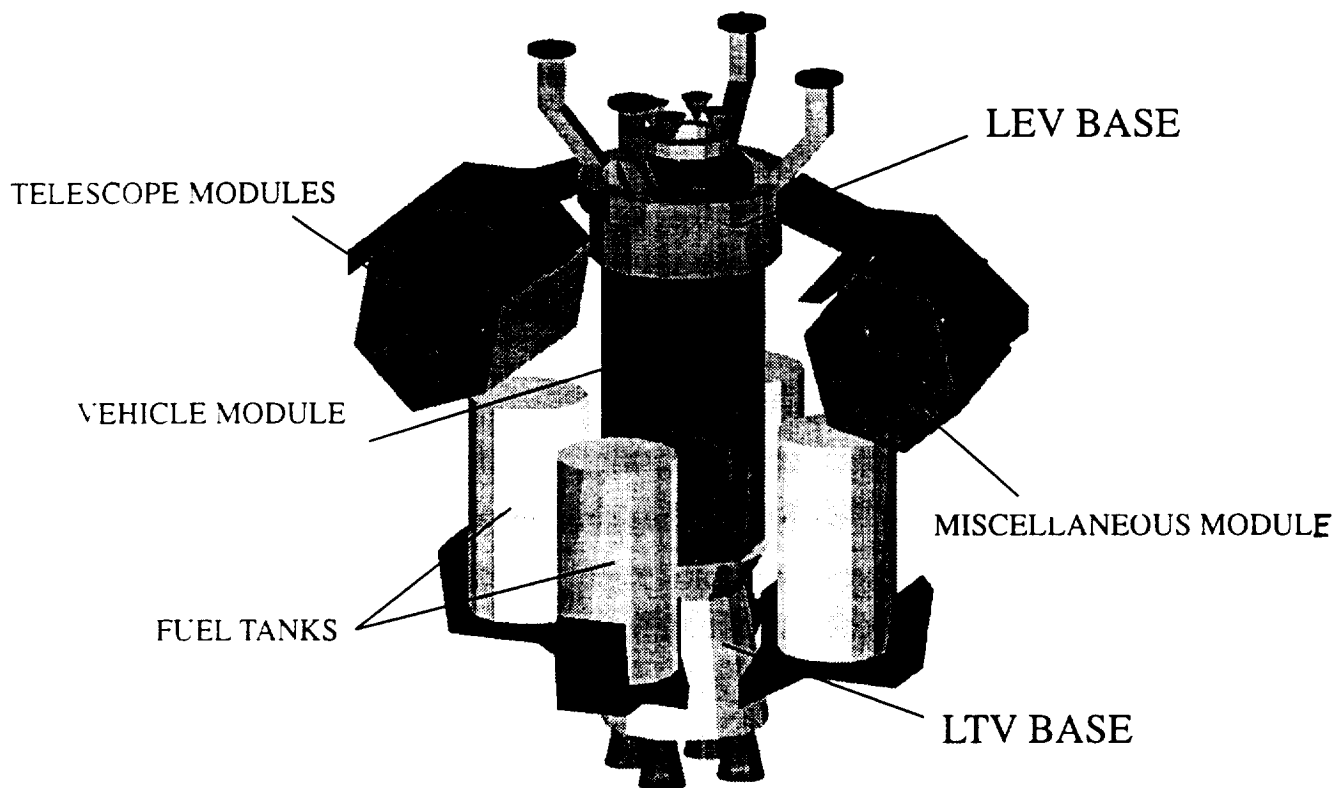
Figure 8.0-3: LTV/LEV Configuration for LEO to LLO Transfer

Launch Vehicles Arrive at SSF

LTV Drops Its Fuel Tanks

LTV and LEV Detach

LTV/LEV Leaves SSF for
Transfer to Lunar Surface

LEV Lands on Moon
with Cargo Modules

LTV Left in LLO

Orbital Assembly of LTV/LEV

Figure 8.0-4: Earth to Lunar Surface Transfer Profile

Shuttle C's bring the four heavier transfer fuel tanks to LEO.

8.2 LEO to Lunar Surface Transfer

A single LTV/LEV transfer vehicle (Fig. 8.0-3) hauls the LOLA cargo from LEO to LLO. It resembles but is not identical to the LTV/LEV associated with the 90-day study. The LTV contains a base, a LEV coupler, and 4 drop tanks and their respective holding arms (Fig. 8.2-1). The two heavier drop tanks are 4.5 m in diameter x 8 m high and the lighter drop tanks are 4.5 m in diameter x 5 m high. The assembled LTV is 12.5 m high x 18 m wide x 18 m deep and weighs 14.5 mt without the fuel tanks. The assembled LEV (Fig. 8.2-1) is 23 m high x 25 m wide x 13 m deep and weighs 28.6 mt. There are two cargo holding arms on the LEV; one of which holds the miscellaneous module, one of which holds the combination of the two telescope modules. This arrangement is to attempt to balance the LEV. The LTV arms, LEV arms, and LEV legs are attached on-orbit. Based on estimates adopted from Ref. 8.2-1 the total on-orbit assembly time will be approximately 932 hours.

The LTV/LEV travels to LLO. The LTV drops its expended fuel tanks, the LTV and LEV detach, and the LEV descends on the lunar surface. The final resting place of the LTV is in LLO and the LEV permanently resides on the lunar surface.

LTV   LEV
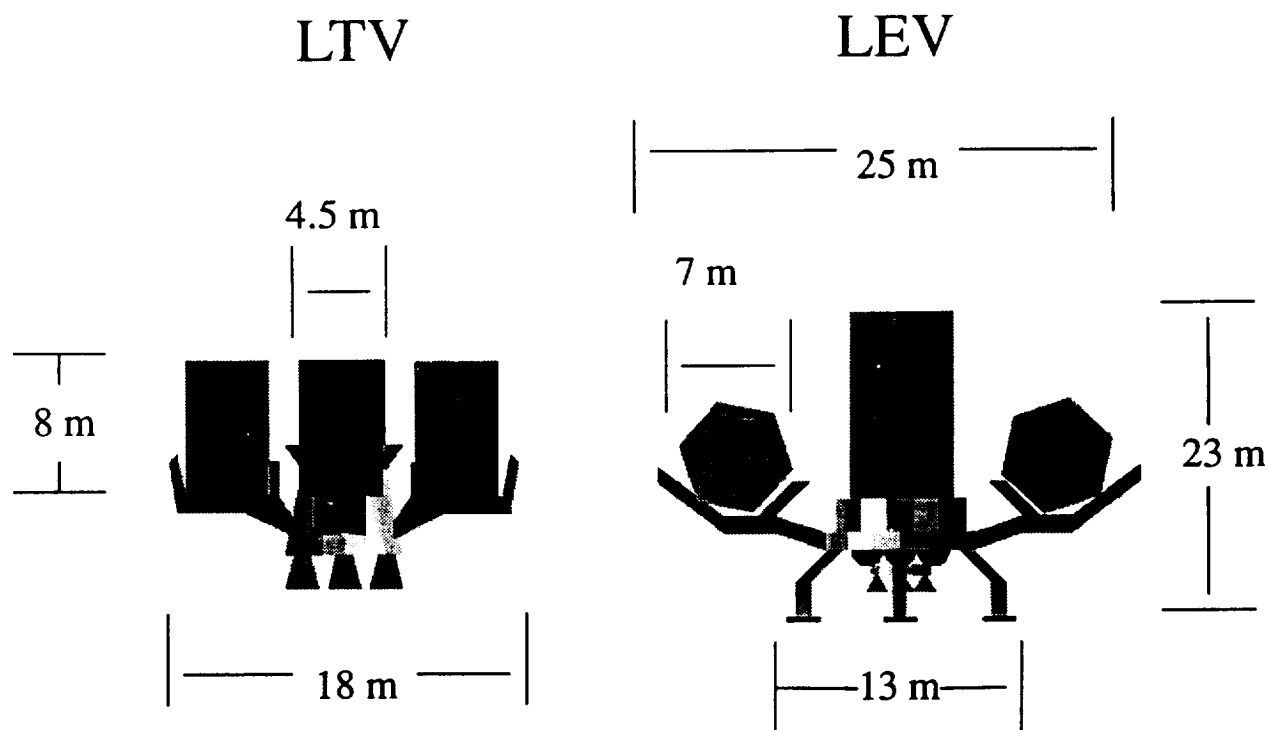
Figure 8.2-1: Dimensions of the LTV and the LEV

9.0 Construction

The Construction of the LOLA project will take place in two phases (Fig. 1.5-1). The first phase will establish the power system, the central instrument area, the communications, and nine telescopes. The array will operate on a limited scale until the second phase brings eighteen additional telescopes. Before any construction takes place, unmanned science missions to the proposed site will take soil samples to predict bearing capacity and settlements of the emplacements. In addition, detailed satellite maps will reveal the contours of the surface and any physical obstacles that must be overcome.

The build-up strategy for the first phase has three stages: site preparation, assembly, and calibration. The site preparation will be done by Earth-operated telerobotics. This will be used to perform the simpler, laborious site preparation tasks because astronaut exposure to the harsh lunar environment is to be minimized. These telerobotics will allow for unforeseeable difficulties associated with lunar construction to be observed and accounted for before the arrival of the crew. The assembly and emplacement of the structures will be done by astronaut Extra-Vehicular Activity (EVA), as these tasks require considerably more manipulation then the site preparation operations. There will be two operating EVA crews of two astronauts each. The last stage will be the calibration and aligning of all the mirrors and instruments. Because of the very time consuming detail that this will demand, a whole stage has been assigned to this purpose, and new crews will be flown in to relieve the assembly crews.

9.1 Vehicles and Assembly Equipment

Vehicles will be specifically designed for the project's completion. Some of the important lunar environmental factors and their influences on the vehicles and equipment are:

Parameter	Considerations
Temperature	material deformations, fluids
Vacuum	soil adhesion, volatile lubricants
Radiation	material and electronic failures
Gravity	greater lift capability, less traction
Dust	impedance of mechanical motion
Soil Density	large exc. energy req'd, ground pressure
Soil Porosity	settlements of structures
Hydrogen	reduction corrosion of emplacements

Two methods of vehicle development were considered: task-specific vehicles and multi-purpose vehicles. Task-specific vehicles increase the efficiency of operations but also increase the number of vehicles required and, hence, the weight required to be placed on the lunar surface. These vehicles are much more appropriate for large base construction with its many distinct functions. Since only a scientific lunar outpost is to be constructed, multi-purpose vehicles will be used to save weight and cost. The vehicles are assumed to be operational only during the day. A vehicle designed for operations at both 90K and 385K is perceived as being not reasonable because of the difficulties of radiators and those associated with mechanical tolerances as well as others. The vehicle requirements for the LOLA project are leveling and debris removal, cargo unloading, cargo positioning, excavation, and transportation. To fulfill these requirements, the following vehicles will

Self-Excavator

Regolith Trailer

Continuous Excavator Shovels

Rover

Astronaut Seating

DIPS
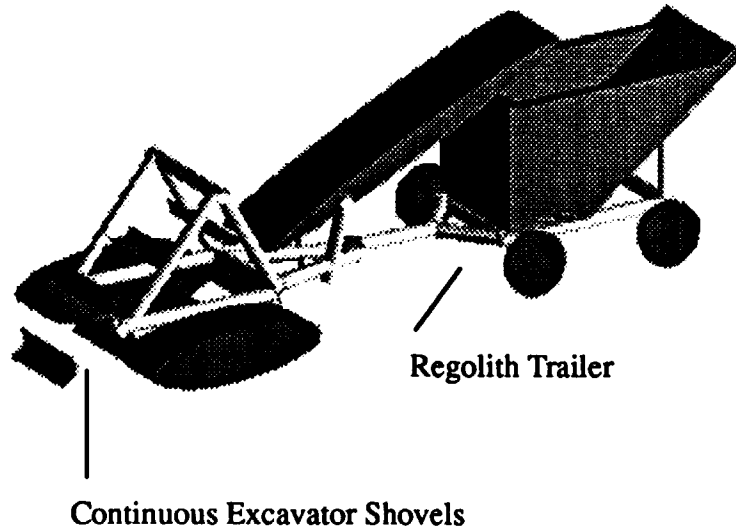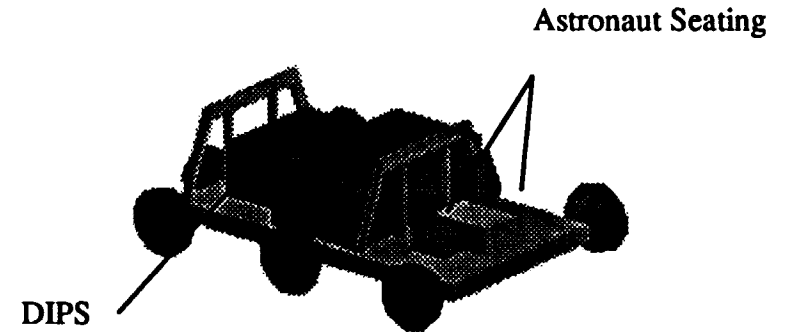
Crane/Excavator with Large Trailer

Telescope Module

Excavator Boom

Small Trailer

Long Delay Mirrors

Long Delay Towers

Dozer Blade

Figure 9.1-1: Lunar Construction Vehicles

be used (Fig. 9.1-1):

> Crane/excavator
> Self-excavating/loading/unloading machine
> Unpressurized rover
> Large trailer
> Small trailer

Crane/Excavator: This machine is 6 m long x 3 m wide x 1 m high and weighs approximately 10,000 kg. It has a 10 m contractible, folding boom and provides the regolith positioning required to excavate the landing pad wall and the lab shield using a clamshell 1.5 m³ bucket. By detaching the bucket, the machine also acts as a crane for the cargo unloading and positioning. Using the heaviest module as a guide, the crane will need a hoisting capacity of 14 kN. A leveling blade capable of pushing 1 m³ of lunar regolith is attached to the front end and the crane uses this for site preparation leveling. Debris is removed with the boom arm and the bucket. A coupler at its rear links it to the large trailer for module transportation. The crane has metal wheels which are well suited to the lunar terrain. The crane/excavator will be capable of both Earth-telerobotic and EVA operation.

Self-Excavator: This is a small machine that excavates the loosely bound top 0.3 m of regolith. The machine pulls a small container trailer behind it into which the regolith is piled. It has a 3 m³ capacity and unloads the regolith by lifting the container on the trailer. This machine will also be capable of both Earth-telerobotic and EVA operation. The self-excavator weighs 500 kg.

Rover: The rover is the vehicle that moves the EVA crews around on the surface. It can attain a speed of 10 km/h, and weighs 2000 kg. It has a smaller coupler at its rear to attach to the small trailer.

Large Trailer: The trailer is 5 m wide x 7 m long x 1 m high and weighs approximately 500 kg. It hauls the modules and the larger cargo.

Small Trailer: This trailer weighs 200 kg and is 4 m long x 3 m wide x 1 m high. It attaches to the rover and hauls the smaller cargo such as the long delay mirrors.

All of the self-propelled vehicles will have self-contained power units that are portable and preferably non-rechargeable, so that there can be continuous constructing during the site preparation stage. Dynamic Isotope Power System (DIPS) comes in many different sizes and power capabilities and is well suitable for the requirements (Ref. 9.1-1).

The general equipment requirements of the construction are:

1.) A _vibratory press_ to place the telescope foundations.
2.) _Hand tools_ to attach the various trusses and towers.
3.) _Cables_ to lift and control cargo.
4.) _Calibration equipment_ to align all mirrors and structures.

9.2 Site Preparation

The site preparation stage begins with the landing of the Lunar Excursion Vehicle (LEV) and its cargo approximately 10 km from the center of the array. The lander is about 20 m high and 23 m wide. The cargo modules are partially self-unloaded and the vehicle module is completely self-unloaded (Fig. 9.2-1). After the vehicles are unloaded, a self-deployed blanket or combination of blankets such as those developed by the University of Texas at Austin (Ref. 9.2-1) cover the lander to give the remaining unloaded cargo limited thermal and micrometeorite protection during the site preparation stage (Fig. 9.2-2). This blanket provides thermal protection for the active instrument cooling system that will be vulnerable in its uninstalled condition. A communication system will be set up to provide video images during the site preparation. There will be an estimated delay of 4.4 seconds for the round trip signal of images and instructions from the moon to the Earth. Although this does decrease the accuracy of movement on the lunar surface, major problems will not be encountered because no delicate manipulations are to be done during this stage. The construction vehicles will then prepare the launching/landing area to minimize the harmful effects of lander outgassing. In addition to the leveling and debris removal in a circle 73 m in diameter, a 1 m high by 2.4 m wide regolith wall will be piled along the outer edges of this landing zone. This will not stop the flow of large impediments from the outgassing but it will redirect it enough so that the effect felt at the array from landings of future missions will not be harmful. The construction vehicles use a stereo camera system which matches a known template to the camera image to locate and level the power source area, the central instrument area, as well as the individual telescope areas (Ref. 9.2-4). The templates are made from detailed surveying maps. A self-excavating, loading, and unloading regolith hauler will excavate an area 150 m x 150 m to acquire the necessary 2,235 m³ of shielding material to cover the instrument lab.

Landing Position   Unloaded Position
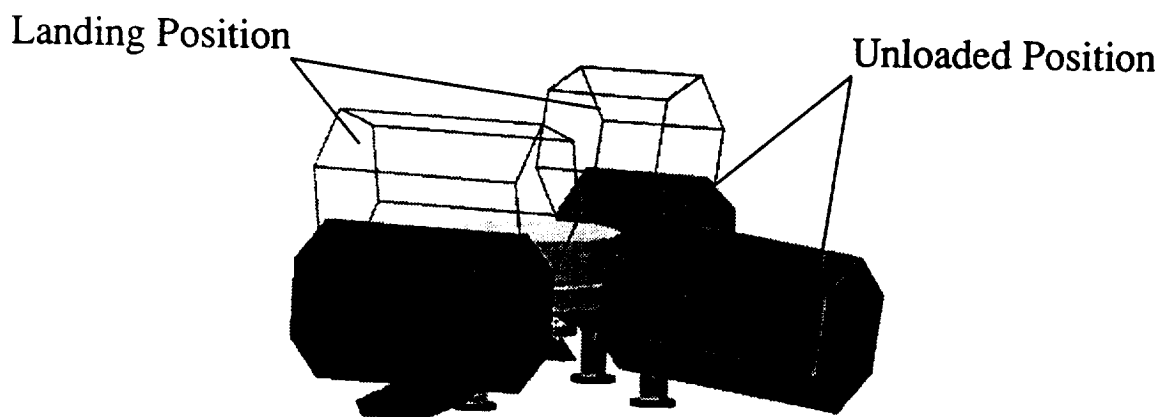
Figure 9.2-1: Example of a Partially Self-Unloaded Cargo Lander
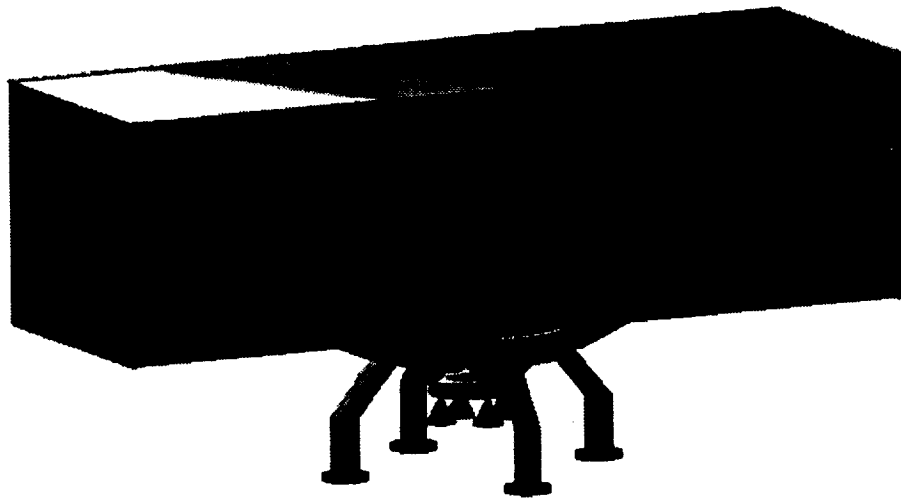
Figure 9.2-2: Fully Deployed Configuration of Protection System

9.3 Assembly

The assembly stage begins with the arrival of the first two EVA crews on the second day of the second lunar cycle of construction. The crew landers serve as habitats (Fig. 9.3-1) for the construction period and the crew returns to these landers after each work day. The landers have an estimated endurance limit of 45 Earth days (Ref. 9.3-1). The tasks of each crew and vehicle are generalized in the timeline and include the assembly and emplacement of the following items:

> Telescopes
> Long Delay Mirrors
> Reflective Towers
> Fine Delay Lines
> Central Building
> Instrument Lab
> Power Source
> Maintenance Tents

Additional tasks include surveying and transporting of the modules.

Telescopes: One EVA crew sets up the telescopes (Fig. 9.3-2). The crane pulls the large trailer on which one of the telescope modules is lying. The crew then unloads one complete telescope set (there are four per telescope module). The foundation points are marked and the spudcan footings are emplaced into the lunar regolith using a vibratory pressing machine. The legs of the telescope are then screwed into its base and the exterior
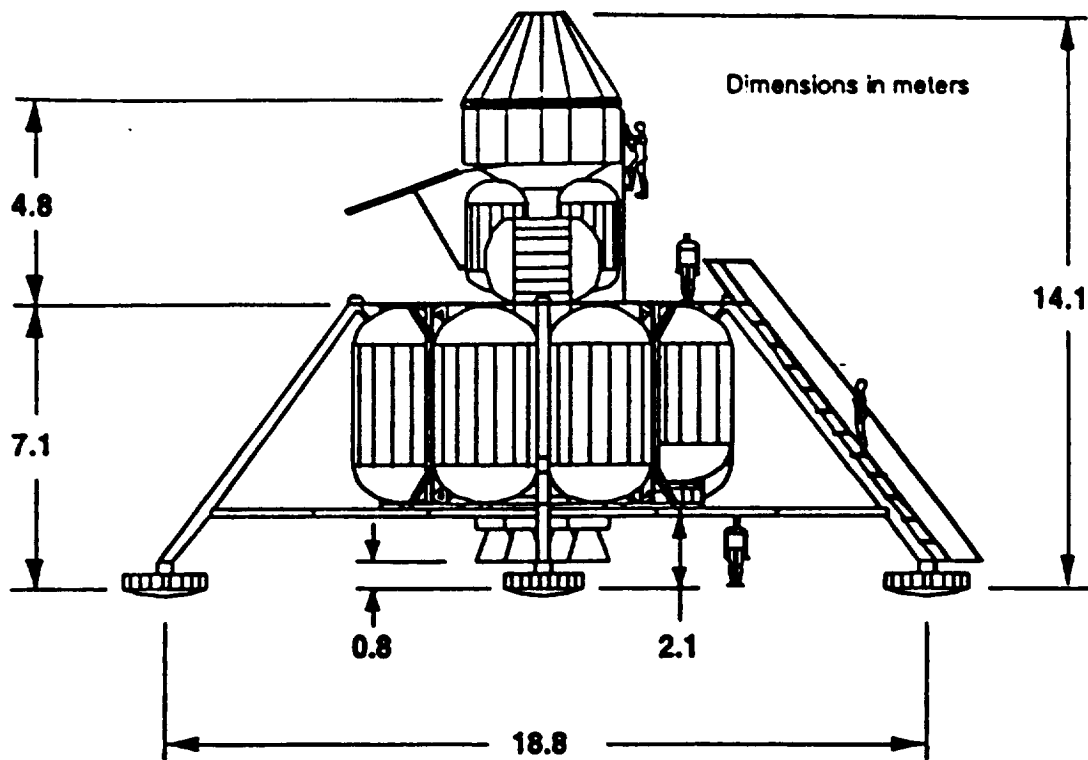
Figure 9.3-1: Piloted Lander Configuration

mirror is attached. The telescope is lowered onto its footings via the crane and connected to them. The counterweight is filled with regolith. The reflecting mirrors are then nominally positioned and the dome shield is set up around the telescope. The tolerances of structures need to be matched to avoid excessive thermal stress and fatigue at connected joints. Connections that are well matched have properly accounted for the different coefficients of expansion of the mated and mating materials. Finally, electrical and data connections are made to the guidance motors, metrology system, and shield.

Long Delay Mirrors: The exact location of the delay mirror is determined by triangulation and surveying. One EVA crew transports the complete delay mirror by pulling the small trailer with the rover. The footpads are driven into the regolith then the supports and the mirror are attached. The dome shields are then snapped together and electrical and data links are made to the shields.

Reflective Towers: The reflective towers bounce the light from the telescopes out to the long delay lines and then from the long delay lines into the fine delay lines. These towers come in three 4.5 m segments and one 2.25 m segment. They are assembled by one EVA crew with the assistance of the crane.

Fine Delay Lines: Both EVA crews assist in the fine delay line assembly. The fine delay lines are 55 m long. They come in 11 segments per fine delay line. The lines are rigidly attached by bars during assembly to make alignment easier. Each delay segment has two leg attachments of two legs each that raises the segment 30 cm off of the ground.
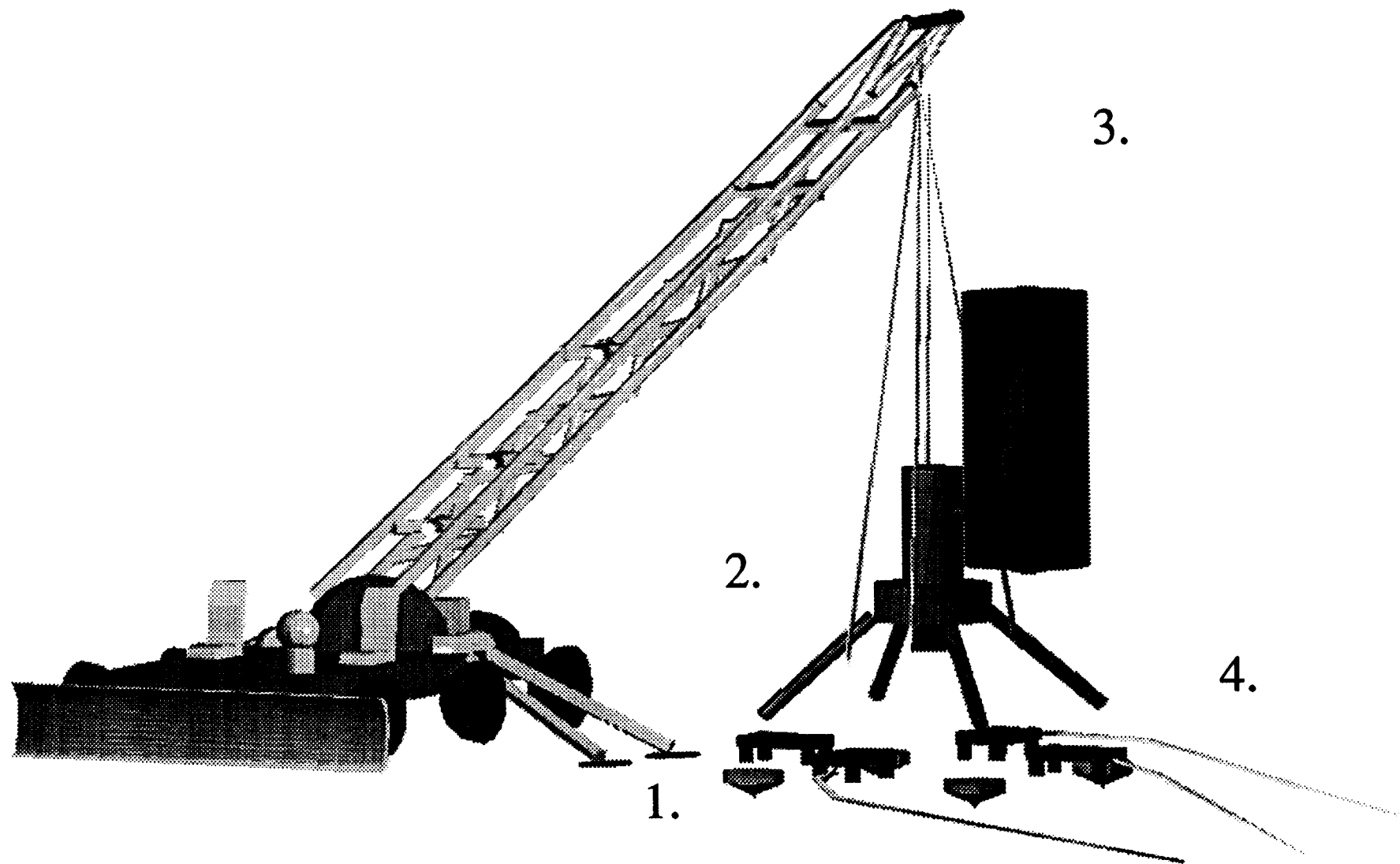
Figure 9.3-2: Telescope Assembly. 1) The spudcan footings are planted. 2) The telescope legs are attached. 30 The telescope is lowered onto and attached to its footings. 4) The metrology and power connections are made and the counterweight is filled with regolith.

These 198 leg attachments are riveted into pre-drilled holes by rivet punches. The inner railings are snapped together. One sensitive area in the design of the array is the attachment point of the segments' railings. The connection must endure thermal cycling fatigue of large temperature swings. The shielding of the central building will assist in the reduction of this thermal fatigue.

Central Building: The central instrument building covers the optical path at the center of the array (Fig. 9.3-3). The building helps to shield the optical path from excess radiation and limits the severity of temperature on the optical path elements. The building consists of boron/epoxy half-circle "tent" poles that arranged over the length of the building. To construct, these "tent" poles are positioned about 10 m apart and rigidly attached to each other. A thin gold foil covering is then rolled out over and in between these "tent" poles. At the interface between the central building and the instrument lab, a more compact radiation shield is needed for instrument protection because of alignment reasons. A 1 m wall of polyurethane will form the protection for the central building side of the instrument protection system.

Instrument Lab: Using an internal angle of friction as 36°, the 1.5 m diameter x 5 m long lab requires at least 2,235 m³ of regolith shielding to maintain 5 m of shielding at all points. This regolith, dug by the regolith self-excavator during the site preparation stage, is piled on a soil net that completely covers the lab. The lab will be placed on a thermal blanket to insulate it against conductive heat transfer.

Power Source: The array will be powered by three 2.5 kWe DIPS. The units are easy to install and will require minimal construction effort. The units are placed on a protective blanket to prevent damaging soil/system. A radiation shield is then placed over the top of the three units to protect them from exposure to ambient radiation. The units' radiators are placed outside the shield, set high enough above the surface so that dust interaction from rising ionized dust is minimized.

Maintenance Tents: These are simple reflecting blankets designed to minimize the effects on the construction vehicles of prolonged exposure to the lunar environment after the construction operations have ceased. This is done so that these vehicles can be used again for new telescope additions and routine maintenance operations. These tents are not designed to be perfect shields and there replacement, as well as the maintenance of the degrading construction vehicles, will be formulated into the maintenance operations.

9.4 Calibration

Due to the lengthy nature of the construction operations, two new crews will be flown in near the beginning of the calibration stage. Holographic optical elements (HOE's) will be used to sense the alignment of the optical system. The process involves the off-axis sensing of holograms (essentially gratings etched into the mirror surface of mirror coating) at each mirror (Fig. 9.4-1). Because the optical paths are not fixed, the system requires a sensor (most likely a small CCD) and a different hologram for each mirror. The calibration crews will set this system up and perform the finishing operations such as clean-up and inspection. The majority of the calibration will be performed by Earth controlled means once the astronauts have left. "The calibration requirements of lunar optical interferom-
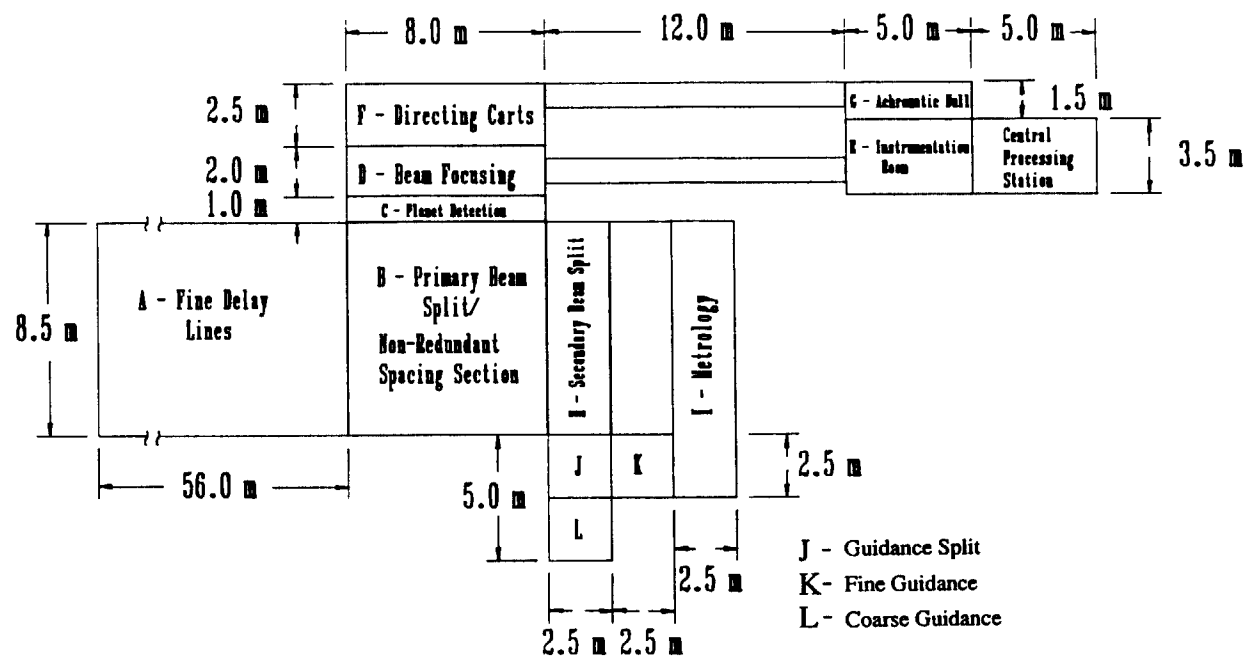
Figure 9.3-3: Central Receiving Station Dimensions and Protective Covering

etry have not yet been defined, but calibration of spaceborne optical systems is done routinely and is not expected to present any technology challenges..." (Ref. 9.2-4).

9.5   Construction Time

The timeline (Fig. 9.5-1) shows that the entire construction period for the first phase will last approximately 4 lunar cycles. This assumes that no operations take place during the lunar night, for the reason stated above. The number of productive hours that an astronaut can be expected to work is limited by factors such as sleep, routine maintenance, EVA preparation (Ref. 9.5-1). EVA work days are assumed to be only 4 productive hours per crew member; as opposed to Earth operated telerobotics which are assumed can be operated 24 hours a day. The next phase will obviously take less time because much of the total 27 telescope array support network will be intact. Figure 9.5-2 shows the breakdown in total hours per construction stage for the first phase. These times were estimated by segmenting operations into individual EVA
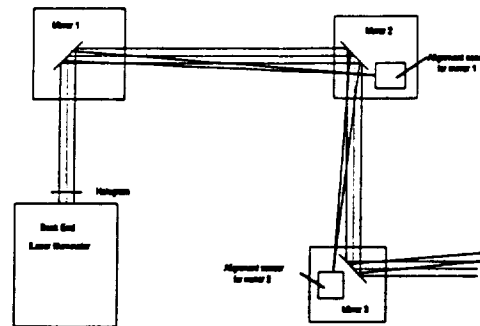
Figure 3-1. Using a Single Hologram for Alignment With Fixed Path Lengths
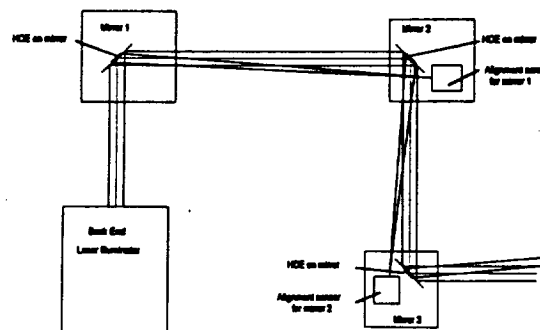
Figure 3-2. Using HOEs on Individual Mirrors for Alignment

Figure 9.4-1: Using HOEs on Individual Mirrors for Alignment

	Excavate	landing	area		Excavate	power	area		Excavate	central	area			Excavate	telescope
crane/excavator															
self-excavator	Excavate	central	area												
rover	Survey														
EVA crew #1															
EVA crew #2															
Days	1	2	3	4	5	6	7	8	9	10	11	12	13	14

LUNAR   CYCLE#1

	area		Unloading	Transport	Power	assembly		Central	area	set-up			Cover
crane/excavator													
self-excavator													
rover			Survey					Central	area	set-up			
EVA crew #1			Unloading	Survey	Power	assembly		Central	area	set-up			
EVA crew #2			Unloading	Transport	Central	area	set-up						Cover
Days	1	2	3	4	5	6	7	8	9	10	11	12	13	14

1st crew's arrival

LUNAR   CYCLE#2

	instrument	chamber	w/regolith	Telescope	assembly								
crane/excavator													
self-excavator													
rover								Set-up	long	delay	mirrors		
EVA crew #1								Set-up	long	delay	mirrors		
EVA crew #2	instrument	chamber	w/regolith	Telescope	assembly		Calibration						
Days	1	2	3	4	5	6	7	8	9	10	11	12	13	14

1st crew's departure

LUNAR   CYCLE#3

crane/excavator													
self-excavator													
rover	Calibration												
EVA crew #1	Calibration												
EVA crew #2													
Days	1	2	3	4	5	6	7	8	9	10	11	12	13	14

2nd crew's arrival

LUNAR   CYCLE #4

2nd crew's departure

Figure 9.5-1: Timeline

Table 9.5-1: Set-up Times

CONSTRUCTION STAGE	TIME (hrs)	EARTH DAYS*	LUNAR CYCLES**
SITE PREPARATION	590	24.6	1
ASSEMBLY	400	25.0	2
CALIBRATION	450	28.0	3
TOTAL	1440	77.6	5

* Earth based telerobtics has a 24 hr day, whereas lunar EVA has a 4 hr day.

** Lunar Cycles are rounded up to the nearest 0.5. Any operations starting after
7 days into the cycle will not be productive because of the 14 day dormant night period.

Table 9.5-2: Site Preparation Set-up Time Estimates

	EVA TIME (hrs)	EVA TO EARTH MULTIPLIERS	EARTH TIME	QUANTITY	TOTAL TIMES
Telescopes					
transport	0.25	5.00	1.25	9	11.25
camera set-up	0.17	3.33	0.5661	9	5.0949
level,debris	1.00	6.70	6.70	9	60.30
Power					
transport	0.50	5.00	2.50	1	2.50
prepare	3.00	6.70	20.10	1	20.10
Launch Pad					
prepare	5.00	6.70	33.50	1	33.50
excavate wall	15.00	4.00	60.00	1	60.00
Central Area					
transport	3.00	5.00	15.00	1	15.00
camera set-up	0.50	3.33	1.665	1	1.665
level, debris	10.00	6.70	67.00	1	67.00
exc. soil	75.00	4.00	300.00	1	300.00
Beacons					
set-up	4	3.33	13.32	1	13.32

Total Site Preparation Time 589.7299

tasks and assigning each task a certain time required for completion. For the Earth telerobotically operated site preparation stage, adjustment factors to convert from estimated EVA times were used, similar to but not exactly like those proposed in Dias, et al. (Ref. 9.5-1) (Fig. 9.5-3).

9.6 Operational Maintenance

Two maintenance teams are flown into the array to do routine system checks every year. They use the construction vehicles for transportation and assistance in any major operations. The major tasks to be accomplished during these maintenance periods include redundancy checks, alignment adjustments, and replacement of degraded equipment.

Redundancy checks

To assure operation during observing periods, certain redundancies are built into support systems such as communications, power, thermal control, and also in instrumentation. During maintenance, these redundancies are checked and replaced, if necessary, with compartmentalized replacement packages. Any replacement of redundant instrument systems requires the re-excavation of a certain portion of the regolith shield and adds greatly to the maintenance time required.

Alignment adjustments

Much of the first maintenance period will be consumed with the re-calibration discussed above. Barring this, even subsequent maintenances will involve re-alignment and adjustment of the slack adjusters. Over time there will likely be some alignment degradation due to thermal cycling. Even an initially perfectly aligned system will permanently strain over many lunar cycles and require some re-alignment. Also, the baselines of the array may be changed from time to time. Because of the easy stepwise procedure of telescope assembly, this process consists of simply planting new footings in the new location, disconnecting the telescope legs from there original footings, disassembling the telescope, moving the telescope pieces to the new location, and re-assembling the telescope.

Replacement of degraded equipment

Some of the parts, such as thermal coatings, motors, and shields will be degraded by dust and may be designed for limited lifetimes. In this case, these parts will need to be replaced during regularly scheduled maintenance periods. Other pieces such as wiring, tubings, and the instrument, metrology, and calibration CCD's may eventually need replacement because of damage from radiation. The extreme temperatures may cause structural components to fail due to thermal fatigue and stresses. They will also cause the need for replacement of the active instrument coolant. Any meteoroid caused damage will need to be repaired during maintenance periods.

9.7 Considerations

In conclusion, construction equipment and methods that are much better than those on previous manned lunar missions must be developed if any lunar construction is to be realistic. The severe environmental factors have to be better managed. Apollo astronauts reported having poor color deciphering and depth perception capabilities because of the

intense and blinding sunlight (Ref. 9.7-1). Here are some examples of the significant dust problems faced on the later Apollo "J-Missions" (Apollo 15-17) even though there was increased time spent on dust control and clean-up (Ref. 9.7-2):

- EVA suit wear, suit wrist disconnects and abrasively worn gloves.

- Degraded Thermal Control Systems: a 10% dust film (unnoticeable to the crew) degraded the reflective surfaces, resulting in higher thermal temperatures.

- Degradation of optical properties that included abrasions to the helmet visor, optical lenses and read-out displays.

- The failure of Velcro for attachments when saturated with dust.

- The accretion of dust on sensors which affected the accuracy of the data gathered.

- The malfunction of the Lunar Rover's tool carrier gate type latch, which had large mechanical tolerances. The dust with lack of atmosphere and subsequent humidity for lubrication caused the latch to be immovable.

- The malfunctioning of EVA sampling tools.

- The human physiological affects of dust. In some cases once the dust got under the astronaut's fingernails, it was only removed by the growth of the fingernails. Also, Russians used lunar soil on rats and found pathological changes in the lung tissue, a decrease in oxygen consumption, and a decrease in body weight (Ref. 9.7-3).

10.0 Cost Analysis

10.1 Structures

Telescope:

Boron/epoxy Members ($110.25 per kg Boron/epoxy)

Legs	$99,666.00
Optical Cylinder	$17,089.00
Arm & Sleeve	$331.00
Support Cylinder & Sleeve	$6,615.00
Mirror Supports	$3,307.00
Motor Chamber	$16,868.00

Mirrors

Primary Mirror

Glass	$21,499.00
Coating	$4,000.00
Polishing	$1,000,000.00

$2^{nd}, 3^{rd}, 4^{th}, 5^{th}$ mirrors

Glass	$304.00
Coatings	$6,620.00
Polishing	$60,000.00

Motors and Bearings

Arm Motor	$6,500.00
Base Motor	$2,000.00
Arm Bearings	$600.00
Base Bearings	$2,500.00
Gears	$500.00

Subtotal for one telescope	$1,248,399.00

Total structural costs for 27 telescopes	**$33,706,773.00**

Research and Development

Structure	$150,000,000.00
Mirror	$100,000,000.00

Total cost for 27 telescopes	**$283,760,773.00**

External Structures

Sending/Receiving Tower
37 Mirrors
(glass, coatings, polishing) $619,048.00
37 Step motors $1,850.00
Boron/epoxy Members $20,480.00

For one tower $641,378.00
For three towers $1,924,134.00

Mirror Tower
Mirror
(glass, coatings, polishing) $49,526.00
Boron/epoxy Parts $2,911.00

For one tower $52,437.00
For 108 towers $5,673,196.00

Metrology Tower
Two Step Motors $100.00
Aluminum Parts $446.00

For one tower $546.00
For three towers $1,638.00

Metrology Building
Boron/Epoxy - Aluminum Parts $25,000.00
Two Motors $200.00
Boron/epoxy Table $258,000.00

Total external structure
material costs $7,882,168.00

Research and Development costs $250,000,000.00

Total External Structures Costs $257,882,168.00

Total Structures Cost   **$541,642,941.00**

10.2 Instrumentation

Detectors, filters, electronics	$2,000,000.00
Inst. Cabinet motors & bearings and associated electronics	$200,000.00
Cooling systems	$200,000.00
Research and Development	$10,000,000.00
Instrumentation Total	**$12,400,000.00**

10.3 Thermal Protection

Aluminized Teflon MLI Coating (cost per square meter)	$897.00/m²
Total surface area on array	890 m²
Total cost of Teflon MLI	$798,330.00
Active cooling system	$400,000.00
Total thermal protection cost	**$1,198,330.00**

10.4 Fine Delay Lines

Materials and subcomponents (per line)	$50,000
Manufacturing	$50,000.00
Development	$10,000.00
Total cost per line	**$110,000.00**
Total cost for 27 lines	**$2,970,000.00**

10.5 Beam Combination

81 Beam splitters ($2500 each)	$202,500.00
27 Mirrors ($1900 each)	$51,300.00
Research and Development	$2,000,000
Total beam combination costs	**$2,253,800.00**

10.6 Guidance and control

54 Variable density filters	$8,100.00
108 Achromatic wedge prisms	$21,600.00
54 Masking disks	$2,700.00
27 Hybrid occulting disks	$5,400.00
27 Single mode fibers	$45,738.00

135 Linear actuators	$1,295,325.00
1024x1024 CCD	$130,000.00
720x720 CCD	$130,000.00
54 step motors	$10,800.00
Control electronics and computers	$500,000.00
Research and Development	$10,000,000.00
Total guidance and control costs	**$12,149,663.00**

10.7 Communications

Transponder	$50,000.00
Two antenna mounts	$10,000.00
Two high gain antennas	$120,000.00
Structure/cabling	$30,000.00
Central computer	$40,000.00
RF amplifier	$20,000.00
Total communication costs	**$270,000.00**

10.8 Power

6 Fueled DIPS power sources	$6,000,000.00
14 km insulated Aluminum cables	$14,000.00
Cable research and development	$10,000,000.00
Transformers and power control equipment	$300,000.00
Total Power costs	**$16,314,000.00**

10.9 Metrology

27 Photodetector units	$270,000.00
27 Function Generators	$270,000.00
114 Transmitting & Receiving Optics	$228,000.00
519 Lasers	$3,114,000.00
Laser plates	$200,000.00
Optics, retroreflectors and misc.	$1,500,000.00
Research and development	$10,000,000.00
Total Metrology costs	**$15,582,000.00**

10.10 Transportation

Total transportation cost of array materials
from Earth surface to Lunar surface $2,129,330,000.00

- Cargo from Earth to LEO $1,265,000,000.00
  includes LEV/LTV and fuel
  ($5,000/kg)
- Cargo from LEO to lunar surface $864,330,000.00
  ($10,000/kg)

Research and development $200,000,000.00
Calibration CCD's and alignment costs $5,000,000.00

Total Transportation costs $2,334,330,000.00

10.11 Total Array Cost $3,222,871,507.00

11.0 Conclusions

In its final completed stage the Lunar Optical Long-baseline Array will consist of 27 telescopes in a Y- configuration with a maximum baseline of 5 km. The telescope positions have been selected to optimize the number of non-redundant baselines, in order to provide the most complete u-v plane coverage. The Y-configuration facilitates the placement of additional telescopes, while providing adequate u-v plane coverage and delay line simplicity not available in other array configurations. This configuration also reduces sidelobe intensity, thereby improving the possibility of Earth-sized planet detection at a distance of ten parsecs. The range of baseline lengths allows detection of radiation from the infrared through the ultraviolet regions of the spectrum.

The telescope structure was designed to provide a minimum number of mirror bounces. Computer analysis and optimization gave the structure sufficiently small deflections while minimizing its mass. The coarse and fine delay systems allow accurate path length adjustments with a relatively few number of mirror bounces.

The incoming beams are sampled by the metrology system to calculate and adjust for varying baseline lengths. The pointing and control system also samples a small fraction of the beam. This guidance system tracks guide stars within 10^{-6} arcseconds in the pupil plane.

After sampling, the beams are combined in a non-redundant manner and sent to instruments where image and spectrographic data are collected. Four instruments are utilized to image the data from the infrared, visible, and ultraviolet spectrums. A communications link provides continuous contact with Earth. This is accomplished through a satellite orbiting the second libration point above the lunar surface allowing direct data transfer to and from the Earth-based Deep Space Network. The lunar communications system, along with all other components of the array, is powered by three 2.5 kW Dynamic Isotope Power Systems.

LOLA offers high-resolution interferometry based on proven Earth based detection methods. Furthermore, the LOLA design takes advantage of the lunar environment thus enabling collection of scientific data that is unavailable through conventional Earth-based astronomy.

LOLA CHARACTERISTICS

Array
  Y-configuration
  2.9 km arms in N, SE, SW orientation
  120 degrees between arms
  27 telescopes (9 per arm)
  5 km maximum baseline
  220 km minimum baseline
  Spectral Range of 150 to 10,000 nm
  Angular Resolution of 20×10^{-6} arcsec
  36 baselines (initial stage)
  351 baselines (final stage)

Array Site
  Maria location
  115 degrees to 180 degrees E or W longitude
  10 degrees N to 10 degrees S latitude

Telescopes
  48 m² total collecting area
  5.85 m high, 4.705 m wide, 4.5 m base diameter
  Off-axis altitude and azimuth configuration
  Mersenne design with 3rd order curved fold mirror
 Collecting mirrors
  Zerodur honeycomb design
  λ/100 surface finish
  Silver coating
  Parabolodial with f# 2.46
  1.50 m diameter primary mirror
        3.692 m focal length
  0.25 m diameter secondary mirror
        3.3 m above primary mirror
  Elliptical fold mirror (2a = 35.4 cm, 2b = 25 cm)
 Directing mirrors
  ULE material
  λ/100 surface finish
  Silver coating
  Flat elliptical mirrors (2a = 35.4 cm, 2b = 25 cm)

Delay System
 Coarse delay
        2 banks of 61 long delay mirrors
        5400 m maximum path delay
        25 cm beam diameter
        Accurate to 90 m

Fine delay
> Bank of 27 modules
> 90 m maximum path delay
> Cassegrain compression of beams from 25 to 4 cm diameter
> Infinite accuracy

Beam Combination
> Non-redundant spacing
> Simulated Herschel mounted mirror

Instruments
> - UV-Visible-IR imagers/spectrographs using large format CCDs (10^8 pixels)
> - Planet Detection Modules

Image Reconstruction
> ^nC_n detector scheme
> Fast Fourier Transform scheme
> Phase closure by self-calibration of HYBRID technique
> Combined CLEAN and MEM deconvolution scheme for sidelobe suppression
> Electronic calibration for effective system performance evaluation

Planet Detection
> 2 phase
> phase 1
> - achromatic nulling interferometer
> phase 2
> - hybrid occulting disk with 3 micrometer radius aperture wheel
> - 1.5 dB/kilometer attenuated single mode birefrigent fiber optic cable
> - electronic masking through image reconstruction algorithm
> Starlight Suppression (both phases) $>10^{-6}$

Metrology
> Optical pathlength measurements
> Combined heterodyning and fringe counting interferometric measurement
> 2 Nd-YAg lasers on opposite ends of beams
>> 100 mW power
>> 10% efficiency
> 2.5 mm beamwidth
> 1 nm accuracy
> Baseline measurements
> Mark III system at each telescope
> 4 lasers reflect from underside of telescope to one of three towers on the site

Guidance and Control
  2 stage guidance system
  10^{-4} course guidance accuracy
   0.1 AU field of view
   1024 x 1024 pixel CCD
  10^{-6} fine guidance accuracy
   0.02 AU field of view
   2048 x 2048 pixel CCD
  Variable density filter protects CCD from intense light

Communication
  X-band
  10 GHz uplink and 9 GHz downlink
  14 dB maximum carrier to noise ratio
  10^{-6} maximum bit error rate
  Data Rates
        100 Mbps downlink
        50 Mbps uplink
  1 m diameter antenna for lunar surface communications station
  Satellite
        Orbits second libration point
        3500 km radius orbit
        2.0 m diameter receiving and transmitting antennae
        Transmits to 34 m dish of the Deep Space Network

Power
  6 Dynamic Isotope Power Systems
        2.5 kW each
        Xe-He (NW 60) working fluid
        Pu 238 radioisotope
        closed Brayton cycle
        3 year life
        25/20 % (BOL/EOL) efficiency
        2142 kg mass
  Transmission lines
        1 mm aluminum core
        1 cm thick insulation
        2700 kg/m^3 density
        2.3 x 10^{-6}/deg C coefficient of thermal expansion

Thermal Control
  Telescopes
        7.0 m radius Teflon MLI surface shield
        7.0 m radius collapsible, hemispherical Teflon MLI dome
        120 K lunar day
        <77 K lunar night (24 earth hours cooling)

Mirrors
>Teflon MLI optical tube radiation shielding
>150 K lunar day
><77 K lunar night (30 earth hours cooling)

Long delay mirrors
>7.0 m radius Teflon MLI surface shield

All external buildings
>Teflon MLI thermal shield coating

Instrumentation
>IR Instrumentation employs active liquid helium cryogenic cooling
>other instrumentation employs passive heat pipe thermal control system

11.2 Mass Statement

Instrumentation	**2100 kg**
instruments	1000 kg
carousel structure	200 kg
instrument chamber	1000 kg
planet detection module	300 kg
Thermal Control	**6625 kg**
active cooling system	1800 kg
aluminized Teflon covers	985 kg
telescope thermal blankets	3840 kg
Metrology	**1677 kg**
54 optical path lasers	123 kg
432 Mark III lasers	981 kg
33 laser towers	75 kg
27 laser plates	136 kg
54 transmitting optics	54 kg
54 receiving optics	54 kg
27 beamsplitters and plate mirrors	123 kg
27 function generators	135 kg
27 photodetector units	270 kg
fiber optic cables	100 kg
Power	**5042 kg**
6 DIPS	2142 kg
2 converters	200 kg
cable	2700 kg
Pointing and Control	**235 kg**
Structures	**64597 kg**
27 telescopes	48087 kg
3 sending/receiving towers	11700 kg
108 mirror towers	3175 kg
3 metrology towers	635 kg
1 metrology building	1000 kg
1 central building	500 kg

Achromatic Null	**170 kg**
2 cart structures	100 kg
optics	20 kg
vibrational damping platform	50 kg

Beam Combination	**405 kg**
81 splitters	81 kg
27 elliptical mirrors	54 kg
270 apertures	270 kg

Fine Delay Lines	**5093 kg**
fine delay line structure	5041 kg
flat mirrors	2 kg
parabolic mirrors	20 kg
computers	27 kg
miscellaneous	3 kg

Communications	**125 kg**
2 two meter antennas	9 kg
2 antenna mounts	23 kg
2 transponders	18 kg
amplifier	7 kg
central computer	18 kg
power system	5 kg
structure, cables	45 kg

Total Launched Mass	**86,833 kg**

References

1.3-1   Large Lunar Telescope (LLT) Report, LLT-001, NASA Marshall Space Flight Center, March 1991, pp. 49-79.

1.3-2   Burke, B., "VLBI at Optical and Radio Wavelengths," European Space Agency paper SP-226, Proceedings of the Colloquium on Optical Arrays in Space, 1985, pp. 177-183.

1.3-3   Simon, R., et al, "Big Optical Array: An Imaging Interferometer,: Naval Research Laboratory, 1990, pp. 4-6.

1.3-4   Hines, B., Shao, M., and M. Colavita, "Use of Laser Metrology Optical Truss for Monitoring Baseline Motion," Proceedings of the SPIE, vol. 1237, 1990, pp. 87-99.

1.3-5   Stockman, H., "Space and Lunar-Based Optical Telescopes," Future Astronomical Observatories on the Moon," 1988, pp. 63-70.

1.3-6   Labeyrie, A., Lemaitre, G., Thom, C., and Vakili, F., "Steps Toward an Optical Very Large Array," pp. 669-693.

1.3-7   Colavita, M., "A Strawman Lunar Interferometer," Presented at the JPL Workshop on Technologies for Space Interferometry, 1990, pp. 233-242.

2.1-1   Burke, B.F., "Astronomical Interferometry On The Moon", Mendell, ed., Lunar Bases, pp. 281-291.

2.2-1   Schmitt, Harrison H., "Constraints on Lunar Base Construction," Engineering, Construction, and Operations in Space, S.W. Johnson and J.P. Wetzel eds., American Society of Civil Engineers, New York, N.Y., pp. 35-43.

2.2-2   Lewis, H. A. G., The Times Atlas of the Moon, Times Newspapers Limited Printing House Square, London, G.B., 1969.

2.3-1   Nein, M., B. Davis, "System concepts for a large UV/optical/IR telescope on the Moon", SPIE Vol. 1494 Space Astronomical Telescopes and Instruments, 1991, pp. 98-110.

2.3-2   Johnson, S., K. Chua and others, "Lunar dust: implications for astronomical observations", SPIE Vol. 1494 Space Astronomical Telescopes and Instruments, 1991, p. 199.

2.3-3   Johnson, C. and K. Dietz, "Effects of the lunar environment on optical telescopes and instruments", SPIE Vol.. 1494 Space Astronomical Telescopes and Instruments, 1991, p. 211.

2.3-4   Ibid, pg. 209.

3.1-1   Johnson, Douglas,"Array Configuration Considerations for the Very Low Frequency Array Final Report", 1988, Ohio.

3.1-2   Colavita, Shao, Hines, Levine, Gershman,"Optical System Design for a Lunar Interferometer", 1-4 April 1991, Orlando, FL.

3.1-3   Napier, Thompson, Ekers, "The Very Large Array: Design Performance of a Modern Synthesis Radio Telescope", Goldsmith, ed., Instrumentation and Techniques for Radio Astronomy, IEEE Press Vol. 71 No. 11, 1983, pp. 125-130.

3.4-1   Oriel Corporation, Optics and Filters, vol. III, 1990, pp. 7-2 to 7-14.

3.4-2   Atherton, P. D., et al, "The Oasis Correlator," in the Proceedings of the
Colloquium on Kilometric Optical Arrays in Space, 1991,
pp. 143-144

3.4-3   Colavita, M. M., et al. "Optical System Design for a Lunar Optical
Interferometer," Proceedings of the SPIE, vol. 1494, 1991,
pp. 168-181.

3.5-1.   Esposito, Larry W. and etc., Strategy for the Detection and
Study of Other Planetary Systems and Extrasolar
Planetary Materials: 1990 - 2000, National Research
Council, 1990, pp. 44 - 56.

3.5-2.   Burke, Bernard F. and etc., TOPS: Toward Other Planetary
Systems, Solar System Exploration Division, 1992, pp. 73 - 99.

3.5-3.   Kingslake, Rudolf, Optical System Design, New York, 1983, pp. 13 - 14.

3.5-4   Colavita, M.M., Shao, M., "Long-Baseline Optical and Infrared Stellar
Interferometry," Annu. Rev. Astron. Astrophys. Vol 30,
1992, pp. 490-492.

3.5-5   Shao, M., Hubble Extra Solar Planet Interferometer, S.P.I.E.,
vol 1494, pp. 347-356.

3.5-6.   Holdaway, M. A., Maximum Entropy Imaging of Polarization in
very long Baseline Interferometry, S.P.I.E., vol. 1351, pp. 714-724.

3.6-1   Hines, Brad, Michael Shao, and M. Mark Colavita. "Use of laser
metrology truss for monitoring baseline motion".
SPIE Vol. 1237 (1990): 87-99.

3.6-2.   Hariharan, P., "Interferometric metrology: Current trends and fututre
prospects," SPIE Vol. 816 Interferometric Metrology, 1987, pp. 4-5.

3.6-3   Personal conversation with Aerometric personnel at Turbo Expo '93,
Cincinnati, Ohio, May 25, 1993.

3.6-4   Danchi, W.C., A. Arthur, R. Fulton, M. Peck, B. Sadoulet, E.C. Sutton,
C.H. Townes, and R.H. Weitzmann. "A high precision telescope
pointing system". SPIE Vol. 628 (1986): 422-428.

3.6-5   Cooley, Thomas, Frederick Breugnot, James Consolover, Herve
Demaries, Jeff Grundvig, Karen Harvey, Patty Jungers,
Zulfiqar Khan, Jim Miller, Vicki Pipal. Lunar Optical
Interferometer System Study Final Report. Pasadena:
California Institute of Technology, 1990.

3.6-6   Colavita, M.M., M. Shao, B.E. Hines, B.M. Levine, and R. Gershman.
"Optical System Design for a Lunar Optical Interferometer".
SPIE Vol. 1494 (1991): 168-181

3.7-1.   Labeyrie, A., Proceedings of the Colloquim on Kilometric Optical
Arrays in Space, France, 1984, pp. 142.

3.7-2.   Newport Catalog, California, 1992, pp. H-32, N-81.

3.7-3.   Jenkins, Francis A. and Harvey E. White, Fundamentals
of Optics, New York, pp. 176-180.

3.7-4.   Gaskill, Jack D., Linear Systems, Fourier Transforms, and Optics,
New York, 359,574.

3.8-1   Johnson, C. and K. Deitz, "Effects of the Lunar Environment
on Optical Telescopes and Instruments," Proceedings for
the SPIE, vol. 1494, 1991, p. 211.

3.8-2   Thompson, R.I., "Infrared Detectors for a 10 m Space or Lunar Telescope," 1989, pp. 310-317.

3.8-3   Moses, D., et al, "Extreme UltraViolet Response of a Tektronix 1024x1024 CCD," Proceedings of the SPIE, vol. 1656, 1992, pp. 526-537.

3.8-4   Personal communication, Bill Stevens, CCD Sales Representative for Tektronix, Inc., 6 April 1993.

3.8-5   Tyson, J. A., et al, "A Large Area CCD Mosaic for Astronomical Imaging," Proceedings of the SPIE, vol. 1656, 1992, pp. 400-408.

3.8-6   Blouke, M. M., et al, "Recent Advances in Short Wavelength AR Coatings for Thinned CCDs," Proceedings of the SPIE, vol. 1656, 1992, pp. 497-507.

3.8-7   McRoberts, J. J., Space Telescope, NASA EP-166, 1982, p. 26.

3.8-8   Lange, G., Weichs, E., Schmidt, U., and Soceikat, D., "Spectrometer/ Radiometer for Measurement of Infrared Signatures from Space," Proceedings of the SPIE, vol. 1340, 1990, pp. 203-216.

3.8-9   Wade, Richard, "A 1-5 micron Cooled Grating Array Spectrometer and Fabry-Perot System for UKIRT," Instrumentation in Astronomy V, Proceedings of the SPIE, vol. 445, 1983, pp. 47-50.

3.9-1   Prasad, S., "Theoretical Sensitivity Limits in Optical Interferometric Imaging", SPIE Vol. 1351, 1990, pp. 674-688.

3.9-2   Roberts, J.A., Indirect Imaging: Measurement and Processing for Indirect Imaging, Cambridge University Press, 1983, pp. 347-371.

3.9-3   Holdaway, M.A., "Maximum Entropy Imaging of Polarization in Very Long Baseline Interferometry", SPIE Vol. 1351, 1990, pp. 714-724.

3.9-4   Gonsalves, R.A., "HST Image Processing: An Overview of Algorithms for Image Restoration", SPIE Vol.1567, 1991, pp. 294-307.

3.9-5   Cornwell, T.J., "The Non-coplanar Baseline Effect in Interferometry", SPIE Vol. 1351, 1990, pp. 706-713.

3.9-6   Proceeding of IEEE Vol. 71 No. 11, Nov. 1983, pp. 1295-1320.

3.9-7   Abernathy, M.F., Wolfe, M.D., "A Simulation of Phased Array Beam Expander to Predict Far-Field Performance", SPIE Vol. 440, 1989, pp. 148-152.

3.9-8   Kulkarni, S.R., "Self-Noise in Interferometers", The Astronomical Journal, Vol. 99 No. 3, Sept. 1989, pp. 1112-1130.

3.9-9   Fienup, J.R., "Experimental Evidence of the Uniqueness of Phase Retrieval From Intensity Data", Roberts, J.A., ed., Indirect Imaging, Cambridge University Press, Cambridge, 1984, pp. 99-109.

3.9-10 Cornwell, and Wilkinson, "Selfcalibration", Roberts, J.A., ed., Indirect Imaging, Cambridge University Press, Cambridge, 1984, p. 216.

3.9-11 "Results and Limitations of Ground-based Optical Arrays", Colloquium on Kilometric Optical Arrays In Space, Cargese, France, 1984, pg. 5.

3.9-12 Davis, "Long Baseline Optical Interferometry", Roberts, J.A., ed., Indirect Imaging, Cambridge University Press, Cambridge, 1984, pp. 125-141.

3.9-13 Crockett, G.A., Strange, D.A., "Computer Model for Evaluating Synthetic Aperture Propagation", SPIE Vol. 440, pp. 77-78.

3.9-14 Levi, L., Applied Optics: A Guide to Optical System Design, Vol. 1, John Wiley and Sons, Inc., New York, pp. 131-155.

5.1-1 Lee, Jim, Director: TOPAZ II Flight Program, "TOPAZ II Flight Program: A National Strategy for Space Nuclear Power."

5.1-2 Thome, Frank, TSET Test Director; Status Briefing for French Delegation from CEA, DGA, CNES; 9 Sept. 1992, Albuquerque, NM.

5.1-3 The John Hopkins University, TOPAZ II Briefing before SDIO.

5.1-4 Lee.

5.2-1 Large Lunar Telescope (LLT) Report, LLP-001, NASA Marshall Space Flight Center, March 1991, pp. 317-344.

5.2-2 Hunt, Maribeth and Richard D. Rovang. "Dynamic Isotope Surface Power Systems," AIAA Conference, 4-6 September, 1991.

5.3-1 Brandhorst, Flood, and Weinberg, "Recent Progress in Space Photovoltaic Systems," NASA Lewis Research Center.

5.3-2 LLT Report.

5.6-1 Upton, Protsik, Gamble, and Otwell, "The Application of SP-100 Technology in a lunar Surface Power System," General Electric Co., 4-6 Sept. 1991.

5.7-1 LLT Report.

5.7-2 Beer, F. P., and Johnston, E. R., Mechanics of Materials, 1981.

5.7-3 Colavita, Shao, Hines, Levine, and Gershman, Optical System Design for a Lunar Interferometer, 1-4 April 1991.

5.7-4 Gaustad, K. L., and Gordon, L. B., "A study of electric power transmission lines for use on the lunar surface," American Institute of Physics, 1991.

6.1-1 Chua, K. M., Kelly M. Golis, and Stewart W. Johnson, "Laboratory Evaluation of Footings for Lunar Telescopes," Engineering, Construction, and Operations in Space, S. W. Johnson and J. P. Wetzel Eds., American Society of Civil Engineers, New York, N.Y., 1992, pp. 1941-1951.

6.1-2 "Large Lunar Telescope," George C. Marshall Space Flight Center, May, 1992.

6.1-3 "Direct Drive DC Motors" (product catalog), Inland Motors, Radford, Virginia.

6.1-4 Gerard, G. and H. Becker, Handbook of Structural Stability - Part III - Buckling of Curved Plates and Shells, NACA Technical Note 3783, 1957, pp. 32-4, 99, 111.

6.1-5 Beer and Johnston, Mechanics of Deformable Bodies,

6.1-6 Roark, R.J. and W.C. Young, Formulas for Stress and Strain, 1975, p. 548.

6.1-7   Gerard and Becker, p. 131.

6.1-8   Roark and Young, pp. 96, 154.

6.1-9   Agrowel, B.N., Design of Geosynchronous Spacecraft, 1986, Table 4.11.

6.1-10   Nicolai, Leland M., Theory of Aircraft Structures

6.1-11   Agrowel

6.1-12   Chua, K.M., S.W. Johnson, and R. Sahu, "Design of a Support and
         Foundation for a Large Lunar Optical Telescope,"
         Proc. SPIE 1494, 1991, pp. 1956-9.

6.1-13   Charles, David, "Unlocking the Potential of Metal Matrix Composites
         for Civil Aircraft," British Aerospace (Commercial Aircraft) Ltd.,
         Bristol (U.K.), Metal Matrix Composites: Proceedings of
         Symposium B on Metal Matrix Composites of the 1990 E-MRS
         Spring Conference, Strasbourg, France, 29 May - 1 June, 1990,
         North - Holland, Amsterdam, 1991, pg. 295.

6.2-1   Marber, A.J., et al, "Lightweight large mirror blanks of Zerodur,"
         Large Optics Technology. Gregory M. Sanger, Editor,
         Proc. SPIE 571, 1986.

6.2-2   Mueller, Rudolf W. and Hoeness, Hartmut W., "Spincast Zerodur mirror
         substrates of the 8 m class and lightweighted substrates for
         secondary mirrors," Advanced Technology Optical Telescopes
         IV, Lawrence D. Barr, Editor, Proc. SPIE 1236, 1990.

6.2-3   Goble, L., Angel, R.P., and Hill, J.M., "Steps toward 8m honeycomb
         mirrors VII. Spin casting an experimental f/1 1.8 m
         honeycomb blank of borosilicate glass," Large Optics Technology,
         Gregory M. Sanger, Editor, Proc. SPIE 571, 1986.

6.2-4   Oriel Corporation, Optics and Filters, Vol. III, 1990,
         pp. 10-1 through 10-9.

6.2-5   Powell, Corey S., "Mirroring the Cosmos," Scientific American,
         November 1991, pp. 113-123.

6.2-6   Roark and Young, pp. 332-373.

6.2-7   Schott Glass Technologies Inc., "Zerodur - Precision from glass ceramics,"
         Company product literature, 1993, pp. 1-31.

6.2-8   National Aeronautics and Space Administration, "Hubble Space
         Telescope Performance Report," Washington, D.C.
         March 25,1991, pp. 3-6.

6.7-1.   Author and Source Unknown, "Infrared Detectors and
         Low-Background Astronomy," p. 155.

6.7-2.   Large Lunar Telescope (LLT) Report, LLT-001, NASA Marshall Space
         Flight Center, March 1991, pp. 277-315.

7.0-1   Large Lunar Telescope (LLT) Report, LLT-001, NASA Marshall Space
         Flight Center, March 1992, pp. 283, 295.

7.1-1   Personal communication, Malcolm Niedner, Hubble Space Telescope
         Scientists, NASA Goddard Space Flight Center, 9 April 1993.

7.3-1   "SIRTF Observatory Design," Proceedings of the SPIE, vol. 619.

7.3-2   Large Lunar Telescope (LLT) Report, LLT-001, NASA Marshall Space
         Flight Center, March 1992, pp. 311.

7.3-3   Wertz, J., and W. Larson, Space Mission Analysis and Design,
         1991, p. 372.

8.0-1   "Large Lunar Telescope," George C. Marshall Space Flight Center, May, 1992.

8.0-2   Chan, Kadett and Alex J. Montoya, "Launching Facility Constraints on the SEI," Engineering, Construction, and Operations in Space, S. W. Johnson and J. P. Wetzel Eds., American Society of Civil Engineers, New York, N.Y., 1992, pp. 2043-2053.

9.1-1   Hunt, Maribeth E., Richard D. Rovang, and Robert Cataldo, "Dynamic Isotope Surface Power Systems," AIAA/NASA/OAI Conference on Advanced SEI Technologies, Cleveland, Ohio, September 4-6, 1991

9.1-2   Cataldo, Robert and Harvey Bloomfield, "Preliminary Assessment of the Power Requirements of a Manned Rover for Mars Missions," Engineering, Construction, and Operations in Space, S. W. Johnson and J. P. Wetzel Eds., American Society of Civil Engineers, New York, N.Y., 1990, pp. 1278-1287.

9.1-3   Gwynne, Owen, et al., "Construction and Development of a Human Base on Mars," Engineering, Construction, and Operations in Space, S. W. Johnson and J. P. Wetzel Eds., American Society of Civil Engineers, New York, N.Y., 1992, pp. 86-95.

9.2-1   University of Texas at Austin, "Design of a Thermal and Micrometeorite Protection System for an Unmanned Lunar Cargo Lander," N90-25161, Fall, 1989.

9.2-2   Schmitt, Harrison H., "Constraints on Lunar Base Construction," Engineering, Construction, and Operations in Space, S. W. Johnson and J. P. Wetzel Eds., American Society of Civil Engineers, New York, N.Y., 1988, pp. 35-43.

9.2-3   Sherwood, Brent, "Lunar Base Elements Designed for Robotic Operations," Engineering, Construction, and Operations in Space, S. W. Johnson and J. P. Wetzel Eds., American Society of Civil Engineers, New York, N.Y., 1990, pp. 994-1004.

9.2-4   Colavita, Mark, Jacob R. Matijevic, and Frank T. Surber, "Lunar Observatory Construction Technologies," Jet Propulsion Laboratory, July, 1992.

9.3-1   "First Lunar Outpost Lunar Habitat Documentation," George C. Marshall Space Flight Center, May 1992.

9.3-2   Chua, K. M. and S. W. Johnson, "Foundation, Excavation, and Radiation Shielding Concepts for the 16m Large Lunar Telescope," SPIE Proceedings, Space Astronomical Telescopes and Instruments, vol 1494, pp. 119-135.

9.5-1   Dias, William C., et al., "Directions for Lunar Construction: A Derivation of Requirements from a Construction Scenario Analysis," Engineering, Construction, and Operations in Space, S. W. Johnson and J. P. Wetzel Eds., American Society of Civil Engineers, New York, N.Y., 1992, pp. 357-367.

9.6-1   Donnelly, J. A., "Simulation of the In-Orbit Maintenance Cycle," Engineering, Construction, and Operations in Space, S. W. Johnson and J. P. Wetzel Eds., American Society of Civil Engineers, New York, N.Y., 1988, pp. 216-218.

9.7-1   Bernold, Leonard E. and Sheri L. Rolfsness, "Earthmoving in the Lunar Environment," <u>Engineering, Construction, and Operations in Space</u>, S. W. Johnson and J. P. Wetzel Eds., American Society of Civil Engineers, New York, N.Y., 1988, pp. 202-215.

9.7-2   Kennedy, Kriss J., and Jeffrey R. Harris, "Dust Control Research for SEI," <u>Engineering, Construction, and Operations in Space</u>, S. W. Johnson and J. P. Wetzel Eds., American Society of Civil Engineers, New York, N.Y., 1992, pp. 398-407.

9.7-3   Kustov, V.; et al., "Biological Effects of Lunar Soil," Problems of Space Biology, Vol. 61, 1989.

Appendix 3.0-1 Signal to Noise Ratio (SNR)

The signal a source emits can be modeled as

$$N = I * W * A * dv / (h * v)$$

where   N = number of photons arriving

       I = Intensity of source (Planck's Law)

       W = Solid angle of the source (r2/4R2)

       A = Collecting area (effective)

       dv = bandwidth of frequency

       v = frequency

       h = Planck's constant

and the power (P) inherent in the energy is represented by

$$P = h * v * N$$

There are several sources of Noise (N) but the dominant is shot noise from the instrumentation which is modeled as

$$N = ÖP$$

Therefore, the simplified SNR is

$$SNR = \text{sqrt} \frac{(2 * r^2 * A * dv * i * t)}{(4 * R^2 * (l^2 * e^{(hc/(l*k*T)} - 1)}$$

where   r = radius of target planet

       i = relative intensity to the sun

       t = integration time

       R = distance to the planet from interferometer

       c = speed of light

       k = constant

       T = temperature

       l = wavelength

and A, dv and h are defined as above. Table 1 shows the implementation of these equations, the baseline configuration of variables and the numerical results for 4 theoretical targets (Earth and Jovian type planets at 5 and 10 parsecs) and the specific contributions of reflective and radiative emission to the signal for an Earth type planet 10 parsecs away. Reflective radiation proves the dominant source of signal across the viewing spectrum.

By inspection of the equations, it can easily be seen that the signal to noise ratio can be improved by increasing the collecting area or increasing the integration time. Additionally, the larger the target, the more reflective radiance will be generated, leading to a better SNR.

There are many other sources of noise (defined as any signal other than the source we are trying to see). The stellar background at 4 K provides some interference in the high infrared range. The temperature of the telescope optics can also be a source of noise but does not become significant until above 10,000 nm. Scattered light from optical elements can also be a problem but is much harder to analyze requiring knowledge of BiReflectance Direction Functions (BRDF) and the photon/quantum nature of light.

Appendix 3.0-1: Signal to Noise Calculations

```
CONSTANTS
pi              3.1415927
h                   6.63E-34 joule sec
k                   1.38E-23 joule/K
c                   3.00E+08 meter/sec
e                   2.72E+00
REQUIREMENTS                                    380 nanometers
S/N                 10              Light       750 nanometers
√ low           2.00E-07 UV             3.80E-07
√ high          1.00E-05 Infrared       7.50E-07
DESIGN VARIABLES
t (time,days)   1.00E+00        86400 sec
√               5.00E-07
v               6.00E+14
bandwith        1.00E+00
Δv              6.00E+14
# of Arrays         27
Diam Array          1.5 Meters
% array         35.00%
Eff CCD             0.7
Effective Area  11.6896701 Meters
TARGET VARIABLES        Earth, 5    Earth, 10   Jove, 5     Jove, 5
Tsun                5800        280         280         300         300 deg Kelvin
I (intensity)   1.00E-09    1.00E-09    1.00E-09    1.00E-07    1.00E-07
rs (planet)     6.38E+06    6.38E+06    6.38E+06    68882400    68882400 meters
parasec to plar 1.00E+01    5           10          10              5 1 parasec =    3.09E+16
W               1.0681E-22  4.272E-22   1.0681E-22  1.2458E-20  4.9833E-20
```

S/N Equation   1.91043449

	Earth, 5 parsec	Earth, 10 par	Jove, 10 parse	Jove, 5
200	0.23045559	0.1152278	1.24446019	2.48892038
500	3.82086897	1.9104345	20.6326924	41.2653849
750	5.91223501	2.9561175	31.9260691	63.8521381
1000	6.87460684	3.4373034	37.1228769	74.2457538
2500	6.98443675	3.4922184	37.7176226	75.4352451
5000	5.7031428	2.8515714	30.8558601	61.7117203
7500	4.94289175	2.4714459	26.8285759	53.6571518
10000	4.46182168	2.2309108	24.2714835	48.5429669

Looking at an Earth Type Planet, 10 parsecs away   60

	Reflective	Radiative	Total	Solar	Telescope
2.00E-07	0.23045559	9.221E-55	0.23045559	3643.82283	#NUM!
5.00E-07	3.82086897	1.099E-21	3.82086897	60413.243	1.5888E-92
7.50E-07	5.91223501	2.011E-14	5.91223501	93480.6435	5.4807E-58
1.00E-06	6.87460684	7.905E-11	6.87460684	108697.078	9.3503E-41
2.50E-06	6.98412358	0.0001566	6.98428016	110428.69	6.5366E-10
5.00E-06	5.67645179	0.0133455	5.68979729	89752.5834	8.48151649
7.50E-06	4.84418099	0.0493554	4.89353637	76593.2266	16740.4526
1.00E-05	4.28707551	0.0873731	4.3744486	67784.6156	683157.641
1.25E-05	3.88412345	0.1174735	4.00159699	61413.384	6012102.85
2.00E-05	3.1298968	0.1637853	3.29368209	49488.0137	137097959
5.00E-05	2.01723672	0.1698038	2.18704053	31895.313	2009160958
1.00E-04	1.43533041	0.1387752	1.57410563	22694.5664	3480052588

Appendix 3.0-2 System Efficiency

The parameter Overall System Efficiency (OSE) affects Total Effective Collecting Area (TECA) by the relation

TECA = Total Collecting Area * OSE

Total Collecting Area is calculated from the surface area of the primary mirrors. OSE is a measure of how much light, of all incoming light that could hit the primary mirror, is actually transmitted to the instruments. OSE is influenced by blockage, such as from secondary mirrors and support struts, and non-ideal reflective surfaces. If the telescope system has 15 mirrors and each is 95% reflective at a given wavelength, only 46% (0.95^{15}) of the incident energy will reach the instruments.

Aluminum and dielectric silver coatings were considered for use. Appendix Figure 3.0-2-1 shows the OSE of the coatings over the operating range of the interferometer. Clearly, silver is the better choice for all wavelengths over 400 nm. Under 400 nm, the reflectivity drops quickly and no energy in the near ultraviolet can be transmitted.

Appendix Table 3.0-2-1 shows the specific OSE after each element in the optical path for a silver coating. This table takes into account the losses due to reflectivity and blockage as well as losses due to planet detection measures.

Total System Efficiency as a Percentage of Received Light Transmitted to Instruments
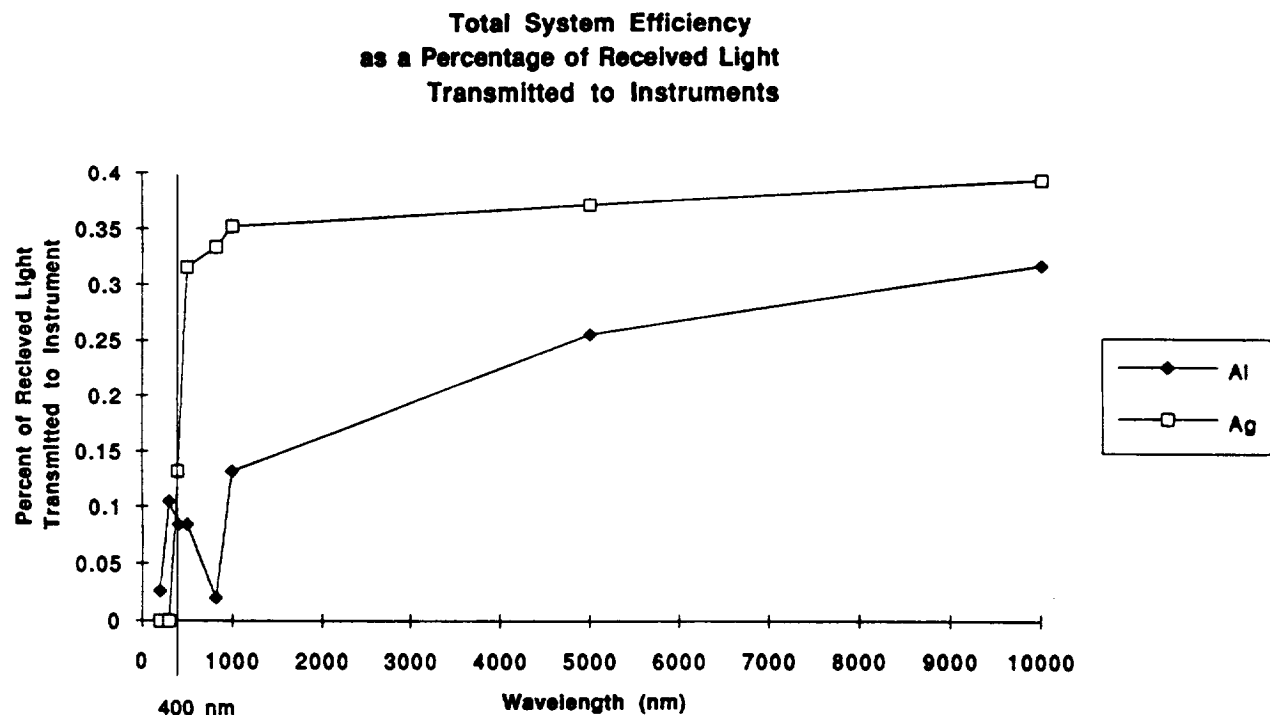
Appendix Figure 3.0-2-1 : Total System Efficiency as a Percentage of Received Light Transmitted to Instruments

Appendix Table 3.0-2-1 : System Efficiency

	Light Path Radius (m)	Blockage Loss (%)	200 nm 0.25	300 nm 0.14	400 nm 0.94	500 nm 0.98	820 nm 0.9825	1000 nm 0.985	5000 nm 0.9875	10000 nm 0.99
Primary *	0.75	8.44%	0.229	0.128	0.861	0.897	0.900	0.902	0.904	0.906
Secondary **	0.125	0.32%	0.057	0.018	0.806	0.877	0.881	0.886	0.890	0.895
Fold	0.125		0.014	0.003	0.758	0.859	0.866	0.872	0.879	0.886
#4	0.125		0.004	0.000	0.713	0.842	0.850	0.859	0.868	0.877
Telescope Exit	0.125		0.001	0.000	0.670	0.825	0.836	0.846	0.857	0.868
LD Receiving	0.125		0.000	0.000	0.630	0.809	0.821	0.834	0.846	0.859
LD Bounce	0.125		0.000	0.000	0.592	0.792	0.807	0.821	0.836	0.851
LD Trans.	0.125		0.000	0.000	0.556	0.776	0.792	0.809	0.825	0.842
FD In	0.125	3.42%	0.000	0.000	0.505	0.735	0.752	0.769	0.787	0.805
FD Com	0.02		0.000	0.000	0.475	0.720	0.739	0.758	0.777	0.797
FD Mobile	0.02		0.000	0.000	0.446	0.706	0.726	0.747	0.768	0.789
FD Bounce	0.02		0.000	0.000	0.420	0.692	0.713	0.735	0.758	0.781
Beam Splitter	0.02	15.00%	0.000	0.000	0.335	0.576	0.596	0.616	0.636	0.658
Aperture	0.02	1.00%	0.000	0.000	0.312	0.559	0.579	0.600	0.622	0.644
Occulting Disc	0.02	5.00%	0.000	0.000	0.279	0.520	0.541	0.562	0.584	0.606
FO prism		15.00%	0.000	0.000	0.223	0.434	0.452	0.470	0.490	0.510
FO Cable		5.00%	0.000	0.000	0.199	0.404	0.422	0.440	0.460	0.480
FO prism		15.00%	0.000	0.000	0.159	0.336	0.352	0.368	0.386	0.404
Inst Filter			0.000	0.000	0.149	0.330	0.346	0.363	0.381	0.400
Inst Mirror			0.000	0.000	0.140	0.323	0.340	0.358	0.376	0.396
Inst Grating			0.000	0.000	0.132	0.316	0.334	0.352	0.371	0.392

* Blockage due to Secondary mirror& support struts (4 at 4 cm radius)
** Blockage due to Metrology Retroreflector of 1 cm diam

		200 nm	300 nm	400 nm	500 nm	820 nm	1000 nm	5000 nm	10000 nm
Reflectivity	Al	0.87	0.93	0.92	0.92	0.86	0.94	0.97	0.98
	Ag	0.25	0.14	0.94	0.98	0.9825	0.985	0.9875	0.99

Appendix 3.1-1 Transformation of Baseline Vectors

I. TRANSFORM BASELINE VECTORS INTO CELESTIAL COORDINATES.

GIVEN: $\begin{bmatrix} N \\ E \\ Z \end{bmatrix}$

KNOW: $\begin{bmatrix} X \\ Y \\ Z \end{bmatrix} = [R] \begin{bmatrix} S \\ E \\ Z \end{bmatrix}$ OR $\begin{bmatrix} X \\ Y \\ Z \end{bmatrix} = [R] \begin{bmatrix} -N \\ E \\ Z \end{bmatrix}$

LET: h = hour of array center

δ = declination of array center

KNOW: $[R] = \begin{bmatrix} \cos h \sin \delta & -\sin h & \cos h \cos \delta \\ \sin h \sin \delta & \cos h & \sin h \cos \delta \\ -\cos \delta & 0 & \sin \delta \end{bmatrix}$

THEREFORE:

Assuming Z due to lunar curvature very small compared to total baseline, let $Z = 0$

$$dX = -dN \cos h \sin \delta - dE \sin h$$
$$dY = -dN \sin h \sin \delta + dE \cos h$$
$$dZ = dN \cos \delta$$

II. TRANSFORM BASELINE VECTORS INTO U - V PLANE.

GIVEN: $u = (-\sin h_s\, dX + \cos h_s\, dY) / \lambda$

$z = (\cos \delta_s \cos h_s\, dX + \cos \delta_s \sin h_s\, dY + \sin \delta_s\, dZ) / \lambda$

$-v = u \times z$

PERFORM CROSS PRODUCT

RESULTS : $-v = (\cos h_s \sin\delta_s\, dX + \sin h_s \sin\delta_s\, dY - \cos\delta_s\, dZ)$

Appendix 3.1-2 Basic Program for Displaying u-v Coverage

```
*    APPENDIX 3.1-2
*
*    BASIC PROGRAM FOR DISPLAYING U-V PLANE COVERAGE
*
*    WRITTEN FOR USE WITH TURBO BASIC
*    FOR COMPILATION TO AN .EXE FILE.
*
**********************************************************************
*
10 REM******SET PLOTTING SURFACE
20
30 SCREEN 2
40 WINDOW SCREEN (1.7E10,1.7E10)-(-1.7E10,-1.7E10)
50
60
70 REM******SET INITIAL VALUES
80
90 WL=.0000005
100 ADEL= 34*3.1415927/180
110 AH=3.1415927/2
120 NUM=27
130 NUMB=NUM*(NUM-1)/2
140
150
160 REM******OPEN INPUT AND OUTPUT FILES
170
180 OPEN "A:BL5.DAT" FOR OUTPUT AS #1
190 OPEN "A:CONFIG5.DAT" FOR INPUT AS #2
200
210
300 REM******READ CONFIGURATION PLACMENTS
310
320 DIM CORD(2,NUM)
330 FOR J=1 TO NUM
340 FOR I=1 TO 2
350 INPUT #2, CORD(I,J)
360 NEXT I
370 NEXT J
380
390
1000 REM******INITILIZE K AND DIMENSION ARRAYS
1010
1020 K=1
1030 DIM BLE(NUMB)
1040 DIM BLN(NUMB)
1050 DIM BLX(NUMB)
1060 DIM BLY(NUMB)
1070 DIM BLZ(NUMB)
1080 DIM BL (NUMB)
1090
1100
1200 REM******COMPUTE BASELINES
1210
1220 FOR H=1 TO (NUM-1)
```

```
1230 FOR I=(1+H) TO NUM
1240 BLE(K) = CORD(1,I)-CORD(1,H)
1250 BLN(K) = CORD(2,I)-CORD(2,H)
1260 BLX(K) = -BLN(K)*SIN(ADEL)*COS(AH)-BLE(K)*SIN(AH)
1270 BLY(K) = -BLN(K)*SIN(ADEL)*SIN(AH)+BLE(K)*COS(AH)
1280 BLZ(K) =    BLN(K)*COS(ADEL)
1290 BL(K) = SQR(BLX(K)*BLX(K)+BLY(K)*BLY(K)*BLZ(K)*BLZ(K))
1300 PRINT #1, K,BL(K)
1310 K=K+1
1320 NEXT I
1330 NEXT H
1340
1350
1400 REM******CLEAR SCREEN AND SET SOURCE DECLINATION
1410
1420 CLS
1430 DEL = 0.0*3.1415927/4
1440
1450
1500 REM******CONSTRUCT COORDINATE AXIS
1510
1520 LINE (-1.5E10,0.0) - (1.5E10,0.0)
1530 LINE (0.0,-1.5E10) - (0.0,1.5E10)
1820
1830
2000 REM******PRINT NOTES
2010
2020 PRINT "Y ARRAY U,V PLANE COVERAGE"
2030 PRINT "CONFIG #5"
2040 PRINT "27 ARRAY ELEMENTS"
2070 IF DEL<0.0 THEN DEL=DEL+3.14159
2080
2090
2100 REM******PRINT U-V ELIPISES
2110
2120 AI=AH-1.5707
2130 FOR K=1 TO NUMB
2140     U=(-1.0*BLX(K)*SIN(AI)+BLY(K)*COS(AI))/WL
2150     V=(SIN(DEL)*(-1.0*BLX(K)*COS(AI)
        -BLY(K)*SIN(AI))+BLZ(K)*COS(DEL))/WL
2160     PSET (U,-V)
2170 FOR A=(AH-1.5707) TO (AH+1.5707) STEP (3.1415927/100)
2180     U=(-1.0*BLX(K)*SIN(A)+BLY(K)*COS(A))/WL
2190     V=(SIN(DEL)*(-1.0*BLX(K)*COS(A)
        -BLY(K)*SIN(A))+BLZ(K)*COS(DEL))/WL
2200     LINE -(U,-V)
2210 NEXT A
2220     U=(-1.0*BLX(K)*SIN(AI)+BLY(K)*COS(AI))/WL
2230     V=(SIN(DEL)*(-1.0*BLX(K)*COS(AI)
        -BLY(K)*SIN(AI))+BLZ(K)*COS(DEL))/WL
2240     PSET (-U,V)
2250 FOR A=(AH-1.5707) TO (AH+1.5707) STEP (3.1415927/100)
2260     U=(-1.0*BLX(K)*SIN(A)+BLY(K)*COS(A))/WL
2270     V=(SIN(DEL)*(-1.0*BLX(K)*COS(A)
```

```
                    -BLY(K)*SIN(A))+BLZ(K)*COS(DEL))/WL
2280       LINE -(-U,V)
2290 NEXT A
2300 NEXT K
3000 END
```

Appendix 3.1-3   Scripts to Create VLA plots and u-v Arcs

```
# "S" script to create Very Large Array (VLA) u-v plot
#  for a particular declination

par(pty='s') # Ensure square plotting region
source 'noplot.400' # initialize plotting surface axes

# form (i,j) pairs for all 351 antenna baselines,
#  and then invoke the plotting macro with each pair
for (il in seq(27)){
        for (jl in seq(27)){
                index1 <- il
                index2 <- jl
                ?uv.vla(index1,index2)
        }
}




MACRO uv.vla(par1,par2)

# S macro to calculate u-v arcs for the VLA

({

# 'hour' is a 20-element vector containing hour angles
        hour <- seq(-pi/2,pi/2,len=20) # 20 points from 6 hrs east to 6 west

# calculate u-v coordinates for the arc (each is also 20 elements)
        ucoord <- (vla.x[$2]-vla.x[$1])*sin(hour) +
                (vla.y[$2]-vla.y[$1])*cos(hour)
        vcoord <- sin(declination)*(-1*(vla.x[$2]-vla.x[$1])*cos(hour) +
                (vla.y[$2]-vla.y[$1])*sin(hour)) +
                (vla.z[$1]-vla.z[$2])*cos(declination)

# plot lines
        lines(ucoord,vcoord,pch='.')
# plot conjugate lines
        lines(-ucoord,-vcoord,pch='.')

})
END
```

Appendix 3.1-4 BASIC Program for Computing Array Taper Ratios

```
*  APPENDIX 3.1-4
*
*  BASIC PROGRAM FOR COMPUTING ARRAY TAPER RATIOS
*
*  WRITTEN FOR USE WITH TURBO BASIC
*  FOR COMPILATION TO AN .EXE FILE.
**********************************************************************
*
10  NUM=27
20  ADEL=0.0
30  AH=3.1415927/2
260  NUMB=NUM*(NUM-1)/2
270  OPEN "A:BLHISTS.DAT" FOR OUTPUT AS #1
280  OPEN "A:CONFIGS.DAT" FOR INPUT AS #2
300  CLS
400  DIM CORD(2,NUM)
500  FOR J=1 TO NUM
600  FOR I=1 TO 2
700  INPUT #2, CORD(I,J)
710  NEXT I
720  NEXT J
1050  K=1:M=0:N=0:O=0:P=0:Q=0:R=0:S=0:T=0:U=0:V=0
1070  DIM BLE(NUMB)
1080  DIM BLN(NUMB)
1100  DIM BLX(NUMB)
1200  DIM BLY(NUMB)
1300  DIM BLZ(NUMB)
1350  DIM BL (NUMB)
1400  FOR H=1 TO (NUM-1)
1500  FOR I=(1+H) TO NUM
1600  BLE(K) = CORD(1,I)-CORD(1,H)
1700  BLN(K) = CORD(2,I)-CORD(2,H)
1800  BLX(K) = -BLN(K)*SIN(ADEL)*COS(AH)-BLE(K)*SIN(AH)
1820  BLY(K) = -BLN(K)*SIN(ADEL)*SIN(AH)+BLE(K)*COS(AH)
1825  BLZ(K) = BLN(K)*COS(ADEL)
1830  BL(K) = SQR(BLX(K)*BLX(K)+BLY(K)*BLY(K)+BLZ(K)*BLZ(K))
1860  IF BL(K)<= 500. THEN M=1+M
1861  IF BL(K)>500. THEN IF BL(K)<=1000. THEN N=N+1
1862  IF BL(K)>1000.0 THEN IF BL(K)<=1500. THEN O=O+1
1863  IF BL(K)>1500.0 THEN IF BL(K)<=2000. THEN P=P+1
1864  IF BL(K)>2000.0 THEN IF BL(K)<=2500. THEN Q=Q+1
1865  IF BL(K)>2500.0 THEN IF BL(K)<=3000. THEN R=R+1
1866  IF BL(K)>3000.0 THEN IF BL(K)<=3500. THEN S=S+1
1867  IF BL(K)>3500.0 THEN IF BL(K)<=4000. THEN T=T+1
1868  IF BL(K)>4000.0 THEN IF BL(K)<=4500. THEN U=U+1
1869  IF BL(K)>4500.0 THEN V=V+1
1890  REM PRINT #1, K,BL(K)
1900  K=K+1
2000  NEXT I
2100  NEXT H
3250  PRINT #1, N,M,O
3251  PRINT #1, P,Q,R
3252  PRINT #1, S,T,U,V
3300  END
```

Appendix 3.2-1 Mersenne Afocal System Equations

The telescope, basically a compression device, was designed from equations utilizing the laws of optical geometry (Ref. 3.2-1). The equations that follow are in terms of the 5 major mirror errors (Sect. 2.5.5) and are written as:

$$A = ((1-W)/2d)3 (Dd1 - WDd2)$$
$$B = At - (1-W) 3 / 8d * Dd2$$
$$C = -2At(t+d/W) +2B(2t+d/W)$$
$$D = 1/2 C + (1-W)2 / 2d W$$
$$E = A t2 (t+d/W) - B t (3t +2 d/W) + C(t + d/2W) + Dt - (1-W) (1+ 3W) / 4W$$

where   A = Spherical Aberration
               B = Coma
               C = Stigmatism
               D = Distortion
               E = Field Curvature
               d = mirror separations
               t = entrance pupil distance
               W = paraxial ray height ratio (compression ratio)
               d1= aspheric deformation constant
               d2= aspheric deformation constant

A can be made = 0 if (Dd1 - WDd2) = 0 thus Dd1 = WDd2. This allows simplification of B & C by dropping out the A term making:

$$B = (1-W) 3 / 8d * Dd2$$
$$C = 2B(2t+d/W)$$

If Dd2 = 0 then C = 0 as well. With both Dd2 and Dd1 = 0 one knows the surfaces of both mirrors must be Cartesian. This leaves distortion and field curvature with:

$$D = (1-W)2 / 2d W$$
$$E = Dt - (1-W) (1+ 3W) / 4W$$

Thus, in designing an afocal mirror system stigmatism, aberrations and coma can be removed by requiring Cartesian mirror surfaces. This leaves the design variables of t, W, and d to adjust. Selection of the proper compression ratio drives E to zero after which D can be reduced.

Appendix 3.2-2 Mirror Control Technology

Delay and directing mirrors have to be controlled to considerable accuracy. Controlled mirrors include the telescope to delay mirror (#5), the long delay receiving mirror (#6) and the long delay transmitting mirror (#8). Each mirror has to be controlled about two axes for which several different design possibilities exist. Motors similar to those found in high precision optical operations (Ref. 3.2-2) can be used to turn the mirrors. An independent 4 beam interferometry metrology system between each mirror set will be used to establish a simple open loop control law to enable fine positioning of mirrors.

Appendix 3.2-3 Telescope / Long Delay Line Placement Systems

Some method of transmitting light to the central delay tower without it suffering interference with other telescopes was necessary. Each telescope during various parts of its operation can block up to a 3 m radius sphere, centered about the upper rotation axis. Placement of each telescope can be assumed to be accurate within 5 cm. Each light path is 25 cm wide therefore 125 cm clearance is needed. The summation of these separate clearances gives a total separation between light paths of 3.13 meters to insure that no blockage occurs.

A nominal line can be drawn from any central target. If sources (in this case telescopes) are distributed on this line the closer ones will block the light of the farther as discussed above. The closer sources will therefore have to be displaced slightly from this nominal line. The farthest can remain directly on the nominal line while the next are displaced off the nominal line. This process continues till all sources are displaced and no longer blocking. As the light travels from displaced sources towards the center, the light path gets closer to the nominal line as it angles in. Thus the closer to the center elements do not have to be placed as far from the nominal line as would initially be supposed.

The developed method of placement takes these solutions into account. The farthest element is located on the nominal center line. The next element is on the right followed by one on the left. This process proceeds with each placement outside of the previous alternating sides. This allows for all light to reach the center with no interference and the smallest reflected angle difference between elements of the line. This method was used for both telescope and long delay bounce mirror placement.

Appendix 3.4-1 Non-redundant Spacing FORTRAN Program

The following is a copy of the program used to determine the nonredundant spacing of the incoming beams prior to combination.

```
*--------------------------------------------------------------

        program  bmspace

        parameter (ntel = 13)

        integer  a(ntel,ntel), b(1200), c(1200), d, h, i, j, k, l
        open (4, file = `con')

        write (4,'(15x,a/)') `Non-redundant beam combination scheme'
        a(2,1) = 1

        do 10 i = 3, ntel

            a(i,1) = a(i-1,1)+i-1

c           Calculate the relative positions of the telescopes
    5       do 20 j = 2, i-1
                a(i,j) = a(i,1)-a(j,1)
   20       continue

            do 30 j = 1, i-1

c           Check non-redundancy with the other values in the matrix
                do 40 k = 2, i
                    do 50 l = 1, k-1
                        if ((i .ne. k) .and. (j .ne. l)) then
                            if (a(i,j) .eq. a(k,l)) then
c                           a redundant spacing was found
c                           increment the telescope placement by one
                                a(i,1) = a(i,1) + 1
                                go to 5
                            end if
                        end if
   50               continue
   40           continue

   30       continue

   10 continue

c    Define the variables needed to relate the data sequentially
c    in terms of the relative spacings
     do 60 n = 1, a(ntel,1)
         do 70 i = 2, ntel
             do 80 j = 1, i-1
                 if ( a(i,j) .eq. n ) then
                     b(n) = i+j
                     c(n) = i-j
                     go to 15
```

```fortran
                end if
 80          continue
 70       continue

          b(n) = 0
          c(n) = 0

 15 continue
 60 continue

          d = mod(a(ntel,1),10)
          h = int(a(ntel,1)-d)

c         Write all of the complete lines of ten spacings
          write (4,(4x,72(=)))
          do 90 i = 1, h, 10
              write (4,500) (i+j, j=0,9)
              write (4,505) ((b(i+j)+c(i+j))/2,,,
     .                      (b(i+j)-c(i+j))/2, j=0,9)
              write (4,(4x,72(=)))
 90       continue

c         Write the remainder of the spacings
          write (4,500) (h+j, j=1,d)
          write (4,505) ((b(h+j)+c(h+j))/2,,,(b(h+j)-c(h+j))/2, j=1,d)
          write (4,(4x,72(=)))

 500 format (dist,10(1x,i4,2x))
 505 format (pair,10(1x,i2,a1,i2,1x))

          end
```

Appendix 3.4-2 Results of Non-redundant Spacing Program

```
dist = spacing in terms of unit value, a
pair = telescope pair with corresponding baseline distance
```

dist	1	2	3	4	5	6	7	8	9	10
pair	2, 1	3, 2	3, 1	4, 3	5, 4	4, 2	4, 1	6, 5	5, 3	7, 6

dist	11	12	13	14	15	16	17	18	19	20
pair	5, 2	5, 1	6, 4	8, 7	10, 9	11,10	6, 3	7, 5	6, 2	6, 1

dist	21	22	23	24	25	26	27	28	29	30
pair	9, 8	15,14	7, 4	8, 6	13,12	12,11	7, 3	22,21	7, 2	7, 1

dist	31	32	33	34	35	36	37	38	39	40
pair	11, 9	8, 5		14,13	9, 7	10, 8	8, 4	17,16		19,18

dist	41	42	43	44	45	46	47	48	49	50
pair	8, 3	12,10	8, 2	8, 1	9, 6	28,27	25,24	16,15		10, 7

dist	51	52	53	54	55	56	57	58	59	60
pair	13,11	11, 8	9, 5	27,26		15,13	12, 9	9, 4	14,12	10, 6

dist	61	62	63	64	65	66	67	68	69	70
pair		9, 3		9, 2	9, 1	11, 7	13,10	10, 5	23,22	16,14

dist	71	72	73	74	75	76	77	78	79	80
pair	18,17		10, 4	20,19		11, 6	10, 3	12, 8	10, 2	10, 1

dist	81	82	83	84	85	86	87	88	89	90
pair	15,12	13, 9		11, 5	14,11	17,15			11, 4	21,20

dist	91	92	93	94	95	96	97	98	99	100
pair		12, 7	11, 3	26,25	11, 2	11, 1	23,21			28,26

dist	101	102	103	104	105	106	107	108	109	110
pair	14,10	12, 6	13, 8	16,13			15,11	17,14	18,16	12, 5

dist	111	112	113	114	115	116	117	118	119	120
pair	19,17		24,23	20,18	12, 4	14, 9	13, 7	22,20	12, 3	

dist	121	122	123	124	125	126	127	128	129	130
pair	12, 2	12, 1	15,10				13, 6		16,12	

dist	131	132	133	134	135	136	137	138	139	140
pair					13, 5		14, 8	15, 9		13, 4

dist	141	142	143	144	145	146	147	148	149	150
pair	26,24	17,13	29,28	13, 3		13, 2	13, 1	27,25	19,16	

dist	151	152	153	154	155	156	157	158	159	160
pair	14, 7				16,11		18,15		15, 8	25,23

dist	161	162	163	164	165	166	167	168	169	170
pair	14, 6			21,19			17,12		14, 5	

dist	171	172	173	174	175	176	177	178	179	180
pair	16,10		15, 7	14, 4				14, 3	18,14	14, 2

dist	181	182	183	184	185	186	187	188	189	190
pair	14, 1	24,22	15, 6		20,17	16, 9	23,20		29,27	

dist	191	192	193	194	195	196	197	198	199	200
pair	15, 5	22,19	17,11	28,25	27,24	15, 4	19,15			15, 3

dist	201	202	203	204	205	206	207	208	209	210
pair		15, 2	15, 1	21,18			16, 8		17,10	24,21

dist	211	212	213	214	215	216	217	218	219	220
pair			18,13						19,14	

dist	221	222	223	224	225	226	227	228	229	230
pair	16, 7		20,16	17, 9					25,22	

dist	231	232	233	234	235	236	237	238	239	240
pair	16, 6	22,18						18,12	16, 5	

dist	241	242	243	244	245	246	247	248	249	250
pair	28,24		29,26	16, 4	17, 8			16, 3		16, 2

dist	251	252	253	254	255	256	257	258	259	260
pair	16, 1		19,13	26,23			25,21		17, 7	

dist	261	262	263	264	265	266	267	268	269	270
pair	23,19			18,11					17, 6	

dist	271	272	273	274	275	276	277	278	279	280
pair	20,15				21,17		17, 5	19,12		18,10

dist	281	282	283	284	285	286	287	288	289	290
pair		17, 4				17, 3		17, 2	17, 1	

dist	291	292	293	294	295	296	297	298	299	300
pair			20,14		18, 9					24,20

dist	301	302	303	304	305	306	307	308	309	310
pair	23,18		22,17	19,11				27,23		

dist	311	312	313	314	315	316	317	318	319	320
pair			21,16			18, 8				19,10

dist	321	322	323	324	325	326	327	328	329	330
pair			26,22				20,13			18, 7

dist	331	332	333	334	335	336	337	338	339	340
pair					19, 9		29,25			18, 6

dist	341	342	343	344	345	346	347	348	349	350
pair	22,16						25,20	18, 5		

dist	351	352	353	354	355	356	357	358	359	360
pair	26,21	20,12	18, 4	28,23		19, 8	18, 3		18, 2	18, 1

dist	361	362	363	364	365	366	367	368	369	370
pair	21,15									19, 7

dist	371	372	373	374	375	376	377	378	379	380
pair		23,17		24,19			27,22	20,11		19, 6

dist	381	382	383	384	385	386	387	388	389	390
pair			21,14	29,24				19, 5	22,15	

dist	391	392	393	394	395	396	397	398	399	400
pair			19, 4	20,10			19, 3		19, 2	19, 1

dist	401	402	403	404	405	406	407	408	409	410
pair					27,21				20, 9	23,16

dist	411	412	413	414	415	416	417	418	419	420
pair	22,14			24,18			21,13			

dist	421	422	423	424	425	426	427	428	429	430
pair	25,19		28,22							20, 8

dist	431	432	433	434	435	436	437	438	439	440
pair										

dist	441	442	443	444	445	446	447	448	449	450
pair	26,20	21,12		20, 7	22,13					

dist	451	452	453	454	455	456	457	458	459	460
pair	28,21			20, 6				23,15		

dist	461	462	463	464	465	466	467	468	469	470
pair	25,18	20, 5					20, 4	21,11		22,12

dist	471	472	473	474	475	476	477	478	479	480
pair	20, 3		20, 2	20, 1						23,14

dist	481	482	483	484	485	486	487	488	489	490
pair				21,10	24,17					

dist	491	492	493	494	495	496	497	498	499	500
pair					27,20	22,11	29,23		21, 9	

dist	501	502	503	504	505	506	507	508	509	510
pair										

dist	511	512	513	514	515	516	517	518	519	520
pair		22,10		23,13	26,19					21, 8

dist	521	522	523	524	525	526	527	528	529	530
pair			24,16				22, 9			

dist	531	532	533	534	535	536	537	538	539	540

pair		25,17		21, 7					23,12	
dist	541	542	543	544	545	546	547	548	549	550
pair	28,20			21, 6				22, 8		
dist	551	552	553	554	555	556	557	558	559	560
pair		21, 5			26,18		21, 4			
dist	561	562	563	564	565	566	567	568	569	570
pair	21, 3	22, 7	21, 2	21, 1	23,11	29,22			27,19	25,16
dist	571	572	573	574	575	576	577	578	579	580
pair	24,15	22, 6								22, 5
dist	581	582	583	584	585	586	587	588	589	590
pair	23,10				22, 4				22, 3	
dist	591	592	593	594	595	596	597	598	599	600
pair	22, 2	22, 1	24,14	29,21		23, 9				
dist	601	602	603	604	605	606	607	608	609	610
pair									27,18	
dist	611	612	613	614	615	616	617	618	619	620
pair					28,19		23, 8	25,15		
dist	621	622	623	624	625	626	627	628	629	630
pair						26,17	24,13			
dist	631	632	633	634	635	636	637	638	639	640
pair	23, 7									25,14
dist	641	642	643	644	645	646	647	648	649	650
pair	23, 6								23, 5	
dist	651	652	653	654	655	656	657	658	659	660
pair		24,12		23, 4	28,18			23, 3		23, 2
dist	661	662	663	664	665	666	667	668	669	670
pair	23, 1			26,16						
dist	671	672	673	674	675	676	677	678	679	680
pair				25,13				24,11		27,17
dist	681	682	683	684	685	686	687	688	689	690
pair				29,20						
dist	691	692	693	694	695	696	697	698	699	700
pair				24,10					25,12	
dist	701	702	703	704	705	706	707	708	709	710
pair									24, 9	
dist	711	712	713	714	715	716	717	718	719	720
pair		26,15						27,16		

dist	721	722	723	724	725	726	727	728	729	730
pair					25,11	28,17				24, 8

dist	731	732	733	734	735	736	737	738	739	740
pair				26,14						

dist	741	742	743	744	745	746	747	748	749	750
pair	25,10			24, 7						

dist	751	752	753	754	755	756	757	758	759	760
pair				24, 6		25, 9		29,19		

dist	761	762	763	764	765	766	767	768	769	770
pair		24, 5		28,16		27,15	24, 4	26,13		

dist	771	772	773	774	775	776	777	778	779	780
pair	24, 3		24, 2	24, 1			25, 8			

dist	781	782	783	784	785	786	787	788	789	790
pair								27,14		

dist	791	792	793	794	795	796	797	798	799	800
pair	25, 7		26,12					29,18		

dist	801	802	803	804	805	806	807	808	809	810
pair	25, 6								25, 5	

dist	811	812	813	814	815	816	817	818	819	820
pair		28,15		25, 4				25, 3	26,11	25, 2

dist	821	822	823	824	825	826	827	828	829	830
pair	25, 1	27,13								

dist	831	832	833	834	835	836	837	838	839	840
pair				28,14	26,10					

dist	841	842	843	844	845	846	847	848	849	850
pair							27,12			26, 9

dist	851	852	853	854	855	856	857	858	859	860
pair										

dist	861	862	863	864	865	866	867	868	869	870
pair								28,13	29,17	

dist	871	872	873	874	875	876	877	878	879	880
pair	26, 8		27,11							

dist	881	882	883	884	885	886	887	888	889	890
pair					26, 7				27,10	

dist	891	892	893	894	895	896	897	898	899	900
pair			28,12		26, 6					

dist	901	902	903	904	905	906	907	908	909	910
pair			26, 5	27, 9			29,16	26, 4		

dist	911	912	913	914	915	916	917	918	919	920
pair		26, 3		26, 2	26, 1				28,11	

dist	921	922	923	924	925	926	927	928	929	930
pair					27, 8					

dist	931	932	933	934	935	936	937	938	939	940
pair					28,10				27, 7	

dist	941	942	943	944	945	946	947	948	949	950
pair									27, 6	28, 9

dist	951	952	953	954	955	956	957	958	959	960
pair					29,15		27, 5			

dist	961	962	963	964	965	966	967	968	969	970
pair		27, 4				27, 3		27, 2	27, 1	

dist	971	972	973	974	975	976	977	978	979	980
pair	28, 8						29,14			

dist	981	982	983	984	985	986	987	988	989	990
pair					28, 7					

dist	991	992	993	994	995	996	997	998	999	1000
pair					28, 6					

dist	1001	1002	1003	1004	1005	1006	1007	1008	1009	1010
pair			28, 5					28, 4		

dist	1011	1012	1013	1014	1015	1016	1017	1018	1019	1020
pair	29,13	28, 3		28, 2	28, 1					

dist	1021	1022	1023	1024	1025	1026	1027	1028	1029	1030
pair										

dist	1031	1032	1033	1034	1035	1036	1037	1038	1039	1040
pair						29,12				

dist	1041	1042	1043	1044	1045	1046	1047	1048	1049	1050
pair										

dist	1051	1052	1053	1054	1055	1056	1057	1058	1059	1060
pair										

dist	1061	1062	1063	1064	1065	1066	1067	1068	1069	1070
pair		29,11								

dist	1071	1072	1073	1074	1075	1076	1077	1078	1079	1080
pair								29,10		

| dist | 1081 | 1082 | 1083 | 1084 | 1085 | 1086 | 1087 | 1088 | 1089 | 1090 |
| pair | | | | | | | | | | |

| dist | 1091 | 1092 | 1093 | 1094 | 1095 | 1096 | 1097 | 1098 | 1099 | 1100 |
| pair | | | 29, 9 | | | | | | | |

| dist | 1101 | 1102 | 1103 | 1104 | 1105 | 1106 | 1107 | 1108 | 1109 | 1110 |
| pair | | | | | | | | | | |

| dist | 1111 | 1112 | 1113 | 1114 | 1115 | 1116 | 1117 | 1118 | 1119 | 1120 |
| pair | | | | 29, 8 | | | | | | |

| dist | 1121 | 1122 | 1123 | 1124 | 1125 | 1126 | 1127 | 1128 | 1129 | 1130 |
| pair | | | | | | | | 29, 7 | | |

| dist | 1131 | 1132 | 1133 | 1134 | 1135 | 1136 | 1137 | 1138 | 1139 | 1140 |
| pair | | | | | | | | 29, 6 | | |

| dist | 1141 | 1142 | 1143 | 1144 | 1145 | 1146 | 1147 | 1148 | 1149 | 1150 |
| pair | | | | | | 29, 5 | | | | |

| dist | 1151 | 1152 | 1153 | 1154 | 1155 | 1156 | 1157 | 1158 | | |
| pair | 29, 4 | | | | 29, 3 | | 29, 2 | 29, 1 | | |

Appendix 3.9-1 Phase Corruption

Phase corruption, if not severe, still allows the use of standard image synthesis algorithms with limitations in the dynamic range of the resulting image (Ref. 3.9-8). To avoid this loss of dynamic range, or to overcome severe phase corruption in the received signal, a "closure phase" analysis is employed. It should be noted, the data and fringe patterns of the proposed array will include substantial amounts of phase information due to the accuracy of the metrology and the optical path delay system. Therefore, it should be possible to employ a uniqueness algorithm to re-construct the image with the partially incoherent data (Ref. 3.9-9) (Fig. 3.9-14, 3.9-15).

A closure phase is the phase associated with a triangle of array elements within a two dimensional array system (Fig. 3.9-16). Let R_{12}, R_{23}, R_{31} be the fringe phasors on the baselines 12,23,31, respectively. The closure phase of the array triangle is then defined to be

$$P_{123} = T_{12} + T_{23} + T_{31}$$

where T_{ij} is the observed or measured fringe phasor on the baseline jk. Letting C_j be the additional phase introduced by the optical path delay errors in the rays reaching the detector. Then

$$T_{jk} = PH_{jk} + C_j - C_k$$

It is fairly strait forward to show that

$$P_{123} = PH_{12} + PH_{23} + PH_{31}$$

Since the number of "unique" closure phases in an n-element array is only $n_c = (n-1)(n-2)/2$, smaller than the number of baselines $n_b = n(n-1)/2$, the total number of phases needed to completely phase an incoherent array could not be previously achieved without baseline redundancy (Ref. 3.9-8).

A new technique has since been developed by Readhead and Wilkinson to overcome the need to employ baseline redundancy. The algorithm rests on the assumption of a model phase distribution. These model phase distribution can easily be supplied by the partially coherent phase information from the actual interferometer observational data. This "hybrid mapping" technique supplies n_c closure phases from the actual observations and $n_b - n_c$ phases are obtained from the model. A new phase model is then obtained from $I(T_x, T_y)$, where x,y refer to the x,y pixel locations in the u,v plane. R^c_{jk} and R^s_{jk} refer to the time averaged fringe visibility at pixel j,k, real and imaginary, respectively.

Note that: $I(T_x, T_y) = (1/n_b)\ a_{ij}(T_x, T_y)R^c_{jk} + b_{jk}(T_x, T_y)R^s_{jk}$

The previous step is then repeated with $n_b - n_c$ phases supplied by the current model and is continued until convergence (Ref. 3.9-8)

As an improvement upon this algorithm, Cornwell and Wilkinson (1981) and Schwab (1980) developed a phase closure algorithm known as Self-Cal, where the C_i's are implicitly solved, without the arbitrary definition of array element triangles - always a source of

---

conceptual dissatisfaction. The condition that the source must be finite in size and positive throughout provides sufficient data constraints for the implicit calculation of the additional closure phases (Ref. 3.9-8).

In current interferometers, the low SNR (less than 3.0) of the fringe phasors (caused by the short coherence time from atmospheric distortion) has caused problems in the application of the Self-Cal method at optical wavelengths (Ref. 3.9-8). However,

1) the longer coherence time of a lunar interferometer due to the lunar stability and lack of atmosphere
2) the higher SNR (approx. 5-10) of the proposed interferometer
3) the exploitation of a CLEAN and MEM combination to increase the separated signal SNR
4) the accuracy of the optical path delay system and the accuracy of the metrology
5) the extreme sensitivity, dynamic range, resolution and accuracy of the chosen photon detector
6) the fact that the SNR limit for fringe detection is lowered for disturbances with fewer degrees of freedom than encountered with atmospheric turbulence -- as is the case for optical path delay errors (Ref. 3.9-10)
7) the partial coherence of the proposed interferometer
8) the beam combination scheme that interferes the 27 light beams at non-redundant angles, increasing visibility of the fringe phasors
9) the use of pupil plane imaging which increases the visibility of the fringe phasors (Ref. 3.9-11) (Fig. 3.9-17)
10) and the presence of a guide star for use as a zero phase reference (Ref. 3.9-11)

should allow the implementation of Self-Cal. Additionally, a variant of the basic hybrid mapping technique (Haniff, 1987, and Nakajima, 1989) (Ref. 3.9-8) or a hybrid speckle phasing technique (Ref 3.9-12), both proven at optical wavelengths, will be employed as backup algorithms.

Finally, the array is constructed to allow for the movement of some of the array elements to create redundant baselines for the more conventional "bootstrapping" methods of optical phasing. In fact, some of the new "bootstrapping" methods do not require strict baseline redundancy. Thus, the initial array configuration may provide enough near-redundant baselines to employ conventional phasing algorithms without and physical rearrangement of the array elements (Ref. 3.9-10). It is important to realize the only present method of determining the required image reconstruction algorithm is by performing extensive simulations on multiple data sets (Ref. 3.9-9 , 3.9-7).
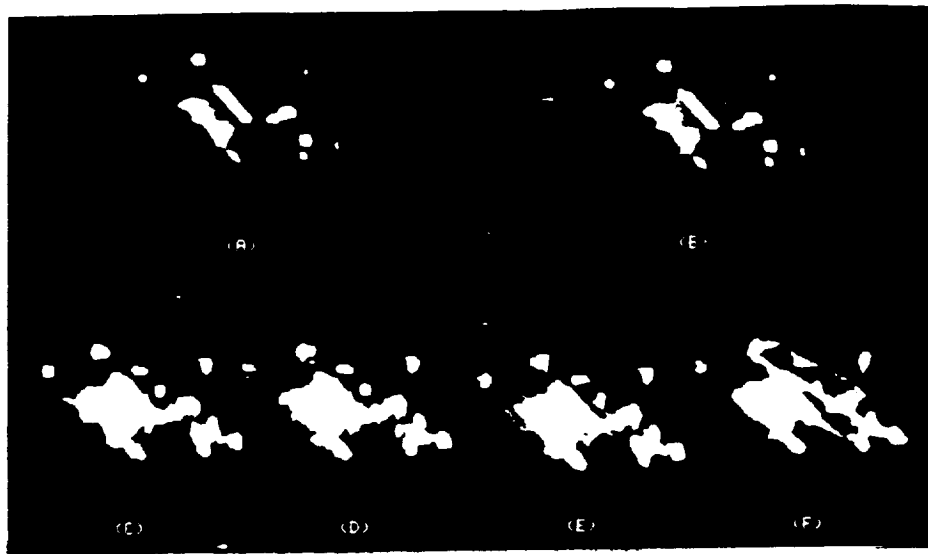
Appendix Figure 3.9-1-1: (a) Original object; (b) image reconstructed from Fourier modulus using iterative algorithm; (c)-(f) four images reconstructed using different starting inputs - these pictures were intentionally overexposed in order to emphasize the stripes (Ref. 3.9-9)
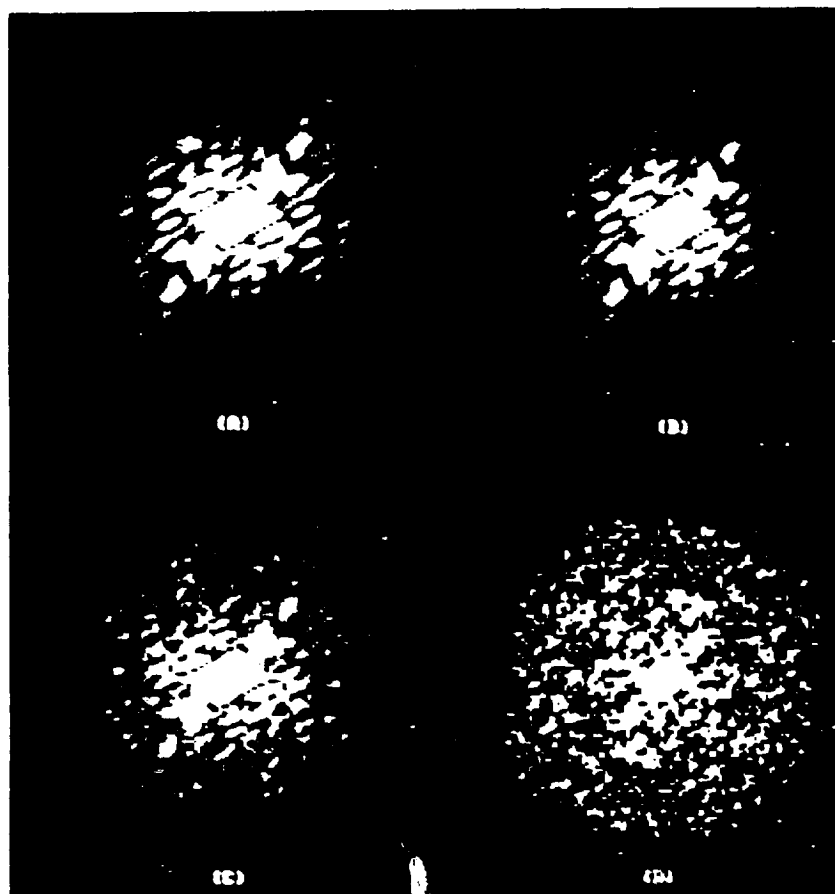
Appendix Figure 3.9-1-2: Fourier Modulus Estimates with Noise, having rms error (a) 0% (b) 2.9%, (c) 32%, (d) 100%. (Ref 3.9-9)
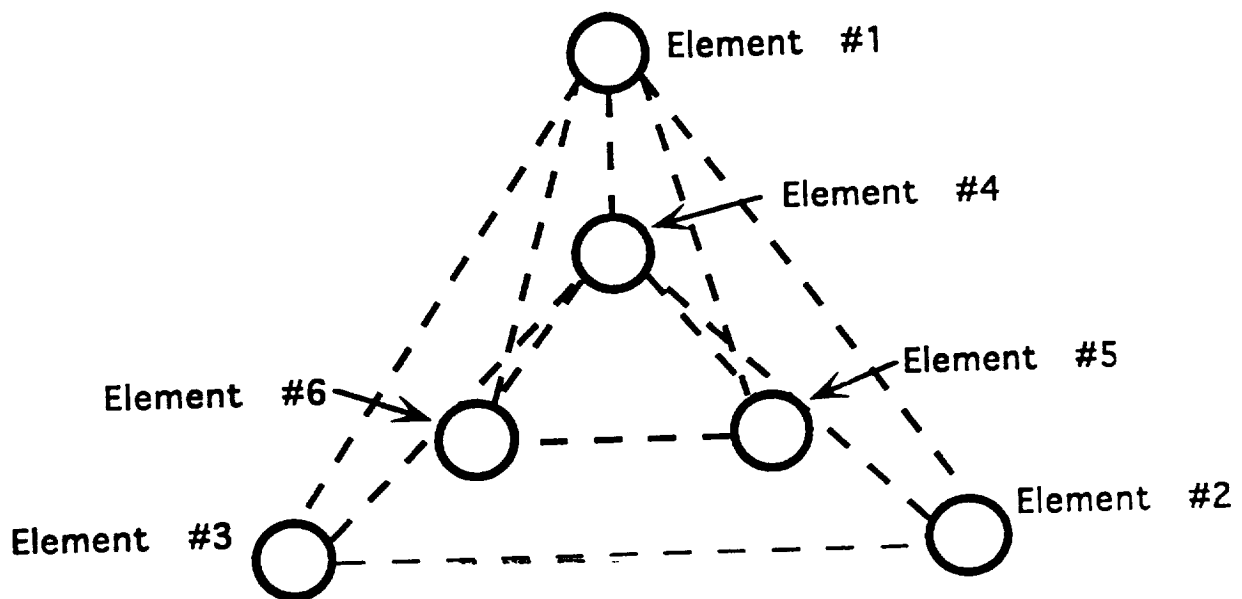
Appendix Figure 3.9-1-3: Six-element Array Showing Representative Phase Closure Triangles
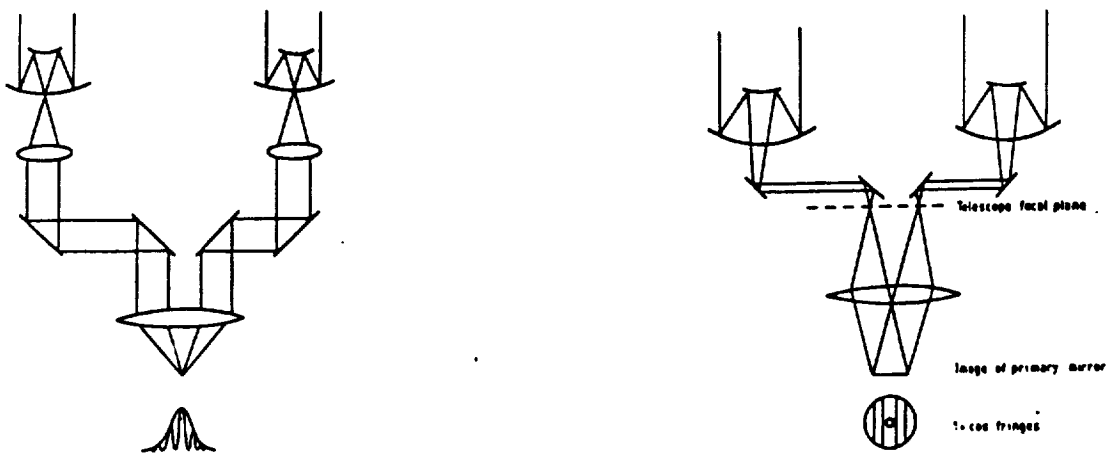
Appendix Figure 3.9-1-4: Image Plane vs. Pupil Plane Interferometry

Appendix 3.9-2 Cleaning Algorithms

The optical system introduces distortion and noise. One model for the data assumes that the distortion is linear and the noise is additive and independent of the distorted object. Therefore, the observed data is a vector D, given by

$$D = PO + N$$

where P is the distortion matrix and N is the noise vector.

The basic problem is to observe the data D and infer the unknown object vector O from the data.

3.9-2.1 Wiener Filter (Fig. 3.9-4)

This can take many forms depending on the assumptions one is willing to make about the statistical behavior of O, N, and P. In the simplest formulation O is assumed to be "white", zero mean, and stationary. That is all elements of O are independent, zero mean random variables with constant variance. Likewise, for the noise. In this case a linear estimator for O will minimizes the mean square error between O and O'. It is:

$$O' = (PP^T + zI)^{-1} D,$$

where z is a noise-to-signal variance parameter.

Usually, neither the noise nor the signal variance is known so one makes several tries at a restored image, with several values for z. From experience, we expect that z=1 will do little (beyond phase) restoration of the object; and z=0.00001 will produce a badly distorted image.

3.9-2.2 Maximum Entropy (Fig. 3.9-4)

One does not necessarily want to drive to zero the mean square error(m), between data, D, and the fit to the data PO'. It is more desirable to drive m to a level that matches the noise energy of the data. It is practical to select the O' that has the largest entropy, where entropy is defined as:

$$h = - \ o'k \ln o'k$$

The FIER (filtered entropy restoration) algorithm uses an iterative method. O'(K+1) is

$$O'(K+1) = WD + sG$$

where WD is the Wiener filtered image, as described earlier, G is the filtered entropy gradients, and s is a step size.

3.9-2.3 Clean Algorithm (Fig. 3.9-3)

This algorithm is widely used, in a variety of forms, by astronomers. It is based on the assumption that the object consists of a multitude of isolated point sources. We adopt a spatial domain notation to explain how it works.

The object is

$$o(x) = a_k \ delta(x-x_k)$$

where a_k is the amplitude of a source located at x_k. The sources are ordered such that $a_1 > a_2 > ...$

The object is distorted by an isoplanic point spread function $p(x)$ so that noiseless data is

$$d(x) = p(x) * o(x),$$

where "*" denotes convolution. When this data is smoothed by $p(-x)$, the result, $g(x)$, will be

$$g(x) = p(-x)*d(x) = \ a_k r(x-x_k),$$

where

$$r(x) = p(-x) * p(x)$$

$r(x)$ is the autocorrelation function (ACF) of the point spread function. Thus $g(x)$ is a weighted sum of autocorrelation functions.

If the sources are widely spaced the peak of $g(x)$ will be at x_1, the location of the brightest source. Thus

$$g(x_1) = \text{peak of } g(x) = a_1 r(0)$$

and

$$a_1 = g(x_1)/r(0)$$

Then, one can subtract this ACF from $g(x)$ and go on to find the next brightest star.

The technique requires modification when star images overlap. This is a reasonably straightforward matrix inversion technique which sorts out the confusion. More serious problems occur when the distortion is not isoplanatic. Then the individual star responses must be estimated before the subtraction.

NOTE: The Appendix 3.9-2 was copied from Reference 3.9-4.

Appendix 3.9-3 Point Spread Function

Optical imaging consists of an effort to combine all spectral radiation of interest from one object point into one point in the image. The distribution of radiation in the image of an object point is called the point spread function (PSF) of the imaging system (Ref. 3.9-13).

$$P(r') - P(x,y) = A(x,y) * \exp(ik \ W(x,y))$$

where: A(x,y) is the amplitude of the field
W(x,y) is the phase disturbance due to optical path delay errors
k is the wave number $(2 * \pi / \lambda)$
r'(x,y) are the pupil co-ordinates centered on the optical axis (Ref. 3.9-14)

The amplitude of the wave arriving at some point in the far-field is given by a 2-D Fourier transform of the PSF.

$$U(r)=U(x,y)=1/(i \ \lambda \ z) \ P(r') \exp (-1 \ (k/2)rr')dr'^2$$

where: r(x,y) are the far-field co-ordinates
z is the propagation distance

In a phased array the pupil function P(r) is best viewed as a sum of N sub-aperture pupil functions.
The irradiance on target is formed by simply adding the N sub-aperture propagated fields and squaring the resulting complex matrix, yielding

$$I(r) = \ u_j(r) \exp ((ik/z) \ r'_j \ r + i \ (\alpha_j)) \ ^2$$

where: I(r) is the irradiant intensity at the target plane
$u_j(r)$ is the diffraction pattern for the jth sub-aperture
α_j are the sub-aperture piston errors (Ref. 3.9-14).

APPENDIX 6.1-1   Moments of Inertia for the Structure

1. Acceleration:
$$\alpha = \Theta/t^2 = (\pi/2 \text{ rad}) / (5 \text{ min} * 60 \text{ sec/min})^2$$
$$\alpha = 1.745 \times 10^{-05} \text{ rad/sec}^2$$

2. Moments of Inertia

ARM MOTOR:
  Optical Cylinder (sectioned at cm):
$$I = [0.5mr^2 + 0.0833ml^2]_1 + [0.5mr^2 + 0.0833ml^2]_2$$
$m_1 = m_2 = 229 \text{ kg}$
$r_1 = r_2 = 0.8 \text{ m}$ $I = 886.241 \text{ kg-m}^2$
$l_1 = 0.762 \text{ m}$
$l_2 = 2.988 \text{ m}$

  Side Arm: $I = mr^2$
    $m = 71 \text{ kg}$ $I = 2.496 \text{ kg-m}^2$
    $r = 0.1875 \text{ m}$

$I = 886.241 + 2.496 = 888.737 \text{ kg-m}^2$

BASE MOTOR:
  Optical Cylinder - use same position for worst case

  Side Arm: $I = 0.5mr^2 + 0.0833ml^2$
    $m = 71 \text{ kg}$
    $r = 0.1875 \text{ m}$ $I = 1.485 \text{ kg-m}^2$
    $l = 0.2 \text{ m}$

  Support Cylinder: $I = mr^2$
    $m = 142 \text{ kg}$ $I = 21.048 \text{ kg-m}^2$
    $r = 0.385 \text{ m}$

  Counterweight: $I = 0.1667ml^2$
    $m = 451 \text{ kg (filled)}$ $I = 43.416 \text{ kg-m}^2$
    $l = 0.75 \text{ m}$

$$I = [886.241 + (458)(1.385)^2] + [1.485 + (71)(0.485)^2]$$
$$+ [43.416 + (451)(2.14)^2]$$
$$= 3912.838 \text{ kg-m}^2$$

APPENDIX 6.1-2   Stress Analysis for the Telescope

Buckling Stress = σ = 0.4CEt/r

    C = constant (from graph of C vs. r/t)
    E = Young's Modulus
    t = thickness
    r = radius

Bending Stress = σ = C_bEt/r

    C_b = constant (from graph of C_b vs. r/t)

Applied Buckling Stress = σ = P/A

    P = applied load
    A = cross-sectional area

Applied Bending Stress = σ = Mr/I

    M = applied moment
    I = moment of inertia

Beam Theory Solutions

deflection of legs = y = -V/kP * [2 tan (kl/2) - kl]

        V = shear load
        P = axial load
        l = length of member
        k = sqrt (P/EI)

deflection of 2nd mirror support rods = y = $-Vl^3/3EI$

Appendix 6.2   Primary Mirror Calculations

MASS CALCUATIONS:

MIRROR EQUATION: $h^2 = 2rz$ WHERE $r = 7.384$

THEREFORE, $h = 3.841614244z^{0.5}$ or $z = 0.067713976h^2$
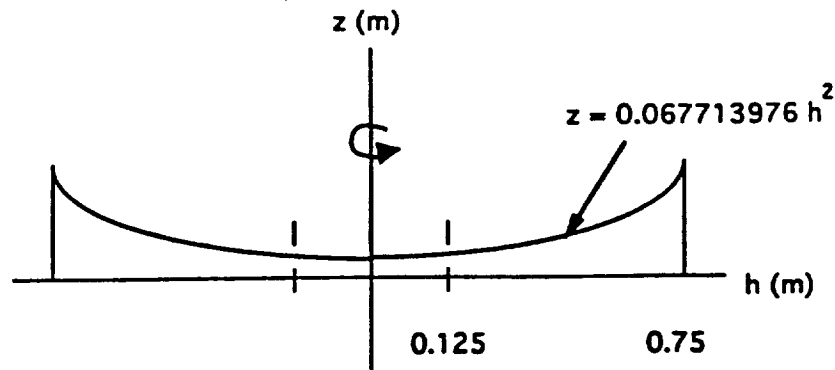
FOR THE CURVED PORTION OF THE MIRROR, USE VOLUME OF REVOLUTION:

$$V = \int_c^d \pi \, [g(y)]^2 \, dy$$

@ $h = 0.125$m, $z = 0.00105803$m

@ $h = 0.750$m, $z = 0.038089111$m

$$V_{\text{curve swept out}} = \int_{0.0010580309}^{0.0380891115} \pi \, [3.841614244 \, z^{0.5}]^2 dz$$

$$V_{\text{curve swept out}} = 14.758\pi \left[\frac{1}{2}z^2 \Big|_{0.0010580309}^{0.0380891115} \right]$$

$$V_{\text{curve swept out}} = 0.03360576871 \text{ m}^3$$

TO ACCOUNT FOR SUPPORT HEIGHT, AND TOP AND BOTTOM MIRROR SUBSTRATE THICKNES
ADD THE FOLLOWING CYLINDRICAL VOLUME:

V_{cylinder} $= \pi \, (0.75^2 - 0.125^2) \, (t_{\text{TOP}} + t_{\text{BOTTOM}} + h_{\text{SUPPORT}} - 0.038089111 \text{ m})$

$= \pi(0.75^2 - 0.125^2) \, (0.02 + 0.02 + 0.16 - 0.038089111) \text{ m}$

$= 0.278172379 \text{ m}^3$

$$V_{total} = V_{curve\ swept\ out} + V_{cylinder}$$
$$= 0.033628539\ m^3 + 0.2178172376\ m^3$$
$$= 0.311800915\ m^3$$

$$mass = V_{total} \cdot \rho_{Zerodur} \cdot 0.25^*$$

* 75% OF HONEYCOMB MIRROR IS AIR

$$mass = 0.311800915\ m^3 \cdot 2530\ \frac{kg}{m^3} \cdot 0.25$$

$$mass_{mirror} = 197.214\ kg$$

GRAPHITE / EPOXY SUPPORT STRUCTURE:

OUTER RIM:
$$V_7 = \pi(0.75^2 - 0.74^2) \cdot 0.3 \qquad = 0.014042919\ m^3 = V_7$$

INNER SUPPORT RINGS:
$$V_1 = \pi(0.125^2 - 0.115^2) \cdot 0.01 \qquad = 0.000075398\ m^3 = V_1$$
$$V_2 = \pi(0.2292^2 - 0.2192^2) \cdot 0.01 \qquad = 0.000140869\ m^3 = V_2$$
$$V_3 = \pi(0.3333^2 - 0.3233^2) \cdot 0.01 \qquad = 0.000206276\ m^3 = V_3$$
$$V_4 = \pi(0.4375^2 - 0.4275^2) \cdot 0.01 \qquad = 0.000271747\ m^3 = V_4$$
$$V_5 = \pi(0.5417^2 - 0.5317^2) \cdot 0.01 \qquad = 0.000337218\ m^3 = V_5$$
$$V_6 = \pi(0.6458^2 - 0.6358^2) \cdot 0.01 \qquad = 0.000402626\ m^3 = V_6$$

$$RING\ MASS = \rho_{Gr/Ep} \cdot (V_1 + V_2 + V_3 + V_4 + V_5 + V_6 + V_7)$$
$$= 1.49 \times 10^3\ \frac{kg}{m^3} \cdot (0.015477053\ m^3) = 23.06\ kg$$

SUPPORTS FOR SUPPORT RINGS:

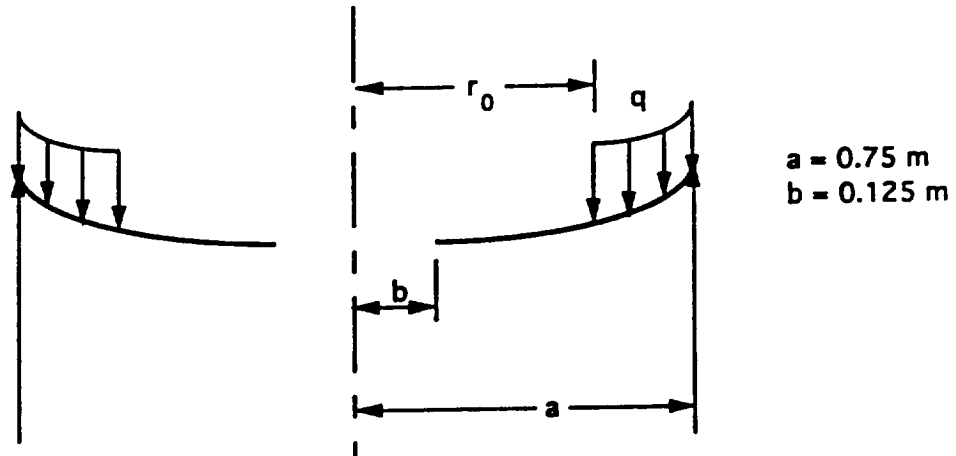$$V_{ring} = \pi \cdot (0.4 \text{ m}) \cdot (0.4375^2 \text{ m} - 0.4355^2 \text{ m}) \qquad \text{AVERAGE VALUES}$$
$$= 0.002194088 \text{ m}^3$$

$$V_{total} = 6 \cdot V_{ring} = 6(0.002194088 \text{ m}^3) = 0.013164529 \text{ m}^3$$

$$mass = \rho \cdot V = 1.49 \times 10^3 \frac{\text{kg}}{\text{m}^3} \cdot 0.013164529 \text{ m}^3$$
$$= 19.62 \text{ kg}$$

$$mass_{total} = m_{mirror} + m_{support\ rings} + m_{supports}$$

$$= 197.214 \text{ kg} + 23.06 \text{ kg} + 19.62 \text{ kg}$$

$$= 239.89 \text{ kg}$$

DEFORMATION CALCULATIONS:

EQUATIONS TAKEN FROM ROARK AND YOUNG'S FORMULAS FOR STRESS AND STRAIN

$$a = 0.75 \text{ m}$$
$$b = 0.125 \text{ m}$$

$$\text{DEFLECTION} = Y_b = \frac{-qa^4}{D}\left(\frac{C_2 L_{17}}{C_8} - L_{11}\right)$$

WHERE $\quad D = \dfrac{Et^3}{12(1 - v^2)} \qquad t = \text{MIRROR THICKNESS}$

$$C_2 = \frac{1}{4}\left[1 - \left(\frac{b}{a}\right)^2\left(1 + 2\ln\frac{a}{b}\right)\right]$$

$$L_{17} = \frac{1}{4}\left\{1 - \frac{1-v}{4}\left[1 - \left(\frac{r_0}{a}\right)^4\right] - \left(\frac{r_0}{a}\right)^2\left[1 + (1 + v)\ln\frac{a}{r_0}\right]\right\}$$

$$C_8 = \frac{1}{2}\left[1 + v + (1 - v)\left(\frac{b}{a}\right)^2\right]$$

$$L_{11} = \frac{1}{64}\left\{1 + 4\left(\frac{r_0}{a}\right)^2 - 5\left(\frac{r_0}{a}\right)^4 - 4\left(\frac{r_0}{a}\right)^2\left[2 + \left(\frac{r_0}{a}\right)^2\right]\ln\frac{a}{r_0}\right\}$$

Appendix 7.1-1 Radiative Heat Transfer - Surface to Telescope

Estimations for Radiative Heat Transfer from the Lunar Surface to the Telescope Structure

A. Effective Surface Area for Radiative Heat Transfer

Large Lunar Telescope approximate height = 20 m
Radius of surface area where 98 percent
   of radiative heat transfer occurs   = 100 m

LOLA telescope height   = 6 m
Radius surface area where 98 percent
   of radiative heat transfer occurs   = 'x'

Apply similar triangle ratios: $x/100 = 6/20$

solution: $x = 30$ m

B. Effect of surface shield calculations:

Over the 30 m radius, the intensity of the energy radiated from the regolith decreases as $1/r^2$. The surface shield has inner and outer radii of 1 m and 7 m, respectively. Based on these factors, the surface shield, along with the laser metrology plates at the base of each telescope, block approximately 41 percent of the radiated energy which would reach a telescope which did not have any surface shielding. From this analysis, a shield factor (SF) is defined as the fraction of the energy which is not blocked by the surface shielding. For the thermal shield used here, SF is 0.59.

Appendix 7.1-2 Thermal Analysis of Telescope, Delay Mirrors

A. Notation

LS	- lunar surface
TS	- telescope structure
FS	- free space
eps	- emissivity
abs	- absorptivity
SB	- Stefan-Boltzmann constant
Q	- heat transfer
T	- temperature
A	- area
time	- time as measured in Earth days
rad	- radiative heat transfer
SF	- shield factor (see Appendix 7.1-1)

B. Heat balance equation for telescope structure

For the range of temperatures on the lunar surface, heat conduction from the lunar regolith to the aluminum footpads for the telescope legs is several orders of magnitude lower than the radiative heat transfer between the surface and the telescope. For this reason, conductive heat transfer in not included in the heat balance equation.

Heat balance equation:
$$SF * (Q(rad\text{-}LS) * abs(TS)) = eps(TS) * Q(rad\text{-}FS)$$
where,

$$Q(rad\text{-}LS) = eps(LS) * SB * A * (T(LS)^4 - T(TS)^4)$$
$$Q(rad\text{-}TS) = eps(TS) * SB * A * (T(TS)^4 - T(FS)^4)$$

T(LS)	$= 60 * exp(\text{-}time) + 90$ (in Kelvin)
T(FS)	$= 3$ (in Kelvin)
eps(TS)	$= 0.64$
abs(TS)	$= 0.125$
eps(LS)	$= 0.95$
FS	$= 1.0$ for no shield, 0.59 with shield

The above equation determines an equilibrium temperature for the telescope. At the start of the lunar night, this equation predicts a telescope temperature of approximately 90 K. However, the protected telescope is heated somewhat during the lunar day. This produces a telescope structure temperature of approximately 120 K when the protective dome over the telescope is lowered at the start of the lunar night. To model this temperature difference, the following equation is employed:

$$T(TS\text{-}final) = (120 - T(TS@time=0)) * exp(\text{-}time) + T(TS)$$

This equation is plotted in Figure 7.2-2 for the telescope with and without a surface shield.

C. Long delay mirror temperature calculations

For the analysis of the long delay mirror temperature, the same procedure and equations are used as described above. However, the thermal coefficients for the mirror are as follows:

eps(TS)   = 0.79
abs(TS)   = 0.077

The results of these calculations for the mirror, both with and without a surface shield, are plotted in Figure 7.2-3.

Acknowledgments

The authors wish to thank the following for their most valuable contributions and suggestions: